High-performance III-V Quantum structures and devices grown on Si substrates

Zizhuo Liu

A thesis submitted to University College London for the degree of *Doctor of Philosophy (Ph.D.)*

Department of Electronic and Electrical Engineering
University College London

2021

Statement of originality

I, Zizhuo Liu, confirm that the work presented in this thesis is my own. Where information has been derived from other sources, I confirm that this has been indicated in the thesis.

Signed:

_____

Date:

_____

Abstract

III-V material laser monolithically grown on silicon (Si) substrate is urgently required to achieve low-cost and high-yield Si photonics. Due to the material dissimilarity between III-V component and Si, however, several challenges, such as dislocations and antiphase domains, remain to be solved during the epitaxial growth. In this regard, quantum dot (QD) laser diodes have been demonstrated with impressive characteristics of temperature insensitive, low power consumption and defects tolerance, and thus QD material is regards as an ideal material for laser directly grown on Si substrate. In this thesis, both QD laser diodes with 1.3 μm wavelength and quantum dot cascade laser with mid-infrared wavelength have been investigated.

To understand the unique advantages of QD material, the comparison of QD and quantum well (QW) materials and devices grown on Si substrate is carried out in chapter 3. Based on identical fabrication and growth conditions, Si-based QW devices are unable to operate at room temperature, while the room-temperature Si-based QD is obtained with threshold current density of 160 A/cm^2 and single-facet output power of >100 mW under continuous wave (c.w.) injection current driving. Besides, Si-based QD laser also shows remarkable temperature stability which the c.w. operation temperature reaches 66 ℃. The results point out that QD material has great potential in monolithic growth of III-V on Si for silicon photonics. Then, a novel approach of all-MBE grown QD laser on Si substrate is reported in chapter 4, with the optimization of buffer layer. The all-MBE grown QD laser on on-axis Si substrate with maximum operation temperature of 130 ^{o}C is achieved by utilizing thin Germanium (Ge) buffer.

The mid-infrared silicon photonics has wide applications and market, but the lack of Si-based mid-infrared laser is a subsistent problem. Because the bandgap of conventional QW and QD materials is impossible to match the wavelength in mid-infrared range (3 μm to 20 μm), the Si-based quantum cascade laser (QCL) devices is regarded as an effective method to meet the requirement. Therefore, the high-performance QCL is firstly explored in chapter 5, and then, several methods in fabrication process are researched to enhance the performance for QCL devices. After

the optimization of structure design and development of fabrication process, the InP-based QCL shows impressive properties with 600 mW emission power and over 100℃ operation temperature under c.w. mode. Following the previous work on Si-based QD laser, the quantum dot cascade laser (QDCL) is expected as a suitable solution for Si-based QCL devices. With the continuous improvement in structure design, the QDCL with multilayer QDs shows comparable performance, compared with conventional QCL devices. It is noted that the QDCL generates both TE and TM modes output, which is a breakthrough towards surface emitting QCL because the common QW-based QCL has only-TM emission in principle. Finally, the Si-based QCL is attempted with different structure design based on the pervious results.

Impact Statement

The aim of this thesis is to develop III-V laser monolithically grown on Si substrate for high performance Si-based laser devices for silicon photonics. Silicon photonics provides low-cost, reliable, and high-speed data transmission, which meets the demand of increasing data traffic. Based on the mature complementary metal-oxide-semiconductor (CMOS) integration technology, the silicon photonics also achieves low-cost and large-scale manufactory after the generation of several Si-based components such as optical modulators, photodetectors and waveguide. However, the reliable Si-based laser source is still missing, which is a main bottleneck of Si-based photonic integrated circuits.

The study in this thesis has the significant impact on III-V material monolithically grown on CMOS-compatible on-axis Si substrate for silicon photonics. Firstly, the QD laser has been demonstrated on on-axis Si substrates. Our research confirms that the QD materials and devices are far more suitable for Si-based lasers, compared with QW-based one. High performance O-band Si-based QD laser is reported with low threshold current density and high operation temperature. Then, all-MBE grown QD laser on on-axis Si substrate is realized by utilizing Ge buffer, which is a meaningful approach for saving the cost of Si photonics manufacturing.

In addition, mid-infrared (3 μm to 20 μm) Si-based light source, particularly quantum cascade laser (QCL), is of great importance in various mid-infrared applications including gas sensing, spectroscopy, and free-space communication, as well as mid-infrared Si photonics. The high performance InP-based QCL with extremely high output power (600 mW) and excellent temperature stability is demonstrated firstly as a preparation for Si-based QCL. Because of the defect tolerance of QD material, this thesis also focuses on the quantum-dot cascade laser (QDCL). Based on the QD multilayer in active region, the QDCL reported in this thesis shows comparable performances, compared with conventional QW-based QCL. Moreover, both the output power and highest operation temperature are the best results among the

published QDCL results. It is first revealed that the QDCL can produce the TE-polarized light emission, which cannot be achieved in the conventional QCL.

Acknowledgements

This thesis was carried out under the supervision of Professor Huiyun Liu and Dr Siming Chen. First of all, I would like to extend my deepest thanks to my supervisor Professor Huiyun Liu, without his support and guidance throughout all my PhD life, it is impossible to complete my projects. I would also like to acknowledge my lovely and friendly second supervisor Dr Siming Chen, the leader and guider for my cleanroom works, his support, encouragement and guidance throughout my work.

I gratefully acknowledge Dr Mingchu Tang and Dr Jae-Seong Park, particularly. I really acknowledge to Dr Mingchu Tang for patience explaining MBE operations in details and growing my samples, also thank a lot for my great partner Dr Jae-Seong Park of saving my poor English writing.

I would also like to acknowledge my colleagues from the MBE group of UCL: Dr Jiang Wu, Dr Mengya Liao, Dr Dongyoung Kim, Dr Yunyan Zhang, Dr Pamela Jurczak, Mr Kevin Lee, Dr Xuezhe Yu, Dr Hao Xu, Mr Shun Chan, Mr Junjie Yang, Miss Shujie Pan, Miss Ying Lu, Miss Victoria Cao, Miss Manyu Dang, Mr Keshuang Li, Mr Haotian Zeng and Mr Huiwen Deng, for their wonderful collaboration. Research is not always easy but thanks to all of you it has been a pleasure.

My gratitude also goes to Jinchuan Zhang and Ning Zhuo, not only for great cooperation but also for guidance in research method. I would like to greatly thank Mrs. Ping Liang for excellent support in sample fabrication, she is the most hardworking people among all people I known. Thanks to Dr. Zenghui Gu and Fengmin Chen for enthusiastically teaching me several simulation software and helping sample test.

Finally, I would like to express my gratitude towards my families, especially my parents. Without their understanding and support, I have no courage to continue the PhD researches, and without their consolation, I could not focus on my research. I really appreciate their encouragement when I feel depressed about my research. I would like to give special thanks to my wife Yunjing Zhang, who has always supported my work everywhere. I know she put a lot of efforts when I was away home, such as

taking care of Garfield Tabi, visiting my parents and dealing with life trivia. I really appreciate her making my life easier and happier.

List of Abbreviations

AFM: Atomic force microscopy
APB: Antiphase boundary
APD: Antiphase domain
CMOS: Complementary metal-oxide-semiconductor
DOS: Density of state
DFL: Dislocation filter layer
DWELL: Dot-in-well
ES: Excited state
FWHM: Full-width-at-half-maximum
GS: Ground state
IC: Integrated circuit
LIV: Light-current-voltage
LI: Light-current
MBE: Molecular beam epitaxy
MOCVD: Metal organic chemical vapor deposition
ML: Monolayer
OEIC: Optoelectronics integrated circuit
PL: Photoluminescence
PIC: Photonic integrated circuit
QW: Quantum well
QD: Quantum dot
QCL: Quantum cascade laser
QDCL: Quantum dot cascade laser
RHEED: Reflection high-energy electron diffraction
RT: Room temperature
SEQCL: Surface emitting quantum cascade laser
SOI: Si-on-insulator
SEM: Scanning electron microscope
SLS: Strained layer superlattice

TEM: Transmission electron microscope

TD: Threading dislocation

TDD: Threading dislocation density

UHV: Ultra-high vacuum

VCSEL: Vertical-cavity surface-emitting laser

WDM: Wavelength division-multiplexing

XRD: X-ray diffraction

Contents

Table of Figures

Publication List

Journal Publications

[1] Liu, Z., Hantschmann, C., Tang, M., Park, J. S., Liao, M., Baron, T., Chen, S., Seeds, A., Martin, H., Lu, Y., Pan, S., Sanchez, A., Beanland, R., Penty, R., White, I.,& Liu, H. (2020). Origin of Defect Tolerance in InAs/GaAs Quantum Dot Lasers Grown on Silicon. *Journal of Lightwave Technology*, *38*(2), 240–248.

[2] Liu, Z., Yang, J., Jurczak, P., Tang, M., Li, K., Pan, S., Sanchez, A., Beanland, R., Zhang, J. C., Wang, H., Liu, F., Li, Z., Shutts, S., Smowton, P., Chen, S., Seeds, A., & Liu, H. (2021). All-MBE grown InAs/GaAs quantum dot lasers with thin Ge buffer layer on Si substrates. *Journal of Physics D: Applied Physics*, *54*(3).

[3] Hantschmann, C., Liu, Z., Tang, M., Chen, S., Seeds, A. J., Liu, H., White, Ian. H., & Penty, R. V. (2020). Theoretical Study on the Effects of Dislocations in Monolithic III-V Lasers on Silicon. *Journal of Lightwave Technology*, *38*(17), 4801–4807.

[4] Li, K., Liu, Z., Tang, M., Liao, M., Kim, D., Deng, H., Sanchez, A. M., Beanland, R., Martin, M., Baron, T., Chen, S., Wu, J., Seeds, A., & Liu, H. (2019). O-band InAs/GaAs quantum dot laser monolithically integrated on exact (0 0 1) Si substrate. *Journal of Crystal Growth*, *511*(January), 56–60.

[5] Zhou, T., Tang, M., Xiang, G., Xiang, B., Hark, S., Martin, M., Baron, T., Pan, S., Park, J. S., Liu, Z., Chen, S., Zhang, Z., & Liu, H. (2020). Continuous-wave quantum dot photonic crystal lasers grown on on-axis Si (001). *Nature Communications*, *11*(1), 1–7.

[6] Wang, Y., Chen, S., Yu, Y., Zhou, L., Liu, L., Yang, C., Liao, M., Tang, M., Liu, Z., Wu, J., Li, W., Ross, I., Seeds, A. J., Liu, H., & Yu, S. (2018). Monolithic quantum-dot distributed feedback laser array on silicon. *Optica*, *5*(5), 528.

[7] Li, K., Yang, J., Lu, Y., Tang, M., Jurczak, P., Liu, Z., Yu, X., Park, J. S., Deng, H., Jia, H., Dang, M., Sanchez, A. M., Beanland, R., Li, W., Han, X., Zhang, J. C., Wang, H., Liu, F., Chen, S., … Liu, H. (2020). Inversion Boundary Annihilation in GaAs Monolithically Grown on On-Axis Silicon (001). *Advanced Optical Materials*, *8*(22), 1–8.

[8] Liao, M., Chen, S., Liu, Z., Wang, Y., Ponnampalam, L., Zhou, Z., Wu, J., Tang, M., Shutts, S., Smowton, P. M., Yu, S., Seeds, A., & Liu, H. (2018). Low-noise 13 μm InAs/GaAs quantum dot laser monolithically grown on silicon. *Photonics Research*, *6*(11), 1062.

[9] Pan, S., Cao, V., Liao, M., Lu, Y., Liu, Z., Tang, M., Chen, S., Seeds, A., & Liu, H. (2019). Recent progress in epitaxial growth of III-V quantum-dot lasers on silicon substrate. *Journal of Semiconductors*, *40*(10).

[10] Pan, S., Huang, J., Zhou, Z., Liu, Z., Ponnampalam, L., Liu, Z., Tang, M., Lo, M.-C., Cao, Z., Nishi, K., Takemasa, K., Sugawara, M., Penty, R., White, I., Seeds, A., Liu, H., & Chen, S. (2020). Quantum dot mode-locked frequency comb with ultra-stable 255 GHz spacing between 20°C and 120°C. *Photonics Research*, *8*(12), 1937.

[11] Wang, J., Bai, Y., Liu, H., Cheng, Z., Tang, M., Chen, S., Wu, J., Papatryfonos, K., Liu, Z., Huang, Y., & Ren, X. (2018). Optimization of 1.3 μm InAs/GaAs quantum dot lasers epitaxially grown on silicon: Taking the optical loss of metamorphic epilayers into account. *Laser Physics*, *28*(12).

Conference Proceedings

[1] Liu, Z., Liao, M., Hantschmann, C., Wang, Y., Zhou, T., Tang, M., Park, J. S., Zhang, Z., Chen, S., Seeds, A., Penty, R., White, I., Yu, S., & Liu, H. (2019). Roadmap of 1300-nm InAs/GaAs quantum dot laser grown on silicon for silicon photonics. *International Photonics and OptoElectronics Meeting 2019. Optical Society of America 2019*, paper OTh1C.1.

[2] Hantschmann, C., Liu, Z., Tang, M., Seeds, A., Liu, H., White, I., & Penty, R. (2020). *Impact of dislocations in monolithic III-V lasers on silicon: a theoretical approach*. *March 2020*, 16.

[3] Dang, M., Liu, Z., Lu, Y., Park, J. S., Liao, M., Tang, M., Chen, S., & Liu, H. (2019). Silicon-based III-V quantum-dot laser for silicon photonics. *Optics InfoBase Conference Papers*, *Part F138-*, 2019–2021.

[4] Pan, S., Liao, M., Liu, Z., Lu, Y., Cao, V., Tang, M., Park, J. S., Wu, J., Chen, S., Seeds, A., & Liu, H. (2018). O-band InAs Quantum Dot Light Sources Monolithically Grown on Si. *CLEO Pacific Rim Conference 2018, Optical Society of America 2018*, paper W1F.2.

[5] Pan, S., Huang, J., Zhou, Z., Liu, Z., Ponnampalam, L., Tang, M., Lo, Z., Cao, Z., Seeds, A., Liu, H., & Chen, S. (2018). Ultra-stable 25.5 GHz quantum dot mode-locked frequency comb operating up to 120 °C. *Conference on Lasers and Electro-Optics, Optical Society of America 2021,* paper SF2F.3.

Other Conference Presentations

[1] Quantum Dot Laser and Quantum Well laser Monolithically Grown on On-axis (001) Si Substrate. UK Semiconductor 2018, Sheffield, United Kingdom

[2] III-V Quantum dot materials and devices grown on on-axis (001) Si substrate. Semiconductor and Integrated OptoElectronics (SIOE) 2019, Cardiff, United Kingdom

[3] III-V Quantum dot laser devices grown on on-axis (001) Si substrate. UK Semiconductor 2019, Sheffield, United Kingdom

Chapter 1
Introduction

1.1 Silicon Photonics

1.1.1 Silicon Photonics

The data throughput of the optical communication system has increased substantially and rapidly over the past decade. In order to meet the demands of information explosion, the optical interconnectors in data centres need to attain higher integration density, communication speed and reliability [1-3]. The use of photonic integrated circuits (PICs) has been regarded as a viable way because photons, instead of electrons, are used as a medium for data transmission [4]. Also, the PICs is partially free from the electrical resistance heating, compared to electronic circuits [5]. Furthermore, silicon (Si) photonics integrating PICs on a Si platform has been attracting great interest due to the merits of low costs and compatibility with mature complementary metal oxide semiconductor (CMOS) technology [6]. In this regard, it is imperative to realise the Si photonics considered as an ideal candidate for low-cost and high-speed on-chip optical communication [7-9].

Compared with other semiconductor materials, Si has large difference of refractive index with its native oxide, SiO_2, which can be easily grown on Si, providing an easy approach for forming waveguides. In addition, SiO_2 acts as the insulating section for semiconductor devices to reduce the dissipation of electrons [10]. Based on these properties, Si is the most suitable material for the fabrication of complementary metal oxide semiconductor (CMOS) [11]. Besides, the Si has numerous advantages，such as low-cost, high-stability, and high-purity. The reserves of Si element and SiO_2 are abundant in the earth crust, implying that the Si is one of the most costless raw material in the semiconductor industry [12].

As mentioned above, Si photonics combining the PICs on Si substrates emerged to overcome the networking bottlenecks and reduce the cost of both data centre and ownership [13]. Till now, over 95% semiconductor devices are based on Si platform,

and the CMOS manufacturing is very mature and cheap [14]. Nowadays, based on Si substrate compatible with the CMOS manufacturing, most of the components for integration system has been developed. In the near future, therefore, the Si photonics is expected to occupy majority market share of information communication [15].

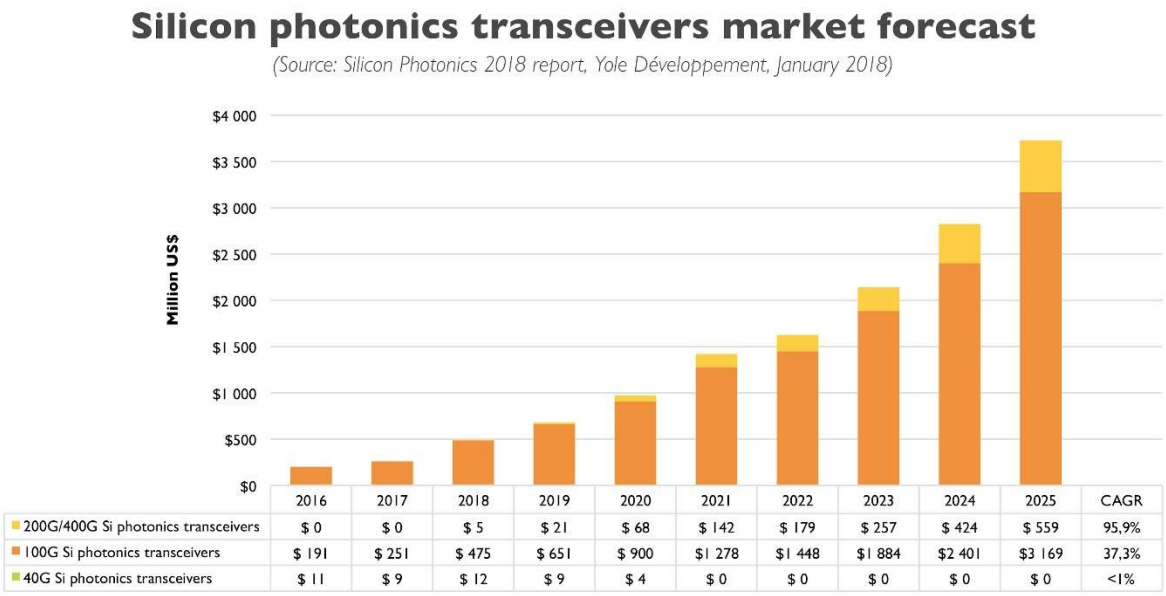

	2016	2017	2018	2019	2020	2021	2022	2023	2024	2025	CAGR
200G/400G Si photonics transceivers	$ 0	$ 0	$ 5	$ 21	$ 68	$ 142	$ 179	$ 257	$ 424	$ 559	95,9%
100G Si photonics transceivers	$ 191	$ 251	$ 475	$ 651	$ 900	$1 278	$1 448	$1 884	$2 401	$3 169	37,3%
40G Si photonics transceivers	$ 11	$ 9	$ 12	$ 9	$ 4	$ 0	$ 0	$ 0	$ 0	$ 0	<1%

Figure 1.1 the rising market of the silicon photonics transceivers [16].

The enormous market of Si photonics promises to obtain $774.1 Million income in 2018 [16]. Based on the booming rate of Si photonics market share in the past few years, a continuous increase rate is estimated to maintain 20.8% from 2018 to 2023. Silicon photonics has the advantage of high integration density, which leads to energy conservation, low power consumption transceivers are most important products in silicon photonics market. Exploding demands of Si photonics come from the desired low power consumption transceivers in data centres and the increased supply of Si photonics devices used for data transmission with high bandwidth. The transceivers include transmitter and receiver, and the semiconductor light source acts as a key component of transmitter which takes the responsibility to produce optical signals [17]. The motivation of research and development of transceiver modules is to realize energy-efficient and high-speed optical communication system.

1.1.2 The challenge of silicon photonics

At present, commercially available Si photonics, in which most of Si-based optical components such as modulator, photodetector, waveguide, and multiplexer are well-established, is already applied to 100G optical transceiver [18-25]. However, the high-performance Si-based light source is still missing. Due to the lack of monolithic grown Si-based light source, commercially available Si photonics adopted bonding technology to deploy the III-V laser grown on native substrates. However, native substrates such as GaAs or InP substrates have smaller size and higher price than Si substrates, bonding technology leads to low integration density and high costs. As one of the most important part of optical transceivers, therefore, the development of Si-based light sources for Si photonics is urgently needed and has great research value.

However, bulk Si is an indirect bandgap material, resulting in very low recombination efficiency of Si-based active region [27]. Despite recent advances in Si-based lasers such as Ge alloy laser and Si Raman laser, they are still suffering from low-efficiency and optically pumped operation [28, 29]. On the other hand, direct-bandgap III-V compound semiconductors are widely used for various light-emitting/absorbing devices due to their outstanding optical and electrical properties [30]. Therefore, a great deal of effort has been made to grow III-V materials on Si, which aims to produce high-performance Si-based III-V laser devices.

Notwithstanding these efforts, the performance of Si-based III-V lasers was not satisfactory. This is due to the challenges coming from the large difference between Si and III-V materials, such as lattice constant, polarity, and thermal expansion coefficient. The lattice mismatches between Si and GaAs (InP) are around 4 % (8 %), and the difference of thermal expansion coefficient reaches 120 % (77 %), respectively [31]. The large lattice mismatch will generate high density of threading dislocations (TD) over 10^9 cm^{-2}, and the difference between polar material and non-polar substrate will produce anti-phase domain (APD) creating anti-phase boundary (APB) during the growth of III-V on Si substrate [31, 32]. As the defects such as TDs and APBs act as non-radiative recombination centres, carriers are trapped by these defect-sites, resulting in the substantial degradation of laser device performances such as threshold current density and temperature stability.

The research in the field of Si photonics has been impeded by low-efficiency of Si-based lasers due to the high density of threading dislocation and APDs over twenty years [33, 34]. In that period, with the heterogeneous bonding technology, the III-V quantum well (QW) lasers on their native substrate have already dominated the optical communication light source market [35]. Even though a lot of effort has been devoted to growing similar epitaxial structure on Si substrate, the problem caused by defect has been not fully resolved [34]. For instance, the AlGaAs QW lasers grown on Si exhibits over 10 times larger threshold current density (2800A/cm^2) than that grown on native substrate (250A/cm^2) [34, 36].

The lack of a reliable and efficient integrated light source has become the bottleneck of the whole silicon photonics industry. As a result, although the research of Si-based laser has several problems like TDs and APDs, the high-performance semiconductor laser grown on Si still has great potential and application value to meet the strict requirement of Si-based laser.

1.2 Semiconductor laser

1.2.1 Optical property of semiconductor

Electrons in an atom occupy different orbitals, such as the s orbital and p orbitals, with discrete energy levels. If two same atoms are very close to each other to form a molecular, their outermost orbitals of electrons overlap with a quantify interaction force. As shown in Figure 1.2 [37], for example, the outermost orbital of Na atom has one electron in the 3s orbital. According to the Pauli Exclusion Principle, one orbital can only be occupied by two electrons with opposite spins, so the 3s orbital of Na atom is half filled. In a Na molecule, the two original atomic orbitals split into a bonding and an anti-bonding molecular orbital (MO), where bonding orbital is filled by two electrons with different spins and anti-bonding is empty but has higher energy level. As the number of atoms increased, more and more atomic orbitals are separated into bonding and anti-bonding MOs with different energy levels [38]. These successive MOs merge into an almost continuous band, where the band full of electrons is considered as valence band, the band with higher energy level but no electrons is conduction band [38]. The forbidden gap between the valence and conduction band is called the bandgap of this material [37].

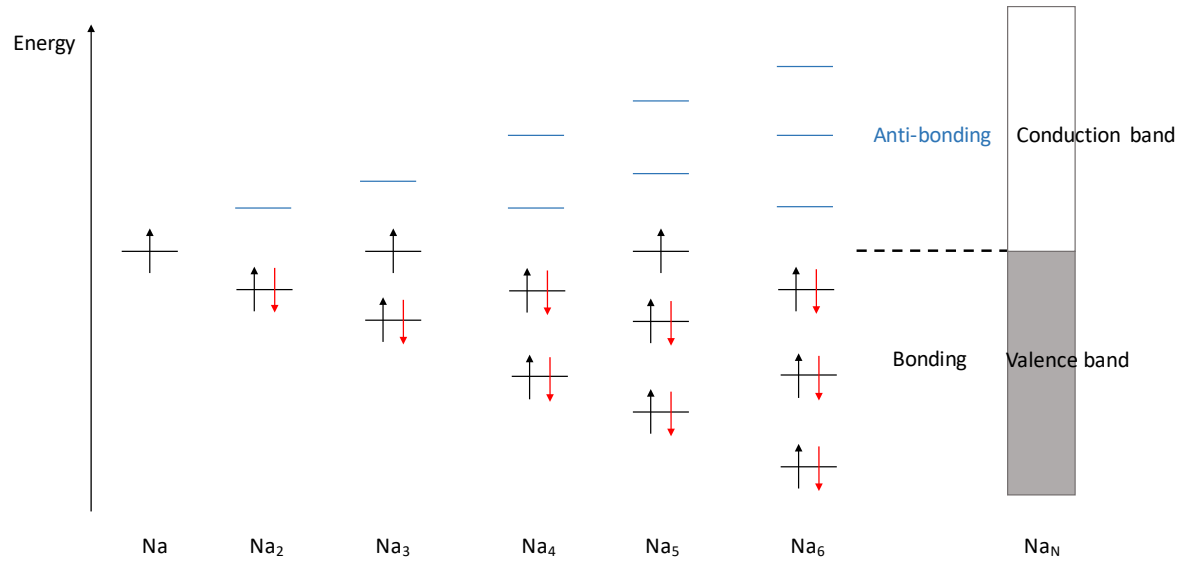

Figure 1.2 Schematic of outermost electron energy levels in Na atom and solid.

In general, solid state materials can be divided into three types: conductor, semiconductor and insulator, which are determined by their bandgap. The conduction and valence bands of conductor are much closer or even overlapped with each other such as metal, and thus electrons in valence bond could easily pass over to the conduction band to achieve electric conduction (Figure 1.2). Compare with conductor, insulator has larger bandgap and fewer free electrons are able to cross over to the conduction band resulting in a poor conductivity [39]. Their bandgaps of such semiconductor materials such as Si/Ge or III-V compounds are in between the conductor and insulator and tuneable by changing the compositions of elements of compounds [40]. This modest bandgap of semiconductor is the most essential condition that causes optical absorption and emission by the electronic transition. The detail of optical absorption and emission will be discussed later.

The semiconductor material without impurities is called intrinsic semiconductor or i-type semiconductor. When temperature equals 0 K, there are no electrons in the conduction band. When the temperature is raised, the electrons are excited into the conduction band by the thermal excitation. The number of electrons (n) in conduction band (E_c) equals to the number of holes (p) in valance band (E_c), n=p，where the Fermi level is on the middle of E_c and E_v [39]. In addition to the intrinsic semiconductor, extrinsic semiconductor involves p-type or n-type materials, which can be achieved by doping excess holes or electrons into the intrinsic materials (Fig. 1.3), respectively [40].

Their Fermi-levels are decided by the doping levels, acceptor level and donor level, which indicate the highest energy level where electrons can occupy at 0 K [39].

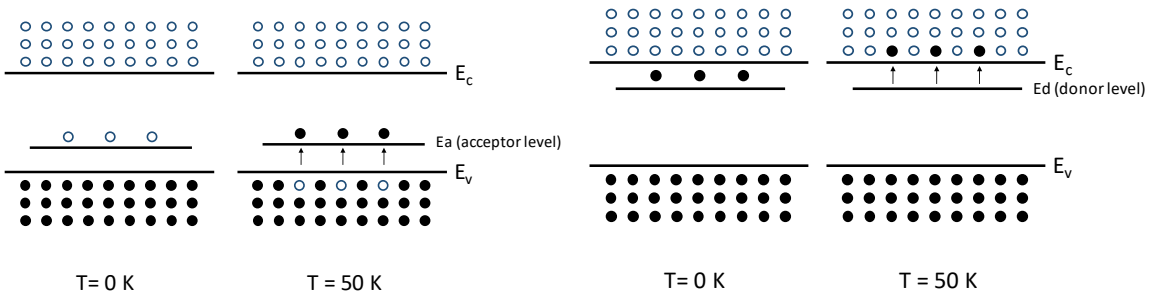

Figure 1.3 Schematic of P-type and n-type materials [41].

Laser diode is a typical p-i-n junction, where the i-region plays the role of an active region and creates lasing. However, not all the semiconductor materials are suitable for the light emitter, e.g., Si material, whose lowest energy states of conduction band and valence band do not have same momentum as shown in Figure 1.4 (b). Si is thus called indirect bandgap material. In contrast, if the minimum of conduction and maximum of valence share same crystal momentum, like GaAs, it is called direct bandgap material [42]. In the direct bandgap structure, the radiative recombination can occur rapidly via two particles process. To be specific, an electron in conduction band can easily recombine with the hole in valence band, releasing the excess energy as a photon as shown in Figure 1.4 (a). For the indirect bandgap materials, the electrons in conduction band are not aligned with the holes in the valence band, and always needs participation of phonons in order to carry out the excess momentum. Therefore, this inefficient recombination process leads to a low interband transition rate in this type of materials. Besides, abundant non-radiative recombination, such as Auger recombination, also degrades the optical transition rate. The carriers (electrons or holes) are excited to the higher energy levels by absorbing the photons from electron-hole recombination. Both radiative recombination and non-radiative recombination exist in indirect bandgap materials, resulting in little photon emission [1].

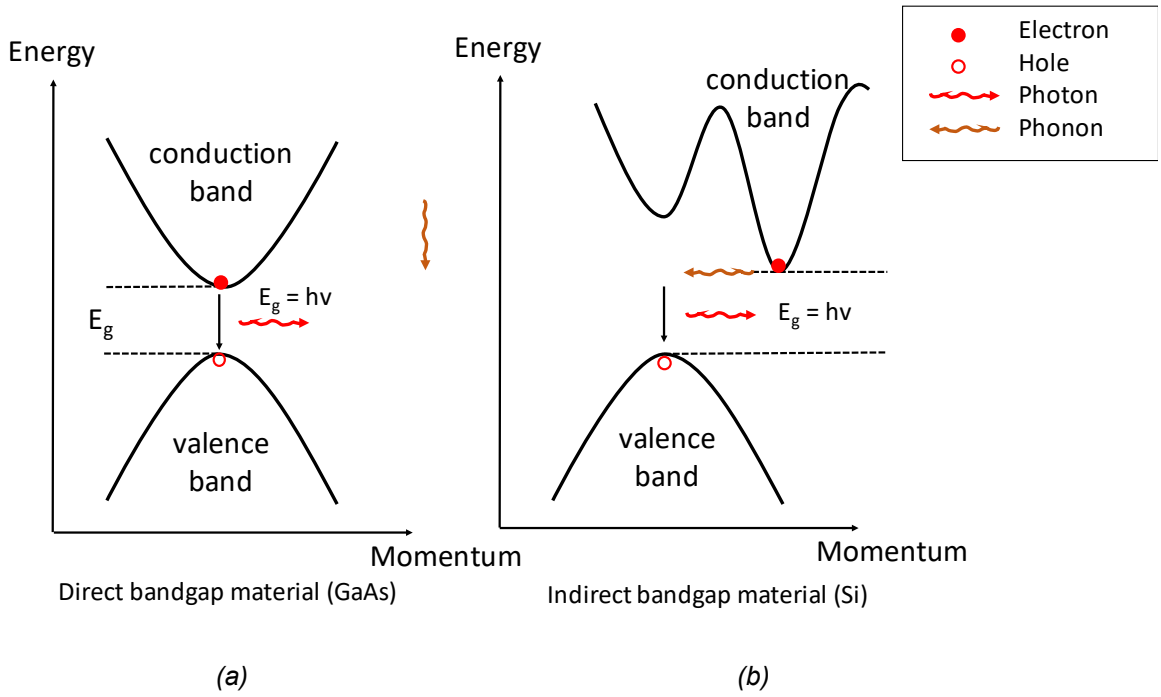

Figure 1.4 Direct and indirect bandgap materials [1].

1.2.2 Semiconductor laser

1.2.2.1 Laser theory

Materials with the direct bandgap structure, such as III-V compounds, are more suitable for laser devices. However, a successful and effective laser device is far more than the material choice. In this section, a brief introduction to the laser theory and factors impacting the laser performance will be given.

Figure 1.5 shows the interband transitions between the lower state and upper state: absorption, spontaneous emission and stimulated emission [43]. An electron can be excited to the unoccupied upper state by absorbing a photon and this transition is called absorption. Spontaneous emission is the optical process that a photon is emitted when the electron transitions from the excited state to a lower state. It should be noticed that the direction and phase of the emitted photon are random. In contrast, for stimulated emission, an incoming photon with specific frequency may interact with an electron from excited energy level dropping to a lower energy level, thus emitting a new photon whose frequency, phase and direction are identical to the incident photon. The stimulated emission is the basis of laser diodes and superluminecent light-emitting diodes [43].

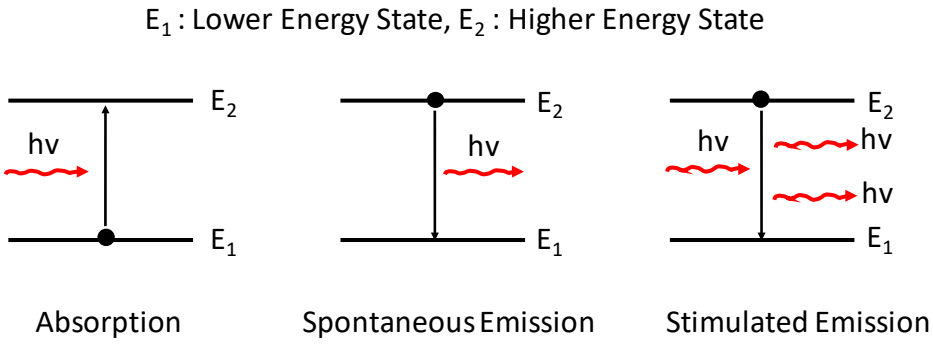

Figure 1.5 Interband transitions of absorption, spontaneous and stimulated emission.

In thermal equilibrium semiconductor material, only a few electrons are in conduction band and thus downwards transition is hardly generated. In order to achieve net optical amplification, the populations of carriers in valence band and conduction band are needed to be inverted. By connecting the forward bias voltage to the p-n junction of laser device, the abundant excess electrons are injected into conduction band, and excess empty states are formed by hole injection in valence band simultaneously. When the population of electrons in conduction band exceeds that in valence band, the rate of optical emission is bigger than the rate of absorption and thus the net optical gain can be observed by this population inversion. Therefore, one of the three critical conditions of lasing are the population inversion [44].

In addition to the population inversion, the presence of optical feedback by reflection in an optical cavity is another key factor for laser action. As mentioned above, spontaneous emission is a random process that emits photons with random directions. Figure 1.6 demonstrates the spontaneous emissions in a laser cavity, where a small fraction, β_{spon}, of photons are transmitted along the axis of the cavity [45]. Only this small fraction of photons can be amplified by the stimulated emissions, otherwise they will be absorbed by laser structure. We call this fraction of β_{spon} as spontaneous emission factor. In a laser cavity, as β_{spon} is amplified by the stimulated emission and propagated to the end of the laser cavity, it is reflected by the end mirrors with several mirror loss and produces coherent light back to cavity (Figure 1.7) [46]. The reflected light is amplified again by means of passing through the gain medium and then attenuated again by another end of mirror of cavity.

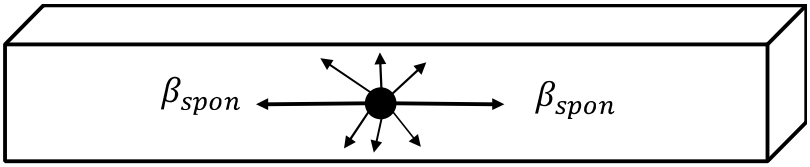

Figure 1.6 Random emitting direction of spontaneous emission in a laser cavity.

According to the above laser cavity mode, and the last critical condition for lasing is that the optical amplification (gain) must be bigger than the total optical loss, the equation of threshold gain (G_{th}, unit A/cm^2) of lasing action can be written as:

$$G_{th} \geq \alpha_i + \frac{1}{2L}\ln(\frac{1}{R_1 R_2}) \quad (1.1)$$

where α_i is internal loss, L is cavity length, R_1 and R_2 are the reflectivity of mirrors of laser cavity [47].

The internal loss represents the optical loss inside the cavity, which is mainly attributed to optical mode leakage, light scattering at cavity defect and free carrier absorption. The second part of right-hand side of this equation represents the additional optical loss due to light output that is why we call this part as mirror loss. From this expression, it is clear to see the lasing operation can only happen when the gain is bigger than internal loss plus mirror loss.

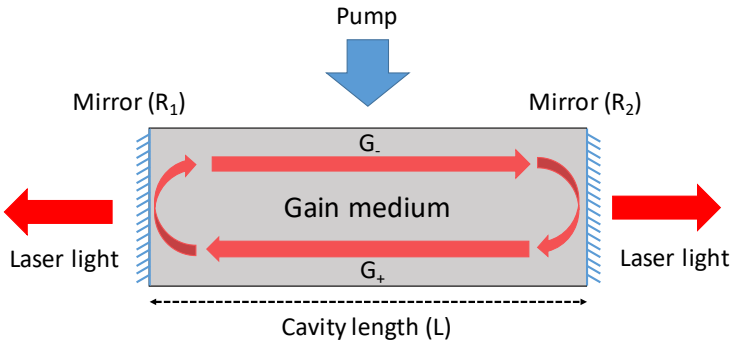

Figure 1.7 Fabry-Perot laser cavity structure with reflection optical feedback [46].

Consequently, the three deciding conditions for lasing are: 1) population inversion of carriers created in conduction and valence band; 2) the presence of optical feedback of laser cavity to produce coherence light; 3) the net modal gain (G_{th}- α_i) compensates for the light lost to facet mirrors.

The laser cavity demonstrated above consists of the amplifying active region sandwiched between two parallel mirrors, which is known as a Fabry-Perrot (F-P) laser. In the F-P laser, it provides longitudinal light confinement, and the amplified resonant light needs to form standing wave pattern, where the wavelengths of light follow the equation:

$$L = n \times \frac{\lambda}{2} \tag{1.2}$$

where L is the length of cavity, n is the integer which leads to integral multiple, λ is the wavelength of light forming the standing wave pattern in this F-P cavity laser. Although for a fixed length cavity waveguide it has a lot of allowed modes (wavelengths), not all of the modes meet the lasing conditions. There is a gain curve that amplifies the mode within the active medium. Figure 1.8 gives the resonant wavelengths that fall within the ground state gain curve. Moreover, as described above, the amplified modes will also experience the optical loss both from internal and external. Thus, only several modes (red lines in Fig. 1.8) satisfy the lasing conditions leading to multi-mode operation for this waveguide.

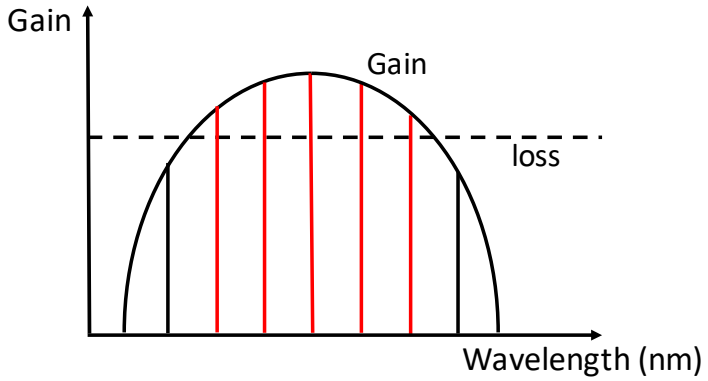

Figure 1.8 Resonant wavelengths that fall within the gain curve.

According to the equation 1.1, the larger cavity length *L* means larger loss of this laser devices which leads to larger required gain, and therefore, less modes are able to meet the criterial of lasing conditions. However, too short cavity also causes the ground state lasing failure resulting in a blueshift in primary lasing wavelength and increased threshold current (excited state lasing).

1.2.2.2 PN junction and double heterostructure

Most of semiconductor devices are fabricated in p-n or p-i-n structures with heavily p-doped and n-doped regions in order to provide a flow of electricity [41]. The recombination of electrons and holes takes place at depletion region which is the interface region between the p-type and n-type, therefore leaving negative ions in the p-side and positive ions in the n-side. When a forward bias voltage is applied to the p-n junction, external electrons will flow from n-type materials to p-type, and holes from p-type to n-type. The width of depletion region is decreased due to the flows of electrons and holes, and thus the electrons can flow to the forward direction with a very small resistance. Otherwise, a reverse bias voltage increases the width of depletion region, leading to fewer carriers diffusing from one side to other side, therefore preventing the conduction of p-n junction. This single direction conducting behaviour contributes to the basic characteristics of the diodes [41].

In order to reduce the absorption of carriers or photons and increase the carrier confinement, the double heterostructure are widely used for the laser devices. In this structure, the same material is used for p-type and n-type materials and an intrinsic layer is grown as the depletion region where the recombination occurs. The intrinsic layer has a higher refractive index than the p-type and n-type material with a lower bandgap. The increased refractive index confines the emitted photons to the intrinsic region, while the lower bandgap allows carriers not to be escaped to the p and n layers due to the energy barrier in band structure. In this case, the p and n layers are referred to as the cladding layers. The figure 1.9 shows a simple double structure pin junction, when forward bias is applied and there is a resultant carrier flow. The recombination can take place between the holes and electrons in the depletion region.

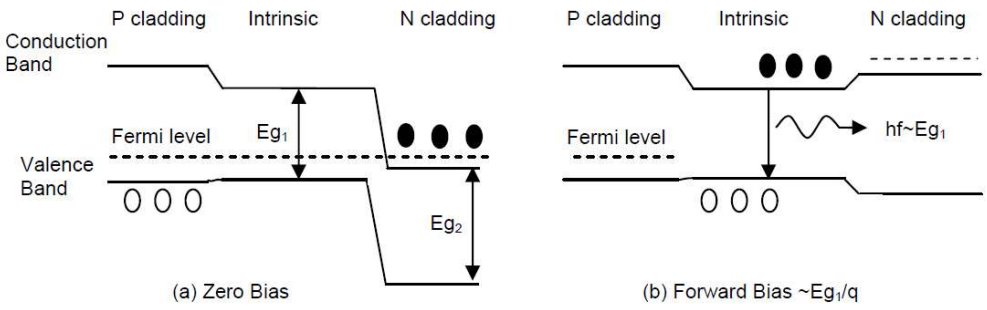

Figure 1.9 Bandgap schematic of a semiconductor pin junction showing (a) unbiased and (b) forward biased energy bands [38].

1.2.3 Applications of semiconductor laser

Since the emission wavelength of semiconductor is related with the material choice, the wavelength of semiconductor laser devices could be designed flexibly with broad wave band [11]. Nowadays, the wavelength of laser devices covers the range from Ultraviolet (UV) wavelength to Terahertz radiation (THZ) wavelength, so that the laser devices are available to be applied as high-quality and high-reliable light source in most of industries [38,39]. With the rapid progress of semiconductor manufactory in last several decades, laser devices exhibit the outstanding performance in large-scale integration with low cost [1]. As a result, the semiconductor laser gradually dominates the market like optical communications, laser pointers, CD/DVD/Blue-ray reading/recording, barcode readers, laser printing, laser scanning and illumination et al [40-44].

1.2.3.1 Light source for optical communication

Due to the increased requirement of data transmission, the demand of information capacity and information quality have promoted the rapid development of high-speed data collection, processing and transmission technology [1,49]. The most representative approach is optical fibre communication systems based on large-scale integrated circuits. The optical loss caused by photon absorption and dispersion occurred in fibre transmission leads to signal distortion and limit the data transmission distance, so that the optical loss is an important issue to be avoided [50]. During the data transmission in optical fibre, different optical loss is displayed under various light wavelength. The relationship between wavelength and optical loss revealed that the light at wavelengths from 1260 nm to 1625 nm has smaller light dispersion and signal distortion with low optical loss [51, 52]. As illustrated in figure 1.10, two most commonly applied communication windows are located around 1310 nm and 1550 nm which produce minimal optical loss.

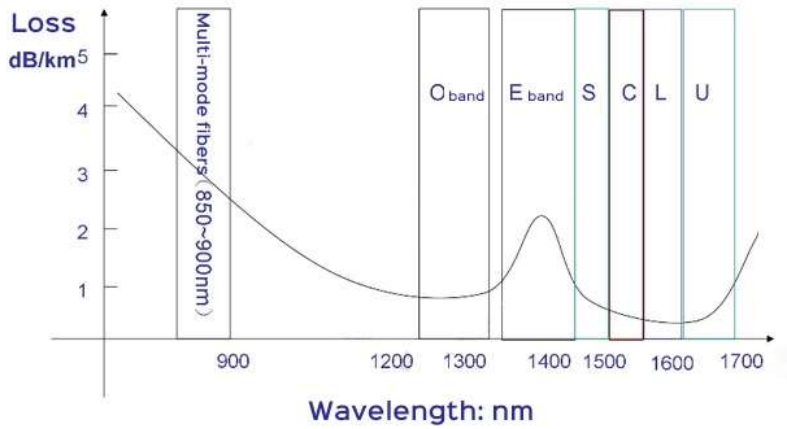

Figure 1.10 the relationship between optical loss and light wavelength in optical fibre [49].

C-band (Conventional Band) covers the wavelength range from 1530 nm to 1565 nm which leads to extremely low optical loss during the transmission based on optical fibre. As a result, the C-band laser device plays an important role in long-distance optical transmission, and it could be flexibly assembled with various optical transmission technologies such as Wavelength Division Multiplexing (WDM) and Erbium Doped Fiber Amplifier (EDFA) in metropolitan area transmission [53,54].

O-band is the original band with wavelength from 1260 to 1360nm. The O-band laser device has minimal signal distortion and is the first wavelength band used in optical communications in history [3]. Based on the mature growth and manufactory of GaAs material system, this first commercial single mode 1.3 μm laser diode was fabricated by Standard Elektrik Lorenz AG company as early as 1986 [55]. With the advances in QD, the lasing property of O-band laser devices has been continuously improved, so that the injection current density drops to only 10.4 A/cm^2 (per layer) and the highest operation temperature reaches 220°C [56]. O-band semiconductor laser devices exhibit impressive advantages such as high temperature stability, low threshold current, and high direct modulation rate. These unique characteristics of O-band lasers realized low-cost and low-power consumption optical signal transmitters used for short-reach intra-data centre networking [1-3].

1.2.3.2 Mid-infrared light source

The laser devices with mid-infrared (from 3μm to 20μm) spectral range has broaden application areas especially in mid-infrared sensing and space optical communication (Figure1.11) [57-63].

For example, there are two atmospheric windows (3 μm – 5 μm and 8 μm – 14 μm) in the mid-infrared range, in which the low loss and weak dispersion of Mie scattering effect could offer over 10 km non-relay transmission distance [64]. Therefore, the mid-infrared laser is important light source for free space optical space optical communication.

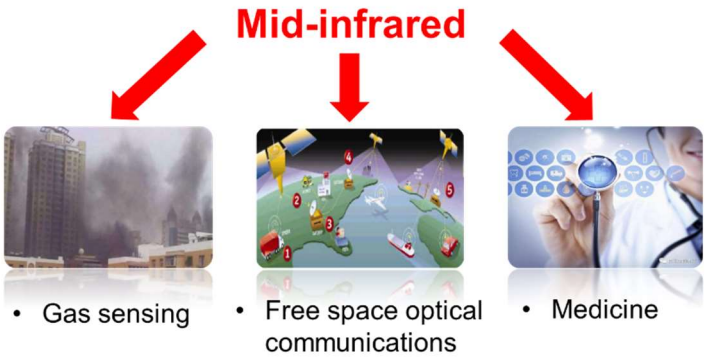

Figure 1.11 the classic applications of mid-infrared laser devices [57, 59, 63].

In addition, gas sensing is another unique market occupied by mid-infrared laser devices [65]. From the gas absorption spectrum shown in Figure 1.12, it is visible that a variety of gases have their own characteristic spectral peaks. The absorption spectrum of each gas could be considered as the 'fingerprint' which can be used to precisely determine the gas component [66]. Mid-infrared range covers the 'fingerprint' absorption spectrum of most harmful pollution gases such as CO, CO_2, NO, NO_2 and O_3, and thus the gas sensing function of mid-infrared laser devices is widely used in air quality and environmental detection [65, 67]. Also, the generation of flammable and explosive gases during the industrial production and mining process threats the working safety. Therefore, the application of mid-infrared sensing devices could reduce the risk of fire or explosion accident. The absorption spectrum of mostly flammable and explosive gas such as CH_4 and NH_3 are also covered by mid-infrared range, and therefore, the mid-infrared laser productions are also urgent required by industry and mining [65, 68].

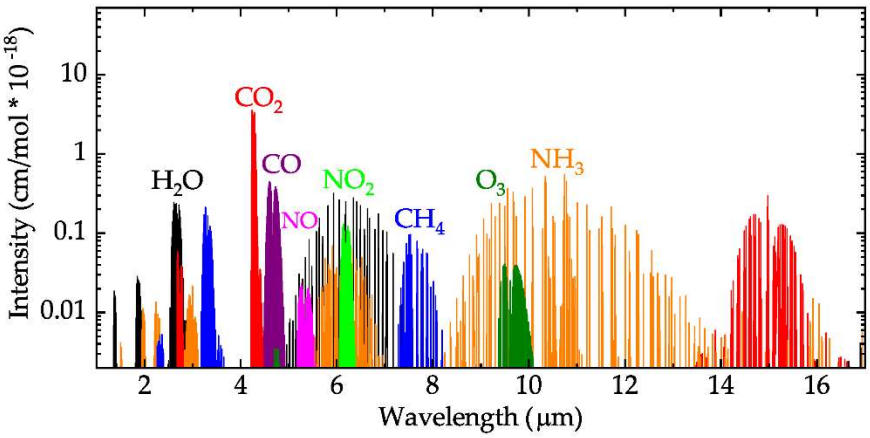

Figure 1.12 the gas absorption spectrum in mid-infrared wavelength range [65].

There are three main methods for the generation of mid-infrared and far-infrared light sources: Nonlinear optical (NLO) technology, Ion-doped crystal technology and semiconductor technology. For the NLO technology, CO_2 laser is the classic mid-infrared laser device [64]. The CO_2 laser provides wavelengths from 9.2μm to 10.8μm, used for 4μm to 6μm mid-infrared laser manufacture by propagating the emitted light on the nonlinear crystal to generate frequency conversion effect [61]. For Ion-doped crystal technology, the key of this technology is finding high-quality frequency multiplication crystals with large nonlinear optical coefficient, small optical absorption coefficient, large phase matching angle, and large thermal conductivity. Due to material limitations, the low efficiency and high threshold have always been the difficulties of this technology.

Semiconductor lasers have always been highly valued due to their small size, light weight, high efficiency, easy modulation, long lifetime, and high degree of integration. In mid-infrared field, the quantum cascade lasers (QCLs), using electron transitions between subbands in the conduction band and phonon resonance-assisted tunnelling to achieve population inversion and acquire mid-infrared emission wavelength, are the most commonly used semiconductor light source. Compared with other mid-infrared light sources, QCLs have unique advantages like small size, low power consumption, high efficiency, and convenient portability. The flexible design is also the characteristic of QCL devices. The energy band could be artificially adjusted by changing the thickness and stress of the growth material, resulting in extremely broad lasing wavelength which covers the whole mid-infrared band and most of the THz band (3 to 24μm, 50 to 300μm) [66].

1.3 Silicon-based III-V laser

1.3.1 Si-based light sources

1.3.1.1 Heterogeneous Approach

Nowadays, GaAs-based and InP-based quantum-dot (QD) and QW lasers have been widely used as the light source for data centers and optical communication system [69]. However, the Si-based III-V lasers, which is capable of being monolithically deployed into Si photonics, are still not commercialized because the performance of laser was limited by the high density of dislocations, antiphase domains (APDs) and thermal cracks. In this regard, heterogeneous integration is a direct way to avoid the problem resulted from direct growth of III-V materials on Si substrate, although there are several challenges of wafer bonding technique such as low yield and high cost [70].

For the heterogeneous wafer bonding, the laser samples are grown on their native substrate with low defect density and then integrated on Si substrate, enabling highly efficient light sources to be employed on PICs [69]. The wafer bonding technology has been investigated more than 30 years, but due to the limitation of equipment and high-cost, the employment of the III-V group semiconductor laser devices become popular in the recent two decades [71]. For hybrid bonding of III-V laser devices on Si, lasing was generated in the III-V material and this section is vertically coupled into Si waveguide by evanescent coupling. As a result, this approach is not limited by the mismatch of lattice constant and thus able to avoid the high density of threading dislocations caused by lattice mismatch [70].

One of the most popular bonding techniques is direct bonding method, which brings two clean and mirror-like surfaces into contact under high pressure to form a strong interfacial bond [70]. Figure 1.13 (a) shows a typical hybrid silicon laser, which consists of the indium phosphide (InP)-based gain materials bonded on top of the silicon waveguide by direct oxygen plasma-assisted molecular bonding [71, 72]. Before bonding, both the silicon wafer and InP epitaxy layer were exposed to oxygen plasma in order to form a thin oxide layer (around 25 atoms of thickness) on the surfaces of Si and InP, respectively. These two thin oxide layers act as glue layers, which could combine the Si substrate with InP gain material under high pressure and temperature

[69]. Metal connections for anode and cathodes were then patterned on InP material as shown in Figure 1.13. When forward biased voltage is applied, the photons generated inside InP layers could be evanescently coupled to the Si waveguide [71], thus realizing the highly efficient light coupling to Si waveguide.

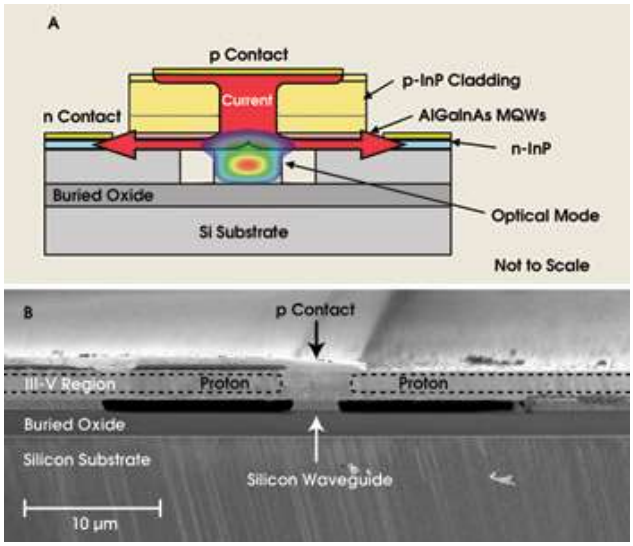

Figure 1.13 (a) the schematic diagram of hybrid silicon laser. (b) the SEM Figures of the cross-section of the hybrid laser device [71].

In addition, to avoid the damage caused by thermal annealing and electric field during direct bonding technique, the adhesive bonding techniques which can be processed in low temperature have been investigated [73]. The bonding polymerization reaction in the low temperature will produce H_2O and H_2, and these gas byproducts will generate the interfacial void and then degrade the performance of the devices. By etching the vertical outgassing channeling on the top layer of SOI and the bottom of III-V semiconductor, the gaseous byproduct is able to be guided into the buried oxide layer. Because of diffusion and storage of the gas byproduct on the buried oxide layer, the density of interfacial voids keeps in a very low level (50000), and in this research, the annealing temperate for fabrication is under 300℃, which is a suitable temperature for laser devices [71].

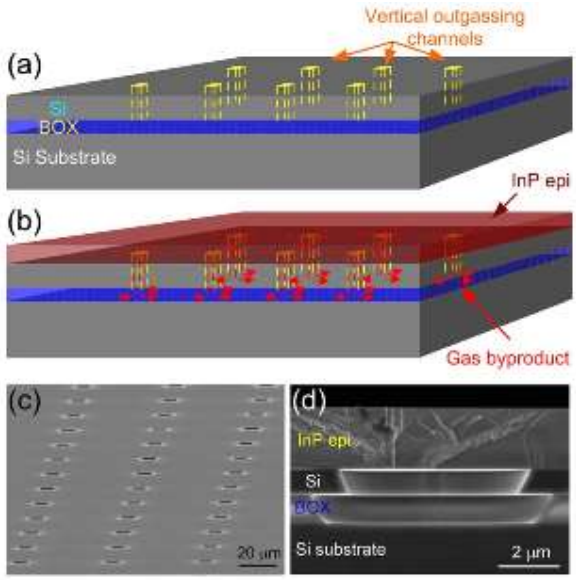

Figure 1.14 low-temperature wafer bonding with vertical outgassing channel [73].

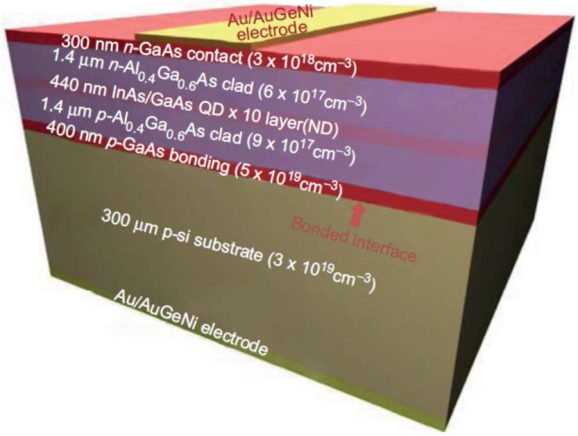

Figure 1.15 schematic diagram of InAs/GaAs QD laser on Si substrate by direct fusion wafer bonding [74].

Ultraclean conditions and atom-scale smooth surfaces are generally required to realize direct bonding, leading to a complex fabrication process. Besides, in order to avert the thermo-deformation, the requirement of low mismatch of coefficient of thermal expansion between sample and substrate also limited the extensive application of wafer bonding [70]. To address this problem, a novel direct fusion bonding technique at low-temperatures was also proposed with an ideal bandgap combination. Based on this technique, a 1.3μm InAs/GaAs QD laser on Si substrate was demonstrated with low threshold current density of 205 A/cm^2 in 2012 [74]. The

double-heterostructure of InAs/GaAs QD laser was grown on GaAs substrate by molecular beam epitaxy (MBE) at first. The epitaxy layer was then transferred onto p^+ Si substrate by means of fusion bonding p^+ GaAs/ p^+ Si substrate at 300 °C [74].

In 2016, the high-quality hybrid silicon evanescent QD laser was demonstrated. In this report, evanescent optical coupling was used to bond III-V QD gain material and the Si waveguide with the insertion of DBRs [75]. Eight layers of high-quality InAs/GaAs QD offered impressive temperature characteristic (T_0) which leads to great temperature stability, in which operation temperature was achieved up to 115 °C with T_0 values of 303K near room temperature [75]. At present, most of the commercialized silicon photonics was achieved by the evanescent coupling and the wafer bonding between InP-based or GaAs based laser devices and the silicon waveguide.

1.3.1.2 Monolithic Approach

In addition to heterogeneous integration, monolithic integration method is another rapid-growing research area due to its cost-effective and massive scalable integration merits [76]. The main issue of monolithic integration is the large material dissimilarity between III–V and group IV materials [1,76]. Fortunately, the problem which comes from APD has been solved by utilizing two-step growth and misoriented Si substrate. Besides, with the development of the III-V/Si buffer layer techniques, the APB could be annihilated or effectively suppressed [77]. However, for the growth of III-V materials on on-axis (001) Si substrate compatible with CMOS and SOI platform, the suppression of APD is still hampered.

The high density of TDs is another remaining problem during III-V epitaxy growth on Si substrate. In this regard, compared with QW or bulk material, QD structure has the unique property of defect-tolerance. For the QD structure, the threading dislocation only can affect very limited number of QDs as shown in figures below. Due to the high density of QD, the number of “surviving” QDs keeps in a considerable level, and the intact QDs continue to provide the optical gain for lasing [23, 78]. In addition, the generation of QD introduces the strain field in the epitaxial layer, and the strong strain is verified to impede the dislocations movement, resulting in the protective effect for QD [79].

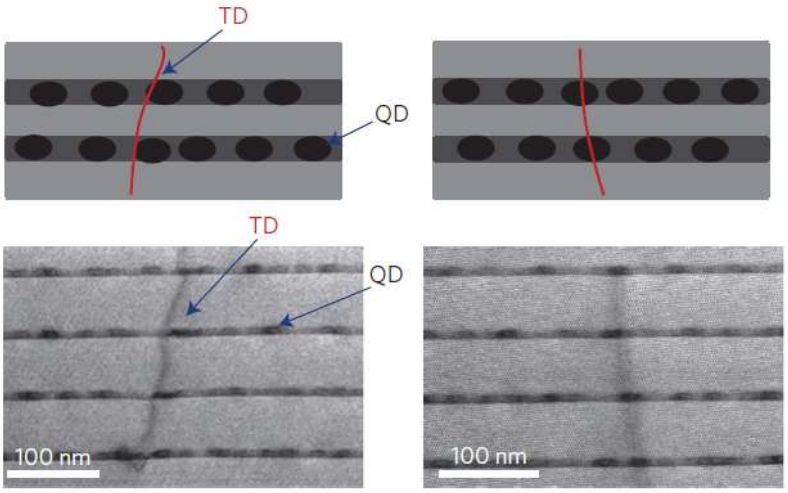

Figure 1.16 The schematic of threading dislocation in Dwell (Dot in well) structure: InAs QD with InGaAs capping layer and GaAs spacing layer [76].

As shown in Figure 1.16 (left), the transmission electron microscopy (TEM) measurement showed that the TD eluded the QD [79]. If the propagation of TD from buffer layer to active region reaches the bottom of QD islands, the dislocation might be bent to generate misfit dislocation below QD and will not influence the function of QDs in active regions [79, 80]. As a result, the QD is expected to have high reliability and to be more insensitive to the defect than that of QW laser. Therefore, the QD lasers are considered as the most suitable candidate for monolithic Si-based light source in Si photonics, in which a number of TDs are inevitably generated.

1.3.2 Quantum confinement and Quantum dot

The direct bandgap property and high carrier mobility of III-V material were applied into laser devices fabrication since the year of 1963 [81]. To achieve high-efficiency semiconductor laser devices, QDs or QWs, based on quantum confinement structures, have been widely employed because the carrier confinement promotes the recombination of carriers and thus enhances the lasing efficiency [82]. In this section, the quantum confinement effect will be introduced and the advantages of QDs material will also be illuminated.

1.3.2.1 Theory of quantum confinement

In quantum-confined structure, the movement of the electron will be confined in one or more dimensions if the size of structure in these dimensions is less than the de Broglie wavelength of a free electron (de Broglie wavelength λ_{deB}). In principle, if Δx is defined as the length of region which confined a carrier in x-axis, the uncertainty of its momentum will be [83]:

$$\Delta p \sim \frac{\hbar}{\Delta x} \tag{1.1}$$

where $\hbar$ is reduced Plank constant. If this particle has m mass, and is free in other directions, the additional kinetic energy of this particle for confinement (E_{conf}) can be written as:

$$E_{conf} = \frac{(\Delta p)^2}{2m} \sim \frac{\hbar^2}{2m(\Delta x)^2} \tag{1.2}$$

The confinement energy should be compatible or larger than the kinetic energy due to thermal motion of the particle in x direction. Thus, the condition for the effective confinement should be:

$$E_{conf} \sim \frac{\hbar^2}{2m(\Delta x)^2} > \frac{k_B T}{2} \tag{1.3}$$

So, based on the equation 1.3, the quantum size follows:

$$\Delta x \leq \sqrt{\frac{\hbar^2}{m k_B T}} \tag{1.4}$$

According to the Schrodinger wave equation and the solution of the infinity one direction confinement well, the energy states will be quantized with discrete levels, one of the solutions is $k = \frac{\mathrm{n}\pi}{\Delta x}$. Due to $P = \hbar k$ and $E_{conf} = \frac{(\Delta p)^2}{2m}$, the confinement energy for each state with $\Delta\, x$ confinement distance equals:

$$E_{conf}(n) = \frac{\hbar^2 n^2 \pi^2}{2m^*(\Delta x)^2} \tag{1.5}$$

The m^* is the effective mass, n is an integer representing the number of energy state levels. For example, n=1 means ground state, n=2 means the first excited state, n=3 means second excited state, et al.

If a particle is confined in one direction, we call this material as two-dimensional (2-D) quantum well (QW) structure; one dimensional (1-D) quantum wire structure for two directions confinements and zero-dimensional (0-D) quantum dot (Q-D) structure with three directions confinements. The confinement energy of each energy state for quantum well and quantum dot can be written as:

$$E_{conf}(n_x) = \frac{\pi^2\hbar^2}{2m^*}\left(\frac{n_x^2}{(\Delta x)^2}\right) \tag{1.6}$$

and,

$$E_{conf}(n_x, n_y, n_z) = \frac{\pi^2\hbar^2}{2m^*}\left(\frac{n_x^2}{(\Delta x)^2} + \frac{n_y^2}{(\Delta y)^2} + \frac{n_z^2}{(\Delta z)^2}\right) \tag{1.7}$$

From equation 1.7 of QD structure, it can be seen that only discrete energies depending on n are allowed due to the three direction confinements [83]. Figure 1.17 demonstrates the functions of the density of states (DOS) for electrons in conduction band with the energy in bulk, 2-D QW, 1-D quantum wire and 0-D QD structures. The unique delta-function-like DOS of QD represents that the carriers are localized in the discrete energy levels.

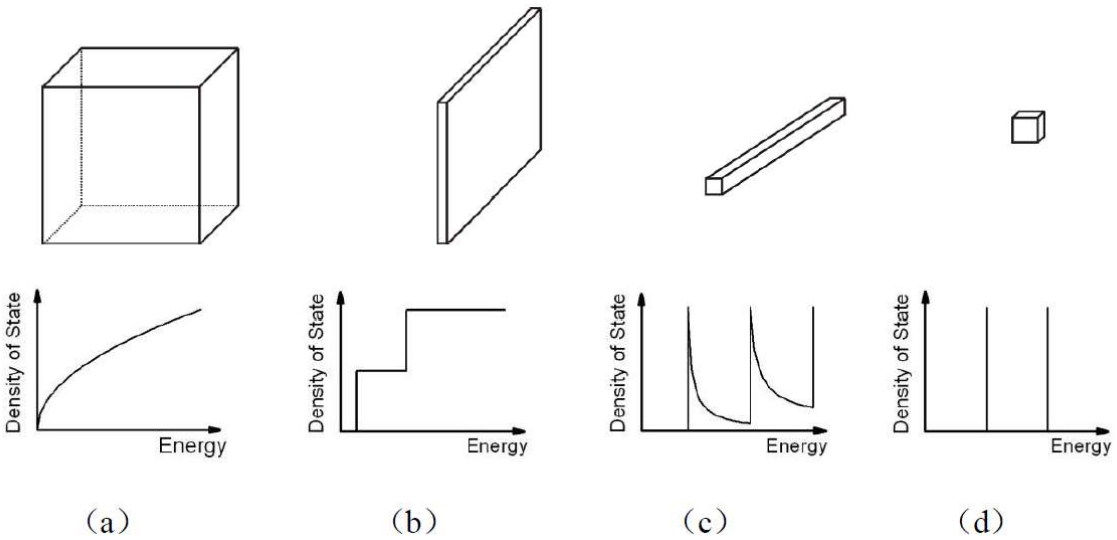

Figure 1.17 Density of state for (a) bulk; (b) quantum well; (c) quantum wire; (d) quantum dot structure [83].

1.3.2.2 Advantages of quantum dot

Based on the quantum-confined structure, Arakawa and Sakaki first proposed the use of QD materials for laser application in 1984 [84]. Compared with the continuous energy levels in QW material, the separated energy levels in QD material can help to trap the electrons and holes in the ground states, and thereby the thermal escape of carriers is impeded [84-86]. As a result, high temperature stability can be achieved as a unique property of QD material over QW material [86,87]. The QD material also offers the advantage of the low threshold current density of laser devices because of the strong confinement of carriers in the dots structure, leading to low power consumption [88,89]. However, in the real case, the perfect delta-function-like DOS of QD does not exist and the energy separation between the energy states of holes is much smaller than that of electrons. Therefore, the practical QD structure is still affected by the temperature changes. Because of this reason, several research groups pay attention to utilizing p-doped active region to fill abundant holes in valence band and thus to prevent the escaping of holes. Thus, the temperature characteristic can be improved dramatically via modulation p-doping in active region [90]. Moreover, the use of QD materials provides great benefit in terms of Si-based light sources generating high dislocation density due to materials dissimilarity between III-V and Si substrate. This is because the QDs are less sensitive to threading dislocations (TDs) than QW structure, attributed to the carrier localization and, thereby, reduced interaction with TDs. Therefore, the laser devices using QD materials are capable of providing low power consumption, robust tolerance to dislocation, and high temperature stability, which is an ideal candidate of Si-based light-emitting sources for realizing Si photonics.

1.3.3 QD laser monolithically grown on Si substrate

Because the QD laser devices have great advantages such as insensitivity to dislocation, low threshold current, and high temperature stability, the QD laser has been considered as ideal candidate that can be monolithically grown on Si substrate [78]. However, the device performance of the QD lasers on Si still suffers from various defects such as APDs and high density of dislocation. Accordingly, a great deal of efforts has been made to overcome these issues.

- III-V QD lasers on Ge and Ge/Si

Compared with the direct growth of GaAs on Si substrate, the lattice mismatch between GaAs and Ge materials is much smaller, which is only around 0.08% [23, 91]. Thus, direct growth of GaAs on Ge is an easier approach to avoid the formation of high density of threading dislocations induced by large lattice mismatch. More importantly, Ge material with the higher hole mobility [91] is a good candidate in both electronics and optoelectronics [1]. Si substrates coated with Ge acting as a “virtual substrate” are compatible with standard complementary metal-oxide-semiconductor (CMOS) fabrication [11]. Thus, many research groups have developed Ge and Ge/Si based laser for silicon photonics at initial stage.

The first room-temperature continuous-wave (c.w.) operation Ge-based QD laser was reported in 2011 [91]. In this work, (100) Ge substrate with a 6° off-cut towards the [111] plane was employed, in order to annihilate the APDs created by the polar and no-polar interface between Ge and GaAs materials. In addition, the initial GaAs buffer layer on Ge was grown by Ga prelayer technique to further suppress formation of APDs and improve material quality. By applying the two strategies of off-cut and Ga prelayer, a single-domain GaAs buffer layer was achieved [91]. An extremely low threshold current density of 55.2 A/cm^2 was achieved with the five QD layers of dot-in-well (DWELL) structure on Ge substrate, corresponding to around 11 A/cm^2 per each QD layer. This low threshold current density is comparable with the record GaAs-based QD laser of 32.5 A/cm^2 for three layers of QD [92]. The measured output power of a single facet for the QD laser on Ge is around 28 mW at an injection current of 500 mA. Figure 1.18 shows the light-current curves of the QD laser devices at different temperatures ranging from 20°C to 60°C under c.w. operation.

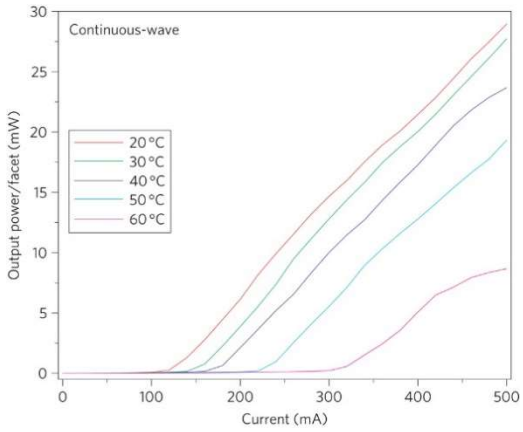

Figure 1.18 L-I curves as function of temperature under c.w. operation, the active region of the Ge-based devices is InAs QD in InAs/InGaAs/GaAs Dwell structure. [92].

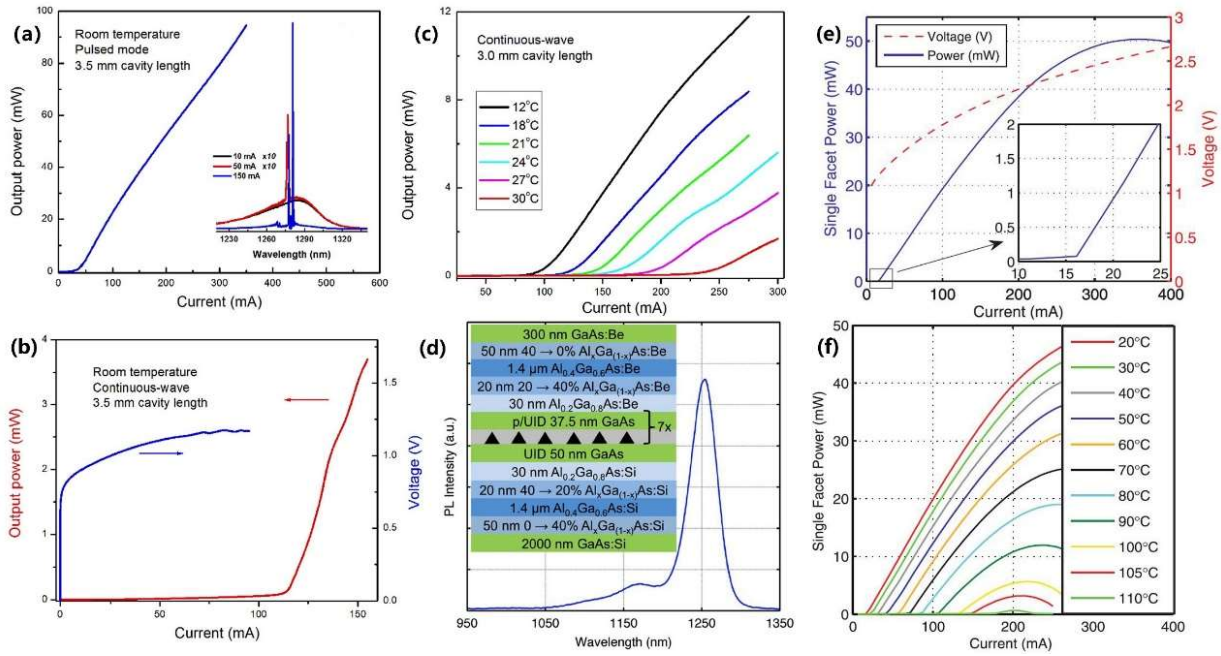

Figure 1.19 (a) the LI curve and the lasing spectrum of Ge/Si based laser with 1.3μm wavelength under pulsed current driving. (b) LIV curve of same sample under room temperature and c.w. mode (c) the temperature dependence results of LI curves with c.w. mode (d) the structure and PL results of QD laser grown on GaAs/Ge/Si virtual substrate. (e) the LIV curve of InAs/GaAs QD laser grown on GaAs/Ge/Si virtual substrate. (f). temperature dependence of QD laser grown on GeSi sub. [93, 94].

The realization of Ge based QD laser set the stage for the growth of QD lasers on Ge/Si substrates, which have a great potential for use in silicon photonics ICs. As a following research, the first room-temperature c.w. Si-based QD laser was fabricated by Liu's group with lasing wavelength of 1.3 μm, which falls within the telecommunication O-band [93]. These structures were realized by a combination of III-V QD epitaxial technology and the application of a Ge/Si virtual substrate. The 3.5

mm cavity length laser device achieved room-temperature lasing, and the 3 mm laser diodes was able to operate up to 30°C (Figure 1.19 (c)). The continuous progress on GeSi-based QD laser is promising for the monolithic integration of QD lasers on Si substrates [93].

A further advance on temperature-stable laser on GeSi substrate was made in 2014 by UCSB and Intel [94]. The optimized epitaxial structure is shown in Figure 1.19 (d). The annealing temperature during the growth of GaAs nucleation layer was also optimized. In this work, a narrow-ridge structure with high-reflection coating (95 %) on the facets were employed. The diode produced a low threshold current density (J_{th}) of only 16 mA (Figure 1.19 e) and the output power of 176 mW. Characteristic temperature stands for the temperature stability which a high characteristic temperature leads to the performance of laser devices will not influence a lot under the rising of operation temperature. In this research, after utilizing modulation p-doping and high-reflection coating, the characteristic temperature (T_0) of the laser device reached 200 K, and 110℃ working temperature (Figure 1.19 f) was attained under c.w. condition. The remarkable decrease of the threshold current and improved temperature stability of the GeSi-based QD laser suggested that it could be a feasible approach to achieve monolithically grown III-V QD lasers on Si substrate for silicon-based PIC.

However, the Ge/Si-based lasers have a limitation as a light source because the Ge has large optical absorption bandwidth which covers telecommunication wavelengths [91].

- III-V QD lasers on off-cut Si

Direct integration of III-V on Si substrate by MBE is more difficult to realize, compared with the growth of III-V on Ge, due to the larger mismatch of 4.1 % (7.5%) between GaAs (InP) and Si [39], producing a high density of defects, typically to the order of 10^{10} cm^{-2}.

In order to overcome these problems, growing a relatively thick and fully relaxed GaAs, InP or AlAs buffer layer between substrate and cladding layer has been developed [79]. The continuous progress of epitaxial growth witnessed the demonstration of first 1.3 μm Si-based InAs/GaAs QD laser with 42 ºC maximum operating temperature and

725 A/cm^2 threshold current density at room temperature in 2011 [95]. In this report, Si (001) substrate with 4° offcut towards [011] plane was used in order to annihilate APD, and the GaAs nucleation layer plays a crucial role to determine the quality of III-V epitaxy layer [95]. Further reduction in the threshold current density to 650 A/cm^2 was achieved by replacing the GaAs nucleation layer with the AlAs nucleation layer [96].

The development of epitaxial structure also contributes to a reduced threading dislocation density from ~10^{10} to ~10^6 cm^{-2}. The remarkable progress is attributed to the demonstration of dislocation filter layer (DFL) grown on the top of buffer layer. In particular, the InGaAs/GaAs and InAlAs/GaAs strained-layer superlattices (SLSs) as the DFL have been widely adopted to reduce the density of TDs [3]. The SLSs consist of the periodic two semiconductor layers with different lattice constant. The lattice mismatch produces strain which can bend the direction of propagating TDs, and thus DFLs restrain the TDs. By utilizing five layers of InAlAs/GaAs SLSs as DFLs, the density of TDs could be effectively reduced to the order of ~10^6 cm^{-2}. Such a low density of TDs led to a good performance of laser which achieved an extremely low threshold current density of 194 A/cm^2 and high output power of ~77 mW at room temperature under pulsed wave operation [97]. Using the same technique, the InAs/GaAs QD laser on Si with 200 A/cm^2 threshold current density, much higher output power of over 100 mW for single facet and lasing up to 111 °C was also reported [98].

Based on the previous studies and the step-by-step investigations, electrically pumped c.w. InAs/GaAs QD laser on silicon substrate with extremely low threshold current density of 62.5 A/cm^2, over 105 mW high output power at room temperature and lasing up to 120 °C has been demonstrated by our MBE group (Figure 1.20) [23]. By fitting the threshold current trend with a sub-linear model, an extrapolated mean time to failure (MTTF) of over 100,158 h was calculated (Figure 1.20 d). Remarkable progress in III-V QD laser monolithically grown on Si substrate has shown promise to achieve high integration density, high efficiency and low cost for Si photonics.

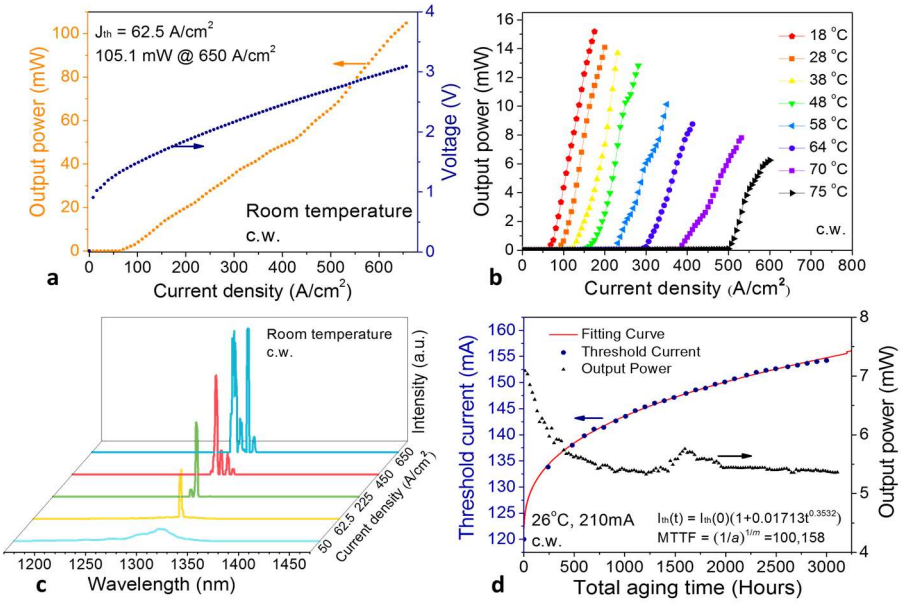

Figure 1.20 (a) Measured LIV curve of InAs/GaAs QDs laser on Si under room temperature and c.w. mode. (b) LI characteristic of lasers with various operation temperature under c.w. mode. (c) the spectrums of the Si-based QD laser with the increasing injection current. (d) The curves of threshold current and output power verse total aging time (hours) with 210mA c.w. injection current and 26℃ operation temperature [23].

- III-V QD lasers on on-axis (001) Si

In previous results, the Si (001) substrates with an 4° offcut angle towards [110] plane were commonly used to annihilate the APBs by forming the desired double-atomic steps on the surface of Si. However, offcut Si substrate is not compatible with standard microelectronics fabrication, where on-axis (001) Si substrate with less than 0.5° offcut angle are typically used [11]. As a result, the growth of III-V lasers on on-axis Si (001) substrate without the APBs has attracted substantial interest in recent years. In 2017, InAs/GaAs QD laser directly grown on on-axis Si (100) substrates without any intermediate buffer layer was fabricated by our research group [25]. In this paper, the laser device lasing at around 1.3 μm at room temperature with c.w. current injection and 43 mW output power was demonstrated [25]. As shown in figure 1.21 (c), the performance of Si (001)-based QD laser is comparable with that of QD laser diodes grown on GaAs with the same growth method.

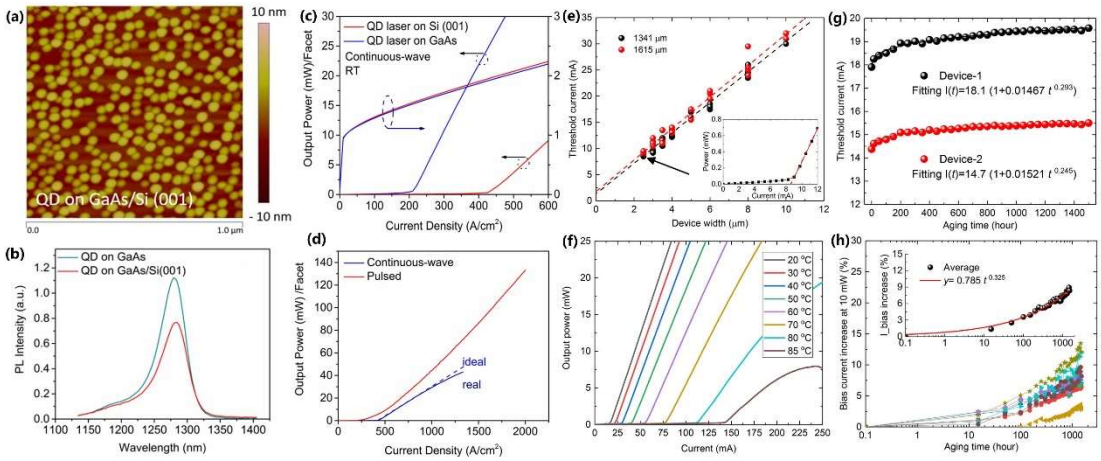

Figure 1.21 ***(a).*** *the AFM result of uncapped InAs/GaAs QDs grown on on-axis Si substrate. (****b).*** *Measured PL results of 5 layers InAs QDs structures grown on both of GaAs and Si (001).* ***(c).*** *the LIV curves.* ***(d).*** *LI curves of Si-based InAs/GaAs QD laser diodes under c.w. and pulse conditions.* ***(e).*** *c.w. threshold current versus device width operation at room temperature.* ***(f).*** *the LI curve verse different working temperature.* ***(g).*** *1500-hour lifetime-test of two 1.6mm length devices based on calculated threshold current under c.w. mode.* ***(h).*** *requirement of injection current to obtain 10mW output power under c.w. mode at 35 °C when the lifetime-test [25,99].*

In the same year, Jung et al further improved the performance of QD lasers grown on on-axis silicon [99]. The mean-time-to-failure of the InAs QD laser achieved 1 million hours, and the injection efficiency reached 87%. In GaAs buffer layer, the insertion of 10 periods of 20nm $In_{0.1}GaAs$/10nm GaAs DFLs was able to accelerate the annihilation of the threading dislocations. As shown in Figure 1.21 (e, f), because of low threading dislocation density, the J_{th} of laser diodes was only 198A/cm^2 and the highest operation temperature reached 85°C without p-type modulation doping in active region. Figure 1.21 (g, h) shows a slow increase of the threshold current and the bias current after the laser diodes is on for a long time [99]. This result demonstrated the promising potential of the QD laser grown on on-axis Si substrate closely compatible with the CMOS fabrication technology [13].

1.4 Quantum Cascade Laser

The attractive market of mid-infrared production encourages the rapid process on the research of mid-infrared laser devices, and various high-performance laser devices were successfully commercialized for mid-infrared applications [100-102]. The quantum cascade laser (QCL) is one of the most valuable and promising laser devices among common mid-infrared light sources, as shown in Figure 1.22. The QCL provides not only the whole mid-infrared spectral range, but also the wide bandwidth,

satisfying the requirement of various mid-infrared applications [87, 101]. In addition, since most of QCLs are based on III-V semiconductors, they provide a variety of advantages such as manufacturing scalability, integration capability, reliability, and low cost, which meets the requirement for analysis and spectroscopy applications [102].

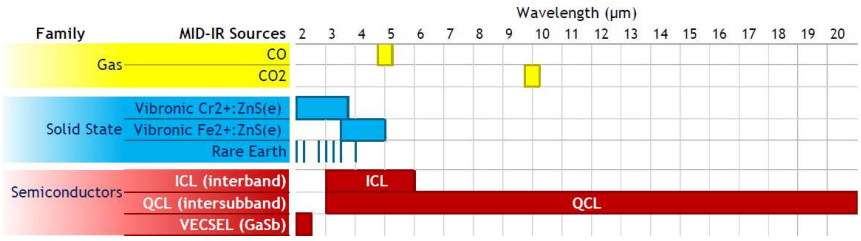

Figure 1.22 the wavelength comparison of common laser devices in mid-infrared range [102].

1.4.1 Progress of quantum cascade laser (QCL)

Figure 1.23 the schematic diagrams of band transition and intersubband transition.

For mid-infrared wavelength lasers, the emitted photon energy between 0.08 eV and 0.4 eV is needed, and this energy is much lower than the energy bandgap of III-V semiconductor materials. Therefore, the wavelength of stimulated emission, based on transition between conduction band and valence band in semiconductors, could not reach mid-infrared band [103]. To overcome the limit of interband transition in semiconductors, the intersubband transition was developed for mid-infrared laser devices.

The original concept of quantum cascade laser was proposed by Kazarinov and Suris in 1971 [104]. In this theoretical model (Figure 1.24), under a certain bias voltage, the

electronic states of multiple QWs satisfy the condition in which the first excited state (E_2) in N+1$_{th}$ period is lower than the ground state (E_1) in N$_{th}$ period. Then, the electrons in ground state of N$_{th}$ period transit to the first excited state N+1$_{th}$ period, emitting the corresponding photon energy. The energy states in N and N+1 period could be adjusted by the bias voltage and thickness of QWs, which can modulate the lasing wavelength [103,104]. However, this concept was not realized at that time due to the lack of advanced growth technology, and this creative design remained as theoretical foundation for the invention of QCL.

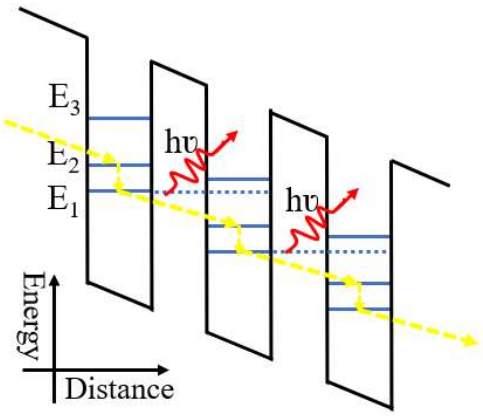

Figure 1.24 the schematic of origin conception of quantum cascade laser.

In 1980s, with the improvement of Molecular Beam Epitaxy (MBE) system, the growth of multiple periods of ultra-thin semiconductor material with high quality became possible, and the design of QCL attracted great interest again [103,105]. In 1986, sequential resonant tunneling between quantum wells was proposed by Capasso et al [105]. As shown in Figure 1.25, the ground state (E1) of N$_{th}$ period could be equally matched with the second excited state (E3) in N+1$_{th}$ period by adjusting bias, which significantly increases the possibility of resonance tunneling [106]. After the tunneling to the second excited state (E3), electrons transit to the first excited state (E2) with the photon emission. Then, the emission of optical phonons could allow the electrons to relax to the ground state quickly. The repeat of this process creates the stimulated emission and offers the necessary optical gain for lasing. However, the carrier lifetime in second excited state (E3) is always much shorter than that in first excited state (E2) in principle, which prevents the population inversion. Thus, the research of intersubband transition laser devices was disturbed by the issue of population inversion for many years [103].

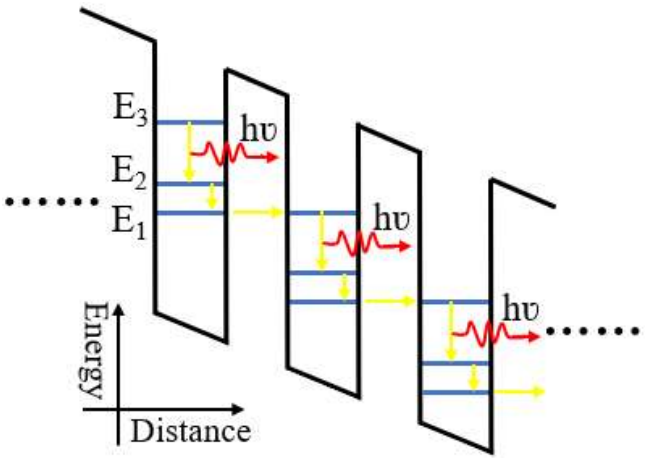

Figure 1.25 the schematic of sequential resonant tunneling.

In 1992, Sirtori et al. proposed a breakthrough which utilizes InAlAs/InGaAs superlattice in both sides of active region to resolve the population inversion issue [107]. The InAlAs/InGaAs superlattice forms the Bragg reflector which promotes to confine the electrons in high energy state of active region, and thus leads to the increased carrier lifetime in high energy state [107,108]. Figure 1.26 illustrates the proposed QCL band structure. In addition to the Bragg reflector formed by superlattices, the coupled low energy states of superlattices create a miniband for electron transport. Therefore, the use of InAlAs/InGaAs superlattices structure provided a solution to tackle the lack of population inversion in QCL [108].

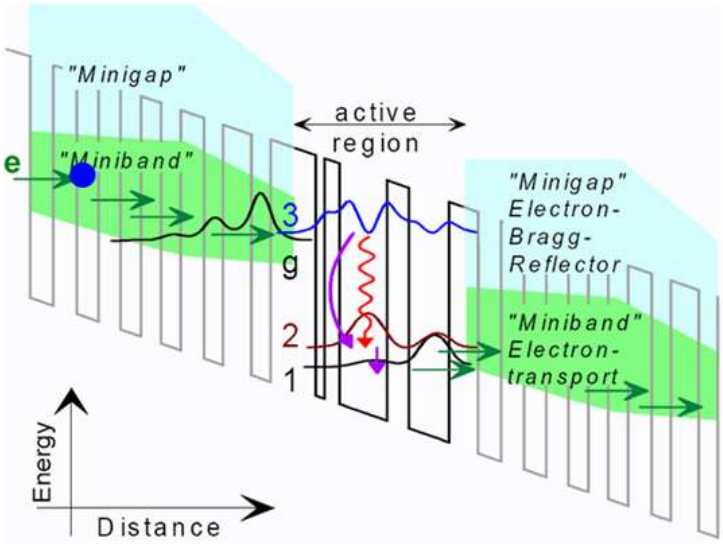

Figure 1.26 the schematic of sequential resonant tunneling

Under constant progress of structure design and material growth, the first QCL device was demonstrated by Bell Laboratories in 1994 [109]. The lasing wavelength of this QCL device was 4.2 μm, and the output power attained 8.5 mW with 0.1% pulse driving (20 ns pulse width) at 10 K operation temperature. Since the first demonstration of QCL, rapid progress in the development had been made. Only 2 years later, the operation temperature of QCL devices rose from 10 K to room temperature [110], and the first room-temperature single-mode distributed feedback (DFB) QCL was reported in 1997 [111]. Since then, a great deal of efforts has been devoted to improving the device performances, as well as expanding the emission wavelength [112,113]. In 2002, Faist et al. reported the first room-temperature QCL under c.w. operation using double-phonon resonance active region design [114]. However, the carrier injection efficiency for the upper laser level is influenced by the parasitic carrier injection into the nearest above level of upper laser level E5, resulting in a drop of population inversion and low output power at relative high temperature. With the further optimization of active region structure, the output power was enhanced by increasing injection efficiency in high energy state and enhancing the electron transport in low energy states [115].

Figure 1.27 (a) demonstrates the band structure of double-phonon resonance design, where two energy states (E1, E2) are used to quickly extract the electrons from E3 and lead to the low carrier lifetime in E3. The energy gaps between E2/E1 and E3/E2 are designed to be equal to a longitudinal optical phonon (LO) energy (35 meV), because one LO phonon energy can offer rapid intersubband resonance scattering by the phonon release, the double-phonon resonance structure prevents the electrons in E2 transporting back to E3 by letting electrons continue to quickly scatter to E1. This structure effectively decreases the carrier lifetime in both E2 and E3, and also reduces the possibility of electron thermal backflow (from E2 back to E3) due to the short carrier lifetime in E2. Double-phonon resonance structure is an ideal design obtains extremely short carrier lifetime in E3 and makes sure the population inversion efficiency. Based on the double-phonon resonance structure, room temperature c.w. mode at 9.1 μm QCL device with 17 mW output power was demonstrated [114].

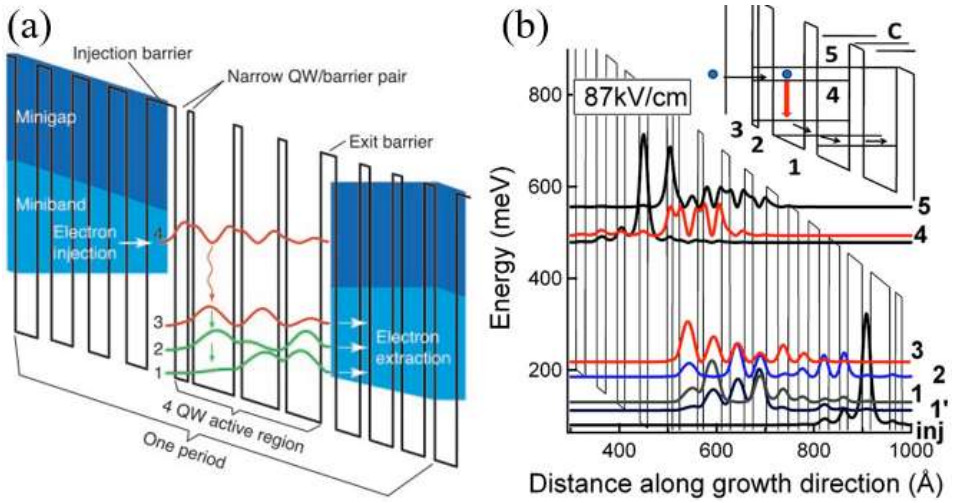

Figure 1.27 the schematic of (a) double-phonon resonance structure (b) nonresonant extraction design [114,115].

Although the double-phonon resonance design has the advantage of lowering carrier population in the lower laser level, the double-phonon condition restricts the flexibility for changing other parameters in active region design. To remove the double-phonon resonance condition, a new active region structure named ‘nonresonant extraction’ (NRE) was proposed by the Pranalytica/Harvard team [115,116]. As shown in Figure 1.27 (b), the lower laser level E3 lifetime in the NRE design was kept short enough by using several parallel transitions from level E3 to E2, E1, and E1'. As a result, the NRE design is more flexible in energy state design and thus gives more space for active region optimization. This additional flexibility can be used to increase E54, which resulted into improved c.w. performance. Under room temperature and c.w current driving, a well-performed QCL device obtained an output power of 3 W with wallplug efficiency of 12.7 % and 4.6 μm wavelength by utilizing NRE design in 2009 [116].

With the continuous progress in QCL, the highest output power under c.w mode and room temperature has reached 5.1W (4.9 μm wavelength) with 21% wallplug efficiency, the pulsed injection current offers better performance, in which the wallplug efficiency has achieved 27% [117]. The single mode QCL devices are also developed rapidly, 2.4W mid-infrared lasing (4.8 μm) is measured with c.w mode and room temperature condition in 2011 [118]. Besides, the application of DFB, DBR, photonic crystals, subwavelength metal grating and other advanced structure continuous enhance the far field capability of mid-infrared QCL devices [119-121].

With the rapid progress of silicon photonics in last two decades, Si-based QCL is continuously desired for mid-infrared silicon photonics [57,58]. Si-based quantum cascade laser with 4.8 μm wavelength via wafer bonding has been reported in 2016, but the performance is still far away to realize the commercial production [122]. The generation of Si-based QCL offers an effective way to approach the huge market of mid-infrared silicon photonics, and it stimulates the more researches paid attention to QCL and Si-based QCL.

1.4.2 The characteristics of QCL

The creation of QCL was initiated with the combination of energy state design and high-accuracy molecular beam epitaxy. Compared with classic double heterojunction semiconductor lasers, the QCLs have several unique characteristics and advantages [103,123-127]:

(1) The intersubband transition allows to engineer the wavelength of QCL covering the range from around 3 μm to 300 μm. The broaden lasing spectrum enables the QCL devices to be widely used in mid-infrared and terahertz band applications as a light source.

(2) The wavelength of laser devices is not directly related with the bandgap of semiconductor material, but depends on the energy state of subband in active region. As the energy states in conduction band can be controlled by the thickness of epitaxial layers, the wavelength of QCL can be engineered by adjusting the thickness of layers, instead of changing the material component.

(3) The active region of QCL is based on the multiple period and cascade mechanism, so that each photon used for the stimulated photon emission will tunnel to the next period and contribute to the intersubband transition again. The repeat of this process produces multiple photons output by each photon injection. For an ideal N periods QCL, one injection photon could generate N photons. As a result, QCL device has the advantage of high internal quantum efficiency, and has the great potential to produce high-power laser light source.

(4) The radiative transition of QCL occurs in the same band, and hence the Auger recombination effect is effectively prevented. Therefore, the decrease of non-radiative recombination could enhance the temperature stability and attain high characteristic temperature.

(5) The carrier relaxation time of intersubband transition is much faster than that of interband transition, and thus the QCL device can provide high-speed response.

1.4.3 InP-based and GaAs-based QCL

GaAs/AlGaAs and InP/InGaAs/InAlAs are two majority material systems used for QCL devices [103]. Owing to the mature production and experienced growth technique of GaAs-based devices in optical fiber communication, the fabrication of GaAs/AlGaAs QCL devices with complex structure and nanostructure is reliable [128,129]. After the demonstration of the first QCL device, GaAs/AlGaAs QCL has been regarded as a new attractive approach to obtain mid-infrared and far-infrared laser [130]. In particular, the GaAs-based QCL has several unique advantages. Firstly, the GaAs/AlGaAs QCL could offer broad lasing spectra from 8 μm to 300 μm wavelength, including mid-infrared, far-infrared and Terahertz band [131]. Second, the matched lattice constant of GaAs and AlGaAs simplifies the epitaxial growth of GaAs/AlGaAs structure because it is unnecessary to consider the strain release during both structure design and growth process [128,129].

During the development of GaAs/AlGaAs QCL, the content of Al is found as a key parameter in active region design [132-134]. Because AlAs material has high band energy, increasing Al component leads to the increase of barrier energy in active region. Therefore, it could enhance the confinement of carriers and prevent the carrier thermal leakage [135-137]. However, the growth of high Al content material is difficult to be realized because the material quality drops rapidly when Al content exceeds 45% [138]. Several research point out that the GaAs/AlGaAs QCL is expected to have best performance with 45% Al content, and this parameter is used for GaAs/AlGaAs QCL samples discussed in my thesis [134].

The InP/InGaAs/InAlAs is also widely used material system in mid-infrared QCL devices [103]. In the spectral range from 3 μm to 10 μm, the InP-based QCL devices display excellent performances with high output power over 5W and high temperature stability with over 100℃ under c.w. current driving [117-118]. The better lasing property of InP-based QCL comes from several theoretical superiorities compared with GaAs/AlGaAs QCL. First of all, the potential well of InGaAs/InAlAs active region of InP-based QCL is deeper than GaAs/AlGaAs material system, and therefore, the higher energy barrier reduces the thermal leakage of electrons, resulting in better thermal performance and higher carrier injection efficiency [139]. Secondly, the InP has higher thermal conductivity than GaAs [140]. Due to the thick waveguide in QCL structure, the heating dissipation in waveguide, related to the thermal leakage of carriers, is important for laser devices. Thus, a higher thermal conductivity of InP is one of main reasons that the InP-based QCL shows better performance than that of GaAs-based QCL. Thirdly, the refractive index of InP substrate is lower than that of InGaAs/InAlAs active region, while the GaAs substrate shows higher refractive index than GaAs/AlGaAs [141]. It means that the GaAs substrate is not able to be used as the optical confined cladding layer, but InP substrate contributes to light confinement in active region. Due to the optical confinement function of InP substrate, InP-based QCL could has thinner waveguide than GaAs-based QCL, which brings benefits to both sample growth and heat dissipation [142]. Finally, the gain for a given emission wavelength is proportional to (me*)-3/2, the gain in InP-based QCL is larger than that of GaAs-based QCL, because of me*(InGaAs)=0.043m0 and me*(GaAs)=0.0665m0.

In conclusion, both of GaAs/AlGaAs and InP/InGaAs/InAlAs are important material systems for QCL devices. In principle, the QCL devices with InP/InGaAs/InAlAs could show better lasing behavior than GaAs-based QCL in mid-infrared field, and GaAs/AlGaAs QCL benefits from the mature manufacture and broaden wavelength band. Both of these two kinds of QCL devices have special characteristics, and these QCLs are attractive laser source in application market.

1.5 Thesis structure

The main objective of my Ph.D study is the research of high-performance and high-reliable Si-based laser devices used for silicon photonics. Due to the impressive progress of O-band QD laser directly grown on Si substrate, my research starts from this entry point to study the design and fabrication knowledge of silicon-based laser, and then try to solve some of the existing problems and improve the laser property. After this preparation, the next step is to extend the research field. QCL occupies majority market in mid-infrared laser field and Si-based QCL is still lacking, so that the Si-based QCL is an attractive and potential approach. Therefore, the research of high performance QCL devices is a necessary project. Since the QD has been proved as a suitable material for Si-based laser devices in previous works, the research of QDCL is also a meaningful project aiming at the generation of Si-based QCL devices.

This thesis begins with the introduction including the background review of silicon photonics, the characteristic of QD and QW materials, and Si-based III-V QD laser devices. Also, the principle of QCL design and the progress of QCL devices are also presented.

Chapter 2 introduces the mothed of experiments in this thesis. The experiment workings in this thesis include material growth, device fabrication and sample measurement. The growth technology and material characterization are first discussed in this chapter. Then, the fabrication process and measurement technologies used in thesis are presented in detail.

Based on experiments of comparisons between QD and QW laser devices, the exploration of suitable semiconductor material used for Si-based laser is researched in Chapter 3. This section starts with the introduction of wafer structure and the material characteristic, and then pays attention to the comparisons of QD and QW laser monolithically grown on on-axis (001) Si substrates. After the data collection, the analysis of measured results proves that Si-based QD laser devices is more insensitive to dislocations and has higher possibility to operate lasing, compared with Si-based QW devices.

According to the result and conclusion in chapter 3, all-MBE QD laser monolithically grown on Si substrates is reported in chapter 4 as continuous research. To obtain all-

MBE grown APB-free QD lasers on on-axis Si substrate, two approaches using Si buffer and Ge buffer were employed to growth QD lasers structures. It was revealed that with the thin Ge buffer layer on Si substrate, the QD laser acquires an improved lasing operation, and this is a reasonable approach to realize high-performance Si-based QD lasers devices without costly MOCVD growth.

Chapter 5 introduces the projects of QCL devices, quantum dot cascade laser (QDCL) devices, and the exploration of Si-based QCL devices. Compared with 1.3μm wavelength QD laser devices shown in pervious chapters, QCL could obtain longer wavelength which is impossible for Si-based InAs QD laser, and QCL with mid-infrared wavelength shows different and broaden application potential. However, the growth of QCL is totally different with the O-band QD laser devices, and thus the research of high performance QCL devices should be prepared for Si-based QCL. Both GaAs-based and InP-based QCL devices are demonstrated in Chapter 5. Several improved fabrication technologies are also applied to QCL devices in this chapter. The continuous improvement in fabrication process leads to the enhancement of QCL devices, and high-performance InP-based QCL devices is demonstrated after utilizing improved fabrication process.

Chapter 5 also pays attention to the research of high performance QDCL devices. In addition to the QW-based QCL, the research of QDCL is also a meaningful approach because of the unique properties of QDs which are suitable for Si-based lasers. Based on the research experience of both QD laser and QCL, the mid-infrared QDCL with better wall-plug efficiency and higher characteristic temperature was demonstrated. The optimization of the number of QD lasers per period of active region was performed in this chapter. Based on the optimization, the performance of QDCL was improved, which is comparable with the typical QW-based QCL. In addition, the polarization measurement shows the unique TE emission of QDCL, which is a breakthrough for surface-emitting QCL.

In the last section of chapter 5, the Si-based QCL was attempted with different structure design based on the pervious results, and the measured results indicated that the Si-based QCL required more optimizing and growth improvement. However, the Covid-19 influences the process of Si-based QCL. Several optimization approaches based on both sample growth and fabrication are suggested, and the final

aim, the realization of Si-based QCL, is possible to be achieved with further material improvement and process development.

In the final of thesis, the summary of this thesis and further works are introduced in chapter 6. Microdisk laser is popular in Si-based laser fabrication, so it is possible to attempt the microdisk QCL structure monolithically grown on Si substrate in my further work. Besides, the surface emitting QCL is also a feasible research, and based on the results in this thesis, both of high-performance QCL with Bragg grating or QDCL with VCSEL structure are reasonable approaches.

References

[1] D. Liang and J. E. Bowers, “Recent progress in lasers on silicon,” *Nat. Photonics*, vol. 4, no. 8, pp. 511–517, 2010.

[2] Z. Wang, B. Tian, M. Pantouvaki, W. Guo, P. Absil, J. Van Campenhout, C. Merckling, and D. Van Thourhout, “Room-temperature InP distributed feedback laser array directly grown on silicon,” *Nat. Photonics*, 9, 837–842, 2015.

[3] E. Tournié, L. Cerutti, J. Rodriguez, H. Liu, and J. Wu, “Metamorphic III–V semiconductor lasers grown on silicon,” *MRS*, 2016.

[4] S. W. Corzine et al., “Large-scale InP transmitter PICs for PM-DQPSK fiber transmission systems,” *IEEE Photonics Technol. Lett.*, vol. 22, no. 14, pp. 1015–1017, 2010.

[5] J. Caton, “Handling the Heat.,” *Am. Sch. Board J.*, vol. 3, no. January, pp. 3–4, 2009.

[6] L. Pavesi, L. Dal Negro, C. Mazzoleni, G. Franzò, and F. Priolo, “Optical gain in silicon nanocrystals,” *Nature,* vol. 408, no. 6811, pp. 440–444, 2000.

[7] M. Smit *et al.*, “An introduction to InP-based generic integration technology,” *Semicond. Sci. Technol.*, vol. 29, no. 8, 2014.

[8] Y. Wang, S. Chen, Y. Yu, L. Zhou, L. Liu, C. Yang, M. Liao, M. Tang, Z. Liu, J. Wu, W. Li, I. Ross, A. J. Seeds, H. Liu, and S. Yu, “Monolithic quantum-dot distributed feedback laser array on silicon,”*Optica,* 5, 528–533, 2018.

[9] B. Tian *et al.*, “Room Temperature O-band DFB Laser Array Directly Grown on (001) Silicon,” *Nano Lett.*, vol. 17, no. 1, pp. 559–564, 2017.

[10] S. Chen *et al.*, “InAs/GaAs Quantum-Dot Superluminescent Light-Emitting Diode Monolithically Grown on a Si Substrate,” *ACS Photonics*, vol. 1, no. 7, pp. 638–642, 2014.

[11] M. Hochberg and T. Baehr-Jones, “Towards fabless silicon photonics,” *Nat. Photonics,* vol. 4, no. 8, pp. 492–494, 2010.

[12] R. Stabile, A. Albores-Mejia, and K. A. Williams, “Monolithic active-passive 16×16 optoelectronic switch,” *Opt. Lett.*, vol. 37, no. 22, p. 4666, 2012.

[13] M. Liao, S. Chen, J.-S. Park, A. Seeds, and H. Liu, “III–V quantum-dot lasers monolithically grown on silicon,” *Semicond. Sci. Technol.*, vol. 33, no. 12, p. 123002, 2018.

[14] G. Brammertz et al., “GaAs on Ge for CMOS,” *Thin Solid Films*, vol. 517, no. 1, pp. 148–151, Nov. 2008..

[15] Z. Wang et al., “array directly grown on silicon,” *Nat. Photonics*, vol. 9, no. 12, pp. 837–842, 2015.

[16] https://www.marketresearchfuture.com/reports/silicon-photonics-market-2809

[17] Z. Wang et al., “Novel Light Source Integration Approaches for Silicon Photonics,” *Laser Photonics Rev.*, vol. 11, no. 4, pp. 1–21, 2017.

[18] G. T. Reed, G. Mashanovich, F. Y. Gardes, and D. J. Thomson, “Silicon optical modulators,” *Nat. Photonics*, vol. 4, no. 8, pp. 518–526, 2010.

[19] D. J. Thomson et al., “50-Gb/s silicon optical modulator,” *IEEE Photonics Technol. Lett.*, vol. 24, no. 4, pp. 234–236, 2012.

[20] J. Michel, J. Liu, and L. C. Kimerling, “High-performance Ge-on-Si photodetectors,” *Nat. Photonics*, vol. 4, no. 8, pp. 527–534, 2010.

[21] B. Lingnau and K. Lüdge, “Quantum-dot semiconductor optical amplifiers,” *Handb. Optoelectron. Device Model. Simul. Fundam. Mater. Nanostructures, LEDs, Amplifiers*, vol. 1, no. 9, pp. 715–

746, 2017.

[22] D. Dai, J. Bauters, and J. E. Bowers, “Passive technologies for future large-scale photonic integrated circuits on silicon: Polarization handling, light non-reciprocity and loss reduction,” *Light Sci. Appl.*, vol. 1, no. MARCH, pp. 1–12, 2012.

[23] S. Chen et al., “Electrically pumped continuous-wave III-V quantum dot lasers on silicon,” *Nat. Photonics*, vol. 10, no. 5, pp. 307–311, 2016.

[24] D. Dai and J. E. Bowers, “Silicon-based on-chip multiplexing technologies and devices for Peta-bit optical interconnects,” *Nanophotonics*, vol. 3, no. 4–5, pp. 283–311, 2014.

[25] S. Chen, M. Liao, M. Tang, J. Wu, M. Martin, T. Baron, A. Seeds, and H. Liu, “Electrically pumped continuous-wave 1.3 μm InAs/GaAs quantum dot lasers monolithically grown on on-axis Si (001) substrates,” *Opt. Express*, 25(5), 4632–4639, 2017.

[26] M. Liao et al., “Low-noise 13 μm InAs/GaAs quantum dot laser monolithically grown on silicon,” *Photonics Res.,* vol. 6, no. 11, p. 1062, 2018.

[27] J. Wu, S. Chen, A. Seeds, and H. Liu, “Quantum dot optoelectronic devices: Lasers, photodetectors and solar cells,” *J. Phys. D. Appl. Phys.*, vol. 48, no. 36, 2015.

[28] R. E. Camacho-Aguilera et al., “An electrically pumped germanium laser,” *Opt. Express,* vol. 20, no. 10, p. 11316, 2012.

[29] S. Wirths et al., “Lasing in direct-bandgap GeSn alloy grown on Si,” *Nat. Photonics*, vol. 9, no. 2, pp. 88–92, 2015

[30] D. Wu et al., “Low threshold current density 1.3 μm metamorphic InGaAs/GaAs quantum well laser diodes,” *Electron. Lett.*, vol. 44, no. 7, pp. 7–8, 2008.

[31] Z. Fang, Q. Y. Chen, and C. Z. Zhao, “A review of recent progress in lasers on silicon,” *Opt. Laser Technol.*, vol. 46, no. 1, pp. 103–110, 2013.

[32] Q. Li, K. W. Ng, and K. M. Lau, “Growing antiphase-domain-free GaAs thin films out of highly ordered planar nanowire arrays on exact (001) silicon,” *Appl. Phys. Lett.*, vol. 106, no. 7, 2015.

[33] O. B. Shchekin and D. G. Deppe, “1.3 μm InAs quantum dot laser with T_0=161K from 0 to 80°C,” *Appl. Phys. Lett.*, vol. 80, no. 18, pp. 3277–3279, 2002

[34] D. G. Deppe et al., “Room-temperature continuous operation of p - n Al x Ga 1− x As-GaAs quantum well heterostructure lasers grown on Si,” *Appl. Phys. Lett.*, vol. 51, no. 9, pp. 637–639, 1987.

[35] R. Alcotte *et al.*, “Epitaxial growth of antiphase boundary free GaAs layer on 300 mm Si(001) substrate by metalorganic chemical vapour deposition with high mobility,” *APL Mater.*, vol. 4, no. 4, 2016.

[36] H. K. Choi and C. A. Wang, “InGaAs/AlGaAs strained single quantum well diode lasers with extremely low threshold current density and high efficiency,” *Appl. Phys. Lett.*, vol. 57, no. 4, pp. 321–323, 1990.

[37] “Metals and Solid-State Materials.” [Online]. Available: http://wps.prenhall.com/wps/media/objects/4680/4793217/ch21_04.htm. [Accessed: 22-Mar-2017].

[38] M. Fox, “Angular momentum in atomic physics,” in *Optical properties of solids*, Second edi., Oxford University Press, 2010, pp. 350–353.

[39] M. Fox, “Band theory,” in *Optical properties of solids*, Second edi., New york: Oxford University Press, 2010, pp. 354–356.

[40] P. Blood, “3.3 III-V semiconductor alloys,” in *Quantum confined laser devices : optical gain and recombination in semiconductors*, First edit., Oxford University Press, 2015, pp. 25–27.

[41] M. Fox, “Semiconductor p-i-n diodes,” in *Optical properties of solids*, Oxford University Press,

2010, pp. 363–364.

[42] M. Fox, “Interband luminescence,” in *Optical properties of solids*, Oxford University Press, 2010, pp. 115–117.

[43] P. Blood, “Stimulated emission and optical gain,” in *Quantum confined laser devices : optical gain and recombination in semiconductors*, First edit., Oxford University Press, 2015, p. 11.

[44] P. Blood, “population inversion and quasi-equilibrium,” in *Quantum confined laser devices : optical gain and recombination in semiconductors*, First edit., Oxford University Press, 2015, pp. 15–16.

[45] P. Blood, “Amplification and threshold,” in *Quantum confined laser devices : optical gain and recombination in semiconductors*, First edit., Oxford University Press, 2015, pp. 50–53.

[46] P. Blood, “What is a laser,” in *Quantum confined laser devices : optical gain and recombination in semiconductors*, Oxford University Press, 2015, pp. 2–4.

[47] V. M. Ustinov, A. E. Zhukov, A. Y. Egorov, and N. A. Maleev, “Optical gain and its relationship with laser threshold,” in *Quantum Dot Lasers*, Oxford University Press, 2003, pp. 15–19.

[48] V. M. Ustinov, A. E. Zhukov, A. Y. Egorov, and N. A. Maleev, “Laser cavity and light confinement,” in *Quantum Dot Lasers*, Oxford University Press, 2003, pp. 6–11.

[49] K. C. Kao and G. A. Hockham. Dielectric-fibre surface waveguides for optical frequencies. *Proceedings of the Institution of Electrical Engineers*, vol. 113, pp.1151-1158, 1966.

[50] A. Willner, C. Yu, Z. Pan, Optical Fiber Telecommunications, Book, Academic Press, ed. 5, 2008, chap. 7

[51] R. H. Stolen, Optical Fiber Telecommunications. New York: Academic, 1979, ch. Nonlinear Properties of Optical Fibers, pp. 125–150.

[52] P. J. Winzer and R.-J. Essiambre, “Advanced optical modulation formats,” in Optical Fiber Telecommunications VB, I. Kaminow and T. Li, Eds. New York: Academic, 2008, pp. 232–304.

[53] M. T. Fatehi and M. Wilson, Optical networking with WDM, McGraw-Hill, New York, 2001.

[54] B. Min, H. Yoon, W. J. Lee and N. Park. Coupled structure for wide-band EDFA with gain and noise figure improvements from C to L-band ASE injection. *IEEE Photonics Technology Letters*, vol. 12, no. 5, pp. 480-482, May 2000, doi: 10.1109/68.841259.

[55] K. Wunstel, A. Mozera, M. Schilling, et al. High-Speed 1.3-um DFB Laser with Modified DCPBH Structure. *Electronics Letters*, 1986, 22(21): 1144-5.

[56] T. Kageyama, K. Nishi, M. Yamaguchi, R. Mochida, Y. Maeda, K. Takemasa, Y. Tanaka, T. Yamamoto, M. Sugawara, and Y. Arakawa. Extremely High Temperature (220°C) Continuous-Wave Operation of 1300-nm-range Quantum-Dot Lasers. *CLEO/Europe and EQEC 2011 Conference Digest*, paper PDA_1.

[57] Rio Calvo, M., Monge Bartolomé, L., Bahriz, M., Boissier, G., Cerutti, L., Rodriguez, J.-B., & Tournié, E. (2020). Mid-infrared laser diodes epitaxially grown on on-axis (001) silicon. Optica, 7(4), 263.

[58] Hu, T., Dong, B., Luo, X., Liow, T.-Y., Song, J., Lee, C., & Lo, G.-Q. (2017). Silicon photonic platforms for mid-infrared applications [Invited]. Photonics Research, 5(5), 417.

[59] Consolino, L., Nafa, M., De Regis, M., Cappelli, F., Garrasi, K., Mezzapesa, F. P., Li, L., Davies, A. G., Linfield, E. H., Vitiello, M. S., Bartalini, S., & De Natale, P. (2020). Quantum cascade laser based hybrid dual comb spectrometer. *Communications Physics*, 3(1), 1–9.

[60] Siciliani de Cumis, M., Viciani, S., Borri, S., Patimisco, P., Sampaolo, A., Scamarcio, G., De Natale, P., D’Amato, F., & Spagnolo, V. (2014). Widely-tunable mid-infrared fiber-coupled quartz-enhanced photoacoustic sensor for environmental monitoring. *Optics Express*, 22(23), 28222.

[61] Capasso F, Paiella R, Martini R, et al. Quantum cascade lasers: ultrahigh-speed operation, optical wireless communication, narrow linewidth, and far-infrared emission. IEEE Journal of Quantum Electronics , 2002, 38(6): 511-532.

[62] Martini R, Whittaker E A. Quantum cascade laser-based free space optical communications. *Journal of Optical and Fiber Communications Reports*, 2005, 2(4): 279-292.

[63] Bielecki Z, Kolosowski W, Mikolajczyk J. Free space optical data link using quantum cascade laser. *PIERS Proceedings,* Cambridge, USA, 2008.

[64] Corrigan P, Martini R, Whittaker E A, et al. Quantum cascade lasers and the Kruse model in free space optical communication. Optics Express, 2009, 17(6): 4355-4359.

[65] d'Humières, B., Margoto, É., & Fazilleau, Y. (2016). Cascade laser applications: trends and challenges. Novel In-Plane Semiconductor Lasers XV, 9767(March 2016), 97671U.

[66] Du, Z., Zhang, S., Li, J., Gao, N., & Tong, K. (2019). Mid-infrared tunable laser-based broadband fingerprint absorption spectroscopy for trace gas sensing: A review. Applied Sciences (Switzerland), 9(2), 1–33.

[67] Bizet, L., Vallon, R., Parvitte, B., Brun, M., Maisons, G., Carras, M., & Zeninari, V. (2017). Multi-gas sensing with quantum cascade laser array in the mid-infrared region. Applied Physics B: Lasers

[68] Nikodem, M., Gomółka, G., Klimczak, M., Pysz, D., & Buczyński, R. (2019). Demonstration of mid-infrared gas sensing using an anti-resonant hollow core fiber and a quantum cascade laser. Optics Express, 27(25), 36350.

[69] W. Sibbett, "Mode-locked quantum-dot lasers," *Mode-locked quantum-dot lasers*, pp. 395–401, 2007.

[70] H. Park, A. W. Fang, S. Kodama, and J. E. Bowers, "Hybrid silicon evanescent laser fabricated with a silicon waveguide and III-V offset quantum wells," *Opt. Express*, vol. 13, no. 23, p. 9460, 2005.

[71] A. W. Fang, H. Park, O. Cohen, R. Jones, M. J. Paniccia, and J. E. Bowers, "Electrically pumped hybrid AlGaInAs-silicon evanescent laser," *Opt. Express*, vol. 14, no. 20, p. 9203, 2006.

[72] M. Paniccia et al., "A Hybrid Silicon Laser: Silicon photonics technology for future tera-scale computing," *Intel white Pap*., 2006.

[73] D. Liang and J. E. Bowers, "Highly efficient vertical outgassing channels for low-temperature InP-to-silicon direct wafer bonding on the silicon-on-insulator substrate," *J. Vac. Sci. Technol. B,* Microelectron. Nanom. Struct., vol. 26, no. 4, p. 1560, 2008.

[74] K. Tanabe, K. Watanabe, and Y. Arakawa, "III-V/Si hybrid photonic devices by direct fusion bonding.," *Sci. Rep*., vol. 2, p. 349, 2012.

[75] B. Song et al., "3D integrated hybrid silicon laser," *Eur. Conf. Opt. Commun*. ECOC, vol. 2015–November, no. 10, pp. 10435–10444, 2015.

[76] Z. Zhou, B. Yin, and J. Michel, "On-chip light sources for silicon photonics," *Light Sci. Appl*., vol. 4, 2015.

[77] R. Alcotte, M. Martin, J. Moeyaert, R. Cipro, S. David, F. Bassani, F. Ducroquet, Y. Bogumilowicz, E. Sanchez, Z. Ye, X. Y. Bao, J. B. Pin, and T. Baron, "Epitaxial growth of antiphase boundary free GaAs layer on 300 mm Si(001) substrate by metalorganic chemical vapour deposition with high mobility", *APL Mater*. 4 046101, 2016

[78] K. Nishi, K. Takemasa, M. Sugawara and Y. Arakaw, "Development of quantum dot lasers for data-com and silicon photonics applications", *IEEE J. Sel. Top. Quantum Electron*.23 1–7, 2017

[79] Z. Mi, J. Yang , P. Bhattacharya, G. Qin and Z. Ma, "High-performance quantum dot lasers and integrated optoelectronics on Si", *Proc. IEEE*, 97 1239–49, 2009.

[80] J. Yang, P. Bhattacharya and Z. Mi, "High-performance In0.5Ga0.5As/GaAs quantum-dot lasers

on silicon with multiple-layer quantum-dot dislocation filters", *IEEE Trans. Electron Devices*, 54 2849–55, 2007.

[81] Z. I. Alferov, R. F. Kazarinov, *Semiconductor laser with electric pumping*, priority as of March 1963.

[82] P. Blood, "3.3 III-V semiconductor alloys," in *Quantum confined laser devices : optical gain and recombination in semiconductors*, First edit., Oxford University Press, 2015, pp. 25–27.

[83] M. Fox, "Quantum-confined structures," in *Optical properties of solids*, Oxford University Press, 2010, pp. 141–144.

[84] Y. Arakawa and H. Sakaki, "Multidimensional Quantum Well Laser and Temperature-Dependence of Its Threshold Current," *Appl. Phys. Lett.*, vol. 40, no. 11, pp. 939–941, 1982.

[85] D. Jung *et al.*, "High efficiency low threshold current 1.3 *μ*m InAs quantum dot lasers on on-axis (001) GaP/Si," *Appl. Phys. Lett.*, vol. 111, no. 12, p. 122107, 2017.

[86] AY. Liu, S. Srinivasan, J. Norman, AC. Gossard, and JE. Bowers, ''Quantum dot lasers for silicon photonics'', Vol. 3, No. 5 ,October, *Photon. Res.*, 2015.

[87] Q. Li and K. M. Lau, "Epitaxial growth of highly mismatched III-V materials on (001) silicon for electronics and optoelectronics," *Prog. Cryst. Growth Charact. Mater.*, vol. 63, no. 4, pp. 105–120, 2017.

[88] AY. Liu, R. W. Herrick, O. Ueda, P. M. Petroff, A. C. Gossard, and J. E. Bowers, "Reliability of InAs/GaAs Quantum Dot Lasers Epitaxially Grown on Silicon," *IEEE J. Sel. Top. Quantum Electron.*, vol. 21, no. 6, 2015.

[89] Q. Li, K. W. Ng, and K. M. Lau, "Growing antiphase-domain-free GaAs thin films out of highly ordered planar nanowire arrays on exact (001) silicon," Appl. Phys. Lett., vol. 106, no. 7, 2015.

[90] O. B. Shchekin, J. Ahn, and D. G. Deppe, "High temperature performance of self-organised quantum dot laser with stacked p-doped active region," *Electron. Lett.*, vol. 38, no. 14, p. 712, 2002.

[91] H. Y. Liu *et al.*, "Long-wavelength InAs/GaAs quantum-dot laser diode monolithically grown on Ge substrate," *Nat. Photonics*, vol. 5, no. 7, pp. 416–419, 2011.

[92] D. G. Deppe, K. Shavritranuruk, G. Ozgur, H. Chen, and S. Freisem, "Quantum dot laser diode with low threshold and low internal loss," *Electron. Lett.*, vol. 45, no. 1, pp. 54–55, 2009.

[93] A Lee, H Liu, A Seeds, "Semiconductor III–V lasers monolithically grown on Si substrates", *Semiconductor Science and Technology*, 28 (1), 015027, 2012

[94] A. Y. Liu *et al.*, "High performance continuous wave 1.3 μm quantum dot lasers on silicon," *Appl. Phys. Lett.*, vol. 104, no. 4, p. 41104, 2014.

[95] T. Wang, H. Liu, A. Lee, F. Pozzi, and A. Seeds, "13-μm InAs/GaAs quantum-dot lasers monolithically grown on Si substrates," *Opt. Express*, vol. 19, no. 12, p. 11381, Jun. 2011.

[96] A. D. Lee, Qi Jiang, Mingchu Tang, Yunyan Zhang, A. J. Seeds, and Huiyun Liu, "InAs/GaAs Quantum-Dot Lasers Monolithically Grown on Si, Ge, and Ge-on-Si Substrates," *IEEE J. Sel. Top. Quantum Electron.*, vol. 19, no. 4, pp. 1901107–1901107, Jul. 2013.

[97] M. Tang *et al.*, "1.3-μm InAs/GaAs quantum-dot lasers monolithically grown on Si substrates using InAlAs/GaAs dislocation filter layers," *Opt. Express*, vol. 22, no. 10, pp. 11528–11535, 2014.

[98] S. Chen *et al.*, "1.3-μm InAs/GaAs quantum-dot laser monolithically grown on Si Substrates operating over 100 C," *Electron. Lett.*, vol. 50, no. 20, pp. 1467–1468, 2014.

[99] D. Jung, Z. Zhang, J. Norman, R. Herrick, M.J. Kennedy, P. Patel, K. Turnlund, C. Jan, Y. Wan, A.C. Gossard, and J.E. Bowers, "Highly reliable low threshold InAs quantum dot lasers on on-axis (001) Si with 87% injection efficiency", *ACS Photonics,* 5 (3), pp 1094–1100, 2018.

[100] Lochbaum, A., Dorodnyy, A., Koch, U., Koepfli, S. M., Volk, S., Fedoryshyn, Y., Wood, V., & Leuthold, J. (2020). Compact Mid-Infrared Gas Sensing Enabled by an All-Metamaterial Design. Nano Letters, 20(6), 4169–4176.

[101] Zemike F, Berman P R. Generation of far infrared as a difference frequency[J]. Physical Review Letters, 1965, 15(26): 999—1001.

[102] Giordmaine J A, Miller R C. Tunable Coherent Parametric Oscillation in LiNbat Optical

[103] Faist J. Quantum cascade lasers. London:Oxford University Press, 2013.

[104] R. Kazarinov and R. Suris, Possibility of amplication of electromagnetic waves in a semiconductor with a superlattice. 1971, 5: 707.

[105] Capasso F, Mohammed K, Cho A Y. Electronic transport and depletion of quantum wells by tunneling through deep levels in semiconductor superlattices. Physical review letters, 1986, 57(18): 2303.

[106] Liu H C. A novel superlattice infrared source. Journal of applied physics, 1988, 63(8): 2856-2858.

[107] Sirtori C, Capasso F, Faist J, et al. Quantum wells with localized states at energies above the barrier height: A Fabry–Perot electron filter. Applied physics letters, 1992, 61(8): 898-900.

[108] Sirtori C, Faist J, Capasso F, et al. Narrowing of the intersubband absorption spectrum by localization of continuum resonances in a strong electric field. Applied physics letters, 1993, 62(16): 1931-1933.

[109] Faist J, Capasso F, Sivco D L, et al. Quantum cascade laser[J]. Science, 1994, 264(5158): 553-556.

[110] Faist J, Capasso F, Sirtori C, et al. Room temperature midinfrared quantum cascade lasers[J]. Electronics Letters, 1996, 32(6): 560-561.

[111] Liu F Q, Zhang Y Z, Zhang Q S, et al. High-performance strain-compensated InGaAs/InAlAs quantum cascade lasers[J]. Semiconductor Science and Technology, 2000, 15(12): L44.

[112] Faist J, Gmachl C, Capasso F, et al, Distributed feedback quantum cascade lasers[J]. Applied Physics Letters, 1997, 70(20): 2670-2672.

[113] Blaser S, Yarekha D, Hvozdara L, et al. Room-temperature, continuous-wave, single-mode quantum-cascade lasers at 5.4 μm. *Applied Physics Letters*, 2005, 86: 1-3.

[114] Beck M, Hofstetter D, Aellen T, et al. Continuous wave operation of a mid-infrared semiconductor laser at room temperature. Science, 2002, 295(5553): 301-305.

[115] A. Lyakh, C. Pflügl, L. Diehl, Q. J. Wang, F. Capasso, X. J. Wang, et al. 1.6 W high wall plug efficiency, continuous-wave room temperature quantum cascade laser emitting at 4.6 μm. *Applied Physics Letters*, 2008, 92: 111110.

[116] A. Lyakh, R. Maulini, A. Tsekoun, R. Go, C. Pflügl, L. Diehl, et al. 3 W continuous-wave room temperature single-facet emission from quantum cascade lasers based on nonresonant extraction design approach[J]. Applied Physics Letters, 2009, 95: 141113.

[117] Bai. Y, Bandyopadhyay. N, Tsao. S, et al. Room temperature quantum cascade lasers with 27% wall plug efficiency. Applied Physics Letters, 2011, 98(18): 181102.

[118] Q. Y. Lu, Y. Bai, N. Bandyopadhyay, S. Slivken, and M. Razeghi, 2.4 W room temperature continuous wave operation of distributed feedback quantum cascade lasers. Applied Physics Letters. 2011, 98: 181106.

[119] Maisons G, Carras M, Garcia M, et al. Directional single mode quantum cascade laser emission using second-order metal grating coupler[J]. Applied Physics Letters, 2011, 98(2): 021101.

[120] Q-Y. Lu, W-H. Guo, W. Zhang, et al. Room temperature operation of photonic-crystal distributed-feedback quantum cascade lasers with single longitudinal and lateral mode performance[J]. Appl. Phys. Lett., 2010, 96(5): 051112.

[121] Yao D Y, Zhang J C, Liu Y H, et al. Small divergence substrate emitting quantum cascade laser by subwavelength metallic grating. *Optics express*, 2015, 23(9): 11462-11469.

[122] A. Spott, J. Peters, M. L. Davenport, E. J. Stanton, C. D. Merritt, W. W. Bewley, I. Vurgaftman, C. S. Kim, J. R. Meyer, J. Kirch, L. J. Mawst, D. Botez, and J. E. Bowers. (2016). Quantum cascade laser on silicon. *Optica* 3, 545–551.

[123] H. C. Liu, and F. Capasso, Intersubband Transitions in Quantum Wells Physics and Device Applications II, Semiconductors and Semimetals, 66,13 (Academic Press, 2000).

[124] J. T. Olesberg, M. E. Flatté. In: A. Krier (Ed.), Mid-infrared Semiconductor Optoelectronics (Springer, 2006).

[125] J. Faist, F. Capasso, C. Sirtori, D. L. Sivco, and A. Y. Cho, In: H. C. Liu, and F. Capasso (Eds.), Intersubband Tansitions in Quantum Wells Physics and Device Applications II, Semiconductors and Semimetals, 66, 13 (Academic Press, 2000).

[126] D. Hofstetter, and J. Faist, In: I. T. Sorokina, and K. L. Vodopyanov (Eds.), Solid-State Mid-Infrared Laser Sources, Topics Appl. Phys., 89,61 (Springer-verlag Berlin Heidelberg, 2003).

[127] J. Faist, Opt. Photonics News., 32 (May 2006).

[128] R. Williams, Modern GaAs Processing Methods, (Artech House Inc. 1990)

[129] A. G. Baca, and C. I. H. Ashby, Fabrication of GaAs Devices, (The Institution of Electrical Engineers, London, UK,2005) .

[130] C. Sirtori, P. Kruck, S. Barbieri, P. Collot, J. Nagle, M. Beck, J. Faist, and U. Oesterle, Appl. Phys. Lett., 73, 3486 (1998).

[131] Bosco L, Franckié M, Scalari G, et al. Thermoelectrically cooled THz quantum cascade laser operating up to 210 K[J]. Applied Physics Letters, 2019, 115(1): 010601.

[132] C. Becker，C.Sirtori, H. Page, G. Glastre, V. Ortiz, X. Marcadet, M. Stellmacher, and J. Nagle, Appl. Phys. Lett., 77, 463 (2000).

[133] W. Schrenk, N. Finger, S. Gianordoli, E. Gornik, and G. Strasser, Appl. Phys. Lett., 77, 3328 (2000).

[134] H. Page, C. Becker，A. Robertson, G. Glastre, V. Ortiz, and C.Sirtori, Appl. Phys. Lett., 78, 3529 (2001).

[135] L. R. Wilson, D. A. Carder, M. J. Steer, J. C. Cockburn, M. Hopkinson, C. K. Chia, G. Hill, and R. Airey, Electron. Lett., 37, 1292 (2001).

[136] S. Anders, W. Schrenk, E. Gornik, And G. Strasser, Appl. Phys. Lett. 80, 1864 (2002).

[137] C. Sirtori, P. Kruck, S. Barbieri, P. Collot, J. Nagle, M. Beck, J. Faist, and U. Oesterle, Appl. Phys. Lett. 73, 3486 (1998).

[138] C. Sirtori, H. Page, C. Becker, and V. Ortiz， IEEE J. Quantum Electron. 38, 547, (2002).

[139] L. R. Wilson, P. T. Keightley, J. W. Cockburn, M. S. Skolnick, J. C. Clark, R. Grey, and G. Hill, Appl. Phys. Lett., 76, 801 (2000).

[140] W. Nakwaski, J. Appl. Phys., 64(1), 159 (1988).

[141] C. Sirtori, P. Kruck, S. Barbieri, H. Page, J. Nagle, M. Beck, J. Faist, and U. Oesterle, Appl. Phys. Lett., 75, 3911 (1999).

[142] J. Q. Liu, X. Z. Lu, Y. Guo, F. Q. Liu, and Z. G. Wang, Chin. J. Semiconductors (in Chinese), 26, 624 (2005).

Chapter 2
Methods of experiment

2.1 Molecular beam epitaxy (MBE)

2.1.1 The structure of MBE system

The QD and QW structures are normally grown by solid source molecular beam epitaxy (MBE) or metal-organic chemical vapour deposition (MOCVD). The samples in this report were grown by the Veeco Gen-930 MBE of UCL as shown in Figure 2.1 [1]. The schematic diagram of MBE system is illustrated in Figure 2.2, where the whole MBE system includes three main parts: load-lock chamber, preparation chamber and growth chamber [2]. Three chambers are isolated from each other by high-vacuum valves, and are equipped with vacuum pumps to ensure the vacuum level of each chamber. A trolley between the chambers transfers samples with sample holder [3].

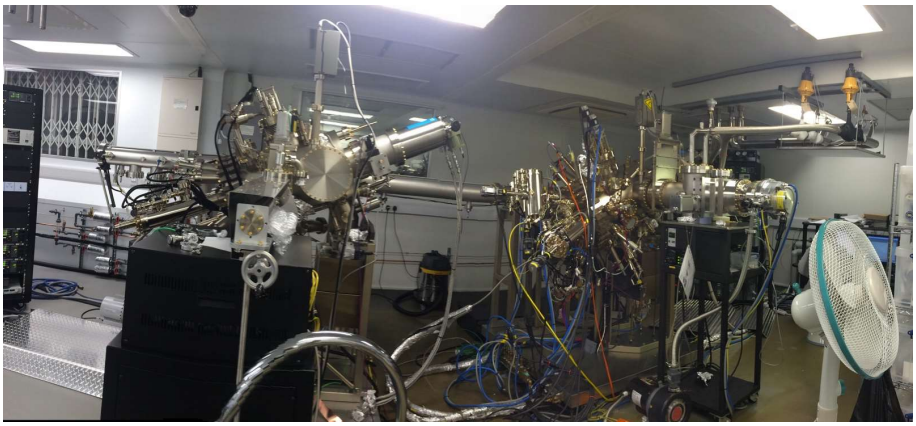

Figure 2.1 The photograph of molecular beam epitaxy system in UCL [1].

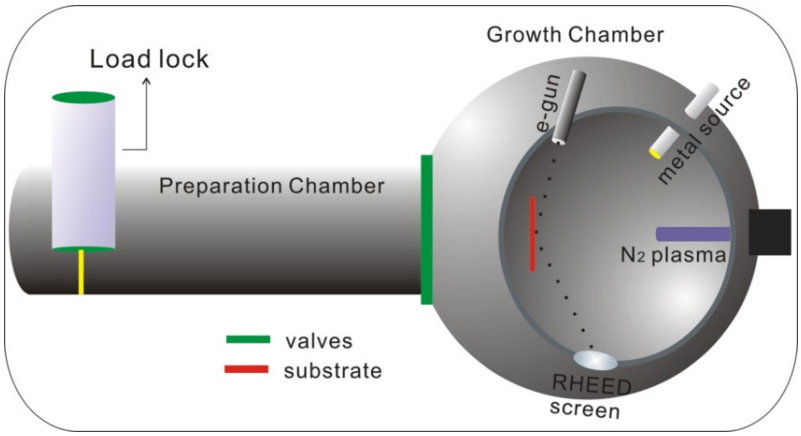

Figure 2.2 Schematic diagram of the solid source molecular beam epitaxy system [3].

The load-lock chamber is used to complete sample loading/unloading and low-temperature degassing of the substrate. Turbo and scroll pump are assembled in this chamber, and the chamber vacuum could be pumped to around 10^{-8} Torr after loading/unloading sample.

The preparation chamber is a middle section between the load-lock chamber and growth chamber [4]. In this chamber, Ion pump is used to offer higher vacuum level around 10^{-10} Torr, and heating station is placed to provide high temperature substrate baking (up to 600°C). After the sample transferred into preparation chamber from load-lock chamber, the high temperature baking could remove the residual water and oxide on the surface of substrate, and the high vacuum make could avoid the vacuum drop of growth chamber when the vacuum valve is opening.

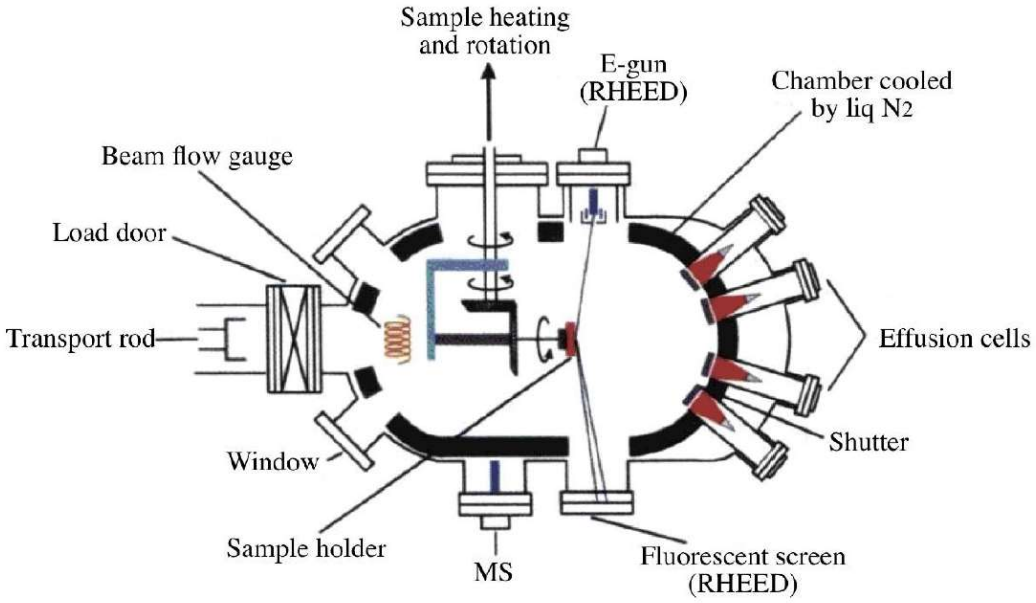

Figure 2.3 Schematic diagram of the detail section in the solid source molecular beam growth chamber [5].

The growth chamber is the core area of the molecular beam epitaxy equipment, where epitaxial growth is carried out [5]. Figure 2.3 demonstrates the simplified internal structure of the growth chamber, which is mainly constituted by the ultra-high vacuum chambers, effusion cells, rotating substrate holder, reflection high energy electron diffraction (RHEED) system and temperature control system [5, 6]. Cryopump is applied to maintain the ultra-high vacuum in growth chamber, and the whole growth process is undertaken in the ultra-high vacuum of 10^{-11} Torr in order to achieve a low impurity level [7].

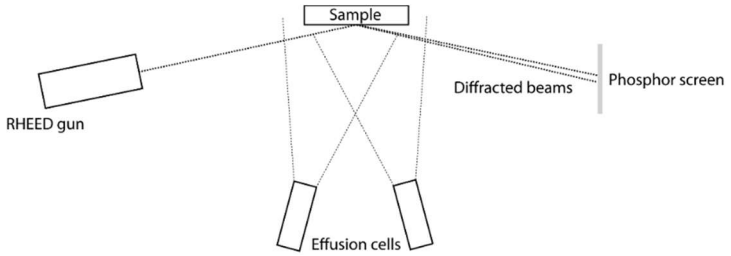

Figure 2.4 Schematic diagram of reflection high energy electron diffraction system.

The reflection high energy electron diffraction (RHEED) system assembled in growth chamber aims to offer an in-situ monitoring of the morphology and quality of the grown epitaxial layer [6,8]. As shown in Figure 2.4, when the electron beam, generated by electron gun in RHEED system, reaches the surface of sample, it is converted to the diffracted beams because of the diffraction effect, and the diffracted beams will be plotted in phosphor screen in the end. If the epitaxial layer is a single crystalline layer, the sample rotating will only change the diffracted angle, and all diffracted beams will be located in a same plane which leads to straight line shown in screen (as Figure 2.5). Otherwise, diffracted beams toward different directions and planes will cause the spotty pattern displayed in RHEED image. Therefore, RHEED is an important in-situ inspection tool to determine the characterization of sample surface and grown layers.

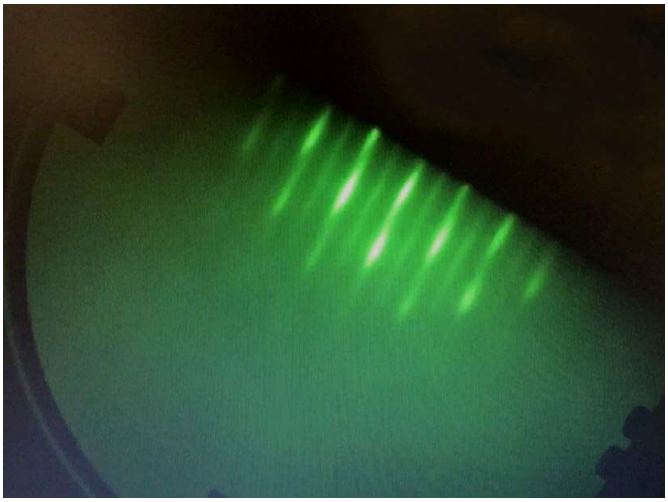

Figure 2.5 RHEED image of a flatten surface grown on substrate. The RHEED images shows the several lines pattern without spotty pattern, this result means the surface of sample is flatten.

2.1.2 MBE growth modes

After transferring into growth chamber, the wafer is located on the rotating substrate holder with controllable spin rate and substrate temperature. The process of epitaxy is completed by the deposition and accumulation of pure atoms emitted by effusion cells [9]. Each of the effusion cells contains different solid elements, such as gallium (Ga), arsenic (As) and indium (In), with individual shutters. By increasing the temperature of effusion cells, the solid elements sublime into gaseous state and condense on the wafer. The opening and closing of the shutters can rapidly switch the elements for deposition. During the growth of III-V alloyed layer, the composition of each element can be controlled by changing the cell temperature which results in modification of elements extrusion rate [10].

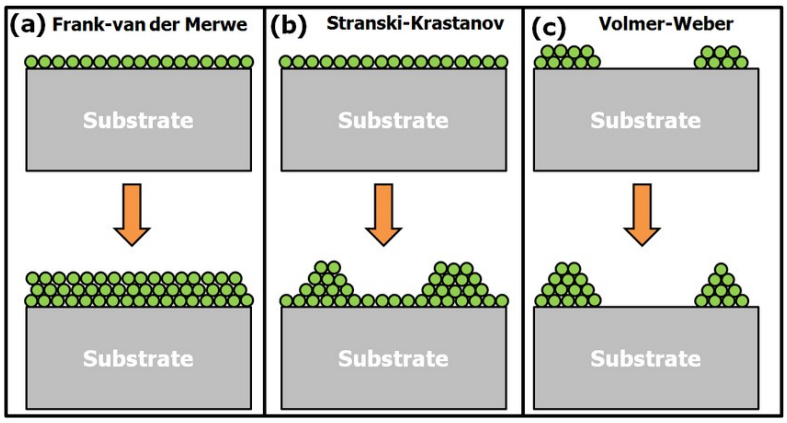

Figure 2.6 Schematic of (a) Franck-Van der Merwe (b) Stranski-Krastanov and (c) Wolmer-Weber mode.

In MBE system, the growth modes are generally classified into three main categories: Franck-Van der Merwe (F-M), Stranski-Krastanov (S-K) and Wolmer-Weber (W-W) modes [11-15]. As shown in figure 2.6, the FM growth mode, based on the layer-by-layer thin film epitaxy, offers smooth interface between grown layers and high crystal quality under homoepitaxy condition. The FM growth mode usually occurs during the lattice-matched material growth.

V-W mode could be used for QD growth, but the requirement is quite high. V-W mode growth need the extremely high temperature and huge force comes from the large lattice mismatch between substrate and growth material. As a result, V-W mode is not suitable for high-quality InAs QD grown, because high temperature will influence the shape of QD and too large mismatch will cause the dislocation and defect.

The QD structures in this project were grown under Stranski–Krastanov (S-K) method [10,13]. The S-K growth method, also known as the layer-island growth method, was proposed by I. Stranski and L. Krastanov in 1938 [13]. In 1994, researchers from Fujitsu Laboratories had coincidentally found the InAs QDs on GaAs emitting at telecommunication wavelength of 1.3 μm by using MBE [16]. Two-dimensional thin layer of GaAs was grown on substrate at first, and then several monolayers of InAs were grown. Because of the lattice mismatch (7%) between GaAs and InAs compounds, when the thickness of InAs layer exceeds a critical value, the deposited layer will be nucleated and assembled as “island” in order to release the strain energy between the GaAs and InAs interface. Then, the QDs are self-organized [17]. The formation of self-organized QDs is a well-accepted approach, because the strain to form QDs can be calculated by the proportion of components. Moreover, in MBE system, the composition of each element can be controlled accurately.

2.1.3 The advantages of MBE

Compare with other epitaxy technologies such as Metal-organic Chemical Vapor Deposition (MOCVD), MBE technology has the following characteristics [18-20]:

(1) The solid source used in MBE is able to offer high-purity and high-stable epitaxy.
(2) The ultra-high vacuum growth environment (10^{-11} Torr) provides excellent crystal quality of the grown films.
(3) The growth rate is as low as 0.1μm/h to 1.0μm/h, and the thickness of the thin crystal film could be controlled with the precision of a single atomic layer. The low growth rate ensures sufficient time for atoms migration on the surface of substrate, so that the growth surface and interface have great flatness.
(4) MBE could realize the growth of high quality AlAs under 400℃ growth temperature, and that of MOCVD requires around 600℃ growth temperature. The low growth temperature leads to slight diffusion effect of the host atoms and dopants during the growth process, and steep doping distribution and flatten epitaxial interface could be obtained.
(5) Various growth states such as crystal quality, surface state, and growth rate of epitaxial layer could be detected in-situ by using RHEED and other instruments.

2.2 Material characterisation

After the sample growth, material characteristics should be measured to check the quality and optical properties of the grown wafers in the beginning. In this section, several experimental techniques used to characterise the quality and parameters of QD and QW materials are introduced: photoluminescence (PL) spectroscopy, atomic force microscopy (AFM), and scanning electron microscopy (SEM) [21]. Transmission electron microscopy (TEM), which is another useful technique to estimate the dislocation density, is also introduced in this section.

2.2.1 Photoluminescence (PL) Spectroscopy

The PL measurement is always performed before the fabrication of devices to check the properties of material such as wafer uniformity and emission wavelength. PL is the light re-emission process after absorbing a photon with higher energy. The material under test first absorbs a photon from a laser source, and then the electron that absorbed the photon energy is excited into the higher energy state. Then, the excited electron is relaxed through electron-hole pair radiative recombination or non-radiative recombination. In the process of the radiative recombination, a photon will be emitted with the energy equal to the bandgap energy [22]. The PL setup in our lab is performed with a RPM2000 PL setup at room temperature, excited by a 635 nm red laser. Because of the design wavelength of our laser devices is longer than 1 μm and longer wavelength leads to lower bandgap energy, so the energy of photon with 635nm wavelength could cover the energy bandgap of the material used in this research. The electrons in valence band could absorb energy form laser source and transited into conduction band, then relax to the bottom of conduction band, and finally make the transmission between conduction band and valence band by emitting the photon with the energy matches the energy bandgap. The emitted photons could be collected by spectrometer and make the analyse.

The spectrometer in the PL set up (Figure 2.7) is used to analyse the information of emitted photons. As a result, the PL is able to measure the potential emission wavelength of the material which will be used to fabricate the laser diodes. The setup also has the vacuum chamber and liquid nitrogen to support the PL measurement under different temperature from 10K to 300K.

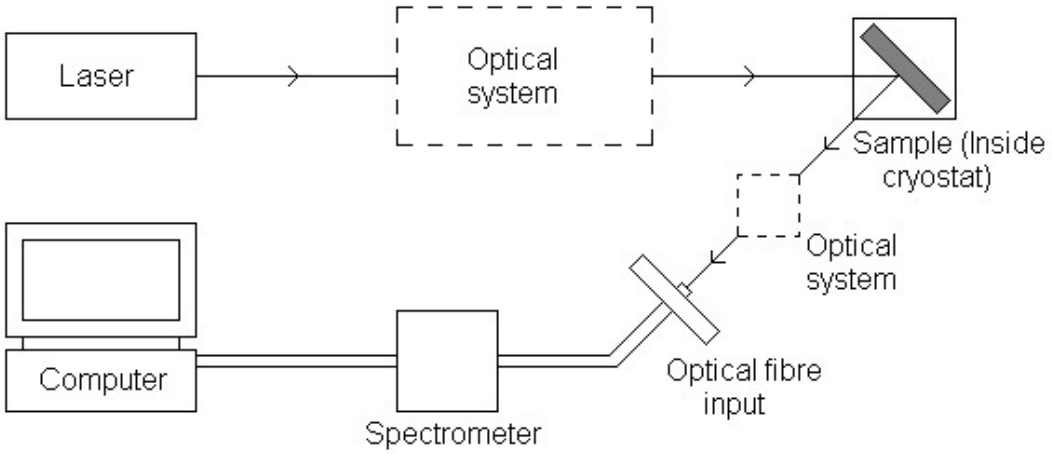

Figure 2.7 The schematic diagram of photoluminescence set up.

PL Spectroscopy is able to test the optical properties and the quality of materials. From the peak wavelength of the PL spectrum, the composition of compounds semiconductors can be determined. Besides, the peak intensity of PL also provides information about the impurities contained in the materials because the impurities or defects act as non-radiative recombination centres which cause the decrease of PL intensity [23]. Additionally, the full width at half maximum (FWHM) of PL spectrum also can be used to characterise the homogeneity of QDs structure. A narrow FWHM means that the size distribution of QDs is uniform.

2.2.2 Atomic Force Microscope (AFM)

AFM is the scanning probe microscope (SPM) with high resolution. In this project, AFM is used to visualise the surface of QD sample, and the QD density could be calculated by the AFM image. AFM contains a free cantilever with a nanoscale-size (5 μm of radius is used) and sharp pyramid tip as shown in Figure 2.8. When the tip is in the proximity to the sample surface, the force between the tip and sample leads to a deflection of cantilever [24]. The AFM scanning image is acquired by measuring the vertical and lateral deflections of the cantilever. This measurement is operated by reflecting a laser beam from the optical level to a detector.

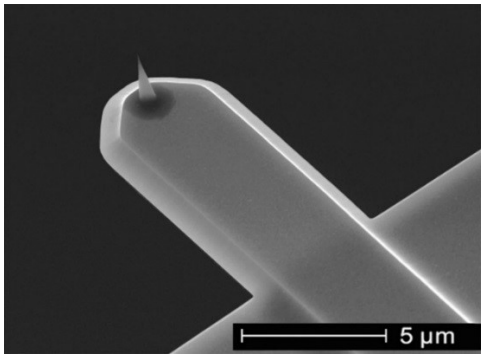

Figure 2.8 The tip of AFM

Figure 2.9 (a) and (b) show the two-dimensional and three-dimensional AFM images of the QD structure, respectively. In Figure 2.9 (a), it is possible to measure the size and density of QDs. Figure 2.9 (b) presents the 3D image which could be used to measure the height of the QDs. As a result, the AFM images offer the size and shape information of the QDs.

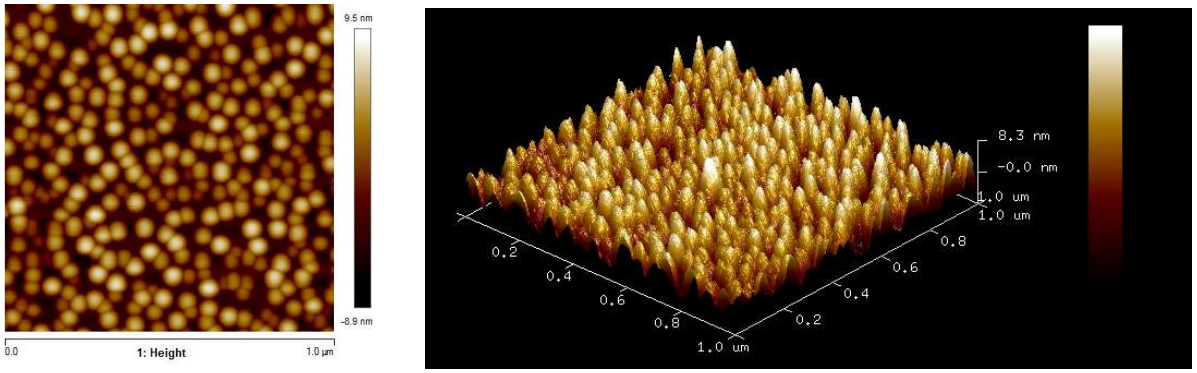

(a) *(b)*

Figure 2.9 (a) two dimensional and (b) three-dimensional AFM image of InAs QDs on Si substrate.

2.2.3 High resolution double-crystal X-ray diffraction

High resolution double-crystal X-ray diffraction (HXRD) is the most direct and effective tool for studying the structural parameters of multilayer heteroepitaxial film materials [21-23]. The parallel X-ray beam is first incident on a crystal used as a monochromator. The reflected near-monochromatic beam is then incident on the surface of the sample, and finally reach the detector through reflection. The detector is fixed at the position of $2\theta_B$ (θ_B is the Bragg angle of the sample), and then records the scattering intensity and obtains the relationship curve of the diffracted light intensity I and θ. The basic principle is based on the Bragg equation:

$$n\lambda = 2dsin\theta$$

In this equation, n is the diffraction order, λ is the wavelength of the X-ray, d is the distance between crystal planes, and θ is the incident angle of diffraction which also named Bragg angle. Differentiate the above formula:

$$\frac{\Delta d}{d} = -cot\theta \cdot \Delta\theta$$

Schematic of the sample with single epitaxial heterogeneous film on the substrate is shown in Figure 2.10 (a). Since the lattice constant of heteroepitaxial film is different with that of substrate, the splitting of the peaks in the I~θ curve will appear when a beam of monochromatic X-rays is incident on the sample surface with slow sample rotating around the Bragg diffraction angle. The strain degree of epitaxial film could be determined by the peak splitting distance Δθ from the equation above. As a result, the composition of the epitaxial film could also be calculated.

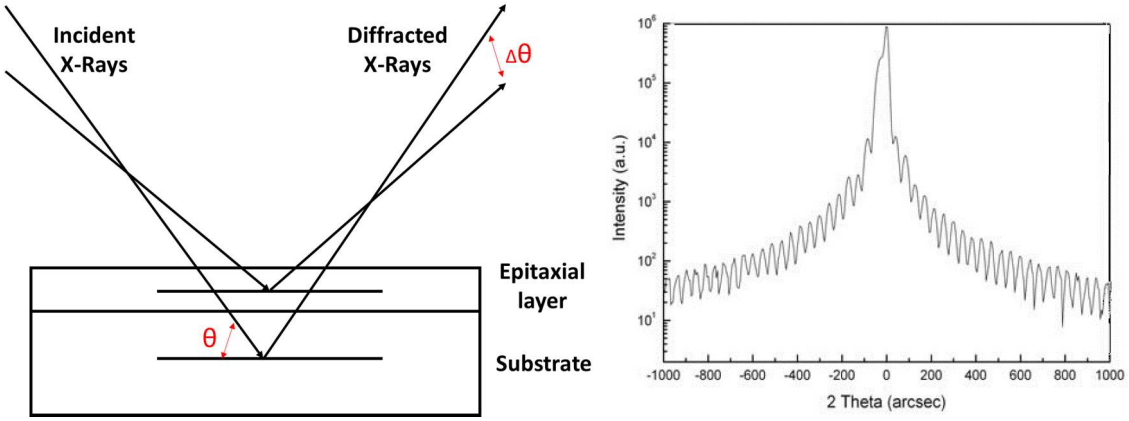

Figure 2.10 (a) Schematic of high-resolution double-crystal X-ray diffraction. (b) HXRD result of periodic multilayer quantum wells structure. The distance between diffraction peaks could be used to calculate the thickness of each period.

Samples with periodic multilayer quantum wells structure such as QCL generally show a series of diffraction peaks near the substrate peak due to the high-resolution X-ray double crystal diffraction results (Figure 2.10b). The diffraction in periodic multilayer also obeys the Bragg equation:

$$2Dsin\theta_l = L\lambda$$

D is the thickness of each period of the periodic multilayer, L is the number of satellite peaks, and θ_l is the Bragg angle in L^{th} level. According to this formula, the period value D can be calculated by the Bragg angles corresponding to any two satellite peaks with different levels:

$$D = \frac{(i-j)\lambda}{2(sin\theta_i - sin\theta_j)}$$

In conclusion, high resolution double-crystal X-ray diffraction could be used to calculate the element composition in epitaxial layer, and it could also be utilized to calculate the period thickness, which is important material characterisation of grown wafers.

2.2.4 Scanning electron microscope (SEM)

Scanning electron microscope (SEM) is a type of microscope which is used to image the surface of sample or cross-section by utilizing electron beam [25]. While AFM provides more detail information about the surface, such as the AFM image in Figure 2.11 (a), SEM image offers the information of the thickness of each layer, the shape, and size of the devices as shown in Figure 2.11. Therefore, SEM is widely used to check whether the fabrication of contact and the as-cleaved facet is well defined. In addition, the information of crystallographic structure and abundance of element can be obtained, because the different types of signals are emitted from samples, including X-rays, back-scattered electrons (BSE), secondary electrons (SE) and et al. [26]. When a beam of electrons is incident on the specimens, the SEM also can be used for measuring the thickness of each layer in structure and the composition of materials, as Figure 2.11(b).

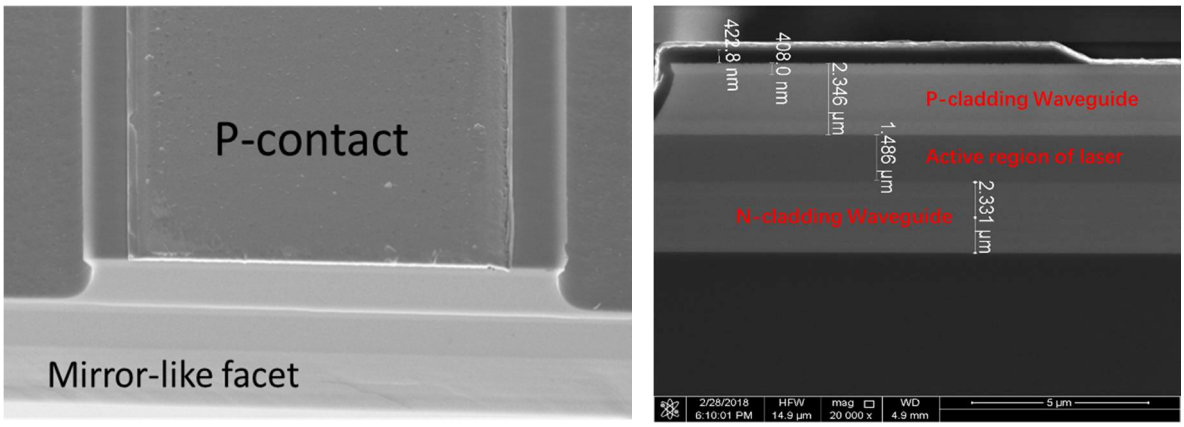

(a) *(b)*

Figure 2.11 (a) SEM image of the p-contact of a laser device with the as-cleaved facet. (b) SEM image of epitaxy grown layers of a laser structure sample before fabrication.

However, the SEM is suitable for the sample with flat surfaces, and difficult to observe the whole device structures. Besides, the electron beam used for scanning is able to damage the facet of samples, and thus the performance of laser devices will degrade after SEM measurement.

2.2.5 Transmission electron microscopy (TEM)

Transmission electron microscopy (TEM) is another imaging technique using electrons beam to produce high-resolution images from nano-sized samples [27]. The main difference between TEM and SEM is that the TEM is based on the transmitted electrons rather than scattered electrons in SEM. TEM can provide more details inside the materials, such as crystallization, lattice stress and dislocations. Although we use TEM to learn the dislocations and surface boundaries of MBE growth, these works are usually done by our cooperating organizations or universities, due to the complicated sample preparation and analysis of TEM. Particularly, in terms of analysing the dislocation density, the TEM results are an important parameter in this research. The TEM results in my thesis is measured by Department of Physics, University of Warwick. The TEM measurements were performed on JEOL 2100 and doubly corrected ARM200F microscopes respectively, both operating at 200 kV.

The dislocations and defects could be measured by TEM, and this is able to decide the quality of grown material. As shown in Figure 2.12, TEM images could be used to count the number of dislocations per unit area and then calculate the dislocation density of epitaxial material.

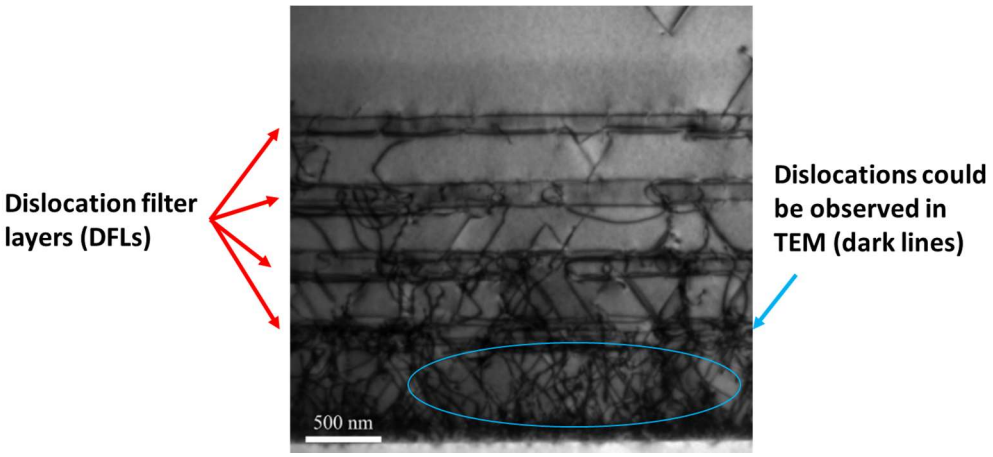

Figure 2.12 The SEM image of DFL structure in Si-based epitaxial material. The dislocations is visible in TEM images, and in this figure, DFLs reduce the density of dislocation obviously.

2.3 Device fabrication

In this section, the two types of fabrication process of a broad-area Fabry-Perot (FP) laser device will be presented. Both of them need four photolithography steps for metallisation and etching. Because the silicon substrate cannot act as contact area, the top-top structure is commonly used for Si-based laser devices. The structure and principle of fabrication of laser devices were identical except for the use of SiO_2 as the insulating layer.

2.3.1 Laser Fabrication without SiO_2

The first step is the preparation of the sample. The surface of a whole wafer sample after MBE growth is inspected under a microscope to check the defects and dirty area. After that, $1/16^{th}$ of wafer with less defects area is cleaved out of the wafer by a diamond tipped scriber and used for the device fabrication. The sample cleaning was performed by using acetone to remove the organic contaminant and isopropyl alcohol (IPA) to clean acetone and other impurities. After that, nitrogen gun is used to dry samples.

After the wafer preparation, the top etching was performed to make mesa structure, as shown in Figure 2.13 (a). In this step, the photoresist of S1818 is deposited by the spin coater, then, standard photolithography is used to define the photoresist pattern which protects the mesa area from being etched. The area without photoresist coating (GaAs) is etched by solution mixture of sulphuric acid: hydrogen peroxide: water (H_sSO_4: H_2O_2: H_2O=1: 10: 80). Compared with dry etch by ions (usually plasma gases),

the wet etching using solution offers a smoother sidewall of ridge, which is important to reduce the optical loss. After etching, we remove the photoresist by acetone and use IPA to clean the sample.

The next step is the formation of top metal (Figure 2.13b), which aims to fabricate the p-contact for laser devices. To open the window in the mesa area coated by photoresist S1818 and LOR10b, second photolithography was performed. The photolithograph removes the photoresist in the ridge, and this area with no photoresist will be deposited by metal. Subsequently, for the he metallisation of p-type ohmic contact, the Ti/Pt/Au (20 /50 /400 nm) layer was deposited by sputtering system. Then, lift-off process was performed by using remover 1165.

Next step is bottom etching similar to the top etching process. As shown in Figure 2.13(c), the photolithography was used to open a window area without photoresist protection, and the epi-layer was wet-etched across the active region and N-type cladding layer until the N-contact layer is exposed.

Finally, the fabrication of bottom metal is also similar to the process of the second step. To form n-type ohmic contact, the pattern was also defined by photolithography and the Ni/GeAu/Ni/Au (10 /100 /30 /200 nm) layer was deposited by thermal evaporation system. Then, the sample will be annealed at 380 °C for 1 mins to form ohmic contact.

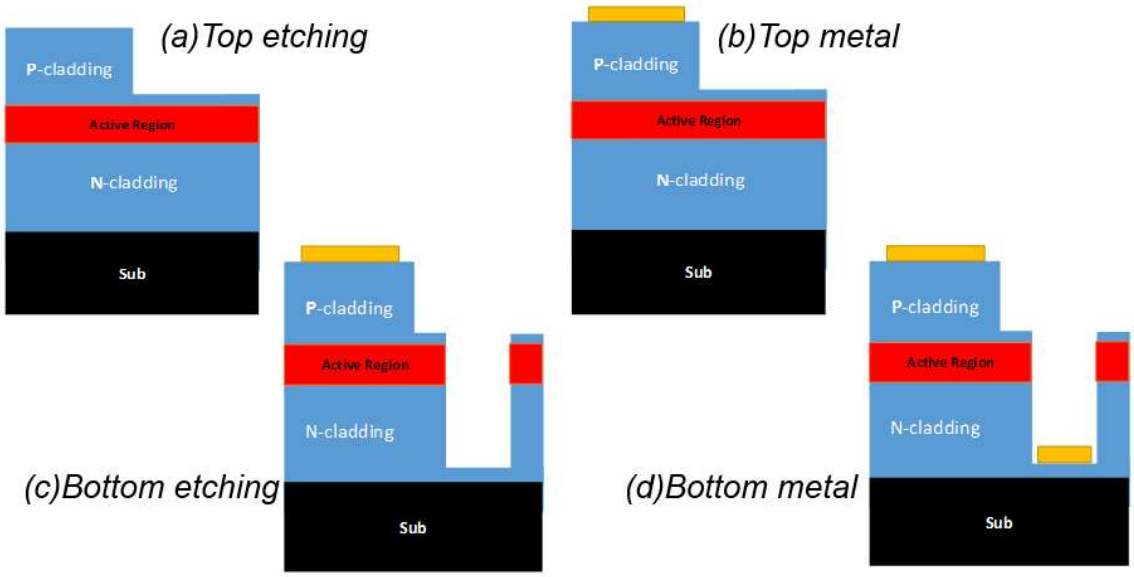

Figure 2.13 The progress of laser devices fabrication, which include: (a) top etching, (b) top metal, (c) bottom etching, and (d) bottom metal.

Figure 2.14(a) illustrates the schematic diagram of a completed laser device. However, it is still suffering from temperature influence. In order to enhance the heat dissipation, the laser bars are mounted on heatsinks (copper plates) and the p-/n-contacts are wire bonded with gold wires of 20 μm diameter (Figure 2.14b). Then, all the fabrication processes of laser devices are done, and they are ready for being tested.

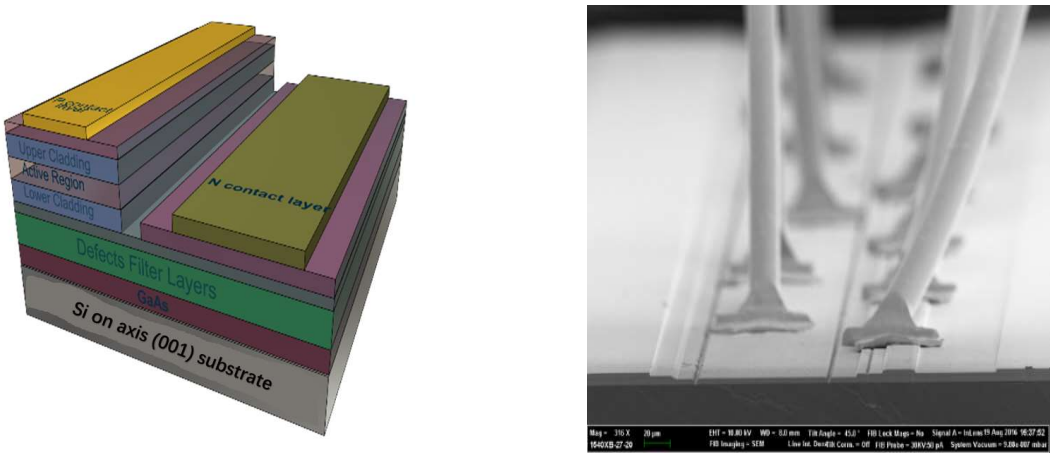

(a) *(b)*

Figure 2.14 (a) the schematic diagram of completed device of laser diode. (b) SEM image of laser device with Au wire bonding.

2.3.2 Laser Fabrication with SiO_2

Generally, the diameter of Au wire tips is around 60-80μm, which may not cause the electrical leakage or short circuit during the bonding of broad-area laser devices in which the width of ridge and contact areas is large enough. However, the fabrication of samples with narrower ridge or complex structure has the problem of no-area for bonding or contact deposition on ridge. As shown in Figure 2.15(a), the diameter of gold wire tips is around 70μm, and ridge width is narrower than 70μm. This makes the bonding material easily connect the sidewall, causing a short circuit. Besides, directly bonding on the top of ridge also damages the mesa structure.

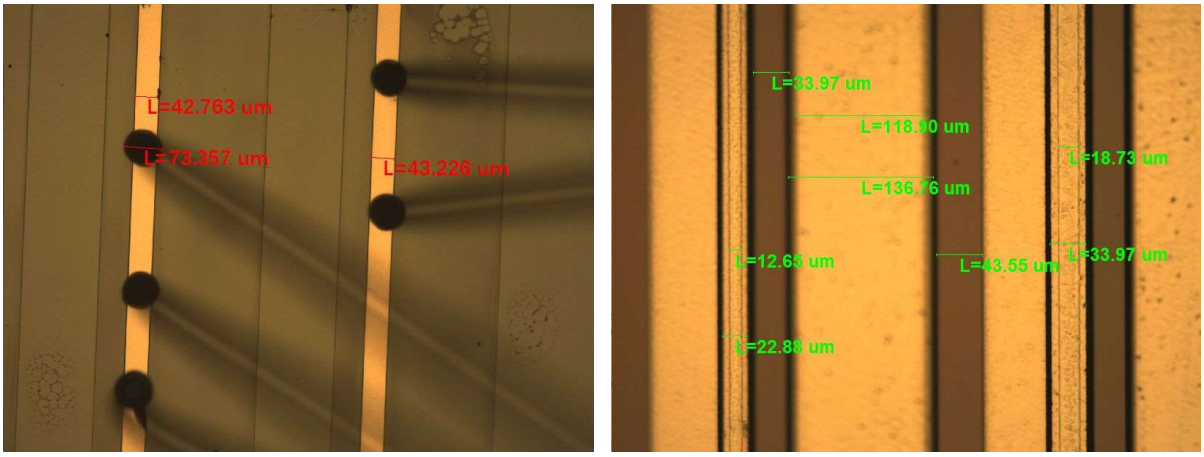

(a) *(b)*

Figure 2.15 microscope images of (a) bonding on single ridge laser structure. (b) laser structure after planarization utilizing SiO_2 as insulating layer.

With the use of SiO_2 insulating layer, it is possible to increase the area for wire bonding and metal contact. Figure 2.15(b) shows the microscope image of laser devices after planarization, in which the SiO_2 insulating layer isolates the side wall of ridge and offers enough space for metal contact and Au wire bonding.

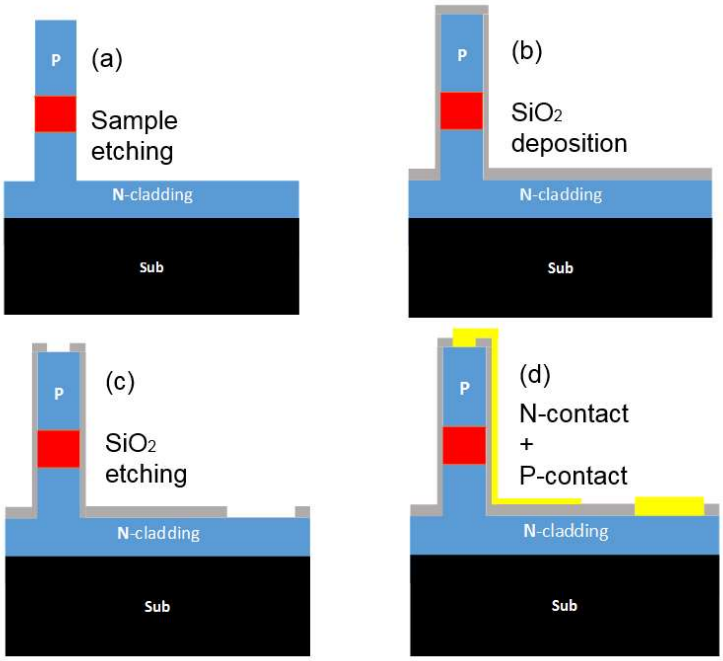

Figure 2.16 The progress of laser devices fabrication with SiO_2 insulating layer, which include: (a) sample etching, (b) the deposition of SiO_2, (c) open window by etching SiO_2, and (d) contact fabrication.

The whole fabrication process of the laser devices with SiO_2 insulating layer has 5 steps, which is similar procedures except the formation of insulating layer. First, the photoresist and photolithography are used to make the pattern in order to etch or

protect the selected-area. As shown in Figure 2.16, the first step is utilizing GaAs wet etching solution to etch the ridge. Then, the SiO_2 insulating layer is deposited by plasma-enhanced chemical vapour deposition. The pattern for etch area was defined by photolithography, and the HF solution was used to etch the SiO_2 to open windows (area) for N and P contact. Finally, the P-contact and N-contact electrodes are deposited in sequence. As illustrated in Figure 2.16(d), the area of P-contact is much larger than that of the ridge. Therefore, it is very convenient to make wire bonding and further packaging process to enhance the performance of laser device. In addition, the Au wire could be bonded on the p-contact metal/SiO_2/N-cladding layer instead of on the top of ridge, which effectively reduces the forced damage from the bonding process.

2.4 Laser measurement and characteristics

Measurement of the lasing characteristics is the most important process to collect the data and information of the material quality and operation performance. One of the most important parameters is the function of light output power against the injection current (L-I curve), from which the laser threshold current density, slope of L-curve, and external differential quantum efficiency can be calculated. The characteristic temperature (T_0) shows the ability of temperature-insensitive operation, which could be calculated from the result of temperature-dependent L-I. Besides, the optical spectra are also captured in order to determine the wavelength and full width at half maximum (FWHM). Finally, there is some cavity length independent parameters, such as internal differential quantum efficiency, internal loss and transparency current density, which can be calculated by measuring a range of different laser bar lengths.

2.4.1 L-I curve, threshold current density and slope of L-I curve

L-I curve can be seen as the most crucial parameter of lasers, since this result is able to illustrate whether the laser is lasing or not directly. Figure 2.17 is a standard L-I characteristic with a function of injection current versus output power per mirror facet. There is no obvious increase of the value of output power in the Y-axis with the increasing injection current before the threshold current (I_{th}) point. When the injection current is larger than the threshold current, the device shows lasing behaviour because the optical gain is larger than the total loss in the laser cavity.

The threshold current is the critical value for lasers because a low threshold current leads to lower power consumption. When comparing samples with different sizes, threshold current density denoted by J_{th} is an adequate parameter to show the performance of laser devices instead of threshold current. The equation of J_{th} is [28]:

$$J_{th} = {}^{I_{th}}/_{A} \tag{2.1}$$

where A is area of laser bar, so J_{th} is independent on the size and area of lasers.

The slope of L-I curve is named as slope efficiency which is another important parameter to show the efficiency of injection current directly transforming into output light. In other words, a high slope efficiency is desirable to get more output light from laser facet with less injection current. As shown in Figure 2.17, the slope efficiency is calculated as $\Delta P/\Delta I$ after the threshold current point, and its unit is Watts per ampere (W/A).

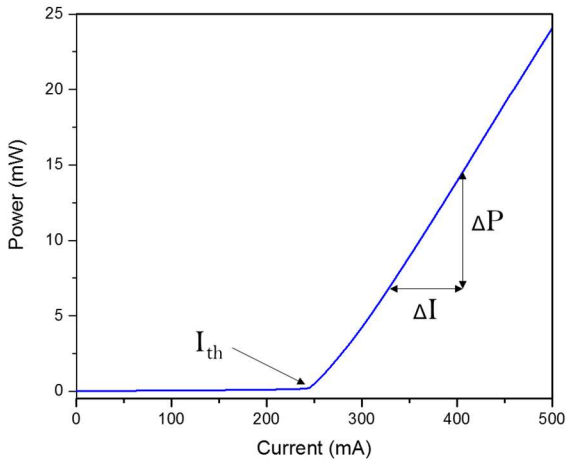

Figure 2.17 The output power against to the current (L-I curve) under c.w operation, the result comes from one of the GaAs-based InAs/GaAs QD laser devices.

During measurement, there is two kind of power sources used to test the laser performance: pulsed-wave and continuous-wave (c.w.) power source. While the c.w. operation offers the power continuously, the pulse-wave provides powers in pulses of some duration at some repetition and gives the device a short time to rest. Thus, a better laser performance can be obtained under pulse operation than c.w. operation because the c.w. operation generates more self-heating. In commercial applications, however, high performance of laser devices under c.w. operation are more desirable but hard to achieve.

2.4.2 External differential quantum efficiency

When we discuss the efficiency of lasers, there is another important indicator which is named external differential quantum efficiency (η_d). This parameter stands for the efficiency of converting the injected electrical charges (electron-hole pairs) into output light (photons emitted). The external differential quantum efficiency of a perfect laser should be 100 % under ideal conditions, which means that all of injected electron-hole pairs would be converted to photons emitted from laser facets without the waste of electrical charges. Actually, because of the non-radiative recombination emitting phonons instead of photons, not all the recombination of electron-hole pairs generates photons. Indeed, the non-radiative recombination is inevitable since it is commonly caused by various defects which largely exist in the QW and QD material. Therefore, the external differential quantum efficiency of a real laser is much lower than 100% and depends on the quality of device materials and fabrication technology. Besides, the external differential quantum efficiency could be used to give expression of dislocation density and the material quality.

In order to measure and calculate the external differential quantum efficiency of lasers in this project, the slope efficiency and wavelength should be calculated. The slope of L-I curve of lasers could be obtained by measurement of L-I curve, and emission wavelength could be measured by spectrum analyser (will be introduced in next section). After that, the external differential quantum efficiency can be derived as [28]:

$$\eta_d = \frac{\frac{\Delta P}{\Delta I}}{\frac{hc}{q\lambda}} \tag{2.2}$$

where $\frac{\Delta P}{\Delta I}$ is the slope efficiency, h is Planck's constant, c is the speed of light, q is the electric charge of a single electron and λ is the wavelength of one photon.

2.4.3 Spectrum and Peak wavelength of emission

Emission spectrum measurement is a straightforward procedure for determining the lasing wavelength and the FWHM of laser output. In addition, the spectrum result is also able to decide whether the device operates lasing or not. For laser devices with O-band wavelength, they are placed on the setup with the current driving through two probes (Figure 2.18a), and emission is collected by optical fibre shown in Figure 2.18

(b). The emission light is transferred to spectrum analyser by fibre, and then the spectrum is plotted by analyser.

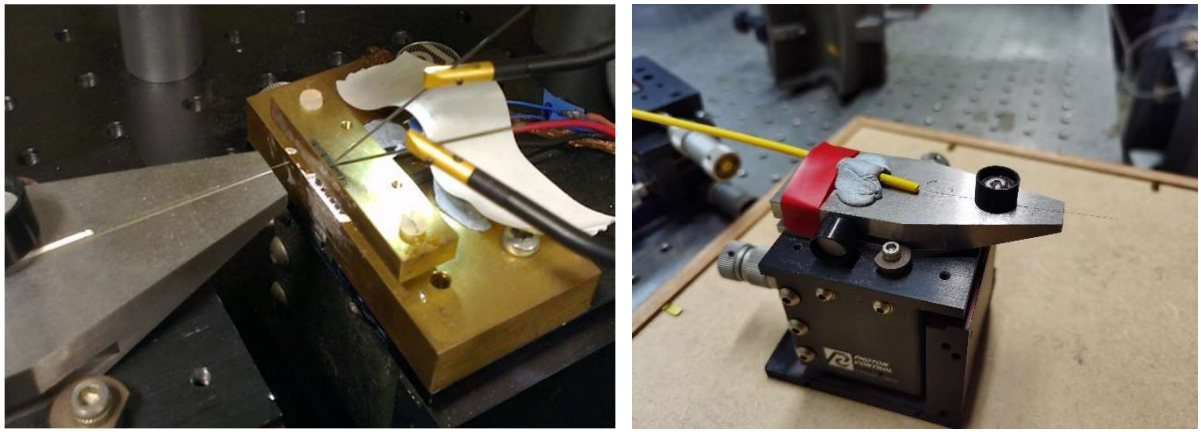

(a) *(b)*

Figure 2.18 (a)setup of spectrum measurement (b) the optical fibre used for lasing collection.

By changing the injection current, the laser behaviours below or above the threshold current can be characterised. Figure 2.19 gives an example of emission spectra of a QD laser diode with different injection current. When the injection current is 60 mA as shown in Figure 2.19 (a), a broad spontaneous emission spectrum is shown with a FWHM of 47 nm at 1320 nm peak wavelength. When the injection current exceeded its threshold current to 160 mA (Figure 2.19b), the peak intensity dramatically increased with FWHM of ~2.5 nm, which represents a typical lasing characteristic. It is confirmed that the 160 mA is higher than J_{th} and generates lasing.

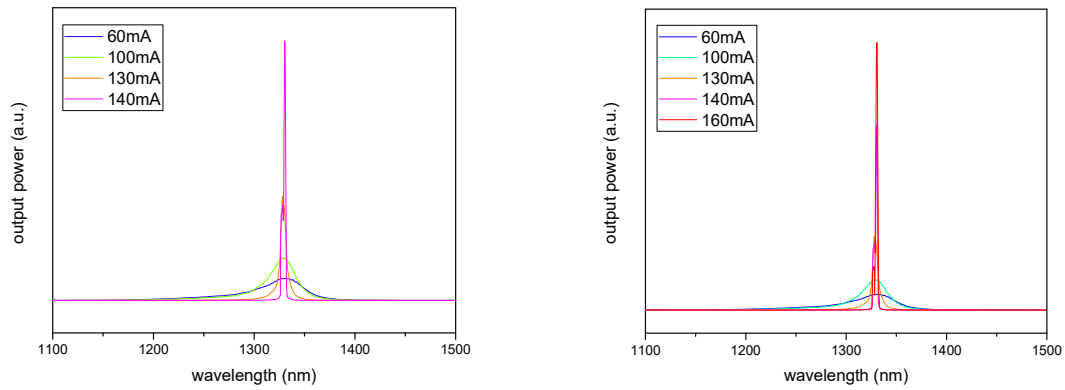

(a) *(b)*

Figure 2.19 Spectra of a laser diode at (a) low injection currents before lasing; (b) various currents after lasing.

Due to the limitation of fibre and spectrum analyser, the spectrum of mid-infrared laser devices is measured by Fourier Transform Infrared Spectrometer which has the characteristics of fast measurement speed and high resolution. The Fourier transform infrared spectrometer is mainly composed of three parts: optical measurement, signal acquisition, and computer controlling system. The core component of the optical measurement part is the Michelson interferometer shown in Figure 2.20 (a), and the majority optical components are fixed mirror, moving mirror and beam splitter (BMS) [26,27]. A 90° off-axis parabolic mirror is used to collimate the light emitted by the laser with divergence angle, and then the collimated light enters Michelson interferometer from the entrance of the spectrometer (Figure 2.20b). The light is firstly divided by the beam splitter into two beams: a beam of transmitted light (LB) and a beam of reflected light (LA), which reach the moving mirror and the fixed mirror respectively. Then, two beams are reflected back to the beam splitter, and the reflection component of LB and the transmission component of LA will be coupled at the detector. The forward and backward movement of the moving mirror will lead to a periodic changing of the light intensity on detector. The moving distance of the moving mirror is exactly half of the lasing wavelength when the light intensity changes for one cycle, so that the lasing wavelength could be measured based on this theory. Because the lasing emission is collected by parabolic mirror instead of fibre, the light collimation and noise reduction of mid-infrared spectral measurement is not as good as the O-band wavelength measurement.

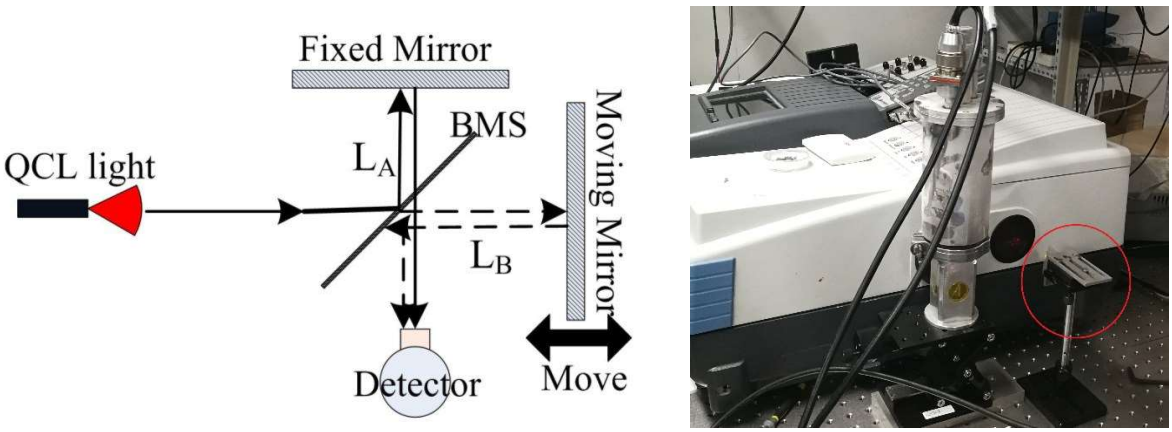

(a) (b)

Figure 2.20 (a) schematic diagram of Michelson interferometer in spectrometer (b) spectrum measurement setup for laser devices with mid-infrared wavelength.

2.4.4 Characteristic temperature

As discussed in Chapter 1, the QD structure theoretically shows a better temperature independent property [29]. In fact, the laser performance is still influenced by the change of temperature. The characteristic temperature, which is normally denoted as the T_0, represents the temperature sensitivity of the laser device. The equation of T_0 is [7]:

$$T_0 = \frac{\Delta T}{\Delta \ln(J_{th})}$$

High T_0 means that the threshold current density and external quantum efficiency are insensitive to the temperature variation. The parameters used to calculate T_0 can be obtained from the measurement of the threshold current at different temperatures.

Figure 2.21(a) illustrates the L-I curves under pulse operation at different temperatures for a laser device of 3 mm length and 50 μm width. Combining the J_{th} data with the T_0 equation, the T_0 calculation was shown in Figure 2.21(b).

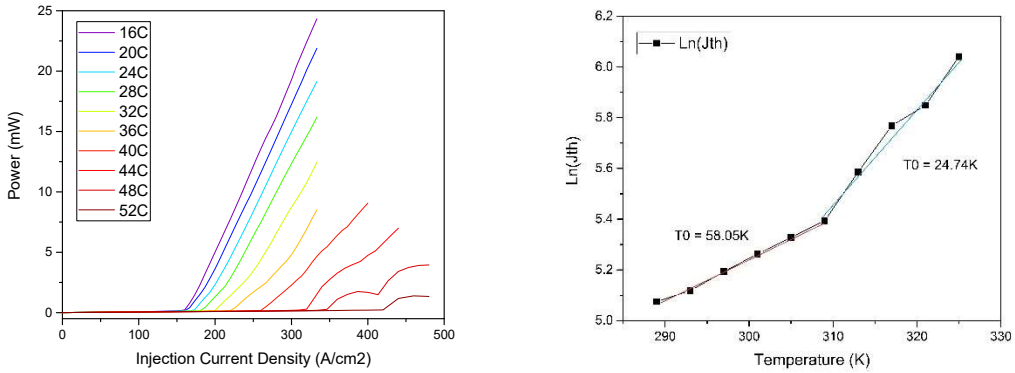

(a) *(b)*

Figure 2.21 (a) L-I curves of laser diode under pulse operation at different temperature. (b)the calculation of T_0

By measuring the slope of the best fitting lines in Figure 2.21(b), the characteristic temperature of this laser diode is around 58 K between 16 to 36 °C and 24.74 K between 36 to 52 °C. Generally, for our laser devices, the T_0 fitting curve shows piecewise in fact, the reason is that the carrier escaping is much stronger with the increase of the temperature, and it leads to more non-radiative recombination. The non-radiative recombination causes the self-heating, and it will further enlarge the carrier escaping, so, this vicious circle makes the fitting curve could not be an idea linear fitting and shows the piecewise results.

2.4.5 Low-temperature measurement

The measurements of samples described in this chapter are based on room temperature. However, a large number of samples are not able to operate under room temperature. As a result, low temperature measurement can be performed to characterise low temperature property of samples. The normal measurement set up has the electric temperature controller (TEC) to keep the temperature stable and reduce the influence caused by self-heating. Basically, the TEC is only able to control the temperature from 0°C to around 130°C. Therefore, for the measurement below 0°C, the Dewar should be used. A normal Dewar was shown in Figure 2.22(a), where the laser samples was protected by Dewar and the glass windows are used to let the lasing emitting out for measurement. After pumping down the vacuum below 10^{-5} bar, liquid nitrogen could be introduced, and then the temperature will drop to around 80K. An electric heater was placed in the Dewar, and it is able to heat and control the inner temperature of Dewar from 80K to room temperature. As shown in Figure 2.22(b), in order to further lower temperature, the measurement needs more precise Dewar. To decrease the temperature under 80K, liquid helium is used in this Dewar instead of liquid nitrogen. As a result, the lowest measurement temperature of this Dewar is able to reach around 10K. Because of the requirement of high vacuum (more than 10^{-6} bar), using this Dewar to test samples suffers from long pumping down time and the long distance between sample and window.

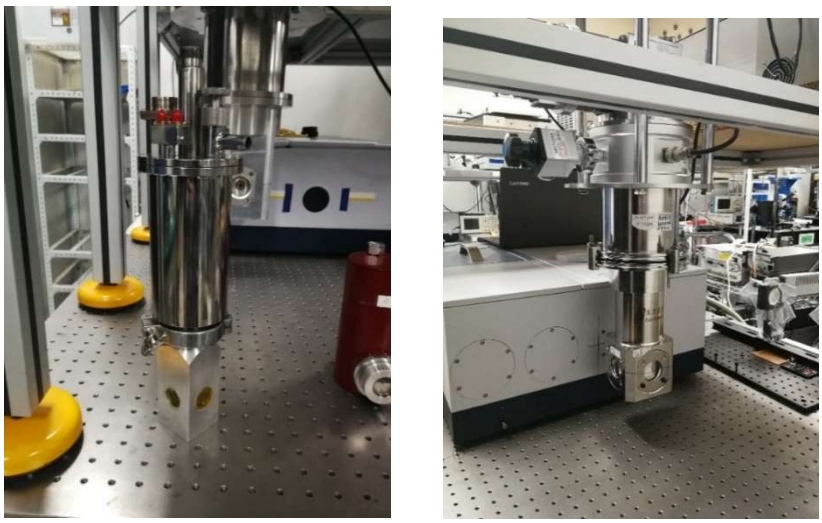

(a) *(b)*

Figure 2.22 (a) Dewar used for low temperature measurement from 80K. (b)the Dewar using liquid helium.

References

[1] GEN 930/ GEN II MBE System Operation Manual, Veeco

[2] A. Cho and J. Arthur, *"Molecular beam epitaxy"*. Progress in Solid State Chemistry, vol. 10, pp. 157-191, 1975

[3] W. P. McCray, "MBE deserves a place in the history books," Nature nanotechnology, vol. 2, no. 5, pp. 259, 2007.

[4] N. N. Ledentsov, "Growth processes and surface phase equilibria in Molecular Beam Epitaxy", Springer-Verlag, 1999

[5] A. Y. Cho. Film deposition by molecular-beam techniques. Journal of Vacuum Science and Technology, 1971, 8(5): S31-S38.

[6] K.-Y. Cheng, "Molecular beam epitaxy technology of III-V compound semiconductors for optoelectronic applications," Proceedings of the IEEE, vol. 85, no. 11, pp. 1694-1714, 1997.

[7] A. Y. Cho, M. B. Panish, and I. Hayashi, Proc, Symp. GaAs and Related Compounds, Aachen. Germany, 1970.

[8] A. Y. Cho. Morphology of epitaxial growth of GaAs by a molecular beam method: The observation of surface structures. Journal of Applied Physics, 1970, 41(7): 2780-2786.

[9] J. Venables, *"Introduction to surface and thin film processes."* Cambridge: Cambridge University Press, 2000.

[10] V. M. Ustinov, A. E. Zhukov, A. Y. Egorov, and N. A. Maleev. Molecular beam epitaxy. *Quantum Dot Lasers*, Oxford University Press, 2003, pp. 43–49.

[11] Günther Bauer and Gunther Springholz. Molecular beam epitaxy-aspects and applications. *Vacuum*, vol. 43, no. 5, pp. 357–365, 1992

[12] F. C. Frank and Jan. H. van der Merwe, "One-dimensional dislocations. I. Static theory". Proceedings of the Royal Society of London Series A Mathematical Physical Sciences, vol. 198, no. 1053, pp.205-216, 1949

[13] T. Ramachandran, R. Heitz, P. Chen, and A. Madhukar, "Mass transfer in Stranski–Krastanow growth of InAs on GaAs", *Applied Physics Letters*, vol. 70, pp. 640, 1997

[14] J. H. Neave and B. A. Joyce. "Structure and Stoichiometry of (100) GaAs surfaces during molecular beam epitaxy." Journal of Crystal Growth, vol. 44, no. 4, pp. 387-397, 1978

[15] M. D. Pashley, "Electron counting model and its application to island structures on molecular-beam epitaxy grown GaAs(001) and ZnSe(001)," Physical Review B, vol. 40, pp. 10481, 1989

[16] H. Sek and , A. Koukitu. Thermodynamic analysis of molecular beam epitaxy of III–V semiconductors. *Journal of Crystal growth*, vol. 78, pp. 342-352, 1986

[17] A. Koukitu, Y. Hasasegawa and H. Seki. Thermodynamic analysis of the moype and mbe growth of pentanary III-V alloy semiconductors. *Journal of Crystal Growth*, vol, pp. 697-703, 1989

[18] A. Y. Cho. Epitaxial growth of gallium phosphide on cleaved and polished (111) calcium fluoride. Journal of Applied Physics, 1970, 41(2): 782-786.

[19] A. Y. Cho. Film deposition by molecular-beam techniques. Journal of Vacuum Science and Technology, 1971, 8(5): S31-S38.

[20] A. R.Barron, Chemistry of Electronic Materials, 2011.

[21] QDLaser, *"White Paper: New era of Quantum dot lasers with evolution history of semiconductor lasers,"* 2008.

[22] M. Fox, *"Photoluminescence,"* in Optical properties of solids, Second edi., Oxford University

Press, 2010, pp. 118–126.

[23] S. Perkowitz, *"Optical characterization of semiconductors : infrared, Raman, and photoluminescence spectroscopy"*. Academic Press, 1993.

[24] G. Binnig, C. F. Quate, and C. Gerber, "Atomic Force Microscope," *Phys. Rev. Lett.*, vol. 56, no. 9, pp. 930–933, 1986.

[25] L. Gross, F. Mohn, N. Moll, P. Liljeroth, and G. Meyer, "The Chemical Structure of a Molecule Resolved by Atomic Force Microscopy," *Science,* (80-.)., vol. 325, no. 5944, 2009.

[26] H. Seiler, "Secondary electron emission in the scanning electron microscope," J. Appl. Phys., vol. 54, no. 53, pp. 1–19, 1983.

[27] D.B. Williams, C.B. Carter, "*Transmission Electron Microscopy*", Springer, 1996, pp 3-17.

[28] K. Mobarhan, "Test and characterization of laser diodes: determination of principal parameters," Newport Corp., 1995.

[29] Y. Arakawa and H. Sakaki, "Multidimensional Quantum Well Laser and Temperature-Dependence of Its Threshold Current," *Appl. Phys. Lett.*, vol. 40, no. 11, pp. 939–941, 1982.

[30] O. B. Shchekin and D. G. Deppe, "1.3 μm InAs quantum dot laser with To=161 K from 0 to 80 °C," *Appl. Phys. Lett.*, vol. 80, no. 18, pp. 3277–3279, May 2002.

Chapter 3
The comparison of QD and QW lasers on on-axis Si substrate

3.1 Introduction

Highly efficient and reliable laser devices on on-axis Si (001) substrate have attracted substantial interest due to their potential to achieve direct integration of photonic integrated circuits (PICs) on Si platform compatible with current CMOS foundries [1]. Accordingly, a great deal of effort has been made to monolithically grow the QD laser structures on on-axis (001) Si substrates in recent years [2, 3]. For example, Liu *et al.* [3] first demonstrated electrically pumped c.w. 1.3 μm QD lasers grown on on-axis (001) GaP/Si substrates in 2017, and reported threshold current densities of 860 A/cm^2 at room-temperature (RT) and single-facet output power of 110 mW. However, most of recent results have used the patterned substrate [2] or GaP intermediate layer [3], which are not practical to be implemented with optical components on SOI platform. In this regard, it is important to further improve the growth method and structure optimization in a way compatible with SOI platform. The first electrically pumped c.w. 1.3μm Si-based laser without patterning or GaP intermediate layer was presented by Chen et al. in 2017 [4]. The threshold current density at RT under c.w. operation is higher than 400 A/cm^2, but the poor temperature stability results in the highest operation temperature of only 36 °C [4]. In this chapter, after the improvement of the wafer growth and the structure optimisation, higher output power and lower threshold current density were realised for laser devices grown on on-axis Si (001), compared with the previous result.

In addition, as mentioned in the chapter 1, active region employing QD materials is less sensitive to dislocation than QW structure, indicating that QD material is more favourable for realizing III-V lasers grown on Si usually generating high dislocation density [5-7]. Although the use of QD, which can alleviate the detrimental effect of dislocations, was proposed as early as 1991 [8], the experimental comparisons between Si-based QD and QW structure were reported very recently [9, 10]. In these papers, it was reported that Si-based QD lasers exhibited higher reliability with longer lifetime under the same dislocation density, compared with that of Si-based QW lasers.

However, the nature behind it is still not clear, and there is no report to describe the detail impact of dislocation.

In this chapter, the QD and QW lasers grown under the same conditions were studied, both of which were analysed by photoluminescence (PL) measurement to characterise material property. After fabrication process, various measurements such as LIV curve, temperature dependence, and spectrum analysis were carried out in order to characterise the lasing performance of QD and QW laser devices.

3.2 Experimental procedure

In this research, both metal-organic chemical vapour deposition (MOCVD) and MBE were used to grow the laser structures on on-axis (001) Si substrate. To obtain APD-free buffer layer, 400 nm-thick GaAs buffer layer was first deposited on the on-axis Si wafers of 300 mm diameter in MOCVD. At the beginning stage of growth on MBE, a nucleation layer of 40 nm-thick GaAs was deposited at low temperature (400 – 500 °C) and, subsequently, the rest of 360 nm-thick GaAs was deposited at high temperature (600 – 700 °C). To obtain QD laser structure, the following epitaxial structure was grown on the optimal GaAs-on-silicon (001) by MBE. As shown in Figure 3.1, the epitaxial structure consisted of the InGaAs/GaAs SLS as DFLs, five layers of InAs/GaAs dot in a well (DWELL) structures separated by 52 nm GaAs spacer layer, which were sandwiched by 1.4 um n-type and p-type $Al_{0.4}Ga_{0.6}As$ cladding layers, and a 300 nm-thick highly doped p-type GaAs contact layer on top.

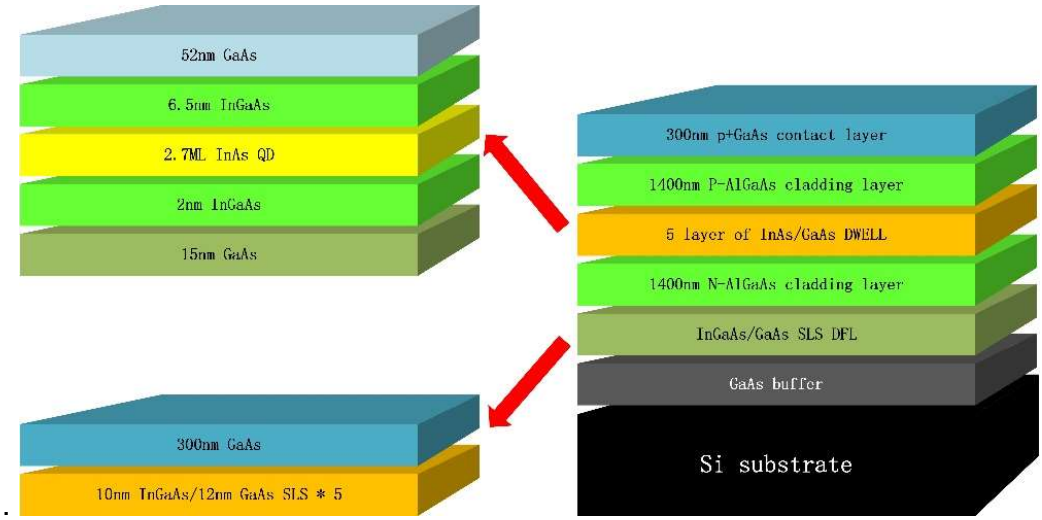

Figure 3.1 The structure of InAs/GaAs QD laser on "on-axis" Si

For the comparison, the QW structure was also grown with the same condition except the active region. As shown in Figure 3.2, the active region of QW laser devices consisted of InGaAs/GaAs QW structure with same thickness of QD active region.

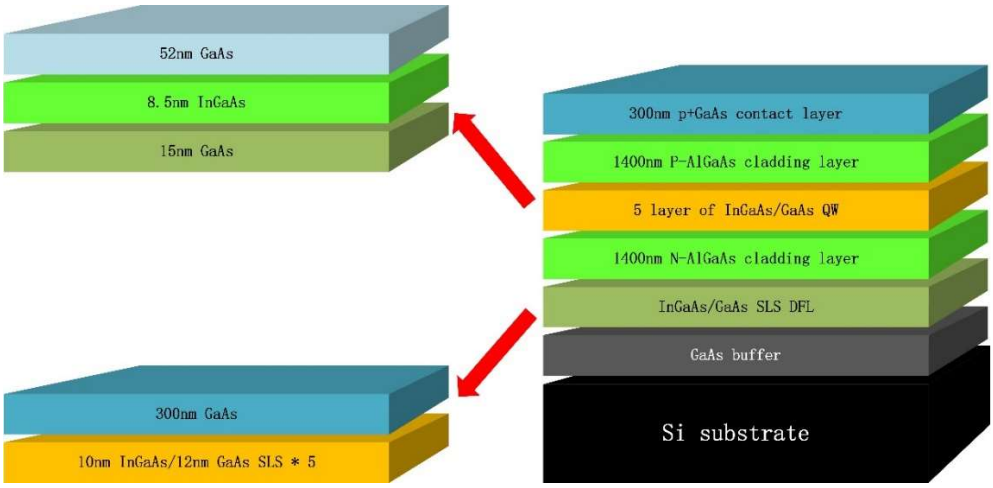

Figure 3.2 The structure of QW (UCL316R15) sample.

Both of QD and QW laser devices were fabricated into broad-area lasers with 25μm and 50μm ridge width. The fabrication process was introduced in chapter 2.2, including standard photolithography and wet etching. The mesa structure was formed by chemical etching (H_2SO_4: H_2O_2: H_2O = 1: 10: 80) until the highly doped n-contact layer was exposed. For the p-type and n-type ohmic contact, the Ti/Pt/Au (20/50/400 nm) and Ni/GeAu/Ni/Au (10/100/30/200 nm) layer were deposited by sputtering and thermal evaporation system, respectively. Finally, in order to enhance the thermal dissipation, the silicon substrate of laser devices was lapped to around 100 μm. The laser bars were cleaved into the same cavity length of 3 mm, and the identical packaging processes such as mounting to heatsinks and bonding with gold-wire were performed.

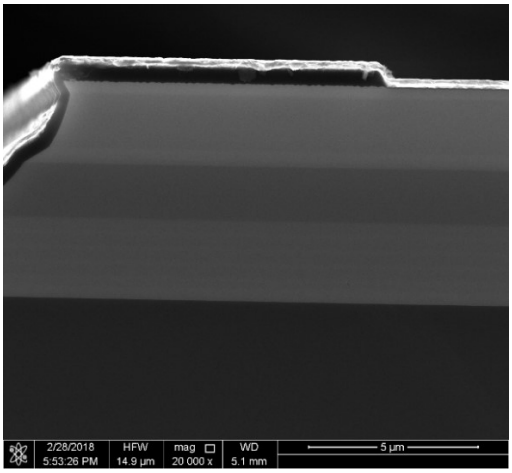

Figure 3.3 The SEM result of cross-section

Figure 3.3 presents the SEM image of the facet after cleaving, indicating that the p-contact metal layers were well defined, and the mirror-like facet was obtained. In addition, there is no obvious cracks on the laser devices. In conclusion, the fabrication is successful.

3.3 Results and discussion

The PL measurement provides the information of the optical properties and the quality of materials. Figure 3.4 shows the PL measurement of the Si-based QD and QW samples with a wide range of temperature from 20 K to 300 K. The peak wavelengths of QD and QW samples are around 1320 nm (2^{nd} communication window) and 920 nm (1^{st} communication window), respectively. Both peak intensities of QD and QW samples decrease as the temperature increases, but it can be seen that the decline of peak intensity of QW structure is much quicker than that of QD structure. This can be explained by the fact that the QD structure provides higher quantum confinement and less sensitivity to dislocation than QW structure [11].

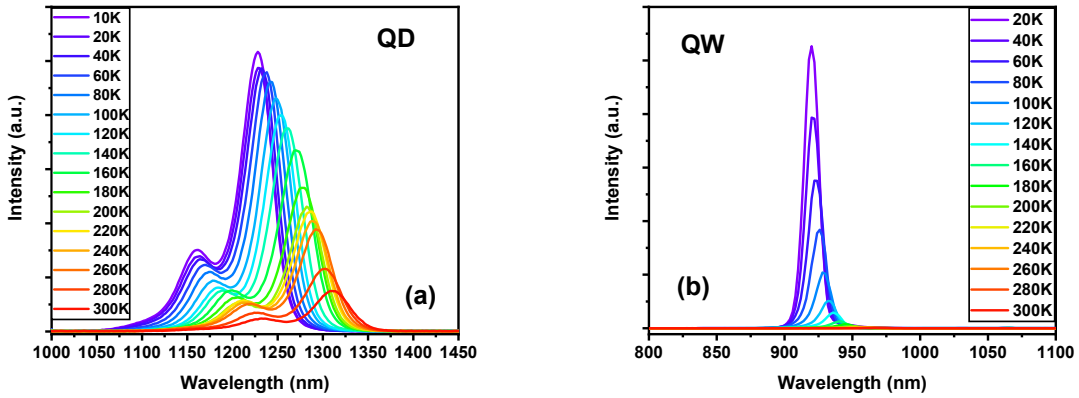

Figure 3.4 The temperature dependence PL measurement of Si-based (a) QD and (b) QW wafer.

As shown in figure 3.5, after transferring the intensity to logarithms to base 10 (log10), the trend of intensity decrease is more obvious with the increase of temperature. Because the value of each major tick is 1, Figure 3.5(a) points that the intensity change between 10K and 300K of QD sample is around one order of magnitude, and the result in 300K reaches 10% intensity of the value with 10K temperature. By contrast, the peak intensity in 10K and 300K displayed in Figure 3.5(b) shows over 3 order of magnitude attenuation. The value of intensity in 300K is less than 0.1% compared with that of 10K. The rapid intensity decline suggests the thermal escape of electrons, which means that the QD structure grown on Si has much better carrier confinement and remarkable thermal insensitivity. It is noted that in Si-based devices, the dislocations will cause non-radiative recombination and lead to thermal generation, and therefore the thermal issues will be enlarged in laser structure grown on Si substrate. The results are matched with the previous expectation of QD material, since the QD provides higher quantum confinement and reduce the thermal leakage [11].

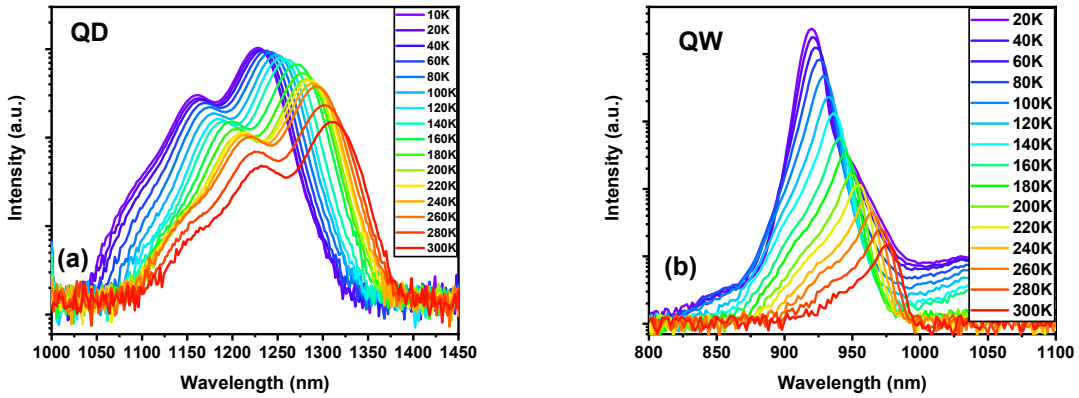

Figure 3.5 The temperature dependence PL measurement of Si-based QD (left) and QW (right) wafer with intensity calculated as logarithms to base 10.

The separated energy levels of QDs also help to trap the carriers, so that the possibility of thermal escape of carriers is lower than that of QWs. Besides, the QD material is expected to have a higher thermal activation energy than QW material [12]. The Arrhenius equation in 3.1 shows the relationship between the PL intensity and thermal activation energy:

$$I = \frac{I_0}{1+C\ \mathrm{ex}\ \left({}^{-E_a}/_{k_B T}\right)} \tag{3.1}$$

where k_B is the Boltzmann constant, C is a constant, and I_0 is the PL intensity with absolute zero in Kelvin scale. I and E_a are intensity of PL and thermal activation energy, respectively. By using this equation and measured PL results, the value of thermal activation energy could be estimated from fitting the intensity of PL versus Kevin temperature. The thermal activation energy of both QD and QW material is estimated in Figure 3.6. The value of QD material (240.7 meV) is nearly 7 times higher than that of QW material (35 meV), indicating that the carriers in QD material have higher barrier to transit to the continuum.

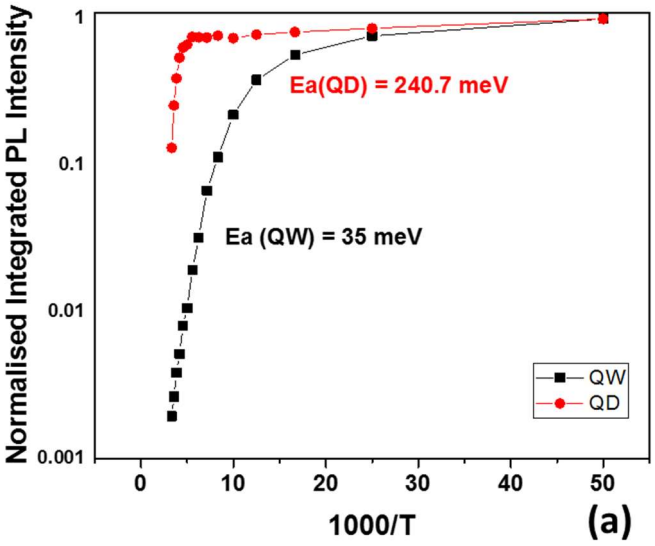

Figure 3.6 The calculated thermal activation energy of QD and QW. The solid points come from the PL results and the lines is the fitting curves based on the equation 3.1.

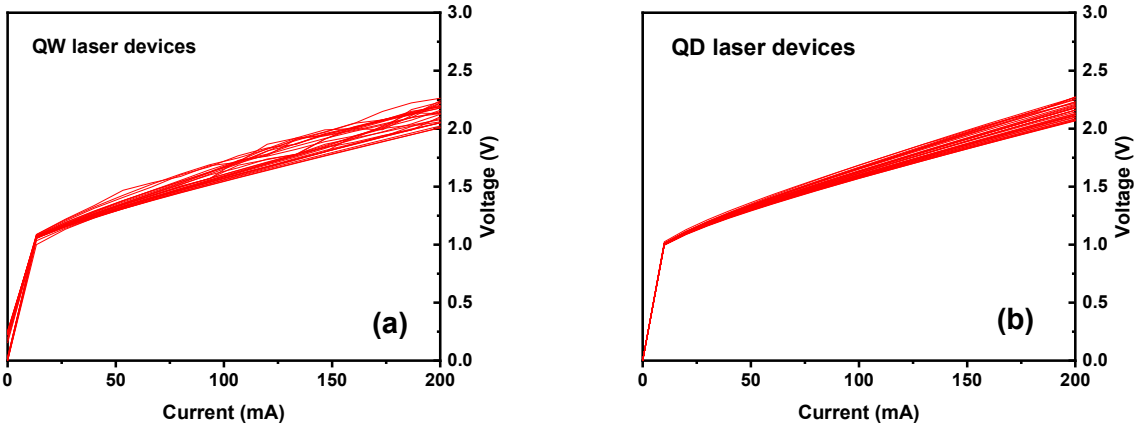

Figure 3.7 (a) The series resistance of QW devices (the number of QW devices shown is 43, total number is 50, 7 devices do not work.), (b) the series resistance of QD devices (the number of QD devices is 48, total number is 50, 2 devices do not work.).

In order to make an equitable comparison between QD and QW lasers, all the device fabrication procedures, including etching, metallization, and so on, were identically performed. Besides, the doping level and etch depth of epitaxial layer also have the same conditions. Therefore, it can be expected that the series resistance of them would produce similar values. In Figure 3.7, it is revealed that the I-V characteristics of the fabricated QD and QW lasers exhibits similar series resistance, which ensures impartial comparison.

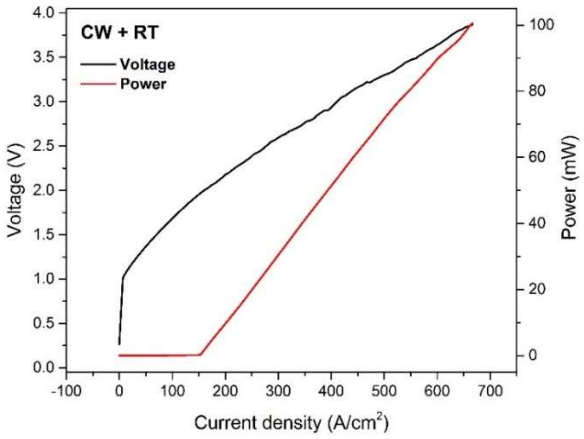

Figure 3.8 The LIV curve of Si (001) based QD laser.

Figure 3.8 shows the typical light-current-voltage (LIV) characteristics of an InAs/GaAs QD laser grown on a silicon (001) substrate under c.w. operation at room temperature. The laser device with 50 μm × 3 mm size produced threshold current density of 160 A/cm^2 and single facet output power of 101 mW at an injection current density of 667 A/cm^2. The series resistance and the slope efficiency of the device were measured to be 4 Ω and 0.13 W/A, respectively, which was estimated from the LIV curve shown in Figure 3.8. It should be noted that the 667 A/cm^2 current density is the highest injection current density because the maximum c.w. injection current offered by current source is 1000 mA. Considering that the output power curve in Figure 3.8 does not show the rollover, the maximum output power of this QD laser device is expected to produce higher value.

In addition, it is worthwhile to note that the QD laser devices were processed with as-cleaved facet. It means that the accurate output power should be double of the output power measured by single facet, and thus the total output power more than 200 mW is able to be achieved. The use of high-reflection (HR) coating on the as-cleaved facet will further improve the device performance such as threshold current density and light output power.

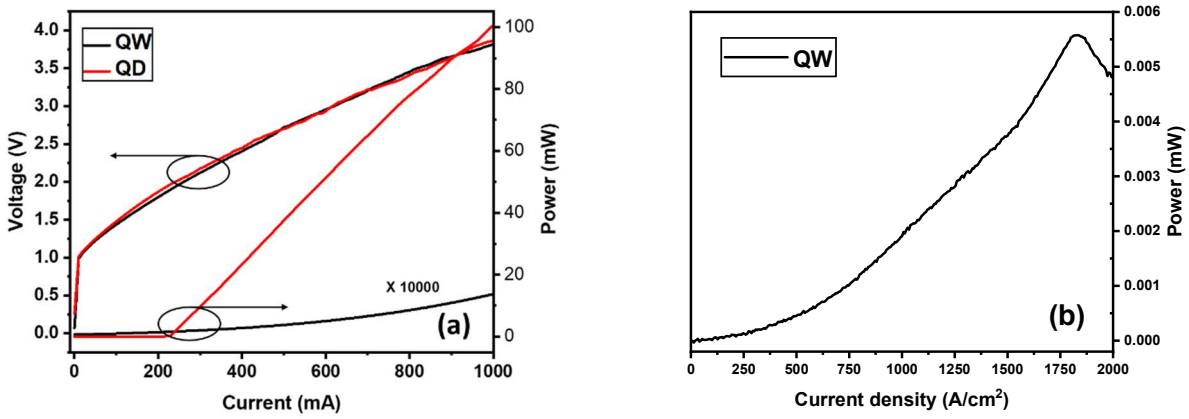

Figure 3.9 (a) The LIV curve of QW and QD devices under c.w. mode, (b) the LI curve of QW devices under Pulse mode.

Contrary to the QD laser device, QW laser devices fail to generate lasing operation under both c.w. and pulse mode input current at room temperature as shown in Figure 3.9. Under pulse mode, a rollover of the output power is observed when the injection current density reaches 1800 A/cm^2 (Figure 3.9 (b)), indicating that this QW device is unlikely to achieve lasing at room temperature even with the further increase of injection current.

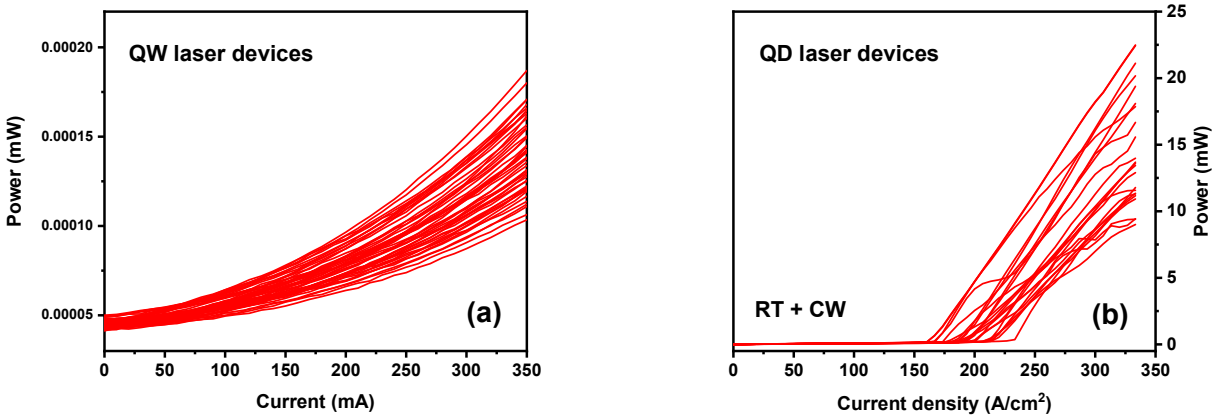

Figure 3.10 (a) The LI-curve of QW devices (the number of QW devices shown is 43, total number is 50, 7 devices do not work.), (b) the Li-curve of QD devices (the number of QD devices is 48, total number is 50, 2 devices do not work.).

In order to compare the light output properties between QW and QD devices, the measured light output-current (LI) characteristics under c.w. operation are measured, as shown in Figure 3.10. For the QW devices, there is no devices able to operate lasing with the increase of injection current and the increase of the output power is infinitesimal, as shown in Figure 3.10 (a). With the further increase of the injection

current, the QW devices still show no lasing (as shown in Figure 3.9), which implies that QW lasers need higher quality wafer to achieve lasing. On the contrary, the QD devices exhibited lasing operation with the threshold current density lower than 300 A/cm^2 (Figure 3.10 (b)). This different behaviour of the QD devices is mainly due to both quantum confinement effect and insensitivity to dislocation. Compare with QW material, the QD material confined the carriers in 3 dimensions, which shows better carrier confinement than QW material (only confined in 1 dimension). Based on the stronger confinement, the carrier escaping in QD is less than QW. Besides, the energy level in QD is separated and that of QW is continuous, so, the electrons in ground state is easier to transit to excited energy state in QW. Additionally, dislocations are the problem could not be avoided in Si-based samples, it will cause the non-radiative recombination and leads to heating, then, it makes the carrier escaping stronger. Under these conditions, Si-based QD devices could show better results than QW devices grown on Si substrate.

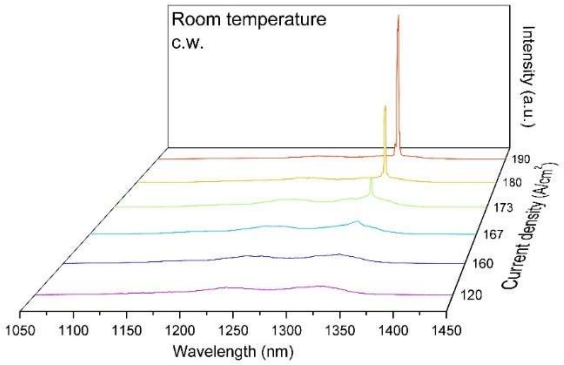

Figure 3.11 The spectrum of Si (001) based QD laser with 3mm cavity length and 50μm ridge width.

Emission spectrum is important evidence to prove the lasing behaviour, which provides much information of lasing. Figure 3.11 presents the wavelength spectrum of the QD laser devices as a function of injection current density. A spontaneous emission spectrum is obtained with a broad full width at half maximum (FWHM) of 35 nm at 1320 nm wavelength at an injection current density of 120 A/cm^2. As the injection current density increased to 180 A/cm^2 (threshold current density), a typical lasing spectrum with much narrower FWHM of around 2 nm and sharp increased intensity was achieved. Because of the transition from ground state requires lower energy than

that of excited state, the emission wavelength of ground state is longer than that of excited state. As a result, the figure 3.11 also confirmed that the emission wavelength corresponded to ground state emission, since the peak of lasing wavelength located on the longer wavelength region and the calculated bandgap energy matched with the design of band structure.

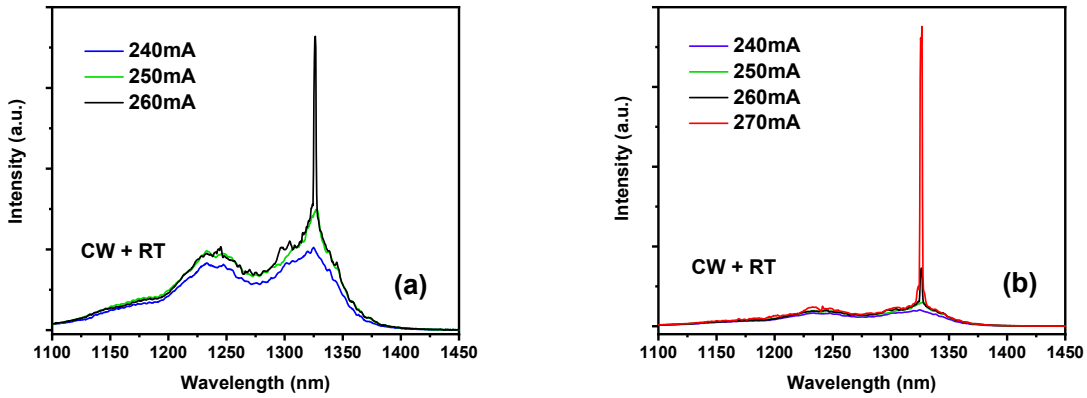

Figure 3.12 (a) the emission spectra of Si (001) based QD laser with different injection current from 240mA to 260mA. (b) From 240mA to 270mA.

As can be seen in Figure 3.12, it is found that the peak intensity is around 1325 nm wavelength, corresponding to ground state emission wavelength, and the highest intensity is enhanced with increased injection current. With the further increase of the injection current to 260 mA, the intensity peak rises rapidly. The threshold current of 260 mA (since the area of active region is 3mm*50μm, the calculated threshold current density is around 170 A/cm^2) estimated from the emission spectrum is accorded with the result of LIV curve in Figure 3.8.

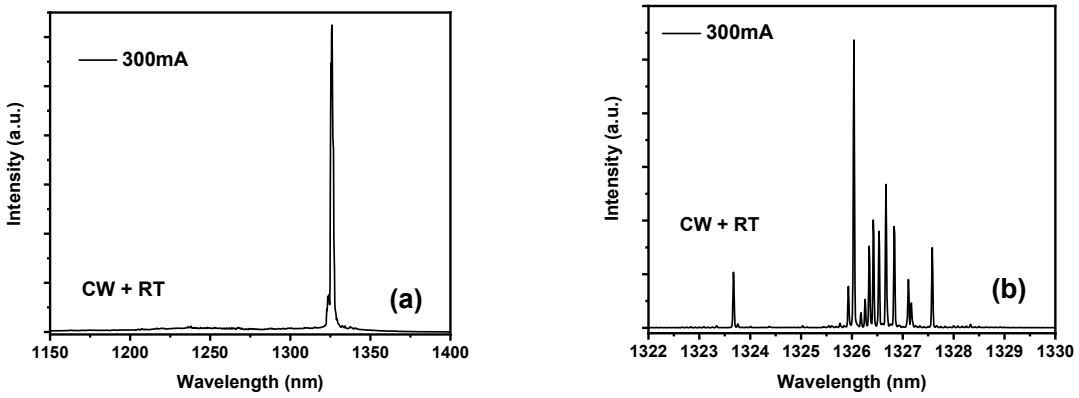

Figure 3.13 (a) the emission spectra of Si (001) based QD laser with 300mA injection current (200A/cm^2 injection current density) under normal resolution scanning. (b) under high resolution scanning.

The Figure 3.13 (a) shows the emission spectrum of QD laser on on-axis Si substrate with 300 mA injection current driving under the normal resolution scanning (0.5nm resolution). A sharp emission spectrum is obtained with 20 nm full width at half maximum (FWHM) at 1325 nm wavelength when the injection current is 200 A/cm^2. By using the high-resolution scanning (0.02nm resolution), several obvious peaks appear in the ground state in Figure 3.13 (b), indicating that the peak in Figure 3.13 (a) consists of various peaks and hence this laser device produced multi-mode lasing in the ground state emission.

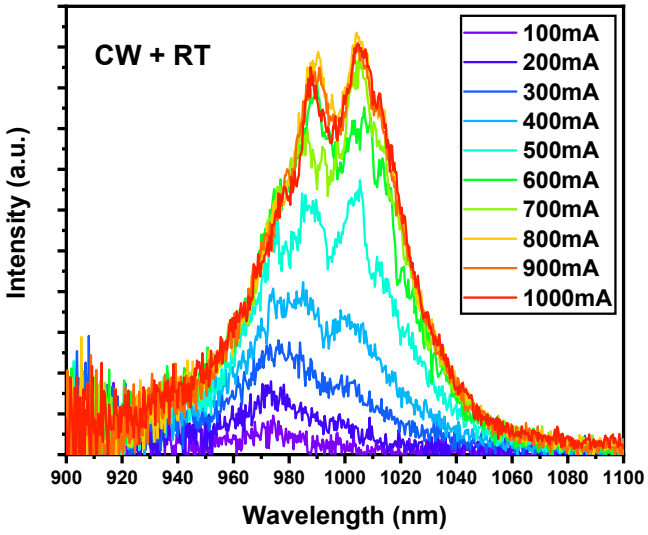

Figure 3.14 The emission spectrum of QW laser devices.

Due to no lasing states of QW laser on on-axis Si, the emission spectra show obvious spontaneous emission, as shown in Figure 3.13. The peak wavelength is at around 980nm in the beginning and then shifts to around 1020 nm with the rising of current. With the increase of the injection current, the FWHM still keeps as high as 60 nm and there are no obvious excited emission peaks. The increase of injection current does not induce a rapid increase of intensity, and the further increase of injection current over 800 mA even leads to the decrease of intensity. This indicates that the output power has already experienced rollover, and higher injection current will not cause the lasing operation. Moreover, a visible red-shift was also confirmed in QW devices. The most common reason for wavelength red-shift is the increase of temperature, namely, the thermal energy from resistance and self-heating. Because the series resistances are similar in both QD and QW samples, the heating caused by resistance keeps the

same level and, thereby, the QW generated more thermal energy by self-heating. In general, the non-radiative recombination caused by dislocations creates phonons instead of photons, resulting in the heating and low output intensity. Therefore, the spectrum result points out that the QW is deeply influenced by dislocations.

Consequently, based on the same growth condition and identical fabrication process, the totally different performance of QD and QW devices indicates that the QD material is more suitable for lasers grown on Si substrate. The dislocation tolerance and temperature stability make sure the lasing operation of Si-based QD lasers. In addition, the high energy barrier in active region and higher quantum confinement enable the carriers to be well confined, effectively avoiding the thermal leakage and thus enhancing the temperature stability of Si-based QD lasers.

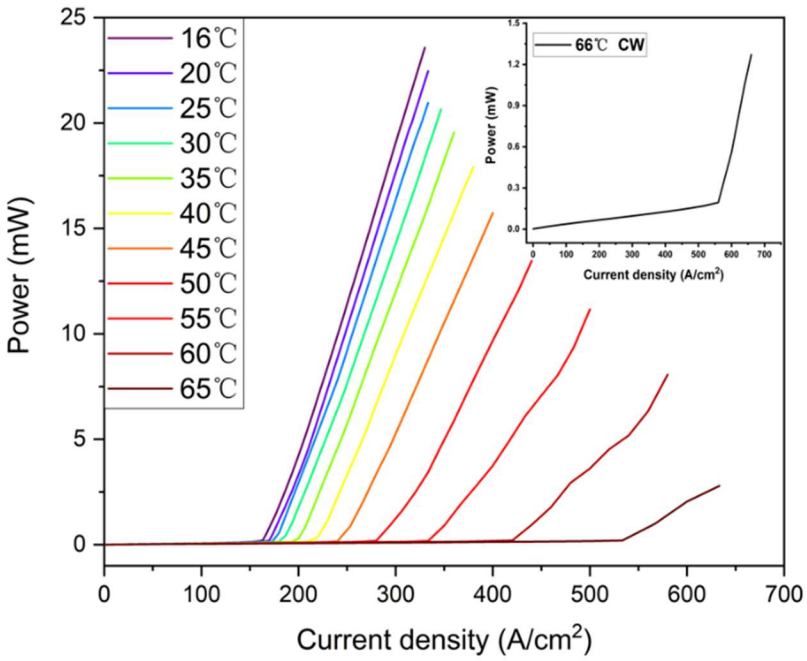

Figure 3.15 The result of temperature dependence light-current curves: output power versus current density for the same Si-based InAs/GaAs QD laser with different temperature under c.w. operation.

Temperature stability is one of important parameters to evaluate the reliability of laser device. Figure 3.15 shows the conventional LI properties of the QD laser grown on on-axis Si (001) at various heat-sink temperature under c.w. operation. The maximum c.w. lasing temperature is limited to 66 °C. With the increase of the operation temperature, the carrier has higher possibility to get energy and transit to the adjacent higher excited level, causing the decrease of the occupation probability of the ground state.

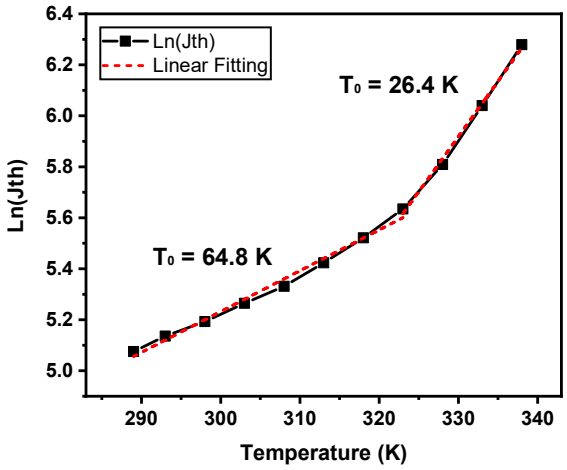

Figure 3.16 The intensity verse temperature curve for Si-based InAs/GaAs QD laser under c.w. operation. Based on the fitting of this curve, the characteristic temperature is calculated to be 64.8 K at range from 290 K to 320 K and 26.4 K from 320 K to 340 K.

To calculate the characteristic temperature, the natural logarithm (ln) value of threshold current density was presented as a function of temperature, as shown in Figure 3.16. The characteristic temperature (T_0) was measured to be 64.8 K (290 K – 320 K) and 26.4 K (320 K – 340 K).

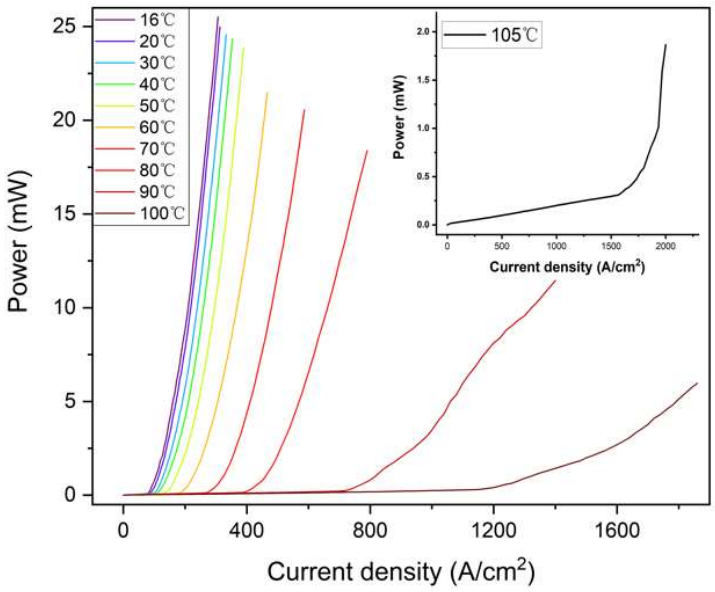

Figure 3.17 Output power versus current density for the same Si-based InAs/GaAs QD laser with different temperature under 2% duty cycle pulsed injection current operation.

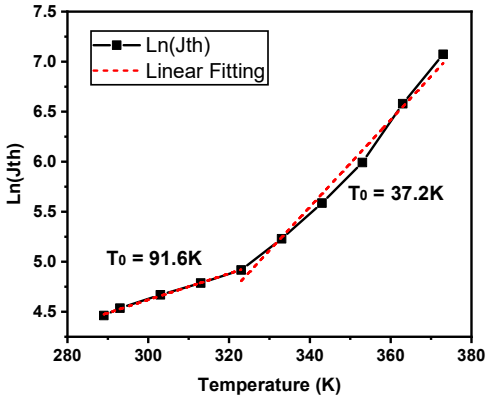

Figure 3.18 The intensity verse temperature curve for Si-based InAs/GaAs QD laser under pulsed driving.

The Figure 3.17 shows the output power of the QD laser grown on Si (001) at various heat-sink temperatures under 2% duty cycle pulsed injection current operation. The laser device keeps lasing operation up to the temperature of 105 °C. This is because the laser devices less suffer from self-heating under pulse injection current so that the better temperature dependence can be achieved. Noted that the injection current density of 2000 A/cm^2 (injection current of 3000 mA and the size of devices is 3mm*50μm) is the highest value due to the limitation of pulse source. Therefore, the maximum operation temperature of this QD laser is likely to further increase, because rollover was not observed in the output power curve (Figure 3.17). The characteristic temperature (T_0) is calculated in Figure 3.18, the T_0 is fitted as 91.6K in room temperature range and gradually decreases to around 37.2K with the rising temperature reaches 330K.

3.4 Conclusion

The QW and QD lasers grown on on-axis Si substrates with same epitaxial growth condition, dislocation density and fabrication process show entirely different behaviour. The LIV results indicate that QW lasers on Si require much lower density of TDs to obtain lasing operation, while the QD lasers on Si have better immunity to the TDs than QW lasers. From the PL results, it was found that the thermal escape of carriers in QD is less than that of QW structure, benefited by high thermal activation energy owing to the separated energy level of QD material. In addition, the insensitivity to dislocation is also helpful for QD laser to reduce the detrimental effect of non-radiative recommendation. Unlike the QW lasers on Si, therefore, the QD lasers on Si less suffer

from the heating problem caused by dislocation-induced non-radiative recombination. As a result, under the same growth condition (dislocation density), the QD material is able to confine and trap more carriers, contributing to better performance of QD laser on Si. In conclusion, the use of QDs as active region provides insensitivity to the TDs, and thus enables the realisation of high-performance Si-based QD lasers for Si photonics.

The results of QD laser on on-axis Si substrate in this work is comparable with that of the QD laser grown on an off-cut Si substrate, although the performance of laser is degenerated in terms of the high threshold current density and poor temperature characteristics [7]. Compared with the previous on-axis Si (001) laser devices, the threshold current density in this project was reduced from 425A/cm^2 to around 160A/cm^2, and the highest c.w. operation temperature increased to 66 °C [4]. In addition, the highest characteristic temperature in previous researches is only 46K, but the characteristic temperature reaches 64 K in this work, which is the highest value of all the reports of QD laser monolithically grown on on-axis Si (001) substrates without any intermediate buffer layers [4]. The significant improvement of the device performance can be attributed to the optimization of the material growth. These results demonstrated the potential of QD lasers as a promising light source on CMOS-compatible on-axis (001) Si substrate, capable of being monolithically integrated on PICs for Si photonics.

References

[1] Q. Li and K. M. Lau, “Epitaxial growth of highly mismatched III-V materials on (001) silicon for electronics and optoelectronics,” *Prog. Cryst. Growth Charact. Mater.*, vol. 63, no. 4, pp. 105–120, 2017.

[2] Q. Li, K. W. Ng, and K. M. Lau, “Growing antiphase-domain-free GaAs thin films out of highly ordered planar nanowire arrays on exact (001) silicon,” *Appl. Phys. Lett.*, vol. 106, no. 7, 2015.

[3] A. Y. Liu *et al.*, “Electrically pumped continuous-wave 1.3 μm quantum-dot lasers epitaxially grown on on-axis (001) GaP/Si,” *Opt. Lett.*, vol. 42, no. 2, pp. 338–341, 2017.

[4] S. Chen, M. Liao, M. Tang, J. Wu, M. Martin, T. Baron, A. Seeds, and H. Liu, “Electrically pumped continuous-wave 1.3 μm InAs/GaAs quantum dot lasers monolithically grown on on-axis Si (001) substrates,” *Opt. Express*, 25(5), 4632–4639 (2017).

[5] T. Wang, H. Liu, A. Lee, F. Pozzi, and A. Seeds, “1.3-μm InAs/GaAs quantum-dot lasers monolithically grown on Si substrates,” Opt. Express 19, 11381–11386, 2011.

[6] A. Lee, Q. Jiang, M. Tang, A. Seeds, and H. Liu, “Continuouswave InAs/GaAs quantum-dot laser diodes monolithically grown on Si substrate with low threshold current densities,” Opt. Express 20, 22181–22187, 2012.

[7] S. Chen, M. Tang, J. Wu, Q. Jiang, V. Dorogan, M. Benamara, Y. Mazur, G. Salamo, A. Seeds, and H. Liu, “1.3 μm InAs/GaAs quantum-dot laser monolithically grown on Si substrates operating over 100°C,” Electron. Lett. 50, 1467–1468, 2014.

[8] J.-M. Gerard and C. Weisbuch, “Semiconductor structure for optoelectronic components with inclusions,” U.S. patent 5,075,742, 1991

[9] AY. Liu, S. Srinivasan, J. Norman, AC. Gossard, and JE. Bowers, ‘‘Quantum dot lasers for silicon photonics’’, Vol. 3, No. 5 ,October, Photon. Res., 2015

[10] AY. Liu, R. W. Herrick, O. Ueda, P. M. Petroff, A. C. Gossard, and J. E. Bowers, “Reliability of InAs/GaAs Quantum Dot Lasers Epitaxially Grown on Silicon,” *IEEE J. Sel. Top. Quantum Electron.*, vol. 21, no. 6, 2015.

[11] Y. Arakawa and H. Sakaki, “Multidimensional Quantum Well Laser and Temperature-Dependence of Its Threshold Current,” *Appl. Phys. Lett.*, vol. 40, no. 11, pp. 939–941, 1982.

[12] M. Tang, S. Chen, J. Wu, Q. Jiang, V. G. Dorogan, M. Benamara, Y. I. Mazur, G. J. Salamo, A. Seeds, and H. Liu, “1.3-μm InAs/GaAs quantum-dot lasers monolithically grown on Si substrates using InAlAs/GaAs dislocation filter layers,” *Opt. Express*,22(10), 11528–11535 (2014).

[13] M. F. Schubert, J. Xu, Q. Dai, F. W. Mont, J. K. Kim, and E. F. Schubert, “On resonant optical excitation and carrier escape in GaInN/GaN quantum wells,” *Appl. Phys. Lett.*, vol. 94, no. 8, pp. 2007–2010, 2009.

Chapter 4
All-MBE grown high performance QD laser devices on Si (001) substrates

4.1 Introduction

High-performance Si-based laser monolithically grown on CMOS-compatible on-axis Si (001) substrate is desired for Si-based photonic integrated circuits (PICs) [1-5]. Although the impressive progress in Si-based lasers has been demonstrated in last two decades, most of the reported Si-based QD lasers used GaAs/Si or Ge/Si virtual substrate [6-9]. Particularly, the majority of well-performed GaAs/Si and Ge/Si virtual substrates are manufactured by MOCVD, which requires a costly usage of both MOCVD and MBE systems for growing the whole Si-based laser structure [10-12]. It is no doubt that this will increase the complexity and difficulty for wafer epitaxy, as well as the cost. Therefore, all-MBE growth is a direct and effective method to reduce the cost in equipment and manufacture [13,14]. With the continuous development in III-V epitaxial technology, the realization of all-MBE grown QD III-V lasers on on-axis Si substrate becomes possible, and a few results of all-MBE grown Si-based lasers were reported recently [14]. However, the growth mechanism is still not clear and the performance of the fabricated devices is unsatisfactory [14]. It is therefore imperative to develop and achieve high-performance all MBE-grown QD lasers on on-axis Si.

In this chapter, the all-MBE grown Si-based 1.3μm QD laser is demonstrated firstly, of which the structure design and growth condition are identical with the QD lasers in chapter 3. The only difference is buffer growth, namely growing GaAs/Si buffer on Si substrate within UCL twin-MBE system instead of using GaAs/Si virtual substrate grown by MOCVD. After the comparison and analysis of measured results, the needs of performance improvement stimulate the further optimization of buffer layer growth. Second, thin Ge buffer is originally grown on the surface of Si (001) substrate, which contributes to enhance the quality of buffer layer and reduce the density of threading dislocation effectively. Based on this approach, the all-MBE grown QD laser on Si (001) substrate with thin Ge buffer layer acquires improved lasing performance, and the discussion and research of this progress is also involved in this chapter.

4.2 All-MBE grown QD lasers on on-axis Si substrate with Si buffer

4.2.1 Experimental procedure

Without the utilizing of manufactured GaAs/Si virtual substrate, the dislocations, cracks and APBs are problems which should be overcome [13,15]. As a result, in order to reduce the influences for laser structure, the growth of initial buffer layers should be improved [16,17]. As shown in Figure 4.1, based on the requirement of high-quality epitaxial surface, the all-MBE growth process starts with the growth of 200 nm Si buffer layer with 1200 °C annealing. After this preparation, 1000 nm GaAs buffer and 4 sets of dislocation filter layers (DFLs) are grown to reduce the density of TDs and APBs [18]. Each DFL layer includes 4 groups of Si-doped InGaAs/GaAs superlattices and 300 nm GaAs capping layer. The active region consists of 7 groups of InAs dot-in-well structure with the 50 nm GaAs space layer, which is sandwiched between the 1.3 μm N-doped and P-doped $Al_{0.4}GaAs$ cladding layer. Two 300 nm high-doped N-type and P-type GaAs contact layers are located outside N-type and P-type cladding layer, respectively. The consistent growth condition and method are also utilized in this research, and the laser structure maintains the similar structure design with pervious Si-based QD laser devices.

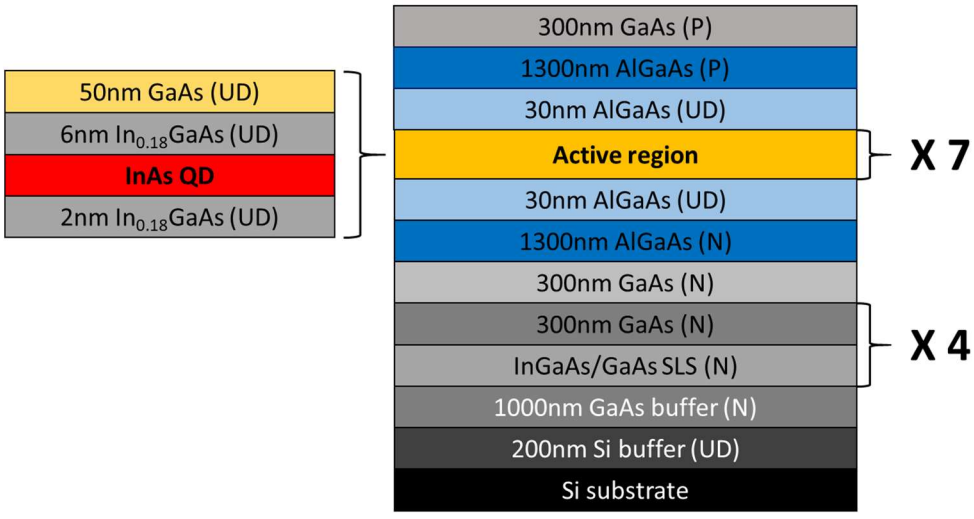

Figure 4.1 The structure of all-MBE growth 1.3μm QD laser monolithically grown on Si (001) substrate.

The photoluminescence (PL) results for characterising the optical property are plotted in figure 4.2, where the peak wavelength of all-MBE sample is located around 1300 nm with approximate 28 meV full width at half maximum (FWHM). Based on the same measurement setup, the PL intensity of all-MBE grown sample is comparable with that of devices discussed in chapter 3, although its intensity is around 1/3 of samples grown on mature GaAs/Si virtual substrate. The PL results imply that the all-MBE grown sample with Si buffer could not totally reduce the issues such as TDs and APBs caused by mismatch between GaAs and Si.

The laser devices with top-top configuration without SiO_2 insulating layer were fabricated, based on the identical process introduced in chapter 2. After metal contact formation, the substrate of devices is lapped to around 90 μm and cavity length is cleaved to 3 mm.

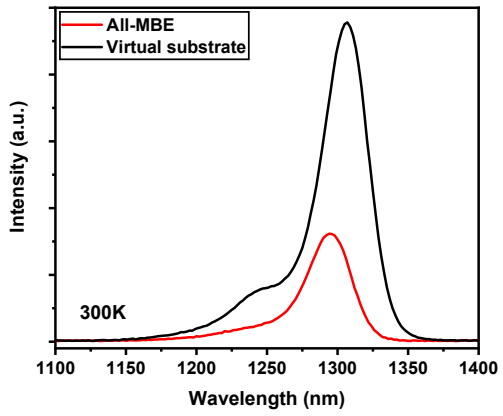

Figure 4.2 The PL results of the comparison between wafers grown on different substrates.

4.2.2 Result and discussion

The output power of samples with 50 μm width and 3 mm cavity length was tested under 2% (duty cycle) pulsed injection current at 16 °C. In Figure 4.3(a), the fabricated lasers produce the threshold current density of 260 A/cm^2 and output power of over 22 mW at an injection current density of 1000 A/cm^2. The spectrum results with various injection current density are also collected, as shown in Figure 4.3(b). The lasing peak wavelength is at around 1300 nm which is matched with O-band communication window. The spectrum of spontaneous emission is attained before injection current density reaches 260 A/cm^2.

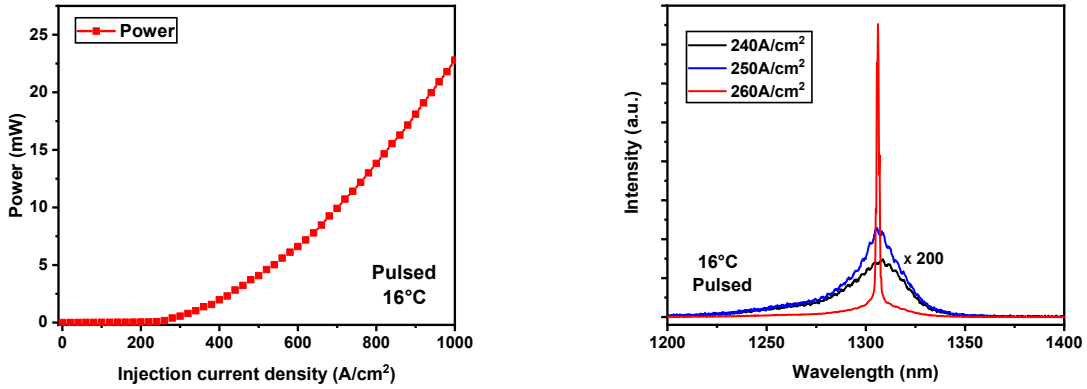

(a) *(b)*

Figure 4.3 (a)the output power verse pulsed injection current density at room temperature, (b) the spectrum results of all-MBE grown sample before and after threshold current density.

The temperature dependence light output measurement under pulse mode (20 °C – 110 °C) was also carried out, as shown in Figure 4.4(a). The maximum operation temperature of 110 °C was achieved, and a small increase of injection current density in operation temperature range from 20 °C to 60°C reveals robust temperature stability.

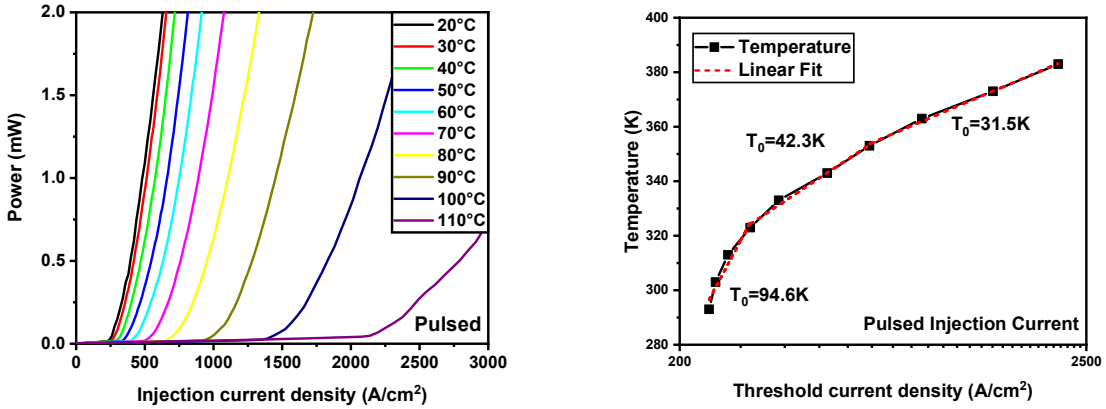

(a) *(b)*

Figure 4.4 (a) the output power verse injection current density under different operation temperature with pulsed injection current, (b) the linear fitting of temperature verse threshold current density for characteristic temperature.

To further characterise the temperature stability, the characteristic temperature (T_0) was calculated via the linear fitting of threshold current density versus temperature in Figure 4.4(b). The T_0 as high as 94.7K is obtained from 20°C to 50°C, but it gradually decreases to only around 31 K with the further increase of operation temperature. The T_0 drop might come from the influence of defects. The non-radiative recombination

and carrier thermal leakage, caused by various defects, are also enhanced with the increase of operation temperature.

In conclusion, all MBE-grown QD laser on on-axis Si substrate with Si buffer is reported in this section. Under room temperature and pulsed current driving, the output power of over 22 mW and threshold current density of 260 A/cm^2 are achieved. The devices also show good temperature stability with 94.7 K T_0 in temperature range from 20 °C to 50 °C and acquire 110 °C highest operation temperature. The laser structure all-MBE grown on Si (001) substrate still has several issues, and the performance gap between all-MBE grown devices and samples grown on mature virtual substrate manifest the space for further improvement of QD laser all-MBE grown on Si (001) substrate.

4.3 1.3μm all-MBE grown QD laser on Si (001) substrate with thin Ge buffer layer

Germanium (Ge) buffer layer has unique superiority in the monolithic growth of III-V laser on Si substrate: the lattice mismatch of only 0.08 % with GaAs [19]. The neglectable lattice mismatch between Ge and GaAs leads to the less generation of defects during the growth GaAs on Ge film, compared with the direct growth of GaAs on Si [20-22]. Moreover, the thermal expansion coefficient of Ge is also closer to that of GaAs, indicating that the issue of thermal crack during the growth can be mitigated evidently [23]. Nowadays, the Ge-on-Si platform and Ge/Si virtual substrates occupy great proportion in silicon photonics, and several impressive achievements in laser devices on Ge/Si virtual substrate are reported [24-27]. However, the Ge/Si virtual substrates made by MOCVD dominate this market [28-30]. In this work, we utilized a thin Ge buffer layer to grow APB-free Ge/Si virtual substrate using MBE, and achieved all-MBE grown QD lasers on on-axis (001) Si substrate.

4.3.1 Experimental procedure

The design of improved all-MBE grown QD laser on CMOS-compatible Si substrate have same growth condition and structure of previous QD lasers. The major difference of development is the growth of the thin Ge buffer as an initial epitaxy. A 300 nm Ge buffer is grown to form the Ge/Si virtual substrate, comprised of 50 nm, 100 nm and 150 nm epitaxial layers with different growth temperature. The 50 nm and 100 nm Ge

layers are grown at 250°C and 500°C, respectively, and then the thermal cycle annealing from 450 °C to 850 °C is repeated five time for quality promotion. The top 150 nm Ge layer in Ge buffer is grown at 600°C, and this capping layer is used to flatten the Ge buffer and offers the smooth surface for laser structure epitaxy. In order to further decrease the density of TDs, 350 nm GaAs buffer and 4 sets of DFL in which 5 groups of Si-doped $In_{0.2}GaAs/GaAs$ superlattices and 300 nm GaAs capping layer are included are grown on Ge/Si virtual substrate. As shown in Figure 4.5, the QD laser structures consist of 300 nm n-GaAs contact layer, 1300 nm n-$Al_{0.4}GaAs$ waveguide, InAs QD active region, 1300 nm p-$Al_{0.4}GaAs$ waveguide, and 300 nm p-GaAs contact layer. In the active region, InAs QDs are sandwiched by 2 nm $In_{0.18}GaAs$ wetting layer and 6 nm $In_{0.18}GaAs$ capping layer, and seven sets of QD layers are divided by 42 nm GaAs space layer containing 10 nm p-doped GaAs layer.

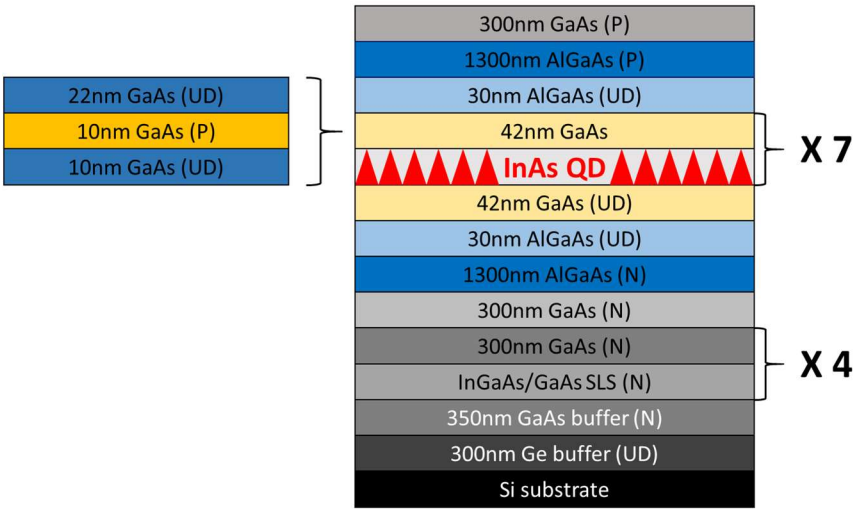

Figure 4.5 The structure of all-MBE grown QD laser on on-axis Si substrate with 300nm Ge buffer.

To characterise the quality and function of Ge buffer layer, transmission electron microscopy (TEM) measurement was carried out. Figure 4.6 (a) and (b) show the TEM images of DFLs without and with Ge buffer layer, respectively. Unlike the sample without Ge buffer, most of TDs are effectively confined within 300 nm Ge buffer layer and DFLs prevent further propagation of remaining TDs. As shown in Figure 4.6 (a), the density of TDs after GaAs buffer and DFLs was measured to be as high as $10^9/cm^2$ and $10^7/cm^2$, respectively. In contrary, for the sample with 300 nm Ge buffer layer, the density of TDs at the interface above Ge buffer is only $10^8/cm^2$, and the final TD density after applying DFLs is reduced to $4 \times 10^6/cm^2$. The TD density is supressed enough for QD laser growth. In addition, the high temperature annealing during the Ge buffer

growth enhances the mobility of dislocation and thus promotes the self-annihilation of dislocation, resulting in a remarkable improvement in the material quality.

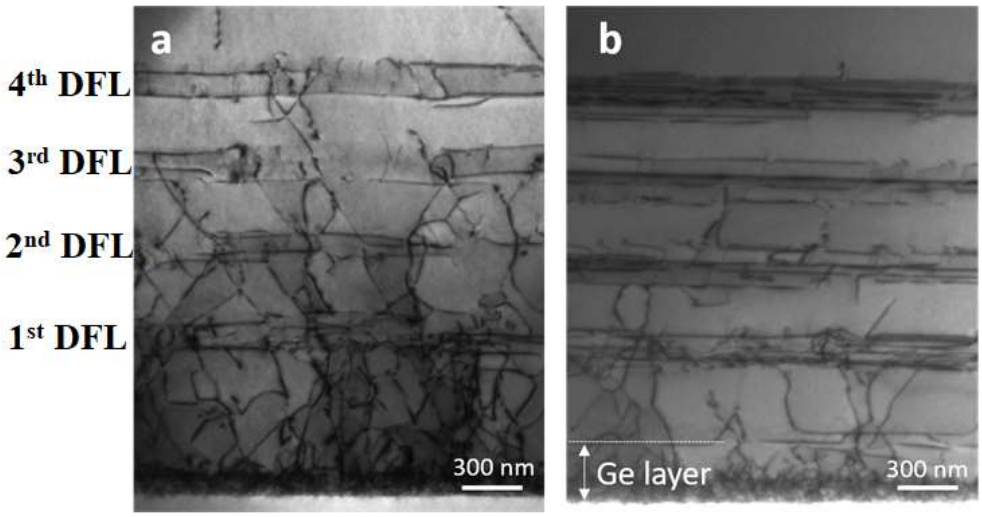

Figure 4.6 The TEM images of all-MBE grown QD laser on Si (001) substrate (a) with 200nm Si buffer (b) with 300nm Ge buffer.

In addition to the low density of TDs, the thin Ge buffer also contributes to effectively reduce the density of thermal crack caused by thermal expansion mismatch between Si and GaAs. Figure 4.7 exhibits the microscope images of samples without and with 300 nm Ge buffer. As shown in Figure 4.7 (b), it is confirmed for the sample with Ge buffer that the separation between thermal cracks is enlarged, compared with the sample without Ge buffer (Figure 4.7 (a)). Indeed, a 60% reduction in the density of thermal crack is acquired, which points out that the material quality is significantly improved with the effective suppression of thermal cracks by utilizing the thin Ge buffer. Because the thermal crack causes several issues such as structure breakage and injection current open circuits after the device fabrication, the decrease of thermal crack density makes the fabrication more reliable and enable more novel structure design for all-MBE grown Si-based laser.

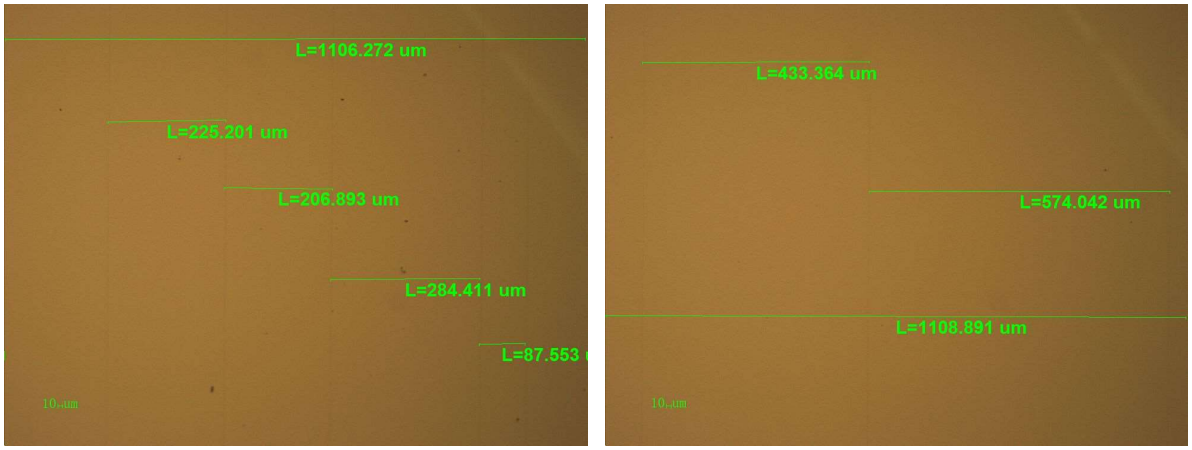

(a) *(b)*

Figure 4.7 The microscope images of thermal cracks density observed in sample (a) without (b) with 300nm Ge. In average, the density of thermal crack are 4.97/mm and 1.98/mm for samples without and with 300nm Ge buffer layer respectively.

After the wafer growth, the top-top structure QD lasers without SiO_2 insulating layer were fabricated, with the same process reported in last chapter. Then, the substrate thickness of devices is lapped to around 80μm and 3mm cavity length is cleaved equally.

4.3.2 Result and discussion

To characterise the performance of fabricated laser devices, output power was first measured based on pulse injection current at 16 °C. Figure 4.8 (a) exhibits the typical L-I curve, where the threshold current density of the all-MBE grown QD lasers with Ge buffer on on-axis Si is around 200 A/cm^2 under 2% (duty cycle) pulsed current. The output power reaches 78 mW at an injection current density of 1200 A/cm^2. Then, the emission spectra under different current were measured to check the wavelength and lasing state, as shown in Figure 4.8 (b). The conspicuous spontaneous emission spectra are observed at injection current densities of 170 A/cm^2 and 190 A/cm^2. The ground state lasing is obtained at an injection current density of 200 A/cm^2, matched with the estimated value of threshold current density in Figure 4.8(a). The peak wavelength of lasing spectrum is located at 1280 nm which could be used for O-band optical communication.

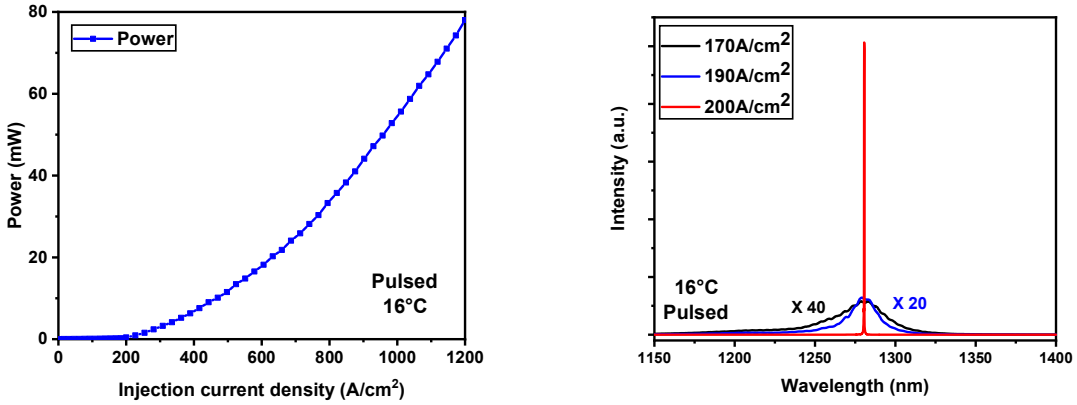

(a) (b)

Figure 4.8 (a) the LI curve of all-MBE grown sample with Ge buffer under 2% pulsed mode. (b) the emission spectra of all-MBE grown Si-based QD laser with different injection current density.

Figure 4.9 displays the comparison of L-I curves of all-MBE grown samples with/without Ge buffer on Si substrate and sample grown on Ge/Si virtual substrate. The sample with Ge buffer produces better lasing properties in terms of slope efficiency and threshold current density, compared with the sample without Ge buffer. Although the sample grown on mature Ge/Si virtual substrates still shows best performances, the comparable result of optimized all-MBE grown sample indicates the material quality improvement after growing initial thin Ge buffer.

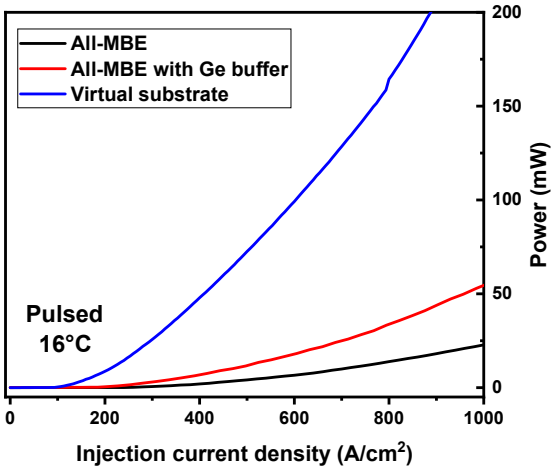

Figure 4.9 the comparison of L-I curves of all-MBE grown samples with/without Ge buffer on Si substrate and sample grown on Ge/Si virtual substrate. The threshold current density of three samples are around 100, 200, 240 A/cm² under 2% duty cycle pulsed injection current, respectively.

Figure 4.10 presents the temperature dependent L-I curves of sample with Ge buffer under 2% pulsed driving. Because of the limitation of electric-heating tile, the highest temperature of measurement setup could rise to only 130°C. In the temperature range from 16 °C to 130 °C, the threshold current density increases with temperature rising, and the slope efficiency slightly decreases without sharp drop even when operation temperature reaches 130 °C. Since the L-I curve at 130°C shows no obvious power saturation, it is no doubt that the highest working temperature of all-MBE grown laser device with Ge buffer is expected to be higher than 130 °C. Compared with the temperature dependent results of all-MBE sample with Si buffer shown in figure 4.4(a), the tendency of both the threshold current increase and electro-optical efficiency decrease reveals the better temperature stability of the samples with Ge buffer. In order to further investigate the temperature stability of samples, the T_0 is calculated from Figure 4.11. A remarkable high T_0 is calculated as 154.6 K around room temperature range (289K to 309K), and the T_0 decreases to approximate 50 K when operation temperature exceeds 320 K. As the T_0 of samples with Si buffer in last section is calculated as only 94.6 K and 31.5 K in low and high temperature range, respectively, the increased T_0 also proves the better thermal performance of all-MBE grown samples with Ge buffer.

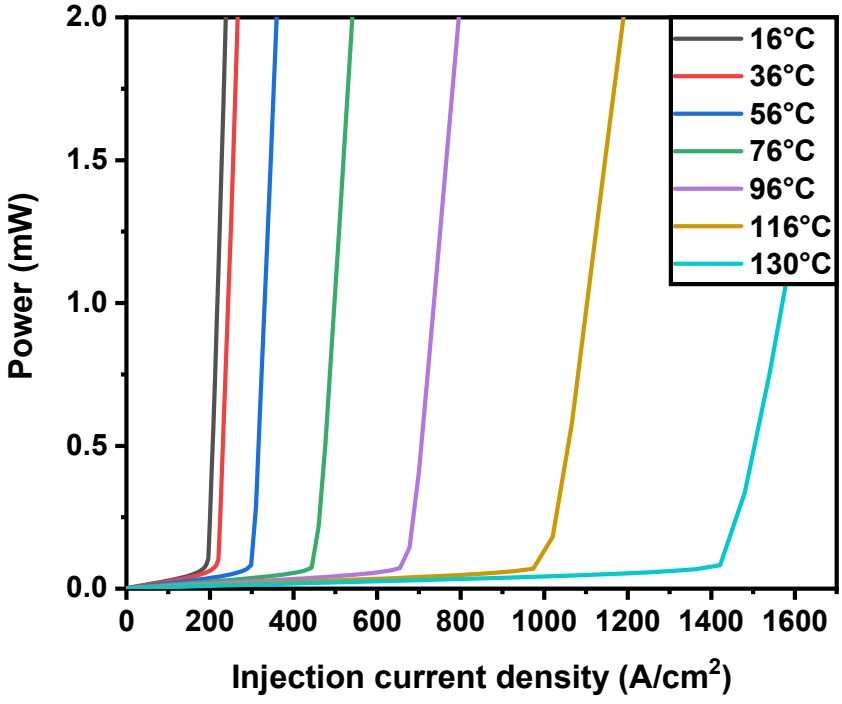

Figure 4.10 Output power versus current density for the all-MBE grown Si-based InAs/GaAs QD laser with different temperature under pulse condition.

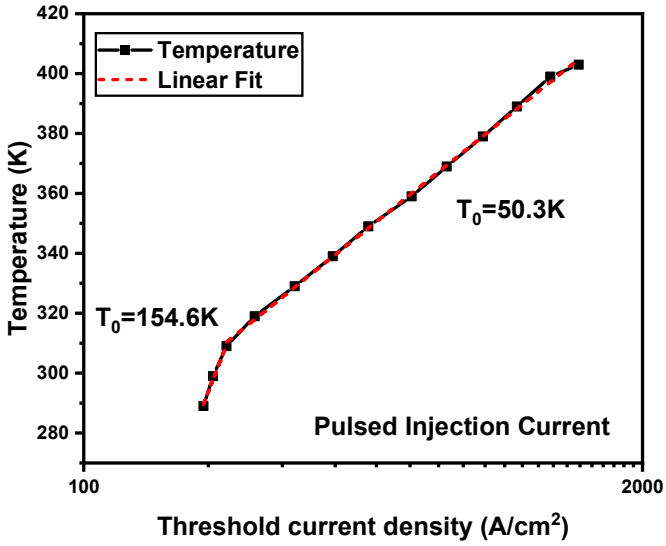

Figure 4.11 The intensity verse temperature curve for Si-based InAs/GaAs QD laser grown by all-MBE under pulsed current driving.

The temperature dependence spectral measurement was also tested by Fourier spectrometer. Since the output emission is collected by spherical mirror focussing instead of optical fibre, the noise of spectrum results shown in figure 4.12 is higher than previous spectrum, but the peak wavelength of spectrum under different temperature is clear enough to be identified. The evident redshift of peak wavelength is observed with the increase of temperature from 20°C to 110°C as the temperature increase constringing the bandgap and thus leads to the emission of longer wavelength. With further temperature rising, the emission wavelength suddenly drops to 1210 nm (120 °C) from 1320 nm (110 °C). This is because the excited state carrier transition replaces the ground state transition and thus the higher energy level offers larger bandgap and shorter wavelength. As a result, the all-MBE grown sample is able to operate ground state lasing under 110 °C background temperature and display excited state lasing at operation temperature 120°C. Ground state lasing under 110°C could meet the requirement of majority data centres, and the good temperature stability shows great potential of saving cost in cooling [1,6].

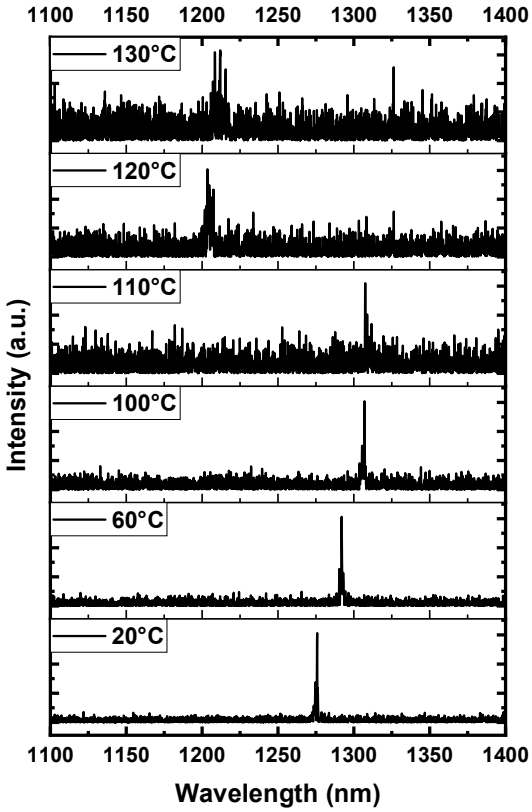

Figure 4.12 The intensity verse temperature curve for Si-based InAs/GaAs QD laser under c.w. operation.

Compared with the all-MBE grown QD laser on Si (001) substrate with GaAs/Si buffer layer, samples employing the thin Ge buffer represents comprehensive improvement of laser property such as 200 A/cm^2 low threshold current density and the doubled output power under pulsed injection current at 16 °C. The all-MBE grown Si-based QD laser with thin Ge buffer also shows impressive temperature stability, with the highest operation temperature above 130°C and the T_0 as high as 154.6K in room temperature range. The enhanced lasing properties can be attributed to the reduction in the density of dislocations and thermal cracks.

4.4 Conclusion

In this chapter, QD lasers all-MBE grown on CMOS-compatible Si (100) substrate were investigated to simplify the whole growth process of Si-based lasers. Under pulsed injection current driving, the QD laser with GaAs/Si (1000 nm/ 200 nm) buffer grown on on-axis Si substrate produced J_{th} of 260 A/cm^2, T_0 of 95 K, and highest operation temperature of 110 °C. To further improve the material quality, the Ge, which offers small mismatch of lattice and thermal expansion for GaAs epitaxy, was

employed as a buffer layer instead of the Si buffer. The distinct development in material quality and laser performance was obtained by QD laser all-MBE grown on Si (001) substrate with Ge buffer, including low threshold current density of 200 A/cm^2 with double electro-optical efficiency and the highest operation temperature of 130°C. The devices based on Ge buffer also provide impressive temperature stability. The calculated T_0 is 154.6K around room temperature, and the laser device maintains ground state lasing even at the operation temperature of 110°C.

Although the performance of QD lasers all-MBE grown on on-axis (001) Si substrate is unsatisfactory, compared with that grown on mature GaAs/Si substrate by MOCVD, the continuous development in growth technology and material quality demonstrated great potential of the all-MBE grown devices. Growing Ge/Si virtual substrate by MBE is demonstrated as a reasonable approach to realize high-performance Si-based laser devices grown without MOCVD, and the well-performed lasing operation in this chapter indicates the great application potential for Si-based photonic integrated circuits.

References

[1] Liang, D., & Bowers, J. E. (2010). Recent progress in lasers on silicon. Nature Photonics, 4(8), 511–517.

[2] Wu, J., Chen, S., Seeds, A., & Liu, H. (2015). Quantum dot optoelectronic devices: Lasers, photodetectors and solar cells. Journal of Physics D: Applied Physics, 48(36).

[3] Jung, D., Norman, J., Kennedy, M. J., Shang, C., Shin, B., Wan, Y., Gossard, A. C., & Bowers, J. E. (2017). High efficiency low threshold current 1.3 μ m InAs quantum dot lasers on on-axis (001) GaP/Si. Applied Physics Letters, 111(12), 3–7.

[4] Zhou, T., Tang, M., Xiang, G., Xiang, B., Hark, S., Martin, M., Baron, T., Pan, S., Park, J. S., Liu, Z., Chen, S., Zhang, Z., & Liu, H. (2020). Continuous-wave quantum dot photonic crystal lasers grown on on-axis Si (001). Nature Communications, 11(1), 1–7.

[5] Jung, D., Zhang, Z., Norman, J., Herrick, R., Kennedy, M. J., Patel, P., Turnlund, K., Jan, C., Wan, Y., Gossard, A. C., & Bowers, J. E. (2018). Highly Reliable Low-Threshold InAs Quantum Dot Lasers on On-Axis (001) Si with 87% Injection Efficiency. ACS Photonics, 5(3), 1094–1100.

[6] Chen, S., Li, W., Wu, J., Jiang, Q., Tang, M., Shutts, S., Elliott, S. N., Sobiesierski, A., Seeds, A. J., Ross, I., Smowton, P. M., & Liu, H. (2016). Electrically pumped continuous-wave III-V quantum dot lasers on silicon. Nature Photonics, 10(5), 307–311.

[7] Li, K., Liu, Z., Tang, M., Liao, M., Kim, D., Deng, H., Sanchez, A. M., Beanland, R., Martin, M., Baron, T., Chen, S., Wu, J., Seeds, A., & Liu, H. (2019). O-band InAs/GaAs quantum dot laser monolithically integrated on exact (0 0 1) Si substrate. Journal of Crystal Growth, 56–60.

[8] Arakawa, Yasuhiko, Nakamura, T., & Kwoen, J. (2019). Quantum dot lasers for silicon photonics. Semiconductors and Semimetals, 101(5), 91–138.

[9] Norman, J. C., Jung, D., Wan, Y., & Bowers, J. E. (2018). Perspective: The future of quantum dot photonic integrated circuits. APL Photonics, 3(3).

[10] Tang, M., Park, J. S., Wang, Z., Chen, S., Jurczak, P., Seeds, A., & Liu, H. (2019). Integration of III-V lasers on Si for Si photonics. Progress in Quantum Electronics, 66(May), 1–18.

[11] Wan, Y., Inoue, D., Jung, D., Norman, J. C., Shang, C., Gossard, A. C., & Bowers, J. E. (2018). Directly modulated quantum dot lasers on silicon with a milliampere threshold and high temperature stability. Photonics Research, 6(8), 776.

[12] Ironside, D. J., Skipper, A. M., Leonard, T. A., Radulaski, M., Sarmiento, T., Dhingra, P., Lee, M. L., Vučković, J., & Bank, S. R. (2019). High-Quality GaAs Planar Coalescence over Embedded Dielectric Microstructures Using an All-MBE Approach. Crystal Growth and Design, 19(6), 3085–3091.

[13] Li, K., Yang, J., Lu, Y., Tang, M., Jurczak, P., Liu, Z., Yu, X., Park, J. S., Deng, H., Jia, H., Dang, M., Sanchez, A. M., Beanland, R., Li, W., Han, X., Zhang, J. C., Wang, H., Liu, F., Chen, S., … Liu, H. (2020). Inversion Boundary Annihilation in GaAs Monolithically Grown on On-Axis Silicon (001). Advanced Optical Materials, 8(22), 1–8.

[14] Kwoen, J., Jang, B., Lee, J., Kageyama, T., Watanabe, K., & Arakawa, Y. (2018). All MBE grown InAs/GaAs quantum dot lasers on on-axis Si (001). Optics Express, 26(9), 11568.

[15] Liu, Z., Hantschmann, C., Martin, M., Baron, T., Chen, S., Seeds, A., Penty, R., White, I., Liao, M., Tang, M., Lu, Y., S., Sanchez, A., & Liu, H. (2020). Origin of Defect Tolerance in InAs/GaAs Quantum Dot Lasers Grown on Silicon. *Journal of Lightwave Technology*, 38(2), 240–248.

[16] Wang, T., Liu, H., Lee, A., Pozzi, F., & Seeds, A. (2011). 1.3 μm InAs/GaAs quantum-dot lasers monolithically grown on Si substrates. Optics Express, 19(12), 11381.

[17] Wan, Y., Zhang, S., Norman, J. C., Kennedy, M. J., He, W., Liu, S., Xiang, C., Shang, C., He, J.-J., Gossard, A. C., & Bowers, J. E. (2019). Tunable quantum dot lasers grown directly on silicon. Optica, 6(11), 1394.

[18] Tang, M., Chen, S., Wu, J., Jiang, Q., Kennedy, K., Jurczak, P., Liao, M., Beanland, R., Seeds, A., & Liu, H. (2016). Optimizations of defect filter layers for 1.3-μm InAs/GaAs quantum-dot lasers monolithically grown on Si substrates. IEEE JSTQE, 22(6), 50–56.

[19] Brammertz, G., Caymax, M., Meuris, M., Heyns, M., Mols, Y., Degroote, S., & Leys, M. (2008). GaAs on Ge for CMOS. Thin Solid Films, 517(1), 148–151.

[20] Leuthold, J., Koos, C., & Freude, W. (2010). Nonlinear silicon photonics. Nature Photonics, 4(8), 535–544.

[21] Wirths, S., Geiger, R., Von Den Driesch, N., Mussler, G., Stoica, T., Mantl, S., Ikonic, Z., Luysberg, M., Chiussi, S., Hartmann, J. M., Sigg, H., Faist, J., Buca, D., & Grützmacher, D. (2015). Lasing in direct-bandgap GeSn alloy grown on Si. Nature Photonics, 9(2), 88–92.

[22] Luan, H. C., Lim, D. R., Lee, K. K., Chen, K. M., Sandland, J. G., Wada, K., & Kimerling, L. C. (1999). High-quality Ge epilayers on Si with low threading-dislocation densities. Applied Physics Letters, 75(19), 2909–2911.

[23] Yang, V. K., Groenert, M., Leitz, C. W., Pitera, A. J., Currie, M. T., & Fitzgerald, E. A. (2003). Crack formation in GaAs heteroepitaxial films on Si and SiGe virtual substrates. Journal of Applied Physics, 93(7), 3859–3865.

[22] Kang, Y., Liu, H. D., Morse, M., Paniccia, M. J., Zadka, M., Litski, S., Sarid, G., Pauchard, A., Kuo, Y. H., Chen, H. W., Zaoui, W. S., Bowers, J. E., Beling, A., McIntosh, D. C., Zheng, X., & Campbell, J. C. (2009). Monolithic germanium/silicon avalanche photodiodes with 340GHz gain-bandwidth product. Nature Photonics, 3(1), 59–63.

[25] Mi, Z., Yang, J., Bhattacharya, P., Qin, G., & Ma, Z. (2009). High-performance quantum dot lasers and integrated optoelectronics on Si. Proceedings of the IEEE, 97(7), 1239–1249.

[26] Liu, A. Y., Zhang, C., Norman, J., Snyder, A., Lubyshev, D., Fastenau, J. M., Liu, A. W. K., Gossard, A. C., & Bowers, J. E. (2014). High performance continuous wave 1.3 μ m quantum dot lasers on silicon. Applied Physics Letters, 104(4), 3–7.

[27] Liu, H., Wang, T., Jiang, Q., Hogg, R., Tutu, F., Pozzi, F., & Seeds, A. (2011). Long-wavelength InAs/GaAs quantum-dot laser diode monolithically grown on Ge substrate. Nature Photonics, 5(7), 416–419.

[28] Michel, J., Liu, J., & Kimerling, L. C. (2010). High-performance Ge-on-Si photodetectors. Nature Photonics, 4(8), 527–534.

[29] Michel, J., Camacho-Aguilera, R. E., Cai, Y., Patel, N., Bessette, J. T., Romagnoli, M., Dutt, B. R., & Kimerling, L. C. (2012). An electrically pumped Ge-on-Si laser. Optics InfoBase Conference Papers, 20(10), 11316–11320.

[30] Yang, J., Jurczak, P., Cui, F., Li, K., Tang, M., Billiald, L., Beanland, R., Sanchez, A. M., & Liu, H. (2019). Thin Ge buffer layer on silicon for integration of III-V on silicon. Journal of Crystal Growth, 514(February), 109–113.

[31] Yang, J., Liu, Z., Jurczak, P., Tang, M., Li, K., Pan, S., Sanchez, A., Beanland, R., Zhang, J. C., Wang, H., Liu, F., Li, Z., Shutts, S., Smowton, P., Chen, S., Seeds, A., & Liu, H. (2021). All-MBE grown InAs/GaAs quantum dot lasers with thin Ge buffer layer on Si substrates. Journal of Physics D: Applied Physics, 54(3).

Chapter 5
High performance Quantum cascade laser for Si-based mid-infrared laser device

5.1 Introduction

As discussed in chapter 1, silicon photonics is promising technology due to low-cost and high reliable integration utilizing mature silicon platform [1-3]. For mid-infrared integration, high performance Si-based modulators, photodetectors, couplers and multiplexers have been reported in many researches, but the lack of Si-based mid-infrared light source still impede the whole mid-infrared integrated circuits on Si platform [3-6]. The growing research interest in Si-based mid-infrared light source impel the explorations of Si-based QCL devices, because QCL has better performance compared with other light sources in mid-infrared spectral regions. Heterogeneous integration is an effective way to approach Si-based QCL on silicon-on-insulator (SOI) or silicon-on-nitride-on-insulator (SONOI) platform, and several researches realize this conception in last few years [7,8]. However, the heterogeneous integration still suffers from the complex process and limited scalability, compared with the monolithic integration approach. In this regard, the monolithic integration of Si-based QCL is a promising way to achieve mid-infrared Si photonics [9].

GaAs/AlGaAs and InP/InGaAs/InAlAs designs are two majority material systems widely used for QCL devices. For silicon photonics, GaAs has the benefit of smaller lattice mismatch with GeSi virtual substrate and Si substrate than InP, and offers mature experience of growing GaAs on Si such as 1.3 μm InAs QD lasers on Si [10]. However, as mentioned in 1.4.3, the laser property of GaAs-based QCL is not as good as that of InP-based QCL. Therefore, two approaches for achieving Si-based QCL, including the growth of GaAs-based QCL on Ge/Si substrate and InP-based QCL on InP/Ge/Si substrate, will be discussed in this chapter.

In the beginning of this chapter, the basic research of both GaAs and InP-based QCLs is carried out for Si-based QCL. Then, to obtain high-performance QCL, a great deal

of efforts has been devoted to developing heating dissipation and advanced fabrication processes. After the optimization of high-performed QCL devices, the quantum dot cascade laser (QDCL) is researched as follow, because quantum dot material is more suitable for Si-based laser growth, compared with QW material commonly used for QCL epitaxy. Finally, several QCL structures are grown on Si substrate.

5.2 GaAs-based and InP-based Quantum Cascade laser

5.2.1 Background

Quantum-cascade lasers (QCLs) are important mid-infrared light source which can be applied in sensing, space communication and military domain, due to their characteristic of broaden wavelength coverage in mid-infrared region [11]. At present, most of QCLs are based on two kinds of III-V material systems: GaAs/AlGaAs system and InP/InGaAs/InAlAs system. In this chapter, the growth and fabrication of these two kinds of QCLs were introduced and the results were also analysed.

GaAs/AlGaAs QCL plays an important role in the solid-state laser source in mid-infrared wavelength (8μm – 13μm) which covers most of atmospheric window (8μm – 14μm) [12]. Since the Ga and Al have the same lattice constant, the growth of GaAs/$Al_xGa_{1-x}As$ material system will not face the problem originating from lattice mismatch and strain [12]. As a result, the structure design and growth of GaAs/AlGaAs QCL are flexible and reliable.

Compared with the GaAs/AlGaAs QCLs, the InP/InGaAs/InAlAs QCLs are more difficult to grow, due to the complex active region structures and the large strain caused by lattice mismatch [12,13]. However, the InP-based QCLs benefit from a higher energy barrier between InP and InAlAs, where the carrier thermal leakage could be avoided effectively [13]. Besides, the reflective index of InP substrate is lower than that of active region, which is helpful for optical confinement and, therefore, the waveguide in InP-based QCLs can be designed to be thinner than that of GaAs-based QCLs [14-16].

In this section, based on the experience of GaAs growth from the epitaxy of O-band QD laser samples, the GaAs-based QCL lasing at the wavelength of 9.15 μm under low temperature background (83K to 103K) is researched firstly. Then, the exploration

and generation of 6.75-μm InP-based QCL operating under room temperature are investigated in the follow. This chapter also pays attention to the improvement of fabrication process which leads to conspicuous enhancement of the laser performance.

5.2.2 GaAs-based QCLs grown on GaAs substrate

5.2.2.1 Epitaxial growth and device fabrication

The composition of Al (x) in GaAs/$Al_xGa_{1-x}As$ QCL determines the band energy in conduction band, which influences the energy barrier and energy band distribution. In this work, the composition of Al is designed to be 0.45 (x=0.45) because the high Al composition could increase energy barrier to enhance carrier injection efficiency (when x=0.33, ΔE_c= 290 meV; when x=0.45, ΔE_c= 390 meV).

N+ GaAs	300nm	5E18 cm^{-3}	
N- GaAs	300nm	5E16 cm^{-3} ~ 5E18 cm^{-3}	
N- GaAs waveguide	3.6μm	5E16 cm^{-3}	
GaAs	34 Å		×40
$Al_{0.45}Ga_{0.55}As$	**17 Å**		
GaAs	30 Å		
$Al_{0.45}Ga_{0.55}As$	**18 Å**	**$4\times10^{17}cm^{-3}$**	
GaAs	28 Å	$4\times10^{17}cm^{-3}$	
$Al_{0.45}Ga_{0.55}As$	**20 Å**	**$4\times10^{17}cm^{-3}$**	
GaAs	30 Å	$4\times10^{17}cm^{-3}$	
$Al_{0.45}Ga_{0.55}As$	**26 Å**		
GaAs	30 Å		
$Al_{0.45}Ga_{0.55}As$	**46 Å**		
GaAs	19 Å		
$Al_{0.45}Ga_{0.55}As$	**11 Å**		
GaAs	54 Å		
$Al_{0.45}Ga_{0.55}As$	**11 Å**		
GaAs	48 Å		
$Al_{0.45}Ga_{0.55}As$	**28 Å**		
N- GaAs waveguide	4.05μm	5E16 cm^{-3}	
N- GaAs waveguide	335nm	5E18 cm^{-3} ~ 5E16 cm^{-3}	
N+ GaAs	0.3μm	5E18 cm^{-3}	
N+ doped GaAs Substrate (3")			

Figure 5.1 The structure of GaAs-based GaAs/$Al_{0.45}Ga_{0.55}As$ QCL sample. The table include the thickness and component of each epitaxial layer, and it also shows the doping level in the right. The period number of active region is 40.

In this research, the epitaxial structure was designed with 4-energy-level GaAs/$Al_{0.45}Ga_{0.55}As$ QCL system. Figure 5.1 shows the schematic illustration of the whole structure of GaAs-based sample, consisting of the n-doped GaAs waveguide grown by MOCVD and 40 periods of GaAs/$Al_{0.45}Ga_{0.55}As$ active region grown by MBE. Each period in active region includes 8 group of lattice-matched GaAs/$Al_{0.45}Ga_{0.55}As$, two of which are doped by Be with density of 4×10^{17} cm^{-3}. The thickness of each

epitaxial layer in active region will affect the energy level distribution. The distribution of energy levels could be calculated based on the quantum confinement equation: for each quantum well, it should obey the equation of quantum confinement energy which introduced in chapter 1 (equation 1.6 and 1.7). In band structure, the energy of quantum confinement display as the distance between energy level and bottom of conduction band. Because of the energy quantum confinement related with the bandgap energy and the thickness of quantum well (Δx in equation 1.6), after calculating the bandgap and thickness of each QW material in active region could make the simulation result of the band structure with energy levels. Therefore, the energy level was simulated by software matlab progress, it calculates bandgap energy based on the proportion of each material, and then calculates the quantum confinement energy according to the thickness and quantum confinement equations. The simulation result of previous QCL structure is shown in Figure 5.2. For each period, 4 groups of GaAs/$Al_{0.45}Ga_{0.55}As$ are used as an injector in which 2 groups are n-doped. The injected electrons transit 4.6 nm-thick $Al_{0.45}Ga_{0.55}As$ to energy level 3, and the transition between energy level 3 and 2 generates radiative transition photon. The energy between level 3 and 2 was calculated to be 141 meV, which suggests that the lasing wavelength would be around 9 μm.

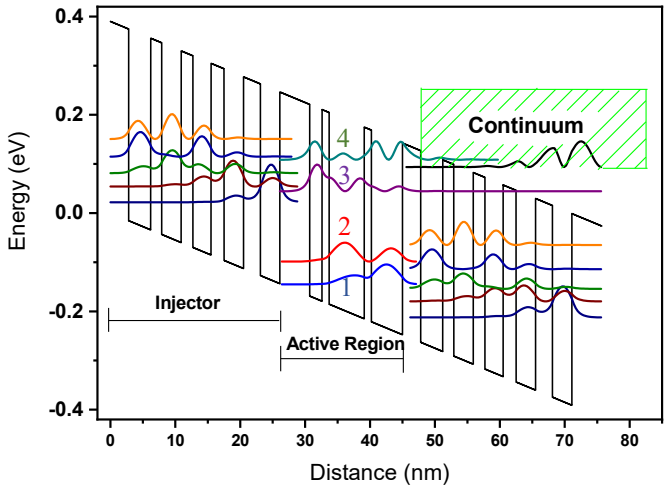

Figure 5.2 The energy level in active region of GaAs-based GaAs/$Al_{0.45}Ga_{0.55}As$ QCL sample.

After the epitaxy of sample, the XRD measurement was performed to check the flatness and thickness of epitaxial layers. As shown in Figure 5.3, the ω/2θ scan shows the outstanding symmetry and uniform separation distance between satellite peaks,

indicating smooth epitaxial layer and identical thickness of each period in active region, respectively. Based on the distance between satellite peaks, the calculated thickness of each period is 44.7 nm, which is very close to the designed thickness (45 nm).

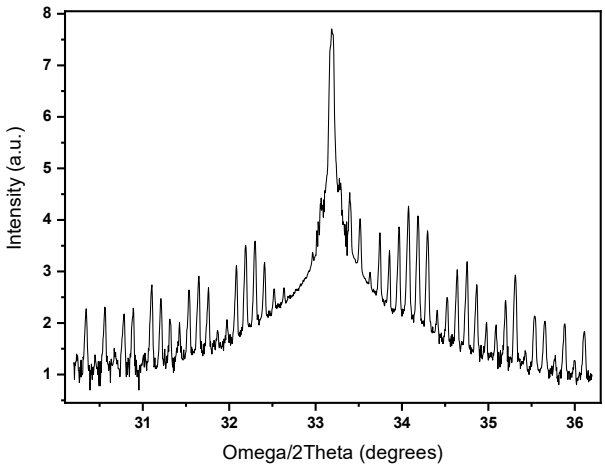

Figure 5.3 The XRD result of GaAs-based GaAs/$Al_{0.45}Ga_{0.55}As$ QCL sample.

The wafer was fabricated into single ridge waveguide QCL using standard photolithography and chemical wet etching. The process details are similar to the laser fabrication with SiO_2 presented in chapter 2. As shown in Figure 5.4, the different ridge widths are designed (20, 30, 50 and 70 μm), and the devices with the width of 30 and 70 μm are shown in Figures 5.4 (a) and (b), respectively. The top contact was formed on the surface of the ridge, and the bottom contact was sandwiched by two adjacent ridges with 135 μm width. Since the substrate is highly conductive n-type GaAs, contact metal was also deposited on the whole bottom surface after lapping.

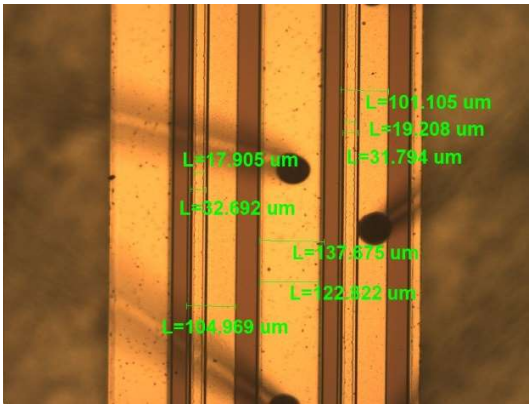

(a)

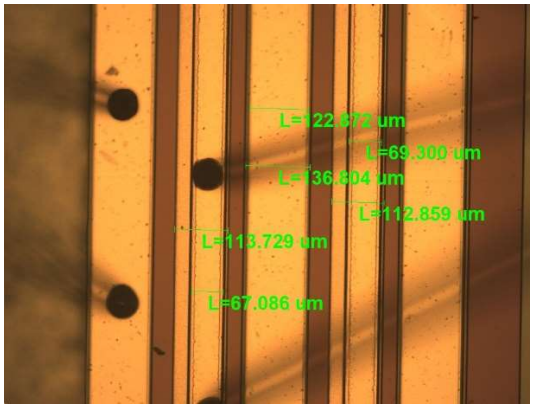

(b)

Figure 5.4 The microscopic image of GaAs/$Al_{0.45}Ga_{0.55}As$ QCL samples with (a) 30μm and (b) 70μm ridge width after fabrication.

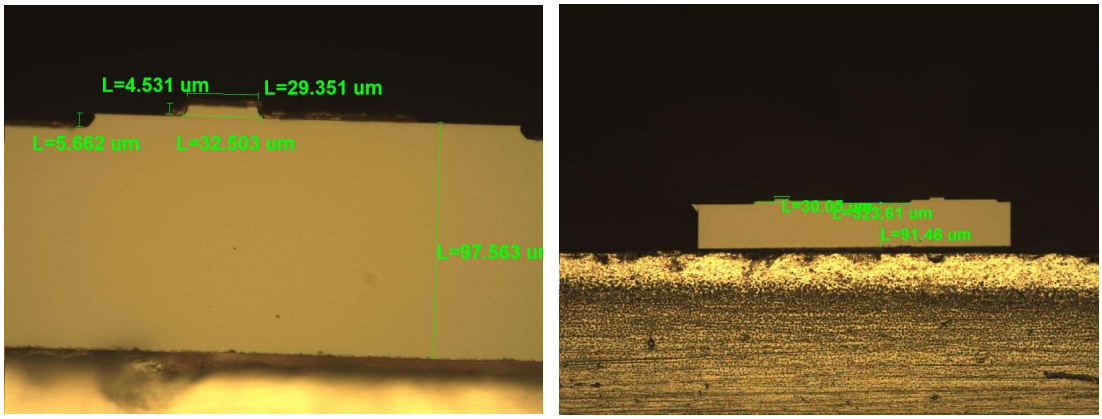

(a) *(b)*

Figure 5.5 The microscope images of the cross section of GaAs-based QCL samples with different resolution: (a) x50 (b) x20.

It is well-known that the thinner substrate is advantageous for heat dissipation in laser applications. Therefore, after fabrication and sample cleaving, the substrate of samples was lapped into around 90 μm, and then bonded onto the top of copper heatsink (shown in Figure 5.5). From the cross-section of samples, the mirror-like facet and well-defined mesa structure of laser devices were confirmed.

5.2.2.2 Result and discussion

Generally, GaAs-based QCLs are difficult to operate at room temperature because of the low thermal conductivity. In this research, we attempted to test the GaAs-based QCLs in room temperature, but even under 0.5% pulse current injection, there was no lasing behaviour. Then, the samples were loaded into duvels and prepared for low-temperature measurement with liquid nitrogen. Following the pumping down and refrigeration, the samples were able to work at 100K.

To measure lasing spectrum, the Fourier spectrometer with 10% pulse (20000hz, 5us) injection current at 90 K was carried out. As shown in Figure 5.6 (a), a peak of lasing spectrum was observed between 1090 and 1098 wavenumber per cm (cm^{-1}), which matches with around 9.15 μm lasing wavelength (Figure 5.6 (b)).

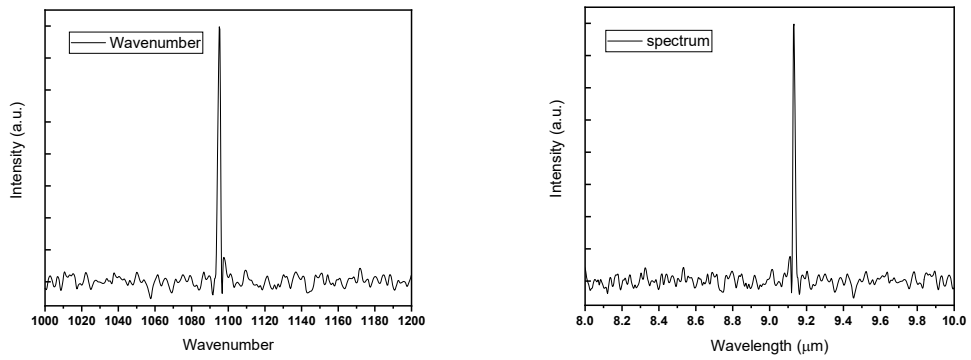

(a) *(b)*

Figure 5.6 The spectrum result of GaAs-based QCL samples with 10% pulse injection current under (a) wavenumber (b)wavelength.

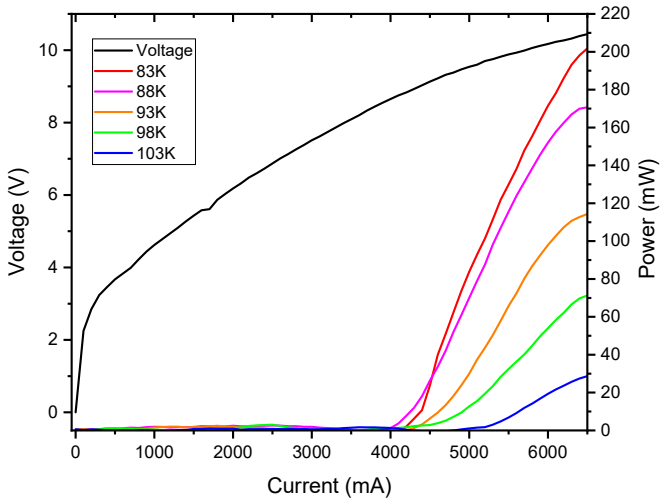

Figure 5.7 The LIV curve of GaAs-based QCL samples at low temperatures under 10% pulse injection current.

Figure 5.7 shows the temperature-dependent LIV curve of the sample with 50 μm ridge width and 4 mm cavity length. Based on 10% pulse (20000hz, 5us) injection current driving, the output power of this GaAs-based QCL reaches 200 mW when the temperature drops to 83 K, and the threshold current is around 4000 mA. With the increase of operation temperature, the property of sample declines conspicuously. The highest operation temperature of GaAs-based sample is only 103 K with the output power of 30 mW. The threshold current density and characteristics temperature were measured to be over 2 kA/cm^2 and 34 K, respectively, indicating a poor temperature stability.

Although the mid-infrared QCL grown on GaAs substrate with GaAs/AlGaAs material system is capable of lasing at low temperatures, the high injection current density and low slope efficiency are still not comparable with other mid-infrared light sources. Besides, the 100 K operation temperature requires duvel (a kind of cryostat) and liquid nitrogen, which hinders the devices packaging and the integration.

5.2.3 InP-based QCLs grown on InP substrate

Since the first QCL devices was designed by Faist et.al in 1994, rapid progress has been made in InP/InGaAs/InAlAs QCLs [15-17]. With the development of III-V semiconductor manufacturing, the InP-based QCLs become more mature and occupy an important position in high-performance mid-infrared light source [17]. Except the material quality, the properties of QCLs are strongly related with fabrication technologies. In this part, we process and measure the InP-based QCLs, and then, different fabrication technologies are applied to InP-based QCL in order to further enhance the device performances.

5.2.3.1 Method and wafer structure

Unlike the GaAs-based QCLs consisting of GaAs and AlGaAs materials, the InP-based QCLs use five different elements (In, Al, Ga, As, and P), e.g., InP waveguide and InAlAs/InGaAs active region. In order, therefore, to avoid material interaction and chamber pollution, both MBE and MOCVD are employed in structure epitaxy instead of all-MBE growth. The 4 μm-thick upper and bottom InP waveguides are grown by MOCVD, and InAlAs/InGaAs active region is grown by MBE. Figure 5.8 shows the epitaxial structure of InP/InAlAs/InGaAs QCL grown on InP substrate. One period of active region consists of 9 repeats of $In_{0.43}Al_{0.57}As/In_{0.6}Ga_{0.4}As$ layers, and whole 40 periods of active region are sandwiched by n-doped 300 nm and 100 nm $In_{0.53}GaAs$ layers. Besides, upper and bottom InP waveguides, 300 nm top InP contact layer and 400 nm InP buffer layer are also grown by MOCVD.

N+ InP 300nm	300nm	5E18 cm^{-3}	**By MOCVD**
N- InP waveguide	4μm	5E17 cm^{-3}	**By MOCVD**
N-$In_{0.53}Ga_{0.47}As$	300nm	4E16 cm^{-3}	
$In_{0.43}Al_{0.57}As$	40 Å		
$In_{0.6}Ga_{0.4}As$	15 Å		
$In_{0.43}Al_{0.57}As$	10 Å		
$In_{0.6}Ga_{0.4}As$	48 Å		
$In_{0.43}Al_{0.57}As$	12 Å		
$In_{0.6}Ga_{0.4}As$	47 Å		
$In_{0.43}Al_{0.57}As$	13 Å		
$In_{0.6}Ga_{0.4}As$	42 Å		
$In_{0.43}Al_{0.57}As$	15 Å		**×40**
$In_{0.6}Ga_{0.4}As$	32 Å		
$In_{0.43}Al_{0.57}As$	17 Å		
$In_{0.6}Ga_{0.4}As$	30 Å		
$In_{0.43}Al_{0.57}As$	18 Å	**1.2E17cm^{-3}**	
$In_{0.6}Ga_{0.4}As$	28 Å	1.2E17cm^{-3}	
$In_{0.43}Al_{0.57}As$	23Å	**1.2E17cm^{-3}**	
$In_{0.6}Ga_{0.4}As$	26 Å		
$In_{0.43}Al_{0.57}As$	34 Å		
$In_{0.6}Ga_{0.4}As$	24 Å		
N- $In_{0.53}Ga_{0.47}As$	100nm	4E16 cm^{-3}	
N- InP waveguide	4μm	5E17 cm^{-3}	**By MOCVD**
N+ InP	0.4μm	5E18 cm^{-3}	**By MOCVD**
N+ doped InP Substrate (3")			

Figure 5.8 The structure of InP/InAlAs/InGaAs QCL grown on InP substrate.

Based on the structure design shown in Figure 5.8, the simulation result of energy level was calculated by software Comsol, and the result was exhibited in Figure 5.9. It is obvious that the intersubband transition of carriers in active region occurs from energy level 6 (Red) to energy level 5 (Blue). The electron energy in these two energy levels is 0.545 eV and 0.361 eV, respectively. Therefore, the wavelength of this InP-based QCL sample is expected to be around 6.74 μm.

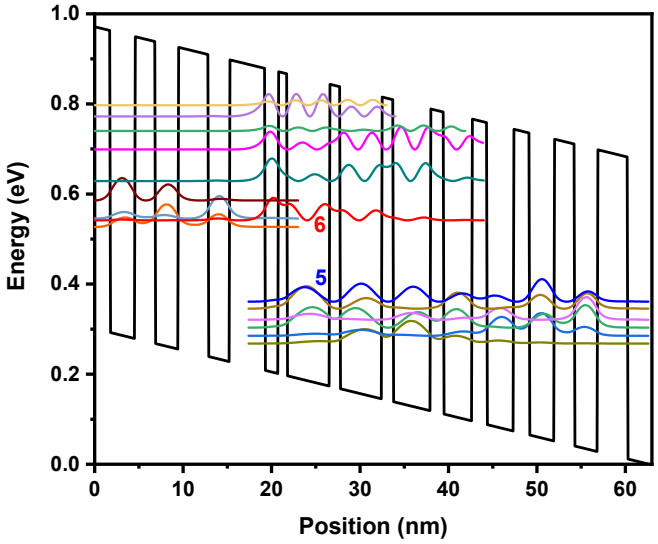

Figure 5.9 The energy level of one period active region of InP-based QCL samples.

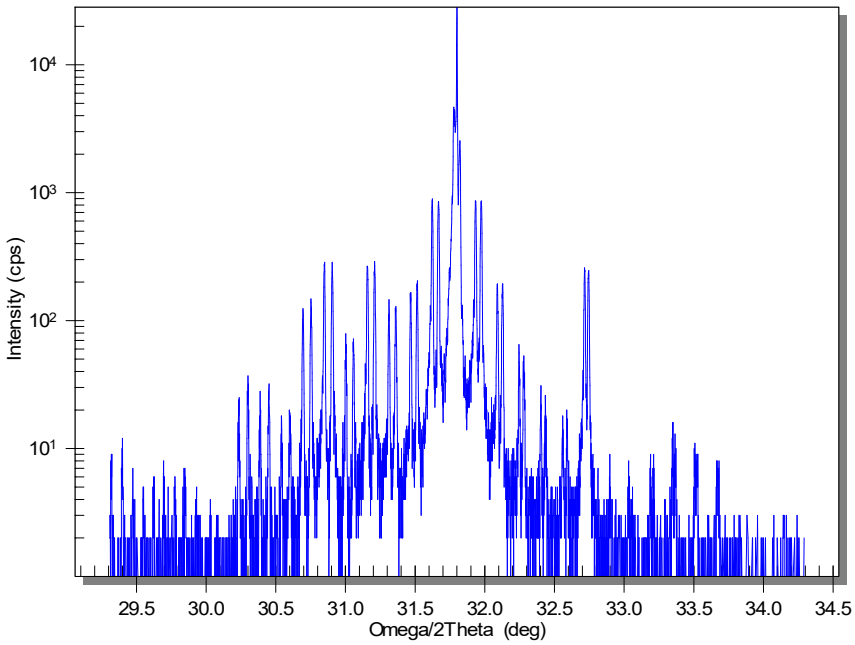

Figure 5.10 The XRD result of InP/In0.$_{43}$AlAs/In$_{0.6}$GaAs QCL sample grown on InP substrate.

The XRD measurement was also performed to investigate the epitaxy quality and the thickness per period by satellite peak spacing. As shown in Figure 5.10, the XRD result shows good symmetry, which means that the surface of each epitaxial layer is flat enough. The distance between each satellite peak indicates that the thickness of each period is around 46.7 nm, corresponding to the designed thickness of 47.4 nm.

5.2.3.2 InP-based QCL with Fabry-Perot (FP)-structure

After the growth, the InP-based QCL samples are processed into typical FP-laser structure with SiO_2, introduced in chapter 2. The ridge structure of laser was formed by chemical etching with H_3PO_4:H_2O_2:H_2O (1:1:10) mixture, as shown in figure 5.11 (a), where the top ridge width is around 10 μm and the width of active region is 15 μm. In order to enhance the heat dissipation, the InP substrate was lapped to around 120 μm, and then, samples are cleaved into 4 mm cavity length and mounted on the copper heatsink, as shown in Figure 5.11 (b).

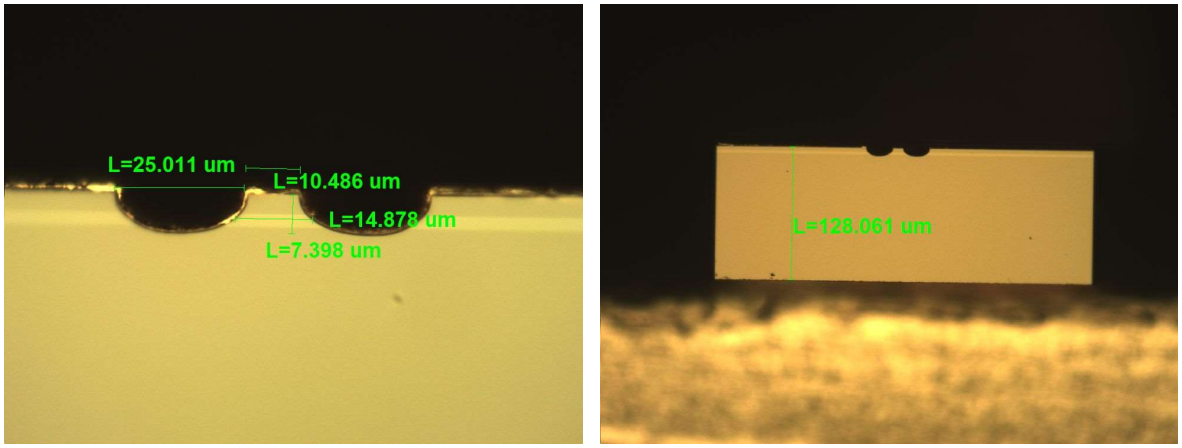

(a) *(b)*

Figure 5.11 The microscope images of the cross section of InP/In0.43AlAs/In0.6GaAs QCL samples with different resolution: (a) x50 (b) x20.

Compared with GaAs-based QCLs, the InP/In0.43AlAs/In0.6GaAs QCLs showed better lasing performance. The InP-based samples could operate at room temperature background. The samples with the active region width (15 μm) and cavity length (4 mm) are measured under 5% pulsed injection current (10000hz, 5us) at 16℃. As shown in Figure 5.12 (a), the threshold current (density) was measured to be around 660 mA (1100 A/cm^2). The lasing spectrum was confirmed by Fourier spectrometer, as shown in Figure 5.12b. The peak of lasing spectrum at an injection current of 700mA is around 6.75 μm, which matches with the designed wavelength of 6.74 μm from the energy level simulation results, and it also proves that the growth of each layer in active region is very accurate.

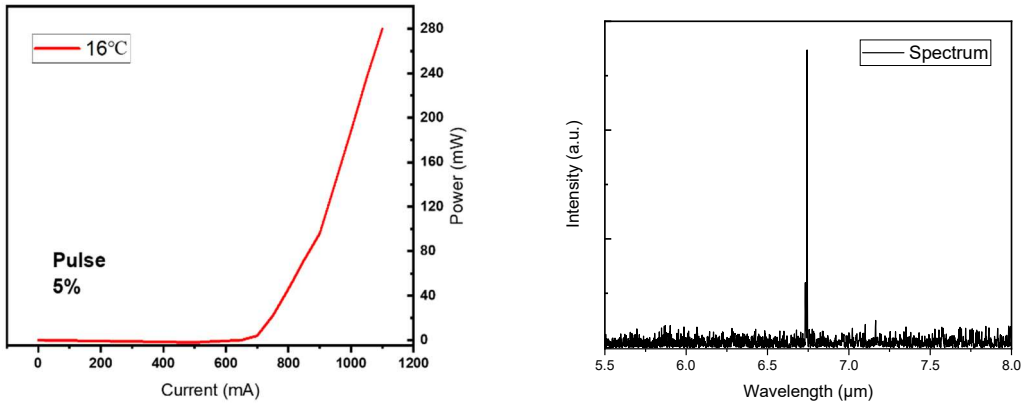

(a) *(b)*

Figure 5.12 (a)The output power verse injection current of InP-based QCL samples. (b)The lasing spectrum images of the InP/In0.43AlAs/In0.6GaAs QCL sample.

In the same fabrication process and FP structure, QCL devices with InP/In0.43AlAs/In0.6GaAs shows much better lasing property than that of GaAs/AlGaAs QCL devices. The result conforms to the expected consequences.

5.2.4 Advanced device fabrication of InP-based QCLs

The fabrication of devices is also very important for high-performance lasers as much as the high-quality material growth. When the optimization of material growth faces to its bottleneck, employing advanced fabrication processes is an effective way to further enhance the performance of laser devices. In this research, flip-chip bonding, anti-reflection (AR)/high-reflection (HR) coatings and buried heterostructure are applied to improve the property of QCL devices.

5.2.4.1 Flip-chip bonding

For the laser applications, the heat released from the laser devices is one of primary degradation mechanisms. Thus, both lapping and mounting processes, which aim to increase the ability of heat dissipation, are commonly employed. However, the substrate cannot be lapped to be less than 80 μm, due to the issues of bending and fragmenting. As shown in Figure 5.13, the substrates of InP-based and GaAs-based devices in this research are lapped to be around 100 μm. Therefore, the distance between the active region and heatsink is over 100 μm. During the operation of laser devices, the active region is a majority heat source. It is noted that the distance

between heat source and heatsink is over 50 times larger than the thickness of heat source, and this will degrade the functionality of heatsink.

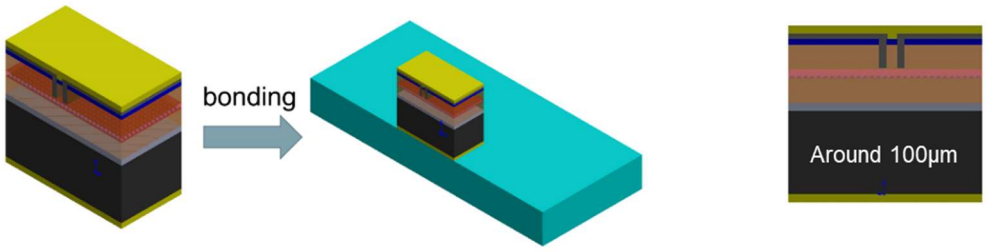

(a) (b)

Figure 5.13 (a)The sketch image of general mounting of laser devices (b) cross-section of sample after lapping.

Software COMSOL could be used to make the simulation of heat dissipation for laser devices. After building the model with actual size of laser devices, each section in the model should be determined the coefficient of heat conduction equal to that of the material in laser devices. Then, the active region should be defined as the heating source since most of the heating in laser devices is generated in the active region. Finally, the heating distribution in the laser model could be calculated by the software.

A heating model was built to simulate the heating distribution in InP-based laser devices with 500 mW output power under room temperature operation. The width of active region and the thickness of InP substrate were designed as 15 μm and 100 μm, respectively. The simulation results are presented in the figure 5.14. The active region temperature reaches 353 K, and it is no doubt that the lasing property will drop with the rising temperature. The simulation result also displays the isothermal contours in laser devices, which is helpful for determining the direction of heat propagation. The isothermal contours in the copper heatsink is quite flat, and the temperature around the top and bottom regions of heatsink is 306 K and 301 K, respectively. Compared with the temperature near the bottom of substrate (309 K), it is obvious that the copper heatsink is ineffective in cooling the laser devices based on this conventional bonding configuration.

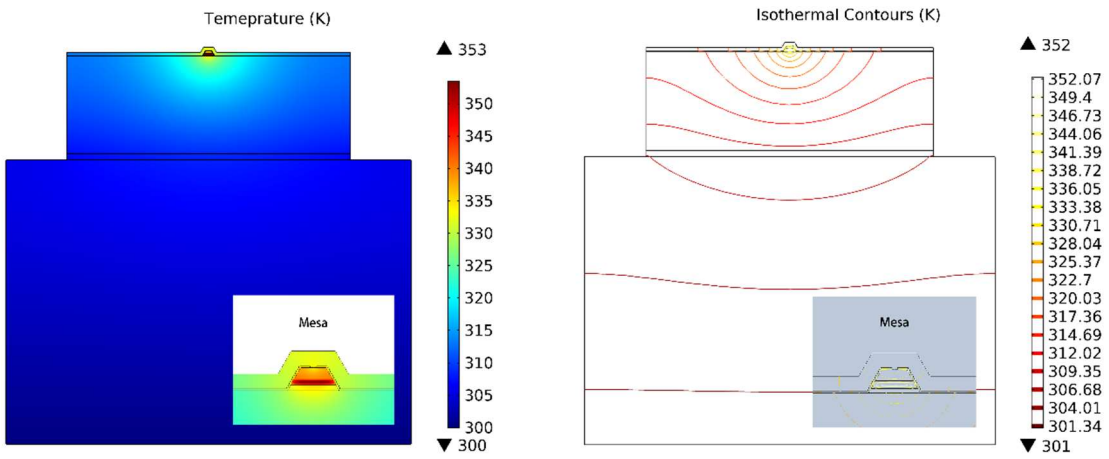

(a) *(b)*

Figure 5.14 The heating distribution simulation result of the laser device with general mounting: (a) heating distribution (b) isothermal contours distribution.

In order to make the active region close to the heatsink and thus improve the heat dissipation, flip-chip bonding technology, in which the top contact region of laser devices is bonded onto the surface of the heatsink, has been widely used. In case of the flip-chip bonding of InP-based QCLs, the distance between the heat source (active region) and heatsink can be reduced to around 5 μm, as shown in figure 5.15.

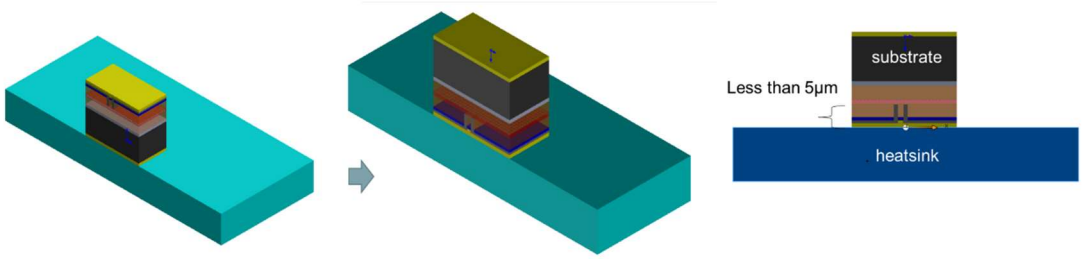

(a) *(b)*

Figure 5.15 the sketch images of (a) laser devices with flip chip (b) the cross-section.

In figure 5.16 (a), the heating distribution with the same parameters of the previous simulation points out that the highest temperature of devices using flip-chip bonding decreases to 336 K. As shown in Figure 5.16 (b), the isothermal contours map also exhibits the improved thermal behaviour. Due to the top surface of heatsink close to active region, the isothermal contours in the upper part of heatsink present the trend of diffusion, which demonstrates that the flip-chip technology could improve the heat dissipation and enhance the property of laser devices.

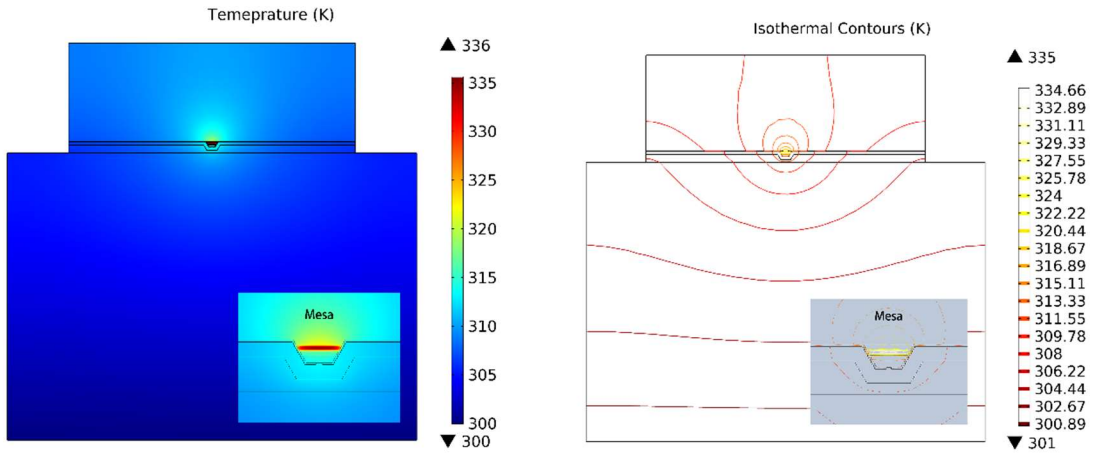

(a) *(b)*

Figure 5.16 The heating distribution simulation result of the laser device with flip chip: (a) heating distribution (b) isothermal contours distribution.

Based on the same InP-based QCL wafer, a group of laser devices are processed with flip-chip bonding configuration. Figure 5.17 shows the cross-section images of flip-chip sample. Compared with the previous laser devices, the mesa shape and cleaving facet are nearly same, and the only difference is the orientation of top contact.

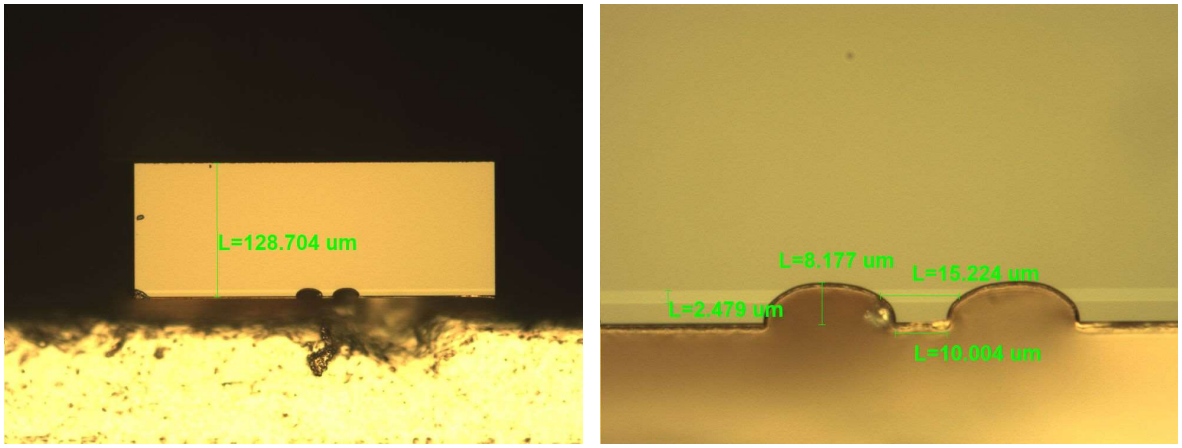

(a) *(b)*

Figure 5.17 The cross-section images of the InP/In0.$_{43}$AlAs/In$_{0.6}$GaAs QCL sample with flip chip fabrication under different resolutions: (a) x20 (b) x50.

The lasing performance matched with the simulation results. As shown in figure 5.18(a), under 5% pulsed driving (10000hz, 5us) and 16℃ operation temperature, the devices (4 mm × 15 um) with flip-chip configuration present lower threshold current of 600 mW and higher output power of 600 mW at an injection current of 900 mA, compared with the devices with conventional bonding structure.

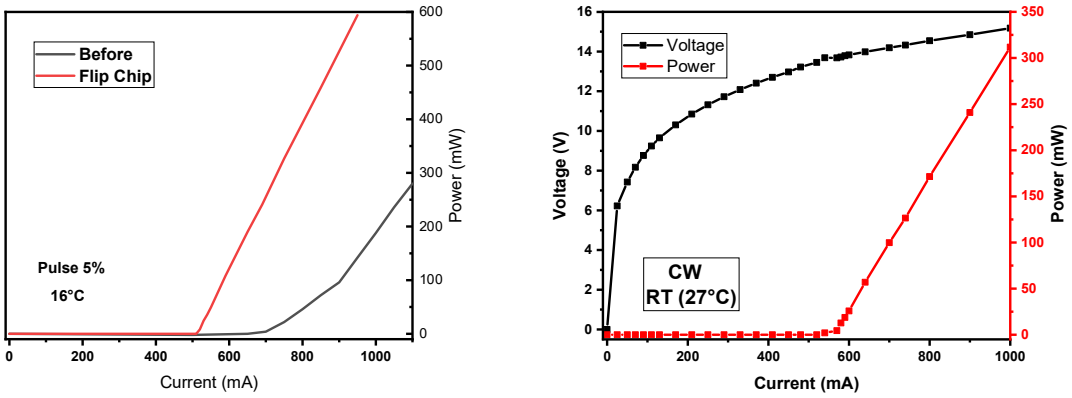

(a) *(b)*

Figure 5.18 (a)the comparison of the output power verse injection current of InP-based QCL samples before and after flip chip. (b)The LIV curve of the InP/In0.43AlAs/In0.6GaAs QCL sample after flip chip.

Figure 5.18(b) shows the LIV curve of the flip-chip bonded QCL under c.w. operation at room temperature. The threshold current and threshold current density are measured to be 580 mA and 966 A/cm^2, respectively. The output power reaches 320 mW at an injection current of 1000mA, and the slope efficiency is 0.714 W/A.

From both theoretical simulation and experiment results, it is confirmed that employing flip-chip technology increases the heat dissipation and thus enhances the lasing properties.

5.2.4.2 High-reflection coatings

Facet coating is another common fabrication technology used to improve the laser performance. As discussed in chapter 1, the facet reflectivity is related with the scattering and mirror loss, and therefore high reflectivity could reduce the mirror loss and increase the operation property. Besides, for the conventional FP laser devices without coating, two facets generate same output power due to the identical reflectivity of two as-cleaved facets. It means that the measured output power from one facet is only around half of whole output power generated in active region. As a result, high-reflective (HR) coating could prevent the light emission in the HR-coated facet, and then concentrate the whole output light to another facet. For an ideal HR coating model, the value of output power could be double after coating. In practice, however, the increased output power is generally less than 80 % because the reflectivity is not able to reach perfect total reflection.

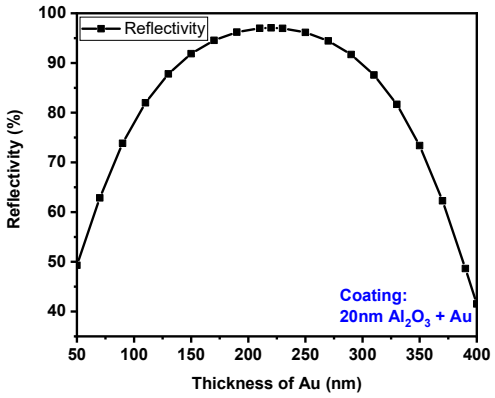

Figure 5.19 The calculated reflectivity for HR coating.

In this research, the coating films are deposited by electron-beam (e-beam) evaporator. The e-beam evaporator in our lab has Al_2O_3, Ge, Ti, and Au sources. Based on these materials, HR coating could be designed. The facet reflectivity depends on the thickness and material properties of films. For the HR coating, the Au is commonly used because of its very high reflectivity in mid-infrared wavelength. In Al_2O_3 and Au coating model, with the increase of Au thickness, the reflectivity gradually increases over 95 % and then shows the falling trend. As shown in figure above, the HR coating could be design by Al_2O_3 and Au films, the peak of the reflectivity curve was calculated to be about 20 nm-thick Al_2O_3 and 230 nm-thick Au films, and this material combination was applied in this research.

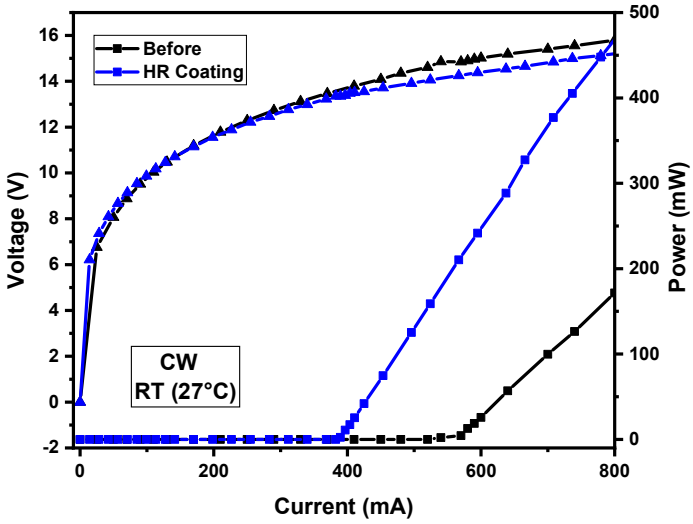

Figure 5.20 The LIV curves of InP-based QCL samples without and with HR coating.

As a result of the HR coating and flip-chip bonding on the heatsink, the InP-based QCL obtains further improvement in the lasing performances. Figure 5.20 shows the LIV curves of the samples with HR coating and flip-chip bonding, compared with the samples with only flip-chip bonding. The threshold current of the sample with HR coating decreases from 580 mA (with only flip-chip bonding) to 380 mA, corresponding to the threshold current density of 633 A/cm^2. Also, the output power was 480 mW at an injection current of 800 mA, and the slope efficiency reaches 1.14W/A, which is 1.6 times higher than that of the sample with only flip-chip bonding.

As expected, the use of AR and HR coatings significantly decreases the threshold current density and improve the slope efficiency by 60%.

5.2.4.3 Regrowth Fe-doped InP waveguide

Generally, the laser devices are fabricated with mesa shape because of the simple and mature fabrication process. For the mesa structure, however, the side wall of active region is cover by SiO_2, resulting in the poor heat dissipation around the side wall due to the low thermal conductivity of SiO_2. In order to achieve better heat dissipation, a buried heterostructure, using semi-insulating III-V material instead of SiO_2, was adopted. Namely, after mesa etching, Fe-doped InP was regrown by MOCVD to form a buried heterostructure. In this research, the doping level of donor Fe in regrowth InP is 2x10^{16}/cm^3 under 500℃ growth temperature to form the semi-insulating InP. As shown in figures 5.21, because the regrowth material is the same material with waveguide and active region, the regrowth area could be merged with laser mesa, which contributes to apportion the heating generated in active region.

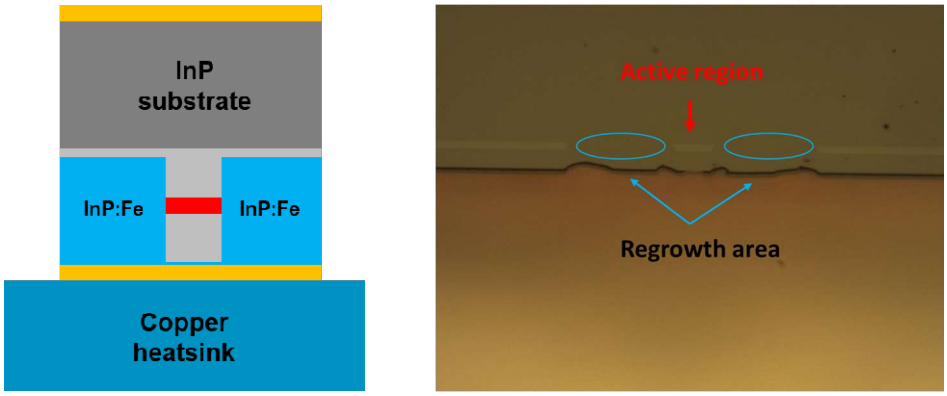

(a) *(b)*

Figure 5.21 (a) the sketch map and (b) cross-section microscope image of InP-based QCL samples with buried heterostructure.

The width of the active region is around 15 μm. The heating simulation model was also carried out to study the heating distribution of InP-based QCLs with both flip-chip bonding and buried heterostructure.

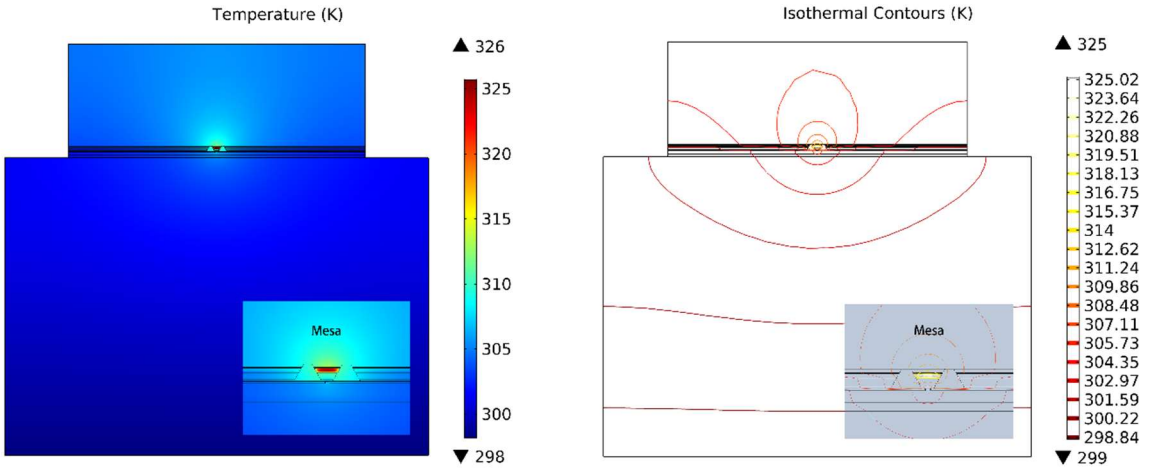

(a) *(b)*

Figure 5.22 the heating distribution simulation result of the laser device with buried heterostructure: (a) heating distribution (b) isothermal contours distribution.

The simulation results show that the buried heterostructure is useful for heating dissipation in active region. As demonstrated in figure 5.22 (a), the highest temperature further decreases to 326 K, which is only 26 ℃ higher than room temperature. Compared with the 353 K in conventional FP laser fabrication, the increased temperature in buried heterostructure is only around half of that of old structure. In isothermal contours mapping, the surrounding isothermal contours of active region are more concentrate. The isothermal contour crosses both regrowth InP area and InP waveguide shows no obvious winding, which also proves that the regrowth of Fe doped InP avoids the impeding of heat dissipation and leads to the increase of proportion of cooling part in active region.

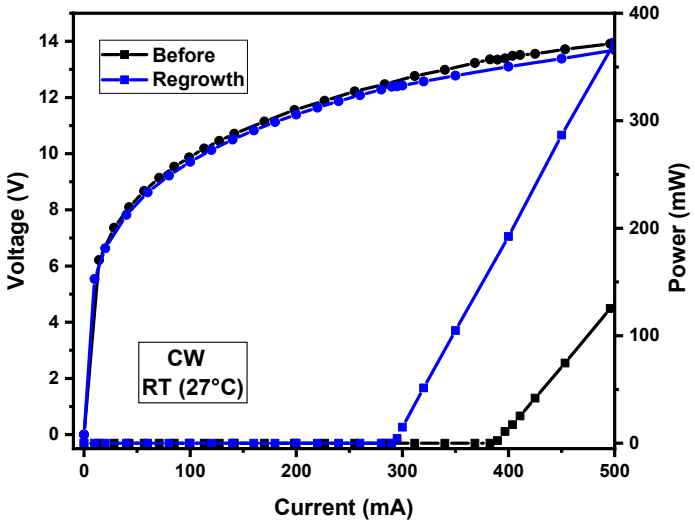

Figure 5.23 The LIV curves of InP-based QCL samples without and with buried heterostructure.

Together with the HR coating, a group of InP-based QCL samples are fabricated into buried heterostructure instead of mesa structure. As shown in Figure 5.23, the LIV characteristic of this sample was measured under c.w. operation at room temperature, and the results were compared with those of only HR-coated sample presented in last section. The threshold current (density) was measured to be only 290 mA (806 A/cm^2), and the slope efficiency rises to 1.73 W/A which is improved by nearly 50%.

As a result, the performance of laser devices could be significantly enhanced by utilizing the buried heterostructure which is formed by regrowth of semi-insulating InP. The regrowth of Fe-doped InP could fit with the InP waveguide and share the heating generated in active region, increasing cooling effect and improving the laser property.

5.2.4.5 Result and discussion

The previous section demonstrates three advanced fabrication technologies for improving the laser performances. The InP-based QCLs obtain remarkable improvement in device performances owing to the flip-chip bonding, AR/HR coating, and buried heterostructure. The cross-section image of InP-based QCL samples after fabrication is shown in figure 5.24. The width of active region is around 15 μm, and the InP substrate is lapped to around 140 μm thickness. Figure 5.24b shows the Fe-doped InP regrowth area integrated with InP waveguide and InP substrate smoothly which means the InP regrowth is success, and the flat as-cleaved facet is also the guarantee for high-quality facets.

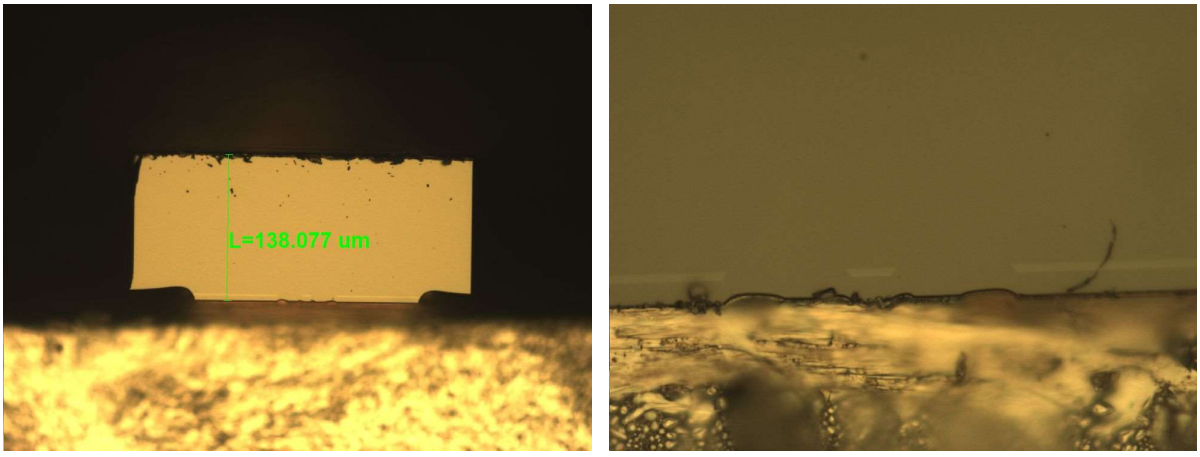

(a) (b)

Figure 5.24 the cross-section images of InP-based QCL samples after continuous improvement under different resolutions: (a) x20 (b) x100.

Figure 5.25(a) exhibits the LIV curve of the QCLs under c.w. operation at 16 ℃. The fabricated QCL produces threshold current (density) of 280 mA (700 A/cm^2) and output power of 600 mW at an injection current of 600 mA. As the power saturation is not observed up to the injection current of 600 mA, the maximum output power is expected to achieve higher value. In addition, a high slope efficiency of 1.86W/A was achieved. The lasing spectrum is also shown in Figure 5.25(b). The peak of spectrum confirmed the emission at 6.75 μm wavelength, which is consistent with the earlier results and designed energy level.

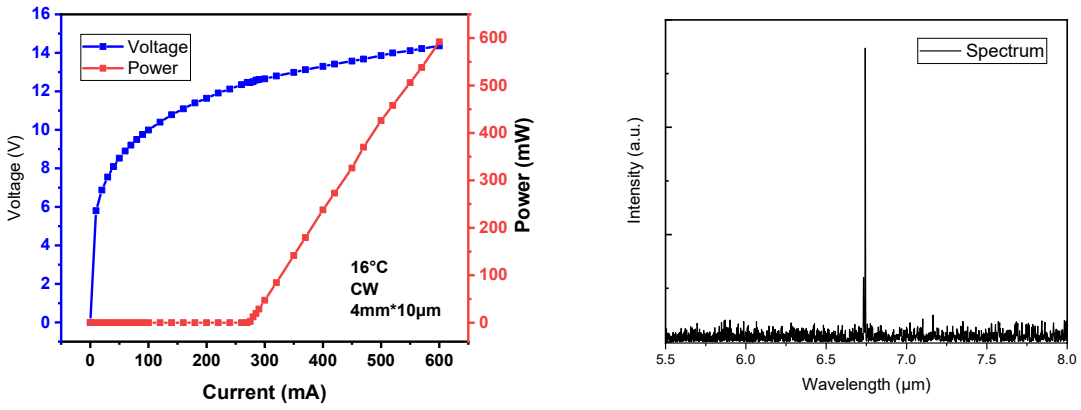

(a) (b)

Figure 5.25 (a) the LIV curve and (b) the spectrum result of improved InP-based QCL samples.

The temperature-dependent output power was measured under c.w. mode in the range from 16℃ to 100℃. It is noted that with the temperature increase to as high as

100℃, the threshold current rises from 280 mA to 520 mA, and slope efficiency slightly decrease to 1.23 W/A. Under 100℃ operation temperature, the output power still attains over 270 mW without saturation trend, and it could be predicted that the highest operation temperature would be much higher than 100℃. As can be seen in figure 5.26, the temperature rise could not cause the apparent degradation in threshold current and slope efficiency, implying that the devices have great temperature stability.

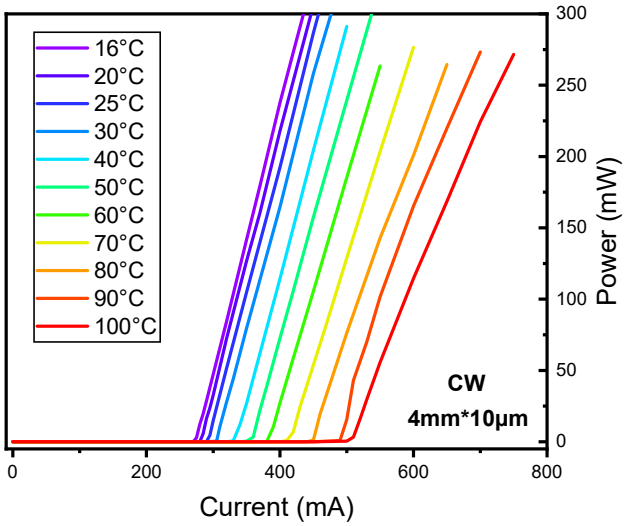

Figure 5.26 the temperature dependence result of improved InP-based QCL samples under c.w. mode.

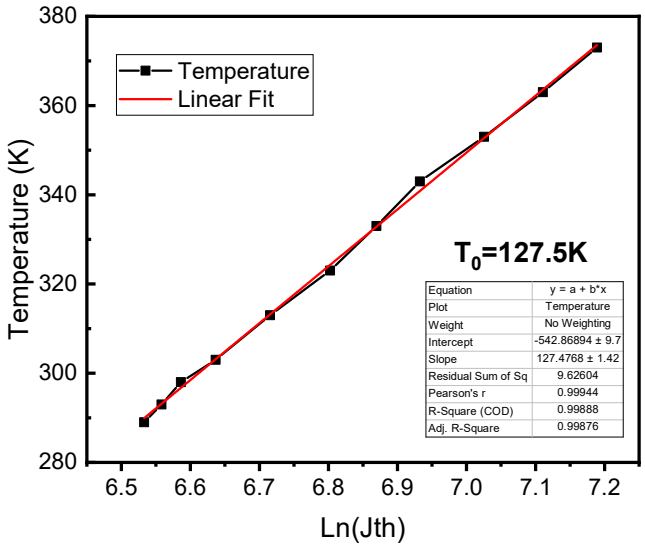

Figure 5.27 the curve used to calculate the characteristic temperature of the InP-based QCL sample.

According to the characteristic temperature calculation expounded in chapter 2, threshold current under different temperature in this research is used to calculate T_0. As shown in Figure 5.27, the slope of curve points out that the T_0 value achieves 127 K which is an outstanding result for QW devices.

5.2.5 Conclusion

In this chapter, both GaAs-based and InP-based QCLs are fabricated. Because of the limitation of lower energy barrier and poor heating dissipation of GaAs material in principle, the performance of GaAs-based QCLs is not as good as that of InP-based QCLs. From the comparison of GaAs-based and InP-based QCL devices in this chapter, it is confirmed that the material system and material quality are the crucial condition of laser devices. Besides, the advanced fabrication technologies are able to significantly enhance the performance of laser devices. For the InP-based QCLs, the advanced fabrication technologies, including Flip-chip bonding, AR/HR coatings, and buried heterostructure with Fe-doped InP, are employed in order to further enhance the performances of the conventional FP QCLs. The flip-chip bonding and buried heterostructure significantly enhanced the capacity of heat dissipation, and the HR/AR coatings enable an efficient single facet lasing with reducing mirror loss. As a result of the advanced fabrication improvements, high-performance c.w. InP-based QCLs at room temperature with low threshold current density (700 A/cm^2), high output power (600 mW) and slope efficiency (1.86W/A) were demonstrated. In addition, the maximum operation temperature of at least 100 ℃, limited by the temperature controller, indicates the extreme temperature stability. The continuous manufacturing improvement is useful not only for QCL devices shown in this chapter, but also for other laser devices and further works.

5.3 Quantum dot cascade laser

5.3.1 Background theory

The QD material for laser applications has many unique characteristic such as high temperature stability, low threshold current, insensitivity to dislocations, and high differential gain as mentioned in chapter 1. Thus, the quantum dot cascade laser (QDCL) is expected not only to improve the performance of QCL devices, but also to realize Si-based QCL for mid-infrared silicon photonics. In particular, for QCL devices, QD material also has more value in terms of broaden gain spectrum and high

population inversion efficiency [18-20]. Since the conventional QCL has the narrow gain spectrum due to its mechanism based on the intersubband transition, the broaden gain spectrum of QD material could make up this limitation [21,22]. In addition, the three-dimensional quantum confinement of QD could reduce the in-plane scattering paths, and therefore increase the carrier lifetime in high energy level and improve the wall plug efficiency [23]. Moreover, the QD also has the potential to overcome the limitation of only TM mode lasing in QCL devices with FP structure. The unique potential of multi-direction output in QD material enables QDCL to fill up the lack of surface emitting quantum cascade laser (SEQCL) without Bragg grating or photonic crystals [24-28]. Therefore, the QDCL is recognized as a propitious candidate for next-generation mid-IR light source.

In this chapter, the InP-based QDCL lasing at around 7.2 μm wavelength under room temperature and c.w. mode current injection was demonstrated. To optimize the QDCL structure, we investigated the effect of the number of QD layers in one period on the device performance. The comparison of QDCLs with different QD layers per period points out that the two-layer QD per period could offer the best performance, and this result matches with the simulation results. The optimized QDCL showed the comparable performance with typical quantum-well (QW)-based QCL, and the lasing operation with TE-mode was first demonstrated without Bragg gratings or photonic crystals.

5.3.2 The mechanism in QDCL and QCL

5.3.2.1 Energy level and inter-subband transition

Generally, the in-plane movement of carriers degrades the lasing property of QCL devices [29]. For the conventional QW-QCL device, the in-plane movement of electrons, caused by the only one-dimensional quantum confinement in the QWs, has fundamentally limited the intersubband transition rate [30]. As shown in the figure 5.28, the electrons in upper state (C2) of QW-QCL can transit to lower state (C1) instead of intersubband transition. The in-plane motion offers the non-radiative transition only related with phonon energy, leading to the drop of recombination efficiency. In contrast, the 3D quantum confinement of QDCL generates the separate energy state, and this unique character could limit the in-plane dispersion though phonon bottleneck effect [23]. In addition, since the in-plane movement of carriers needs energy difference matching with integer multiple phonon energy (35 meV for each phonon), this condition

effectively prevents the in-plane movement [31]. Therefore, the reduced in-plane carrier movement could increase the carrier lifetime in higher state, resulting in the increase of population inversion efficiency in QDCL.

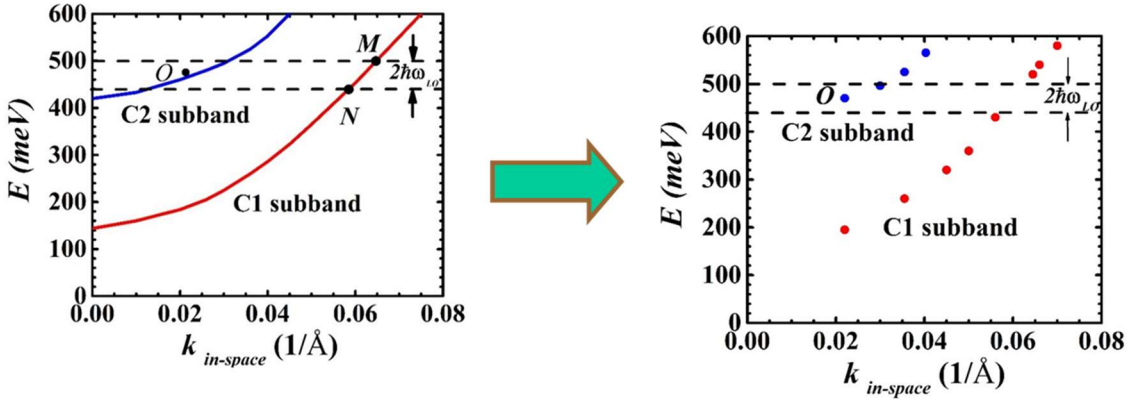

Figure 5.28 The carrier transition in QCL and QDCL devices. The in-plane movement from origin position O to point M or point N by absorbing or emitting phonon (left) could be avoided after utilizing QDCL design, since the energy state in QD is separated (right) and the energy gap is difficult to match the integer multiple of phonon energy [31].

As mentioned above, in principle, 3D quantum confinement of QDs offer better population inversion efficiency than QW, leading to higher slope efficiency and better performance [23]. However, the growth of ideal uniform QDs is still difficult to achieve, so that the current QDCL could not show impressive lasing property [31,32].

5.3.2.2 TE mode and SEQCL

The QCL lasing theory, based on the intersubband transition of electron, offers long wavelength optical output but limits the lasing direction. In quantum mechanics, the transition probability W_{if} of electron from initial state (i) to final state (f) based on the Fermi's golden rule [33, 34]:

$$W_{if} = \frac{2\pi}{\hbar} |z_{if}|^2 \, \delta(E_f - E_i \pm \hbar w_{LO})$$

where δ is the density of state, E_f and E_i means the energy of initial state and final state, $\hbar\omega_{LO}$ is the energy of one phonon, so the $\delta(E_f - E_i \pm \hbar\omega_{LO})$ is density of state under the transition energy. Z_{if} is the matrix element which stated as the transition intensity from initial state i to final state f, it is named as transition element and it could be defined as [35-37]:

$$z_{if} = \langle \varphi_i(r) | e \cdot p | \varphi_f(r) \rangle$$

The φ_i and φ_f are the envelope function in initial state i to final state f which used to envelope approximate the wave function and could define the carrier transition into quantization. Due to the carrier in intersubband transition in QCL devices is electron, the e and p instead of the energy and momentum of electron. After spreading the envelope function into vector function (u) and probability function (f) in transition element, the Z_{if} could be written as [36, 38]:

$$z_{if} = e\cdot\langle u_i(r)\,|\,p\,|\,u_f(r)\rangle\langle f_i(r)\,|\,f_f(r)\rangle + e\cdot\langle u_i(r)\,|\,u_f(r)\rangle\langle f_i(r)\,|\,p\,|\,f_f(r)\rangle$$

Because the initial state and final state in intersubband transition are located in the same energy band, the left section in the last equation is zero, and the value of $\langle u_i(r)|u_f(r)\rangle$ in the right section in previous equation is 1, so the transition intensity Z_{ij} could be calculated as [35, 38]:

$$\begin{aligned}
&z_{if} = \langle f_i(r)\,|\,e\cdot p\,|\,f_f(r)\rangle \\
&= \frac{1}{A}\int d^3r e^{-ikr}\delta_i^*(z)(e_x p_x + e_y p_y + e_z p_z)\delta_f^*(z) \\
&= \frac{1}{A}(e_x p_x + e_y p_y)\int d^3r e^{-ikr}\delta_i^*(z)\delta_f^*(z) + \frac{1}{A}e_z\int d^3r e^{-ikr}\delta_i^*(z)p_z\delta_f^*(z) \\
&= \sigma_{if}\sigma_{kk'}(e_x\hbar p_x + e_y\hbar p_y) + \sigma_{kk'}e_z\int dz\delta_i^*(z)p_z\delta_f^*(z)
\end{aligned}$$

Because of i≠f in the intersubband transition of QCL, the sigma function σ_{if}=0. As a result, the transition element could be simplified as follow:

$$z_{if} = e_z\int dz\delta_i^*(z)p_z\delta_f^*(z)$$

So, the transition element is only influenced by the vector in Z direction which is the growth direction. Because in Fermi's golden rule only transition element Z_{if} is related with vector and other section is only the quantitative value, therefore, it means that the intersubband transition is only related to epitaxial direction (Z), and both radiation and absorption are TM polarized. As a result, in the classical QCL with QW active region, the propagated radiation is limited in the QW plane, and thus the surface emitting quantum cascade laser (SEQCL) cannot be obtained, despite various advantages of surface emission such as stable single mode, easy packaging and better beam quality [30]. At present, various approaches, including second order Bragg gratings and photonic crystal structures, have been developed to achieve SEQCL [22,39]. However, the complex fabrication and regrowth steps, required for fabrication of grating and

photonic crystals, reduce the yield and increase the cost. In this regards, QD material has a unique potential in multi-direction output, which is of great importance for achieving surface emission [40]. More specifically, by combining the anisotropy of QDs in QDCL and vertical-cavity structure, a SEQCL without Bragg grating and regrowth could be obtained.

5.3.3 High performance QDCL grown on InP substrate

5.3.3.1 The design of laser structure

As mentioned in chapter 5, the InP-based QCL sample has better performance than that of GaAs-based samples, and thus the design of QDCL in this research adopts the InP/InAlAs/InGaAs material system with the InAs/GaAs dot-in-well structure in active region. As shown in figures 5.29, the QDCL consists of the upper and lower N-doped waveguides grown by MOCVD and active region grown by MBE. In each period of active region, 3 groups of InAs/GaAs QD layer are sandwiched by 8 couples of $InAl_{0.44}As/InGa_{0.6}As$ layers. Noted that the total number of periods in QDCL is less than that of QW-QCL because 3.5 nm InGaAs capping layer is not able to fully release the strain caused by QD, which limits the total thickness of active region.

N+ InP	850 nm	~ 5 E18cm^{-3} (MOCVD)	
N InP	150 nm	~ From 1 E17cm^{-3} to 3 E17cm^{-3} (MOCVD)	
N- InP	3 μm	~ 4 E16cm^{-3} (MOCVD)	
N-$In_{0.53}Ga_{0.47}As$	300nm	~ 4 E16cm^{-3} (MBE)	
$In_{0.44}Al_{0.56}As$	36.6 Å		×32 (MBE)
$In_{0.6}Ga_{0.4}As$	17.1 Å		
$In_{0.44}Al_{0.56}As$	9.2 Å		
$In_{0.6}Ga_{0.4}As$	36.2 Å		
InAs	*QD-3*		
GaAs	7.7 Å		
$In_{0.44}Al_{0.56}As$	10.2 Å		
$In_{0.6}Ga_{0.4}As$	34.2 Å		
InAs	*QD-2*		
GaAs	7.2 Å		
$In_{0.44}Al_{0.56}As$	12.7 Å		
$In_{0.6}Ga_{0.4}As$	32.2 Å		
InAs	*QD-1*		
GaAs	6.7 Å		
$In_{0.44}Al_{0.56}As$	14.9 Å		
$In_{0.6}Ga_{0.4}As$	32.1 Å		
$In_{0.44}Al_{0.56}As$	17.7 Å		
$In_{0.6}Ga_{0.4}As$	29.5 Å		
$In_{0.44}Al_{0.56}As$	23.3 Å		
$In_{0.6}Ga_{0.4}As$	29.1 Å	1.5×10^{17}cm^{-3}	
$In_{0.44}Al_{0.56}As$	31.5 Å	1.5×10^{17}cm^{-3}	
$In_{0.6}Ga_{0.4}As$	28.4 Å		
N- InP	3 μm	~ 2 E16cm^{-3} (MOCVD)	
N- InP	2 μm	~ 4 E16cm^{-3} (MOCVD)	
N+ InP	substrate	~ 2 E17cm^{-3} (substrate)	

Figure 5.29 the structure of InP-based QDCL samples with 3 layers InAs/GaAs QD.

Based on the structure design and thickness of epitaxial layers shown in Figure 5.29, the energy level simulation of active region was calculated and plotted in Figure 5.30. In this bound-to-continuum design, the lasing property is directly related with the electron transition from subband 8 (red) to subband 7(green). From this simulation, the electron energy states of subband 7 and 8 are calculated to be 358.5 meV and 539.1 meV, respectively, as a result, corresponding to the emission wavelength of 6.9 μm.

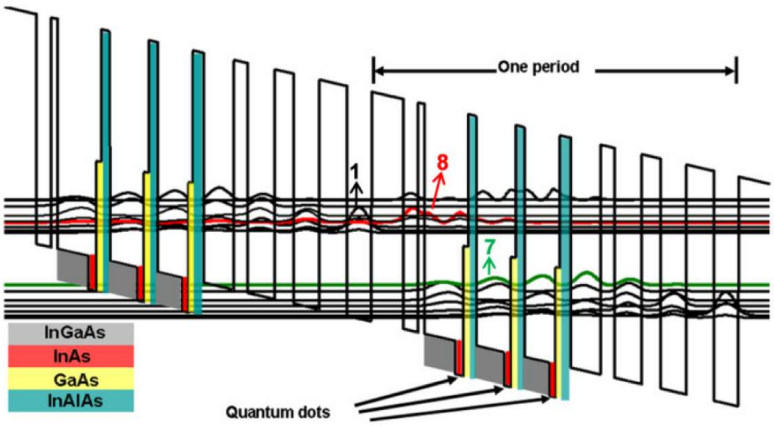

Figure 5.30 the energy level of one period active region of InP-based QDCL samples.

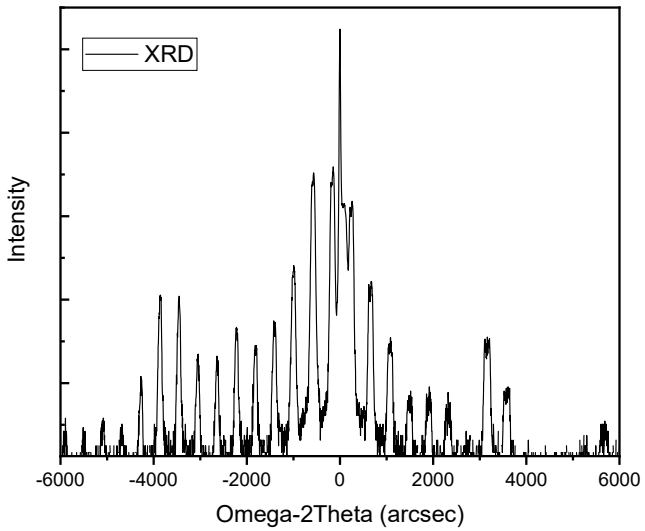

Figure 5.31 the XRD result of InP-based QDCL samples.

After sample growth, a small piece of wafer is cleaved for XRD measurement. In figure 5.31, the XRD result shows eligible symmetrical, although the symmetric is not ideal because of the influence of strain. The thickness of calculated period from XRD is

around 42.6 nm, which is nearly matched with the designed thickness of 41.8 nm, as shown in Figure 5.29. Consequently, the growth of QDCL sample meet the expectation.

5.3.3.2 Sample fabrication

Afterwards InP-based QDCL wafer growth, the wafer was fabricated to FP-laser structure. As the materials consisting of QDCL are similar with those of InP-based QCL, the fabrication of QDCL follows the same processes discussed in chapter 5.2.4, including flip-chip bonding, AR/HR coatings, and buried heterostructures. After wet etching (H_3PO_4:H_2O_2:H_2O = 1:1:10) and Fe-doped InP regrowth, the ridge width of active region (7.5 μm) was formed (Figure 5.32). Then, the InP substrate was finally lapped into around 140 μm thickness for heat dissipation and easy facet cleaving. After lapping, samples are cleaved into 4 mm cavity length and mounted on top of the copper heatsink. From the cross-section image of the fabricated QDCL, the active region shows great colour identification with InP waveguide, and the facet has no visible roughness.

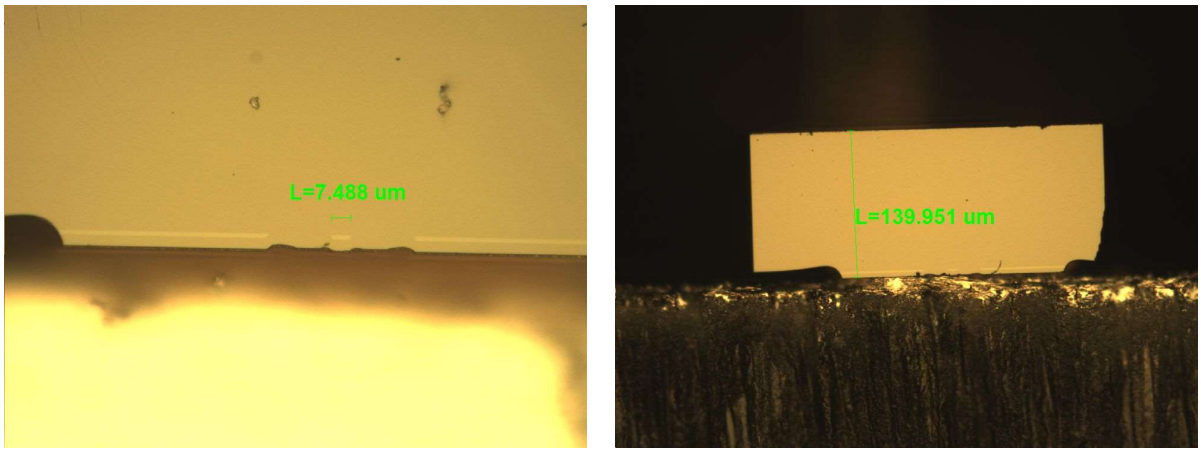

(a) *(b)*

Figure 5.32 the cross-section image of the InP-based QDCL sample after fabrication.

5.3.3.3 Result and discussion

The measurements of the QDCL samples are based on the same setup and operation with QCL measurements reported in chapter 5.2. The LIV measurements of the QDCL samples are tested under 10% pulsed injection current (20000 Hz, 5us) at different operation temperatures. The temperature dependence LIV curve from 15℃ to 45℃ is plotted in Figure 5.33 (a) at the background temperature of 15℃, the output power reaches around 250mW at an injection current of 1100 mA, and the threshold current (density) is measured to be 700 mA (1.94kA/cm^2). With increasing operation

temperature, the threshold current rises to over 1000 mA, and the highest output power drops to 50 mW at the temperature of 45℃. Although this LIV properties are not comparable with that of InP-based QCL devices shown in chapter 5.2, the low threshold current density less than 2 kA/cm^2 at room temperature and the highest operation temperature of 45℃ are promising results among QDCL publications [36].

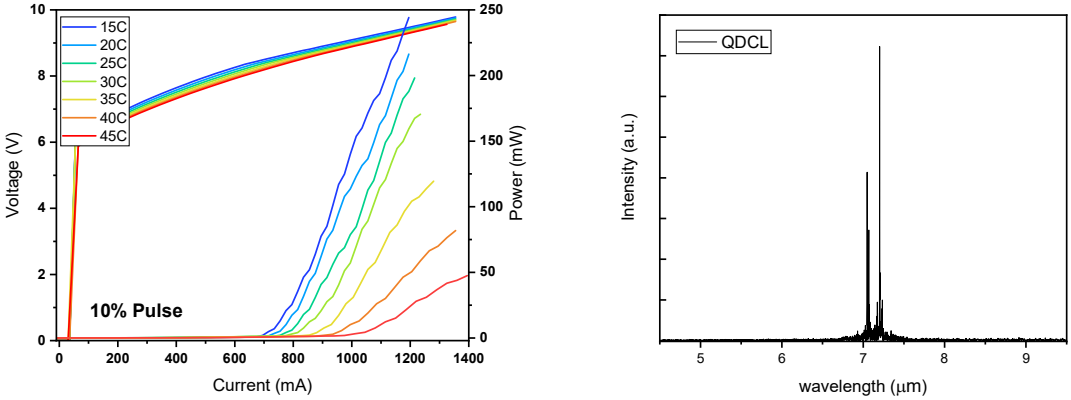

(a) *(b)*

Figure 5.33 the temperature dependence result of the InP-based QDCL sample with 10% pulsed driving. (b) the spectrum of QDCL sample with 3 layer QD per active region period.

The lasing spectrum was measured by Fourier spectrometer. Figure 5.33 (b) shows the emission spectrum of the QDCL at an injection current of 800 mA and operation temperature of 15℃. Two peaks prove the lasing operation of the QDCL samples, and the positions of these two peaks correspond to the lasing wavelengths of 7.05 μm and 7.2 μm, respectively. The measured lasing wavelengths are red-shifted by 0.15 μm and 0.3 μm from the designed wavelength of 6.9 μm, which can be ascribed to non-ideal QDs. The active region structure of QDCL is comprised of three-layer QDs in one period, and the separation between QD layers is around only 5 nm, which is insufficient to release the strain caused by QDs. Thus, the residual strain in active region leads to the formation of various shapes of QDs, rather than uniform QDs, resulting in different wavelengths. Besides, the growth of high-quality QDCL is far nire challenging than that of QW-based QCL because of a number of QD layers. Namely, it is difficult to grow many QD layers because of both the strain release and the stability of beam rate during the growth. In this research, the period number of QDCL active region is 32, which is larger than all QD growth technology and reports. Therefore, the existence of inhomogeneous QD is inevitable in QDCL.

In conclusion, the QDCL with 3 QD layers in one period achieved the threshold current density of 1.94 kA/cm^2 and output power of 250 mW under pulse operation at 15℃. Also, the highest operation temperature of 45℃ was observed. Even though the QDCL has shown its several advantages, it could not show the excellent lasing properties as expected as in the principle design, due to the limitations such as the number of QD layers. With the improvement of growth technology and the optimization of QDCL structure, it is reasonable to believe the performance of QDCL could be qualitatively improved soon after.

5.3.4 Optimization and mechanism research

5.3.4.1 The simulation and optimization of QDCL

The precise design and simulation of energy states in QCL are essential preparation because the population inversion of intersubband transition requires the accurate match of energy states to offer the electrons pump in high energy state. Nevertheless, the simulation of QDCL in present work still uses QCL simulation model by which the energy state of QDCL could be replaced by the equivalent QCL energy state. Although several superior results are reported under this design form, the QDCL energy state after equalling is not an extremely accurate mode, because there is only one-dimension quantum confinement considered in normal QCL simulation rather than three-dimension confinement in QDCL. The electron dynamics in the other two dimensions is incomparable with that of the majority dimension, but the exist confinement will still influence the energy state to a certain extent. Therefore, it is reasonable that there may be a slightly deviation of the practical energy states compared to the ideal state, and for QCL energy state design, this tiny mismatch could lead to the drop of the operation property.

To realize the high performance QDCL, the match of injection area energy state and upper laser state is necessary since it ensures the population reversal efficiency. In this research, the inhomogeneous QD is utilized to optimize energy state design. The growth of QD is always accompanied by the release and accumulation of strain, the thin capping layer and barrier layer between QD layers are not able to exhaustively release the strain, after strain accumulating, it will lead to slightly enlarge for upper QD and form a closely energy state with the origin state [16, 24]. Multilayer of QD coupled these energy state and generate a miniband instead of single energy state [16, 24]. With the increasing of layer number, the energy miniband will be broaden. Inspired by

this phenomenon, a proposal of epitaxy multilayer QD with thin capping layer in each period of QDCL has been put forward to offer broaden miniband for energy state match, and it results in energy state in active region will be easier to match the energy state in injection area. As a result, the multilayer QD is put forward to broaden the energy miniband and effectively reduce the influence of energy state mismatch, and then benefit the alignment of energy state to increase the injection efficiency.

However, with the rise of QD layer number, multilayer QD structure could offer better energy state coherence for carrier injection, it should also face to the wrinkle comes from the unreleased strain. The TEM results of one QD layer and three QD layer are shown in Figure 5.34. It is obviously that the active region with three-layer QD has interface undulation caused by the accumulating strain, and in contrast, the single layer QD exhibit perfect interface flatness. Besides, the QD shape changing is also observed in three-layer QD structure. Based on these statements, the existing of strain accumulation and coupled energy miniband in multilayer QD structure meet the previous expectation. Since the multilayer QD design lead to both advantages and disadvantages for QDCL, it points that the number of QD layer per period is a key parameter in the adjustment of active region design.

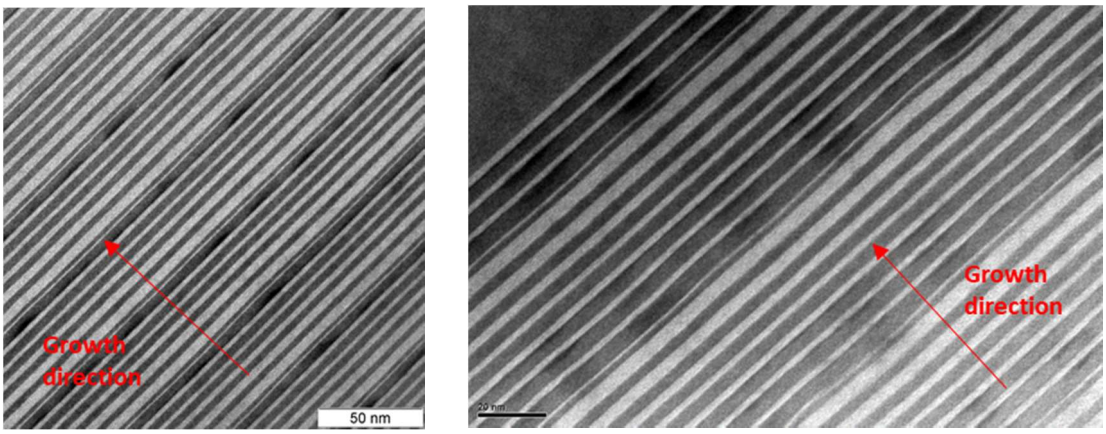

(a) *(b)*

Figure 5.34 the TEM image of the InP-based QDCL sample with (a) 1 layer and (b) 3 layer QD per period.

The different QD layer numbers lead to the changing of active region thickness, as a result, the relationship between injection efficiency, carrier lifetime and active region thickness changing is simulated and the results is demonstrated in Figure 5.35. The carrier lifetime (τ) slight decreases with the increase of active region thickness and the

injection efficiency (η_{inj}) are fluctuated between 62.5% and 64.5%. After calculating, the variation thickness is unable to effectively change the η_{inj}/τ, consequently, the different thickness in active region with 1, 2 and 3 QD layer structure will not cause the obvious changing in laser property.

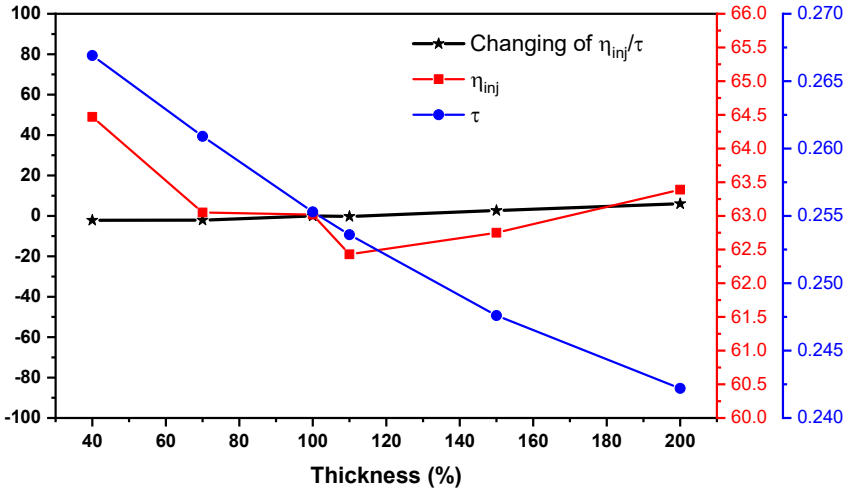

Figure 5.35 the simulation of the InP-based QDCL sample.

In conclusion, the thickness changing will not affect the laser performance, the comparison of QDCL samples with varying QD layers will point out the accurate optimizing comes from the energy state design adjusting.

5.3.4.2 The comparison of QDCL samples with different QD levels

In order to research the QDCL property changing under multilayer QD structure, the QDCL samples with varying QD layer per period with identical structure and fabrication is compared in this research. The single and two QD layer per period has the same structure as the 3 layers structure shown in pervious section, as shown in Figure 5.36, the structure of QDCL samples with different layers has the same material constitution and the similar epitaxial thickness. The growth condition and doping level is also identical for both active region (MBE) and waveguide (MOCVD).

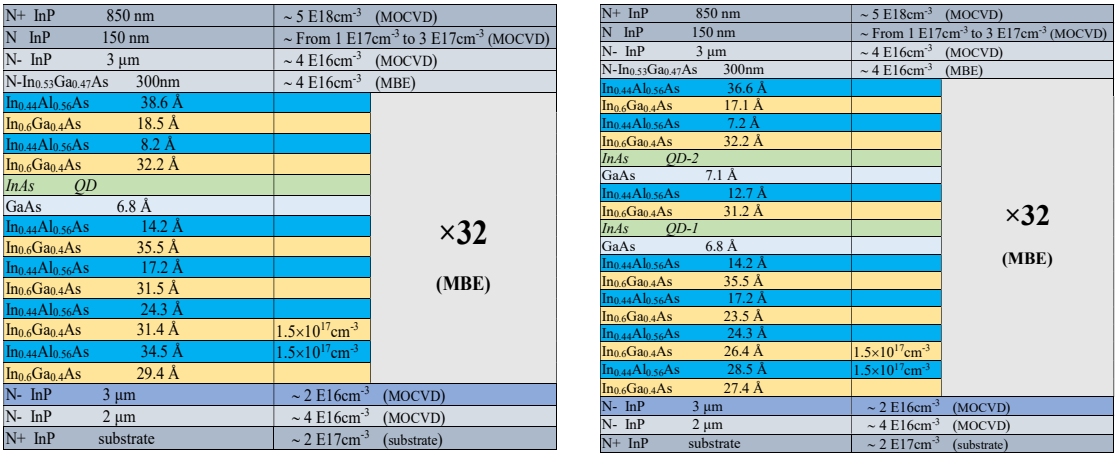

(a) *(b)*

Figure 5.36 the structure of InP-based QDCL with (a) 1 layer QD, (b) 2 layer QD.

In the assumption of the QDCL under multilayer QD structure, samples with 1 layer QD has the problem of energy state mismatch, and samples with 3 layer QD face the trouble of obvious roughness epitaxial layer shown in TEM image (Figure 5.34). The 2 QD layer structure is a mean design between energy state and growth flatness. The XRD results QDCL sample with 2 QD layer is plotted in Figure 5.37. Compare with the result of 3 QD layer structure shown in Figure 5.29, the XRD result of 2 QD layer QDCL samples has much better symmetry, and the outstanding symmetry indicate the interface in active region grown smoothly.

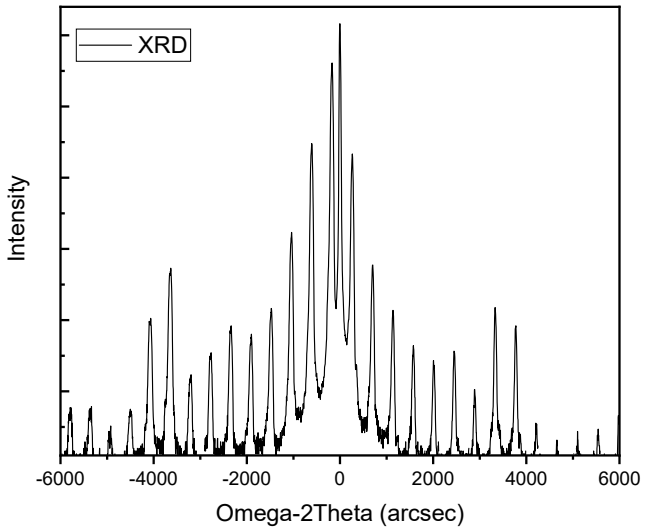

Figure 5.37 the XRD result of QDCL with 2-layer QD per period design.

In order to research the QDCL property changing under multilayer QD structure, the QDCL samples with varying QD layer per period with identical fabrication is compared in this research. All samples were cleaved into 4mm cavity length and applied high-reflective Al_2O_3/Au HR coating in order to reduce the influence of mirror loss and increase the persuasion of comparison.

LI measurement of QDCL with different layer QD per period is tested for comparison, as shown in figures below, the QDCL devices with different QD layers demonstrate entirely different performance. Both of QDCL with 2 and 3 QD structure could operate under RT and c.w. mode, in contrast, the single layer QDCL is only able to work under low temperature and pulse injection current. Three samples are also tested in low temperature with same condition, and the result shown in Figure 5.37 appears that QDCL with 2 layers QD still has the best performance among three samples, which has the highest output power and lowest threshold current.

Considering the few influences caused by active region thickness changing, the impressive progress for laser performance benefit from the coupled QD structure. It is obvious that multilayer QD strategy is expected to guarantee the lasing operation of QDCL, while the inhomogeneous QD make sure the carrier injection because broaden energy state could be helpful for overcoming energy state mismatch. This result validates that QDCL with multilayer QD has better lasing performance than samples with single QD layer owing to its better energy state alignment ability. Among multilayer QD samples, although 3 layers QD structure broaden the miniband for carrier injection, it also suffers from the twisty interface caused by the residual strain. Considering the multilayer QD design increases the error-tolerance in energy state design, but the relevant material recession could not be avoided. The result indicates that 2 layers QD is the appropriate and equal design, it is not only attributed to easier carrier injection but also benefited from less unreleased strain in active region than 3 or more-layer QD samples.

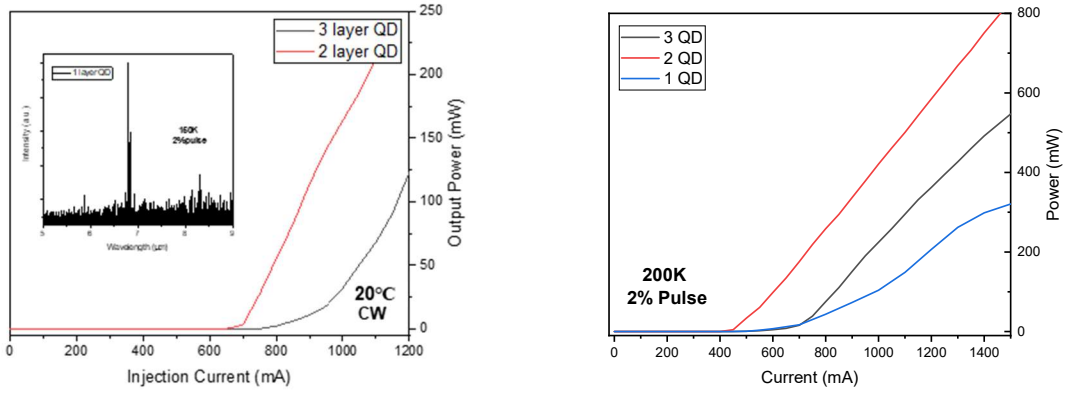

(a) *(b)*

Figure 5.38 the output power comparison among InP-based QDCL sample with varying QD layers (a) under room temperature (b) under 200K.

5.3.4.3 Result and discussion

In the last section, the simulation and comparison experiment revealed that the QDCL with 2 QD layers in one period of active region showed the best lasing performance. While these QDCL samples are not only able to operate under room temperature with the output power over 400mW, which is the highest output power with both room temperature and c.w. mode around all QDCL publications, but also measured two perpendicular directions in terms of lasing operation (Figure 5.41), and the QDCL devices offer persistent lasing operation with whole 360° polarization range.

High performance QDCL

A critical requirement for the practical application of mid-IR light source is to achieve sufficient temperature stability. Theoretically, due to the separation energy level of QD material, QDCL is expected to have better temperature performance and higher slope efficiency. However, due to the limitation of structure design and growth technology, these specialties is not embodied in QDCL at present. In this research, after using the optimizing of 2 layer QD structure and the improvement QCL fabrication process, the performance of QDCL improve a lot, and high performance QDCL devices is shown in this chapter. QDCL samples with 2 QD layer per period continues to utilize flip chip, HR coating and buried heterostructure during fabrication, and cavity length is facet cleaved to 4mm. After optimization, the QDCL obtain impressive performance under room temperature and c.w. mode. As shown in Figure 5.39 (a), the c.w. output power at various temperature indicate the c.w. lasing is maintained even the heatsink

temperature rise to 55℃. According to the temperature dependence results from 25℃ to 55℃, the T_0 in room temperature range is calculated around 138.7K (Figure 5.39b) which leads to a high temperature stability. To the overview of previous reports, this is the first QDCL device c.w. operates with over 50℃ and obtained characteristic temperature as high as 138.7K under c.w. current driving. The requirement of thermo-electric cooling for QCL devices could hence be partly relieved, and the devices could even to keep work without cooling with pulsed injection current.

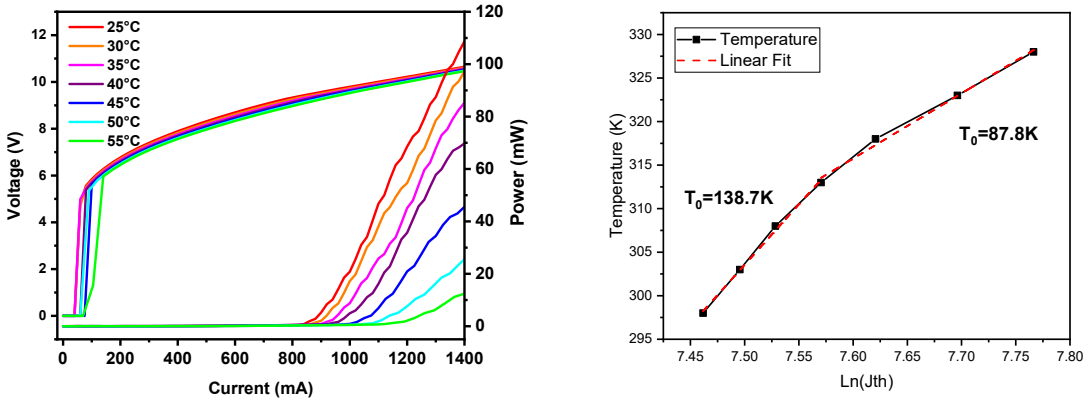

(a) *(b)*

Figure 5.39 (a) the temperature dependence result of InP-based QDCL sample with 2 QD layer per period. (b) the calculated plotting of characteristic temperature

To increase the applicability of QDCL, low threshold current and high optical output power are always desirable goals for laser applications. In order to further improve the lasing performance, the QDCL is face-down mounted on a diamond heatsink instead of copper heatsink. The light-current curve of an outstanding QDCL is plotted in Figure 5.40 (a), at room temperature (16℃), 425mW highest power was observed with 1300mA injection current and the slope efficiency was measured as high as 0.6W/A, which is the record output among past publications. The threshold current of this devices is controlled to around 600mA and the calculated threshold current density is only 1kA/cm^2. The lasing spectrum under 620mA injection current was described in Figure 5.40 (b), the shapely curve and 3nm narrow linewidth is the evidence of superior quality lasing, and it also demonstrates the wavelength of the QDCL in research is around 7.2μm. The value of high output power and low threshold current of this QDCL is comparable to that of QCL, the optimizing in structure design and outstanding progress improve the QDCL property, and results in enhancing the applicability for mid-infrared light sources.

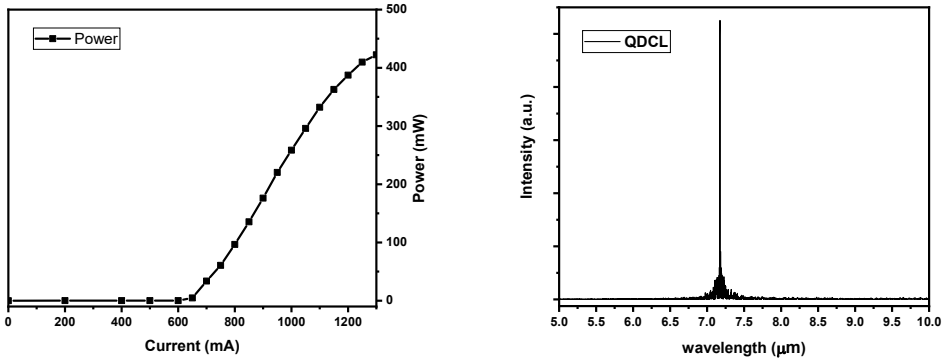

(a) *(b)*

Figure 5.40 (a) the LI curve of InP-based QDCL sample under room temperature and c.w. mode. (b) the lasing spectrum of QDCL samples.

Polarization measurement

As mentioned in the beginning of this chapter, QDCL has the potential to overcome the output direction limitation in TM. In this research, the polarization measurement is tested for the high performance QDCL devices, and the result shows that QDCL has the multi direction output like other QD laser devices [20, 40]. In the polarization measurement, the QDCL samples are tested under room temperature and c.w. mode. A polarizer is placed between the laser devices and power meter, the injection current driving hold on 110mA, and each output power was measured after collimation with one of the 2° polarization angle changing from 0° to 360°.

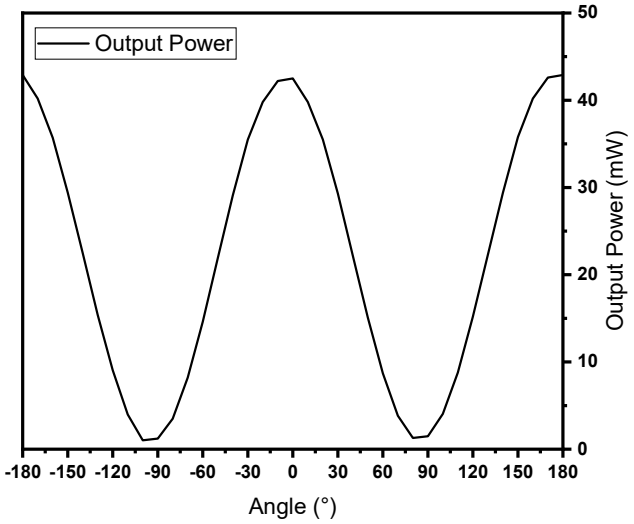

Figure 5.41 the curve of output power verse polarization angle for InP-based QDCL with room temperature and c.w. mode measurement condition.

As shown in Figure 5.41, the curve of power and polarizer angle manifest the QDCL devices shows lasing operation in each direction. The polarization angle with the highest power is defined as the origin point, owing to the measured devices has no HR coating, the laser emits in both facets, and it leads to the result cover two whole variation period. A regular periodic relationship between output power and polarization angle is found, the value of power gradually drops to the bottom during 90° polarizing, and then, it turns back to highest power when the polarization angle further increases to 180°. The laser property with 0° and 90° polarization gives the index of TM and TE mode respectively.

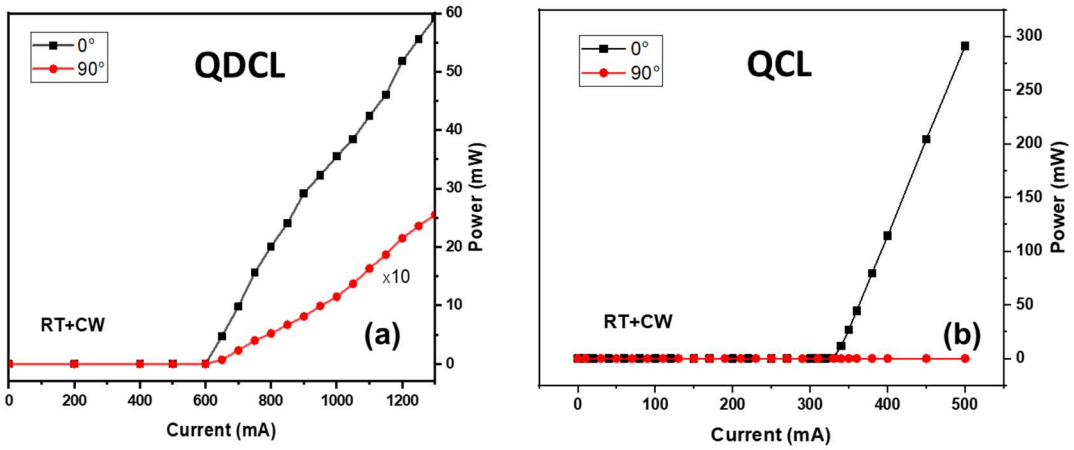

Figure 5.42 the LI curve of the (a) InP-based QDCL sample; (b) QCL sample with 0° (TM) and 90° (TE) polarization.

Based on the standardization of polarization angle, the output power measurement with both 0° (TM) and 90° (TE) polarization is plotted in figures above. As shown in Figure 5.42 (a), the lasing is verity occurring in two orthogonality direction, after 90° polarization, lasing operation was still tested with same threshold current and similar trend. Under room temperature and c.w. mode operation, the output power with 0° polarization reaches 60mW when injection current arrives 1300mA, and that of 90° polarization is only around 2.5mW. Although the output power in TM mode is around 24 times larger than that of TE mode, it is emphasized coexist of lasing operation on both TM and TE mode. Due to the growth of active region could not be absolute flat, the inflect interface will also generate TE mode output in general QW-QCL devices [32-35]. However, in normally operated QW QCL, the proportion of TE mode is only around 0.2%, as shown in Figure 5.42 (b), there is no visible lasing result after

90°polarization for general QCL device. Compare with the 4% TE occupation in QDCL, the TE mode in QW QCL is nearly ignored.

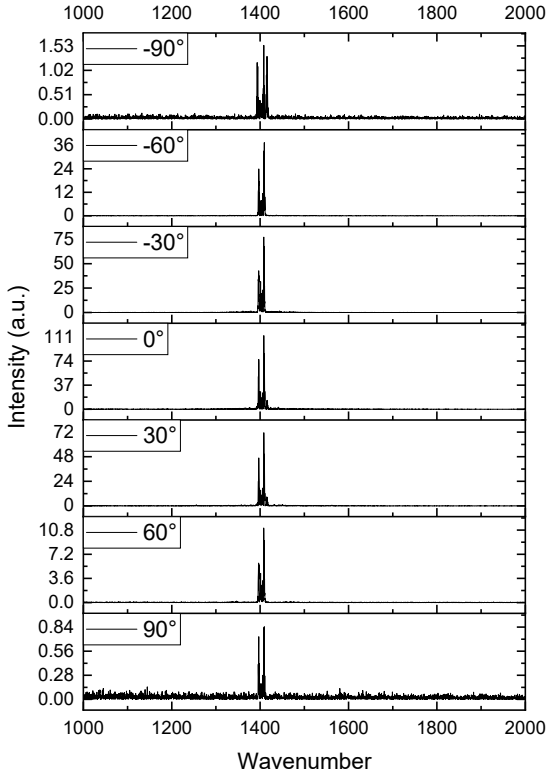

Figure 5.43 the spectrum of InP-based QDCL sample with different polarized angle.

Furthermore, the spectrum is also favoured to identify the lasing, we also measured the lasing spectrum with different polarization angle by Bruker Equinox 55 FTIR spectrometer. The spectrum mapping with various polarization is demonstrated in Figure 5.43. All the shapes of spectrums are identical, and the changing of intensity matches with that of the output power in Figure 5.41, this result is obvious evidence of lasing in each polarization angle. By and large, lasing operation under all polarization angle proves the transition between QD energy states, and it also indicates the great potential of QD in multi-direction lasing. Additionally, the polarization measurement could be regarded as a significant progress based on the breakthrough in the bottleneck of single emitting direct of QCL devices, and it capable of applying for mid-infrared wavelength surface emitting laser.

5.3.5 Conclusion

In this chapter, QDCL continue to use the InP/InAlAs/InGaAs material system, so the structure design and fabrication process of QDCL samples is similar as that of InP-

based QCL devices shown in chapter 5. After demonstrating room temperature operation QDCL devices, we pay attention to the further structure optimization and property improvement. The research of QDCL with different layer QD per period indicate that the 2 layer QD design is found to broaden the energy state and make sure the carrier injection efficiency, it leads to the lasing property progress effectively. After utilizing this structure optimizing method, we demonstrate a room temperature electrically pumped c.w. QDCL with significantly improved lasing performance than previous reports and realize QDCL with both TM and TE lasing operation. Researching and using the multilayer QD mode is contributed to the output power and operation temperature breakthrough 400mW and 55℃ with c.w. injection current. It is noted that the high performance QDCL with both TM and TE direction lasing overcome the theoretical limitation of QCL single output direction, and this breakthrough has great application potential which could open the way of processing the surface emitting QCL and broaden the mid-infrared light source marketing. In addition, based on the great ability of dislocation tolerance, the QDCL is also expected to realize high-performed mid-infrared laser grown on Si substrate for silicon photonics.

5.4 Si-based QCL for mid-infrared integration

5.4.1 Experimental results of QW-QCL on Si

For mid-infrared photonic integrated circuits, several exciting results are reported by using mature Ge-on-Si platform in which the Ge offers perfect waveguide and Si substrate supports the integration of optical components [42-46]. To achieve the Si-based QCLs, both GaAs-based and InP-based material systems were investigated. Due to the lattice mismatch, the Ge/Si template can be used for the epitaxial growth of GaAs and InP QCLs. In particular, for the InP-based QCL, an InP/Ge/Si virtual template is needed due to the large lattice mismatch.

Figure 5.44 (a) and (b) show the active region designs of GaAs-based and InP-based QCLs on Ge/Si virtual substrates, respectively, which are same structures in chapter 5.2. The only difference in both structures is that a thick highly doped layer is first grown on the virtual substrate before growing the QCL structure, in order to form a metal contact at the bottom in top-top configuration Si-based lasers.

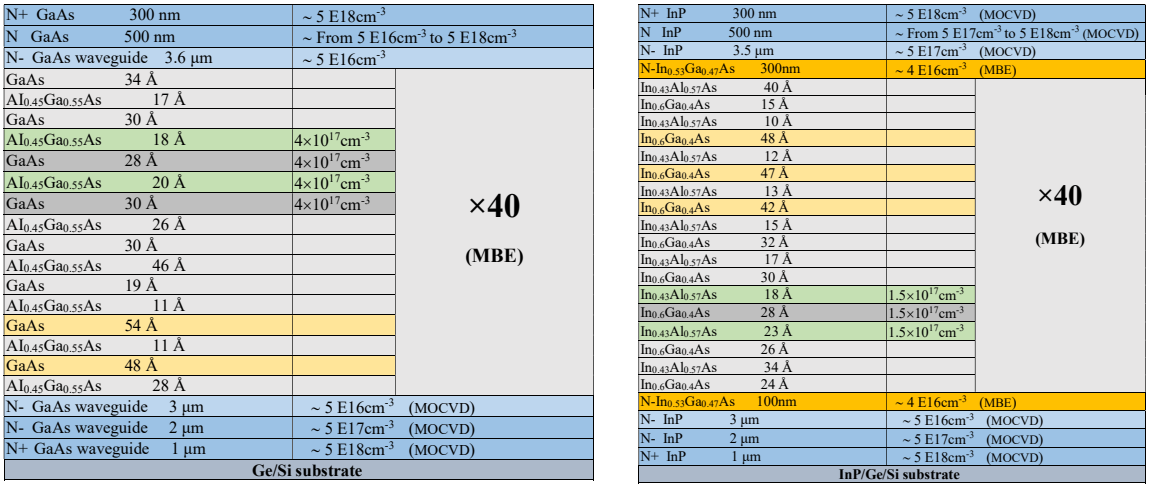

(a) *(b)*

Figure 5.44 the designed structure of (a) Si-based GaAs/AlGaAs QCL (b) Si-based InP/InAlAs/InGaAs QCL.

However, both Si-based GaAs/AlGaAs and InP/InAlAs/InGaAs QCLs didn't show any lasing property at present. There are four main issues for the failure of lasing operation: (1) high density of threading dislocation, (2) change in growth condition (3) thermal cracks, and (4) fabrication limitation by laser structure.

First of all, the high density of threading dislocations, acting as non-radiative recombination centres, significantly degrades the device performance, particularly in case of QW-based lasers as mentioned in chapter 1. Furthermore, the dislocation filter layers (DFLs) were not employed in both structures in Figure 5.44.

Second, the change of growth condition may cause low-quality materials. In MBE system, the growth rate and material quality are significantly affected by the growth temperature. Since the thermal conductivity of Si substrates is totally different from that of GaAs and InP substrates, thermal dynamics on Si-based materials during the growth would be different. Thus, the use of previous growth condition may induce different growth rate and incorrect thickness, resulting in low-quality epitaxial layers.

Third, the formation of thermal cracks, originating from the mismatch of thermal expansion coefficient between III-V and Si, substantially reduces the yield of device fabrication. The thermal crack is the most serious issue because laser devices cannot be fabricated even with the presence of a single crack line. In general, the density of thermal cracks increases with increasing the thickness of epitaxial layers. Thus, the Si-based QCL structure, commonly requiring the whole-layer thickness of at least 10

μm, is highly vulnerable to the formation of thermal cracks. Figure 5.45 (a) and (b) display the microscopic images of thermal cracks on the Si-based GaAs and InP QCLs, respectively. Furthermore, Figure 5.46 shows the cross-section image of a Si-based InP/InAlAs/InGaAs QCL device after fabrication. During the wet etching process, the acid etchant enlarges the thermal cracks, creating grooves and leading to the fragmented device in the end. Therefore, it is obvious that high density of thermal crack on the surface of Si-based QCL wafers significantly reduces the yield of devices and leads to the failure of device operation.

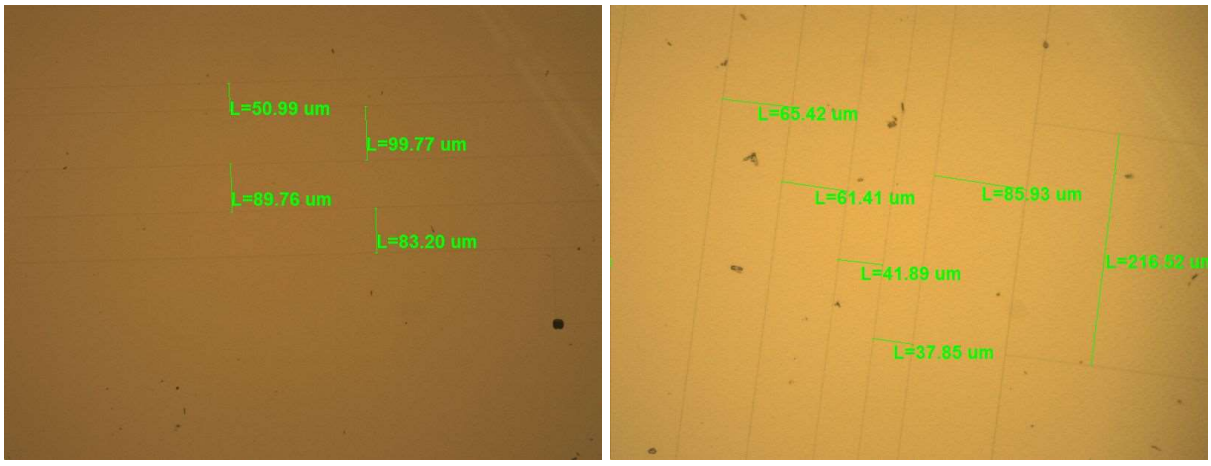

(a) (b)

Figure 5.45 the microscope images of the wafer surface of (a) Si-based GaAs/AlGaAs QCL (b) Si-based InP/InAlAs/InGaAs QCL samples.

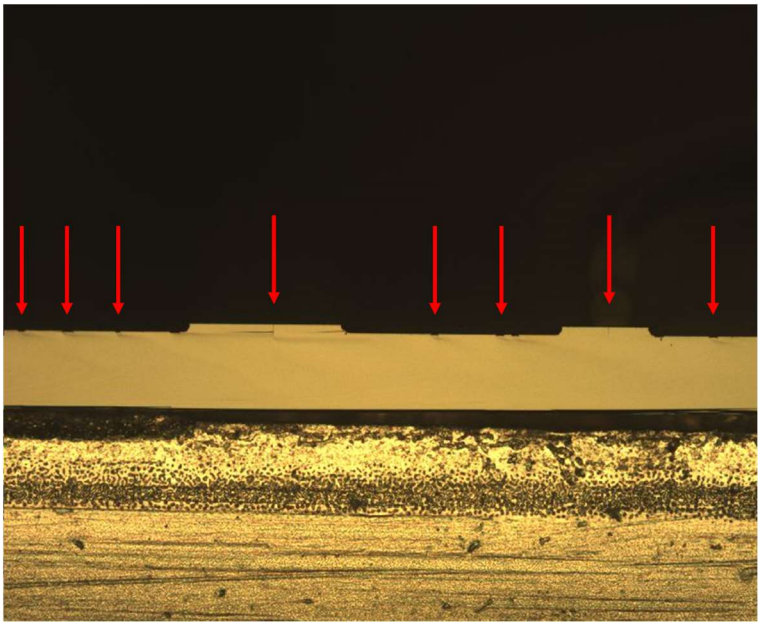

Figure 5.46 the cross-section microscope images of Si-based InP/InAlAs/InGaAs QCL devices with cracks.

Finally, the fabrication limitation, coming from the Si-based device structure (top-top configuration), also impacts the operation failure. Since silicon substrate cannot be used for metal deposition layer, the top-top structure should be utilized in Si-based devices in which two metal contacts are formed on the top surface. Thus, the flip-chip bonding and buried heterostructure shown in chapter 5.2.4, which can substantially improve the device performance, could not be applied to Si-based samples.

5.4.2 Future works for optimizing QCL on Si

In order to solve the issues found in previous section, several optimizing ideas for Si-based QCL are proposed:

- DFLs utilized in previous Si-based O-band QD laser should be applied to Ge/Si substrate before the growth of GaAs and InP QCLs. In addition, together with the DFLs, the GaAs and InP buffer layers on Ge/Si substrates would be effective in reducing the density of threading dislocation, but it is required to optimize the thickness of buffer layer because the thick buffer aggravates the thermal crack issues.
- Further optimization of growth condition, such as growth rate, layer thickness, III/V ratio, and so on, needs to be carried out. To qualify the grown layers, various measurement tools, including TEM, PL, and XRD, will be utilized.
- The thermal crack is an inevitable problem for III-V growth on Si substrate, but it could be partially relieved by reducing the whole QCL thickness. The thickness of active region should not be reduced without careful analysis, but decrease of the thickness of upper and down waveguide could result in effective thickness thinning because waveguide thickness occupies the major proportion in whole QCL thickness. Since the function of waveguide with low refractive index is to confine the light in active region, the simulation should be established to calculate the relationship between waveguide thickness and waveguiding, as well as the effect of doping level, material reflectivity and coherent efficiency.
- The fabrication could also be improved in spite of the limitation coming from silicon substrate and thermal crack. The crack distribution in Figure 5.45 demonstrates that the space between cracks is still able to provide enough place for narrow ridge formation. Therefore, the elaborate arrangement of ridge during the photolithograph could increase the yield of device fabrication. In

addition, using dry etching, instead of wet etching, could avoid the damage caused by permeated acid in thermal cracks.

- To enable the flip-chip bonding with the top-top configuration, a new device structure is designed for Si-based QCL devices. As shown in the Figure 5.47, during the ridge etching, an additional ridge is retained with the equal height to cavity ridge. With the specially made AlN heatsink, two ridges could be face-down mounted on the heatsink with separated metal contact areas.
- As mentioned in chapter 5.3, QDCL is supposed to have better temperature stability and higher slope efficiency in principle. However, the growth of quantum dot in QCL structure is more difficult than general QCL devices, causing poor performance of reported QDCL. Compared with traditional QCL devices, however, QDCL has the unique advantage of tolerance to threading dislocations, which is more suitable for Si-based QCL where a lot of dislocations are inevitably generated. Once the number of periods in active region can be further increased through the optimization of QD growth, the Si-based QDCL might offer higher gain and better performance than the conventional QW-based QCL on Si, owing to the insensitivity to the dislocation. At present, QW-QCL dominates the market in mid-infrared light sources and QDCL is still not able to achieve commercialization. However, in terms of Si-based QCL for mid-infrared Si photonics, the QDCL is more feasible.

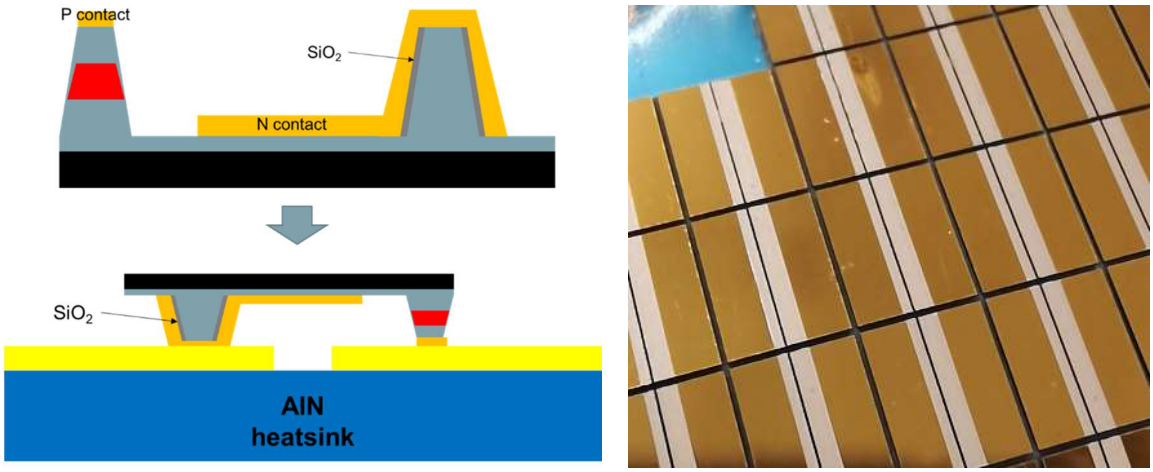

(a) *(b)*

Figure 5.47 (a) the schematic diagram of Si-based devices flip chip (b) the AlN heatsink used for Si-based devices flip chip.

These methods in fabrication and sample growth aim to solve the problem founded in the previous experiment, and it is reasonable to believe that the Si-based QCL could be further improved with the continuous experiment and optimization.

References

[1] Chen, S., Li, W., Wu, J., Jiang, Q., Tang, M., Shutts, S., Elliott, S. N., Sobiesierski, A., Seeds, A. J., Ross, I., Smowton, P. M., & Liu, H. (2016). Electrically pumped continuous-wave III-V quantum dot lasers on silicon. Nature Photonics, 10(5), 307–311.

[2] D. Liang and J. E. Bowers, “Recent progress in lasers on silicon,” *Nat. Photonics*, vol. 4, no. 8, pp. 511–517, 2010.

[3] A. Spott, Y. Liu, T. Baehr-Jones, R. Ilic, and M. Hochberg, “Silicon waveguides and ring resonators at 5.5 μm,” Appl. Phys. Lett. 97, 213501, (2010).

[4] L. Shen, N. Healy, C. J. Mitchell, J. S. Penades, M. Nedeljkovic, G. Z. Mashanovich, and A. C. Peacock, “Mid-infrared all-optical modulation in low-loss germanium-on-silicon waveguides,” Opt. Lett. 40, 268–271,(2015).

[5] N. Hattasan, B. Kuyken, F. Leo, E. Ryckeboer, D. Vermeulen, and G. Roelkens (2012). High-efficiency SOI fiber-to-chip grating couplers and lowloss waveguides for the short-wave infrared. *IEEE Photon. Technol. Lett*. 24, 1536–1538

[6] A. Malik, M. Muneeb, S. Pathak, Y. Shimura, J. Van Campenhout, R. Loo, and G. Roelkens. (2013) Germanium-on-silicon mid-infrared arrayed waveguide grating multiplexers. *IEEE Photon. Technol. Lett*. 25, 1805–1808.

[7] Hu. T, Dong. B, Luo. X, Liow. T, Song. J, Lee. C, and Lo.G. (2017) Silicon photonic platforms for mid-infrared applications. Photon. Res. 5, 417-430

[8] L. Shen, N. Healy, C. J. Mitchell, J. S. Penades, M. Nedeljkovic, G. Z. Mashanovich, and A. C. Peacock, “Mid-infrared all-optical modulation in low-loss germanium-on-silicon waveguides,” Opt. Lett. 40, 268–271, (2015).

[9] Yao, Y., Hoffman, A. J., & Gmachl, C. F. (2012). Mid-infrared quantum cascade lasers. Nature Photonics, 6(7), 432–439. https://doi.org/10.1038/nphoton.2012.143

[10] Liu, Z., Hantschmann, C., Martin, M., Baron, T., Chen, S., Seeds, A., Penty, R., White, I., Liao, M., Tang, M., Lu, Y., S., Sanchez, A., & Liu, H. (2020). Origin of Defect Tolerance in InAs/GaAs Quantum Dot Lasers Grown on Silicon. *Journal of Lightwave Technology*, 38(2), 240–248.

[11] Wang, H., Zhang, J., Cheng, F., Zhuo, N., Zhai, S., Liu, J., Wang, L., Liu, S., Liu, F., & Wang, Z. (2020). Watt-level, high wall plug efficiency, continuous-wave room temperature quantum cascade laser emitting at 77μm. *Optics Express*, 28(26), 40155.

[12] Markus, S., Julian, H., Michael, J., Peter, M., Matthias, G., and Boris, M. (2016) Mid-Infrared Spectroscopy Platform Based on GaAs/AlGaAs Thin-Film Waveguides and Quantum Cascade Lasers. *Analytical Chemistry*, 88 (5), 2558-2562 DOI: 10.1021/acs.analchem.5b04144

[13] Blaser S, Yarekha D, Hvozdara L, et al. Room-temperature, continuous-wave, single-mode quantum-cascade lasers at 5.4 μm. *Applied Physics Letters*, 2005, 86: 1-3.

[14] Beck M, Hofstetter D, Aellen T, et al. Continuous wave operation of a mid-infrared semiconductor laser at room temperature. Science, 2002, 295(5553): 301-305.

[15] A. Lyakh, C. Pflügl, L. Diehl, Q. J. Wang, F. Capasso, X. J. Wang, et al. 1.6 W high wall plug efficiency, continuous-wave room temperature quantum cascade laser emitting at 4.6 μm. *Applied Physics Letters*, 2008, 92: 111110.

[16] A. Lyakh, R. Maulini, A. Tsekoun, R. Go, C. Pflügl, L. Diehl, et al. 3 W continuous-wave room temperature single-facet emission from quantum cascade lasers based on nonresonant extraction design approach[J]. Applied Physics Letters, 2009, 95: 141113.

[17] Faist, J., Capasso, F., Sivco, D. L., Sirtori, C., Hutchinson, A. L., & Cho, A. Y. (1994). Quantum cascade laser. Science, 264(5158), 553–556. https://doi.org/10.1126/science.264.5158.553

[18] P. Blood, “3.3 III-V semiconductor alloys,” in *Quantum confined laser devices : optical gain and recombination in semiconductors*, First edit., Oxford University Press, 2015, pp. 25–27.

[19] M. Fox, “Quantum-confined structures,” in *Optical properties of solids*, Oxford University Press, 2010, pp. 141–144.

[20] Y. Arakawa and H. Sakaki, “Multidimensional Quantum Well Laser and Temperature-Dependence of Its Threshold Current,” *Appl. Phys. Lett.*, vol. 40, no. 11, pp. 939–941, 1982.

[21] H. C. Liu, and F. Capasso, Intersubband Transitions in Quantum Wells Physics and Device Applications II, Semiconductors and Semimetals, 66,13 (Academic Press, 2000).

[22] Dmitriev, I. A., & Suris, R. A. (2008). Quantum dot cascade laser: Arguments in favor. *Physica E: Low-Dimensional Systems and Nanostructures*, 40(6), 2007–2009.

[23] Maulini, R., Lyakh, A., Tsekoun, A., & Patel, C. K. N. (2011). Wall-Plug Efficiency At Room Temperature. 19(18), 4831–4835.

[24] Harrer, A., Szedlak, R., Schwarz, B., Moser, H., Zederbauer, T., MacFarland, D., Detz, H., Andrews, A. M., Schrenk, W., Lendl, B., & Strasser, G. (2016). Mid-infrared surface transmitting and detecting quantum cascade device for gas-sensing. *Scientific Reports*, 6(November 2015), 2–7. https://doi.org/10.1038/srep21795

[25] C. Sciancalepore et al. (2011) Quasi-3D light confinement in double photonic crystal reflectors VCSELs for CMOS-compatible integration. *J. Lightw. Technol.*, vol. 29, no. 13, pp. 2015–2024, Jun. 1.

[26] Ustinov, V. M., Maleev, N. A., Kovsh, A. R., & Zhukov, A. E. (2005). Quantum dot VCSELs. *Physica Status Solidi (A) Applications and Materials Science*, 202(3), 396–402.

[27] Xu, D., Tong, C., Yoon, S. F., Fan, W., Zhang, D. H., Wasiak, M., Piskorski, Ł., Gutowski, K., Sarzała, R. P., & Nakwaski, W. (2009). Room-temperature continuous-wave operation of the In(Ga)As/GaAs quantum-dot VCSELs for the 1.3 μm optical-fibre communication. *Semiconductor Science and Technology*, 24(5).

[28] Wu, J., Chen, S., Seeds, A., & Liu, H. (2015). Quantum dot optoelectronic devices: Lasers, photodetectors and solar cells. Journal of Physics D: Applied Physics, 48(36).

[29] Bai. Y, Bandyopadhyay. N, Tsao. S, et al. Room temperature quantum cascade lasers with 27% wall plug efficiency. Applied Physics Letters, 2011, 98(18): 181102.

[30] J. Faist, F. Capasso, C. Sirtori, D. L. Sivco, and A. Y. Cho, In: H. C. Liu, and F. Capasso (Eds.), Intersubband Tansitions in Quantum Wells Physics and Device Applications II, Semiconductors and Semimetals, 66, 13 (Academic Press, 2000).

[31] Burnett, B. A., & Williams, B. S. (2014). Density matrix model for polarons in a terahertz quantum dot cascade laser. Physical Review B - Condensed Matter and Materials Physics, 90(15), 1–11.

[32] Zhuo, N., Liu, F. Q., Zhang, J. C., Wang, L. J., Liu, J. Q., Zhai, S. Q., & Wang, Z. G. (2014). Quantum dot cascade laser. Nanoscale Research Letters, 9(1), 1–7.

[33] Liu, H. C., Buchanan, M., & Wasilewski, Z. R. (1998). How good is the polarization selection rule for intersubband transitions. Applied Physics Letters, 72(14), 1682–1684.

[34] Jerome Faist, “Intersubband scattering processes”, in *Quantum Cascade Lasers*, Oxford University Press, 2013, pp. 67–90.

[35] Harald Schneider, HuiChun Liu, “Quantum Wells and Intersubband Transitions”, in *Quantum Well Infrared Photodetectors*, Physics and Applications Press, Springer, 2007, pp. 13–40.

[36] G. Bastard, Phys. Rev. B, 25, 7584 (1982).

[37] G. Bastard, Wave Mechanics Applited to Semiconductor Heterostructures, (Les Editions de Physiques, Paris, 1990).

[38] J. P. Loehr, and M. O. Manasreh, In: M. O. Manasreh (Ed.), Semiconductor Quantum Wells and Superlattices for Long-Wavelength Infrared Detectors, (Artech House, Boston, 1993).

[39] Maisons G, Carras M, Garcia M, et al. Directional single mode quantum cascade laser emission using second-order metal grating coupler. *Applied Physics Letters*, 2011, 98(2): 021101.

[40] Victor M. Ustinov, Nikolai A. Maleev, Alexey R. Kovsh, Alexey E. Zhukov. (2005). Quantum dot VCSELs. *Phys. Stat. Sol*. (a) 202, No. 3, 396–402

[41] N Zhuo, Jin-Chuan Zhang, Feng-Jiao Wang, Ying-Hui Liu, Shen-Qiang Zhai, Yue Zhao, Dong-Bo Wang, Zhi-Wei Jia, Yu-Hong Zhou, Li-Jun Wang, Jun-Qi Liu, Shu-Man Liu, Feng-Qi Liu, Zhan-Guo Wang, Jacob B. Khurgin, and Greg Sun. Room temperature continuous wave quantum dot cascade laser emitting at 7.2 μm. *Opt. Express*. 25, 13807-13815 (2017)

[42] Soref, R. (2010). Mid-infrared photonics in silicon and germanium. *Nature Photonics*, 4(8), 495–497.

[43] Hu. T, Dong. B, Luo. X, Liow. T, Song. J, Lee. C, and Lo.G. (2017) Silicon photonic platforms for mid-infrared applications. *Photon. Res*. 5, 417-430

[44] Lin, H., Luo, Z., Gu, T., Kimerling, L. C., Wada, K., Agarwal, A., & Hu, J. (2017). Mid-infrared integrated photonics on silicon: A perspective. *Nanophotonics*, 7(2), 393–420.

[45] Shankar, R., & Lončar, M. (2014). Silicon photonic devices for mid-infrared Applications. *Nanophotonics*, 3(4–5), 329–341.

[46] Spott, A., Peters, J., Davenport, M. L., Stanton, E. J., Merritt, C. D., Bewley, W. W., Vurgaftman, I., Meyer, J. R., Kirch, J., Mawst, L. J., Botez, D., & Bowers, J. E. (2016). Quantum cascade laser on silicon at 4.8 μm. 2016 Conference on Lasers and Electro-Optics, CLEO 2016, 3(5).

Chapter 6
Summary and future work

6.1 Summary

This thesis aims to realize high performance and high reliable Si-based laser devices with O-band and mid-infrared wavelength for silicon photonics. Researches of both QD laser diodes with 1.3 μm wavelength and quantum cascade laser with mid-infrared wavelength are investigated in this thesis.

Chapter 1 introduces the motivation for researching monolithic integrated Si-based III-V laser for Si photonics in the beginning. After that is review of the challenges of III-V material monolithically grown on Si, and then the development of Si-based laser with 1.3μm wavelength is presented. The progress of quantum cascade laser is also reviewed in chapter 1.

The brief introduction of MBE is displayed in the start of chapter 2. Then, this chapter details the experimental methods used to obtain the material characteristics by PL, AFM, HXRD, SEM and TEM. Then, laser devices fabrication process and sample measurement are demonstrated.

Chapter 3 pays attention to the comparisons between QD and QW laser devices grown on on-axis Si substrate. After the data collection, the analysis of measured results proves that Si-based QD laser devices is more insensitive to dislocations and has higher possibility to operate lasing, compared with Si-based QW devices. Besides, high performance QD laser devices monolithically grown on-axis Si (001) with 160A/cm^2 threshold current density and 66 °C c.w. operation temperature is achieved in this chapter.

Chapter 4 reports the all-MBE QD laser monolithically grown on Si substrates following the previous research. two approaches using Si buffer and Ge buffer are employed to growth QD lasers structures to obtain all-MBE grown QD lasers on on-axis Si substrate. Under pulsed injection current driving, the Si-based QD laser with 200nm Si buffer produces J_{th} of 260 A/cm^2, T_0 of 95 K. After utilizing 300nm Ge buffer layer instead of

the Si buffer, the distinct development in material quality and laser performance is obtained by QD laser all-MBE grown on Si (001) substrate, while the threshold current density decreases to 200 A/cm^2 and the highest operation temperature reaches 130°C.

Chapter 5 demonstrated the research process of Si-based QCL for mid-infrared silicon photonics. The research of high performance QCL devices was explored in the beginning, and then, several efforts have been done on the fabrication improvement. The manufacture progress leads to lasing property enhancement apparently, thus a well-performed InP-based QCL device realize operation over 100°C under c.w. mode. Due to QD has been proved as suitable material for Si-based laser, the research of QDCL is also demonstrated in chapter 5. After the optimizing of structure design, the QDCL with multilayer QDs shows comparable performance, compared with conventional QCL devices. The polarization measurement shows that the QDCL generates both TE and TM modes output, which is a breakthrough towards surface emitting QCL. Because of Covid-19 influences the process of Si-based QCL, there is no enough optimizing and growth improvement prepared for Si-based QCL sample, all the grown Si-based QCL wafers show no lasing operation after fabrication. Several optimization approaches based on existing issues are discussed, and it is possible to achieve Si-based QCL devices with further material improvement and process development in future works.

6.2 Future work

6.2.1 QCL devices monolithically grown on Si

6.2.1.1 InP-based QCL directly grown on Si substrate

Mid-infrared laser devices have wide market and the Si-based mid-infrared laser is highly demanded by silicon photonics, hence the continuous researches are focused on Si-based mid-infrared laser [1-4]. QCL has the unique advantages like broaden wavelength range and flexible structure design, the Si-based QCL is desired for meeting the requirement of mid-infrared integration [5-7]. According to the previous results in this work, the performance of GaAs-based QCL is not enough to support the Si-based QCL because the further performance drop comes from dislocation and crack will exterminate the possibility of lasing. The QCL devices with InP material system are benefited by excellent thermal conductivity of InP material and mature structure design of InP/InAlAs/InGaAs system, InP-based QCL with impressive

performance has great potential to be transplanted to Si platform. Following the researches in chapter 5, the continuous improvement and optimizing should be helpful for achieving Si-based QCL. Until now, there is still no Si-based QCL devices working under room temperature and c.w. mode [7]. The objective of my further work is realizing the InP-based QCL grown on Si substrate with high reliable which could operate under room temperature and c.w. condition.

6.2.1.2 Microdisk QCL on Si

III-V microdisk lasers have shown intensive progress in last two decades, due to the advantages of microcavity, such as high Q-factor, small foot-print, and extremely low threshold [8-10]. In particular, the microdisk lasers are also regarded as a promising light source for photonic integrated circuits because of dense integration with low power consumption [11]. In addition, compared with the conventional FP lasers, it is easier for microcavity to achieve longitudinal single-mode lasing due its compact size providing only one mode choice in gain spectrum [12]. With the constant development in III-V microdisk laser, the various methods for cavity fabrication have been realized, as shown in Figure 6.1.

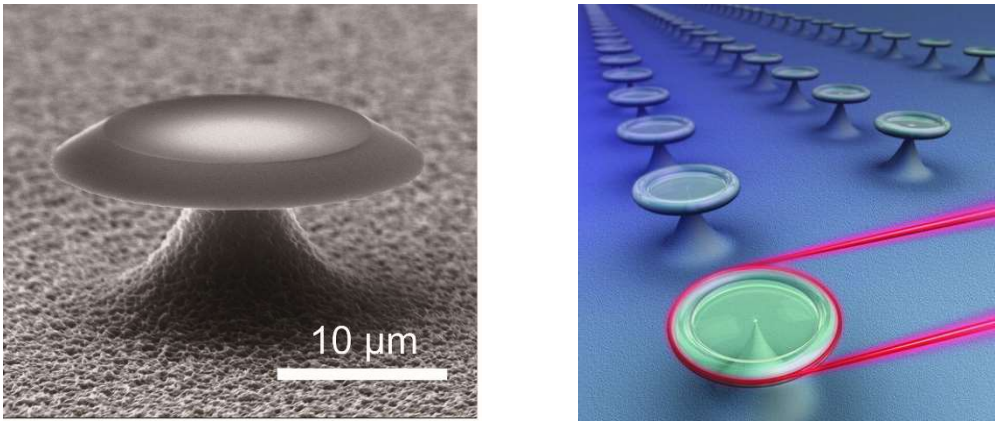

(a) *(b)*

Figure 6.1 (a) the TEM image of single microdisk laser (b) the sketch of microdisk laser array. [11,12]

Particularly, for Si-based laser devices, the microdisk structure reduces the influences coming from dislocation and cracks generated in the interface between III-V epitaxial layer and substrate. Accordingly, several remarkable InP-based microcavity structures grown on Si substrate have been demonstrated.

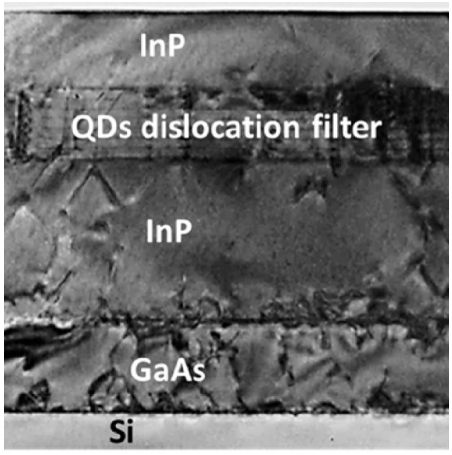

Figure 6.2 the TEM image of single microdisk laser. This TEM image shows the design of buffer layer of Si-based InP samples, the QDs are grown to reduce the density of dislocation which play the roles like the dislocation filter layer in previous researches [13]

Nowadays, InP/GaAs/Si and InP/Ge/Si substrate have been widely used for the growth of InP on Si substrate [13]. As demonstrated in Figure 6.2, high-quality InP epitaxial layer can be grown on top of the GaAs buffer layers with the dislocation filter layers. Combining with the researches in chapter 4, it is expected to further improve the quality of InP on Si substrate via utilizing the Ge buffer and dislocation filter layer before InP growth. With the improvement of epitaxy quality and dislocation tolerance of microdisk structure, the Si-based microdisk QCL is believed to provide high performance.

6.2.2 Surface emitting quantum cascade laser (SEQCL)

As shown in chapter 1, mid-infrared QCL is desirable for various application, such as gas sensing, space communication and medical instruments [14-17]. In order to improve the quality of light in far field and further enhance the application value, SEQCL has been developed by many researchers [18]. Surface emitting laser devices could offer narrow divergence angles and easy integration process [19]. However, due to the nature of intersubband transition which limits the output direction of QW-QCL, several strict conditions are required to obtain the SEQCL [20]. Generally, employing Bragg gratings or photonic crystal is common ways [21,22].

6.2.2.1 InP QCL with Bragg grating

A feasible approach of SEQCL is the use of second-order Bragg distributed feedback grating. The propagation of light in the DFB laser can be described as [23]:

$$\begin{cases} m \cdot \lambda = 2 \cdot n_{eff} \cdot \Lambda \\ \sin\phi = \sin\theta + \dfrac{q \cdot \lambda}{n_{eff} \cdot \Lambda} \end{cases} \tag{6.1}$$

In this formula, λ is the wavelength in vacuum, Λ means the period of grating, n_{eff} is the effective refractive index, ϕ and θ stand for diffraction angle and incidence angle. The second-order mode DFB will be obtained when m=2. After calculating, there are two possible output directions, the optical direction towards 0° and 90° which are horizontal and vertical direction, respectively. As a result, the QCL devices with second order Bragg grating could offer the vertical optical output theoretically. Due to the long wavelength of QCL requiring a high value of Λ, the large period width reduces the difficulty in grating fabrication. The calculated period for second order grating for 7 μm wavelength QCL devices is around 1.4 μm width, meaning that electron-beam lithography and inductively coupled plasma etching could completely cover the requirement of grating process.

After grating fabrication and wafer regrowth, the device fabrication needs to adjust several steps to open the top surface for output light. As shown in figure 6.3, an optical window is opened in the bottom contact, so that the output light could propagate from the top surface after flip-chip mounting.

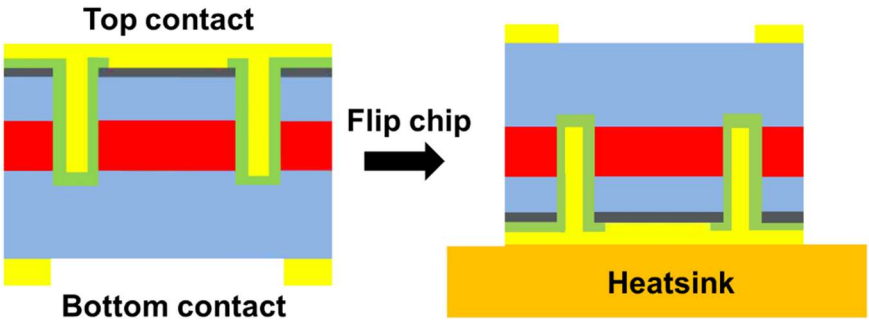

Figure 6.3 the schematic diagram of surface emitting QCL.

Consequently, the fabrication process has no obvious changing with the pervious process, and the sample growth is also reasonable according to the experience of MOCVD and MBE in previous works. Based on the high performance InP-based QCL devices, the research of SEQCL with second-order Bragg distributed feedback grating is a valuable and feasible target in my further work.

6.2.2.2 QDCL VCSEL

Vertical-cavity surface emitting laser (VCSEL) has been considered as one of the most important low-cost light sources in market, due to its advantages such as low foot-print and low power consumption [25-26]. In addition, QD-based VCSELs have already been demonstrated successfully by many research groups, and the manufacture of 1.3μm and 1.55μm QD VCSELs becomes mature and available for commercialization [27-29]. However, a reliable mid-infrared VCSEL is still not commercialized, due to several issues. First of all, the distributed Bragg reflector (DBR) in top and bottom of VCSEL structure should provide high reflectivity and high flatness, acting as a facet in F-P lasers [30]. The growth of mid-infrared DBR has no technical challenging, but the thick grating thickness (Λ in function 6.1) limits the sample growth. For example, the total thickness of 7μm QCL structure and 2 groups of DBRs will exceed 20 μm, devastating heating dissipation and dropping lasing property. Also, 20 μm thickness is not suitable for commercialization and integration [31].

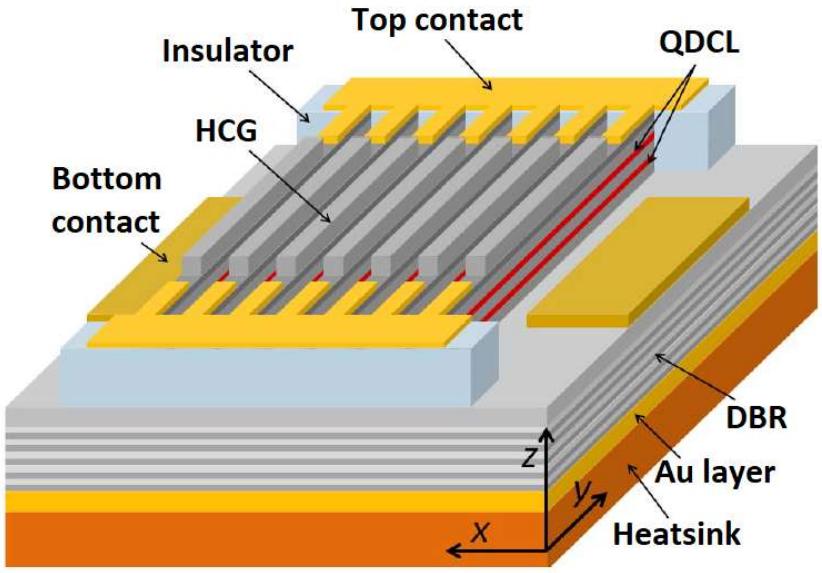

Figure 6.4 the schematic image of QDCL VCSEL structure.

In chapter 5.3, it was shown that the QDCL could be used for SEQCL, due to the unique TE mode emission from QDs [24]. In addition, the use of high-contrast gratings (HCG) offer the possibility of QDCL VCSEL realization. Several publications present that thin HCG layer, instead of thick top DBR, could offer high-refractive-index [32-34], reducing the total thickness and improving the feasibility of QDCL VCSEL [35]. The structure design of the QDCL VCSEL is shown in figure 6.4. The HCG and DBR serve as two facet of FP laser devices. The QD active region offers the optical output in

vertical direction, and the Au layer at the bottom could further increase the reflectivity like HR coating. The fabrication of QDCL VCSEL is related to my pervious works and attractive approach to meet the requirement of mid-infrared surface emitting light source.

References

[1] Soref, R. (2010). Mid-infrared photonics in silicon and germanium. *Nature Photonics*, 4(8), 495–497.

[2] Hu. T, Dong. B, Luo. X, Liow. T, Song. J, Lee. C, and Lo.G. (2017) Silicon photonic platforms for mid-infrared applications. *Photon. Res*. 5, 417-430

[3] Lin, H., Luo, Z., Gu, T., Kimerling, L. C., Wada, K., Agarwal, A., & Hu, J. (2017). Mid-infrared integrated photonics on silicon: A perspective*. Nanophotonics*, 7(2), 393–420.

[4] Shankar, R., & Lončar, M. (2014). Silicon photonic devices for mid-infrared Applications. *Nanophotonics*, 3(4–5), 329–341.

[5] J. R. Reboul, L. Cerutti, J. B. Rodriguez, P. Grech, and E. Tournié. (2011). Continuous-wave operation above room temperature of GaSb-based laser diodes grown on Si. *Appl. Phys. Lett.* 99(12), 121113.

[6] Rio Calvo, M., Monge Bartolomé, L., Bahriz, M., Boissier, G., Cerutti, L., Rodriguez, J.-B., & Tournié, E. (2020). Mid-infrared laser diodes epitaxially grown on on-axis (001) silicon. *Optica*, 7(4), 263.

[7] A. Spott, J. Peters, M. L. Davenport, E. J. Stanton, C. D. Merritt, W. W. Bewley, I. Vurgaftman, C. S. Kim, J. R. Meyer, J. Kirch, L. J. Mawst, D. Botez, and J. E. Bowers. (2016). Quantum cascade laser on silicon. *Optica* 3, 545–551.

[8] T. Zhou, M. Tang, G. Xiang, X. Fang, X. Liu, B. Xiang, S. Hark, M. Martin, M.-L. Touraton, T. Baron, Y. Lu, S. Chen, H. Liu, and Z. Zhang. (2019). Ultra-low threshold InAs/GaAs quantum dot microdisk lasers on planar on-axis Si (001) substrates. *Optica*, Vol. 6, Issue 4, pp. 430-435.

[9] P. Michler, A. Kiraz, Lidong Zhang, C. Becher, E. Hu, and A. Imamoglu. (2000). Laser emission from quantum dots in microdisk structures. Applied Physics Letters 77, 184-186.

[10] V. Bulović, V. G. Kozlov, V. B. Khalfin, S. R. Forrest. (1998). Transform limited, narrow-Linewidth lasing action in organic semiconductor microcavities. *Science*. 23 Jan 1998, Vol. 279, Issue 5350, pp. 553-555

[11] Jiang, X.-F., Zou, C.-L., Wang, L., Gong, Q. and Xiao, Y.-F. (2016). Whispering-gallery microcavities with unidirectional laser emission. *Laser & Photonics Reviews*, 10: 40-61.

[12] F Wang, Y Yang, Y Huang, Z Xiao, and J Xiao. (2018). Single-transverse-mode waveguide-coupled deformed hexagonal resonator microlasers. *Applied Optics*, 57, 7242-7248 (2018).

[13] B. Shi, S. Zhu, Q. Li, Y. Wan, E. L. Hu, and K. M. Lau. (2017). Continuous-Wave Optically Pumped 1.55 μm InAs/InAlGaAs Quantum Dot Microdisk Lasers Epitaxially Grown on Silicon. *ACS Photonics* 4, 204 (2017).

[14] Yao, Y., Hoffman, A. J., & Gmachl, C. F. (2012). Mid-infrared quantum cascade lasers. *Nature Photonics,* 6(7), 432–439.

[15] Malik, A., Spott, A., Stanton, E. J., Peters, J. D., Kirch, J. D., Mawst, L. J., Botez, D., Meyer, J. R., & Bowers, J. E. (2019). Integration of Mid-Infrared Light Sources on Silicon-Based Waveguide Platforms in 3.5-4.7 μm Wavelength Range. *IEEE Journal of Selected Topics in Quantum Electronics*, 25(6).

[16] Jung, S., Palaferri, D., Zhang, K., Xie, F., Okuno, Y., Pinzone, C., Lascola, K., & Belkin, M. A. (2019). Homogeneous photonic integration of mid-infrared quantum cascade lasers with low-loss passive waveguides on an InP platform. *Optica*, 6(8), 1023.

[17] Bai. Y, Bandyopadhyay. N, Tsao. S, et al. (2011). Room temperature quantum cascade lasers with 27% wall plug efficiency*. Applied Physics Letters*, 2011, 98(18): 181102.

[18] Hofstetter D, Faist J, Beck M, et al. (1999). Surface emitting 10.1 μm quantum cascade distributed feedback lasers. *Applied Physics Letters*,1999, 75(24): 3769.

[19] Harrer, A., Szedlak, R., Schwarz, B., Moser, H., Zederbauer, T., MacFarland, D., Detz, H., Andrews, A. M., Schrenk, W., Lendl, B., & Strasser, G. (2016). Mid-infrared surface transmitting and detecting quantum cascade device for gas-sensing. *Scientific Reports*, 6(November 2015), 2–7.

[20] Liu, H. C., Buchanan, M., & Wasilewski, Z. R. (1998). How good is the polarization selection rule for intersubband transitions. *Applied Physics Letters*, 72(14), 1682–1684.

[21] Pflugl C, Austerer M, Schrenk W, et al. (2005). Single mode surface emitting quantum cascade lasers. *Applied Physics Letters*, 2005, 86(21): 211102.

[22] Colombelli R, Srinivasan K, Troccoli M, et al. (2003). Quantum cascade surface emitting photonic crystal laser. *Science*, 2003, 302(5649): 1374.

[23] H. Kogelnik and C. Shank. (1972). Coupled wave theory of distributed feedback lasers. *Journal of applied physics*, vol. 43, pp. 2327 2335, 1972.

[24] Ustinov, V. M., Maleev, N. A., Kovsh, A. R., & Zhukov, A. E. (2005). Quantum dot VCSELs. *Physica Status Solidi (A) Applications and Materials Science*, 202(3), 396–402.

[25] Fumio Koyama. (2006). Recent Advances of VCSEL Photonics. J. Lightwave Technol. 24, 4502-4513 (2006)

[26] Huang, M., Zhou, Y. & Chang-Hasnain, C. (2007). A surface-emitting laser incorporating a high-index-contrast subwavelength grating. *Nature Photonics*, 1, 119–122, 2007.

[27] Xu, D., Tong, C., Yoon, S. F., Fan, W., Zhang, D. H., Wasiak, M., Piskorski, Ł., Gutowski, K., Sarzała, R. P., & Nakwaski, W. (2009). Room-temperature continuous-wave operation of the In(Ga)As/GaAs quantum-dot VCSELs for the 1.3 μm optical-fibre communication. *Semiconductor Science and Technology*, 24(5).

[28] C.-K. Lin, D. Bour, J. Zhu, W. Perez, M. Leary, A. Tandon, et al. (2003). High temperature continuous-wave operation of 1.3 and 1.55μm VCSELs with InP/air-gap DBRs. IEEE J*. Sel. Topics Quantum Electron*., vol. 9, no. 5, pp. 1415-1421, Sep./Oct. 2003.

[29] C. Z. Tong, D. W. Xu, S. F. Yoon, Y. Ding and W. J. Fan. (2009). Temperature Characteristics of 1.3 μm p-Doped InAs–GaAs Quantum-Dot Vertical-Cavity Surface-Emitting Lasers. *IEEE Journal of Selected Topics in Quantum Electronics*, vol. 15, no. 3, pp. 743-748, May-june 2009.

[30] N. Nishiyama, C. Caneau, B. Hall, G. Guryanov, M.H. Hu, X.S. Liu, M.-J. Li, R. Bhat, C.E. Zah. (2005). Long-Wavelength Vertical-Cavity Surface-Emitting Lasers on InP With Lattice Matched AlGaInAs–InP DBR Grown by MOCVD. *IEEE Journal of Selected Topics in Quantum Electronics*, vol. 11, no. 5, pp. 990-998, Sept.-Oct. 2005.

[31] W.W. Bewley, C.L. Felix, I. Vurgaftman, E.H. Aifer; J.R. Meyer, L. Goldberg, J.R. Lindle, D.H. Chow, E. Selvig. (1998). Continuous-wave mid-infrared VCSELs*. IEEE Photonics Technology Letters*, vol. 10, no. 5, pp. 660-662, May 1998.

[32] M. G˛ebski et al. (2015). Monolithic high-index contrast grating: A material independent high-reflectance VCSEL mirror. *Opt. Exp*., vol. 23, no. 9, pp. 11674–11686, 2015.

[33] C. F. R. Mateus, M. C. Y. Huang, Y. Deng, A. R. Neureuther, and C. J. Chang-Hasnain. (2004). Ultrabroadband mirror using low-index cladded subwavelength grating*. IEEE Photon. Technol. Lett*., vol. 16, no. 2, pp. 518–520, Feb. 2004.

[34] M. Dems. (2017). Monolithic high-contrast gratings: Why do they not scatter light. *J. Lightw. Technol.*, vol. 35, no. 2, pp. 159–165, Jan. 15, 2017.

[35] M. G˛ebski, M. Dems, M. Wasiak, J. A. Lott, and T. Czyszanowski. (2015). Monolithic subwavelength high-index-contrast grating VCSEL. *IEEE Photon. Technol. Lett*., vol. 27 no. 18, pp. 1953–1986, Sep. 15, 2015.